Imperial College London

Department of Materials

Effects of Aging on ScSZ/LSCrF Dual-Phase Oxygen Transport Membrane for Syngas Production

Chi Ho Wong

2017

Supervised by Prof. Stephen J. Skinner
Prof. John A. Kilner

Submitted in part fulfilment of the requirements for the degree of Doctor of Philosophy in Materials of Imperial College London and Diploma of Imperial College London

Declaration

I hereby declare that this thesis and the work reported within is a product of my own original research. Information derived from sources beyond this work has been given due acknowledgment and been appropriately referenced.

Chi Ho Wong, 2017

Acknowledgements

I have a few people to thank for their help and support during my time as a PhD candidate at Imperial College London.

First, special thanks go to my supervisors Prof. Stephen Skinner and Prof. John Kilner for their guidance, advice and patience. They were always there to help me whenever I needed it, and their feedback was frequent and highly valued.

My thanks also go out to Dr. Jonathan Lane of Praxair Inc. for his perspectives and suggestions, and Praxair Inc.for funding this project.

I would also like to thank Dr. Sarah Fearn for guidance and operation of the SIMS and LEIS instruments, and Dr. Ignacio Villar-Garcia for assistance on the XPS instrument. I would also like to acknowledge the use of the EPSRC-funded National Chemical Database Service (CDS) hosted by the Royal Society of Chemistry.

I extend my appreciation to the members of the Electroceramics Group, past and present, for their support and conversations towards all things PhD-related. In addition, my thanks go to Chen-Sheng (Jason) Lin, Nick Farandos, and Muneeb Ejaz for their friendship and company, and providing enlightening and interesting perspectives on a wide variety of subjects.

Finally, and most importantly, my gratitude goes to my family: my sisters Vivien and Kitty, and my parents Wai and Anna, whose unending support over these four years in London have allowed me to flourish and grow as a person.

Abstract

A dual-phase composite material comprised of scandia-stabilized zirconia (ScSZ) and doped lanthanum chromite (La,Sr)(Cr,Fe)$O_{3-\delta}$ (LSCrF) was investigated in this work as a potential oxygen transport membrane material in the production of synthesis gas. The main focus of this work was to examine the effects of exposure to three aging environments (air, 4% H_2-96% N_2, 5% H_2-95% CO_2) for two durations (300 hours, 1000 hours) on the oxygen transport kinetics and surface chemistry of ScSZ/LSCrF.

Determination of the oxygen ion conductivity via Electrochemical Impedance Spectroscopy of single-phase ScSZ showed a decrease in the activation energy above 600˚C corresponding to a change in crystal phase at this temperature. Determination of the oxygen transport kinetics in dry oxygen ($^{18}O_2$) atmosphere on single-phase ScSZ via Isotopic Exchange Depth Profiling combined with Secondary Ion Mass Spectrometry showed the material exhibited an oxygen self-diffusion coefficient on the order of 10^{-8} cm^2 s^{-1} at 700˚C for 30 minutes but required the application of a catalytic layer to boost oxygen surface exchange to detectable levels. Examinations of the surface chemistry of polished single-phase ScSZ and LSCrF via Low Energy Ion Scattering and X-ray Photoelectron Spectroscopy showed minimal differences to the ideal bulk stoichiometry.

Determination of the crystal structure of dual-phase ScSZ/LSCrF via X-ray diffraction showed secondary phase formation in the samples after 300 hours of aging in air and 5%H_2-95%CO_2, and in all samples after 1000 hours of aging. Oxygen transport kinetics of dual-phase ScSZ/LSCrF under dry oxygen showed minor differences in D^* and k^* after exposure to the aging environments for 300 hours when compared to the unaged material, but an increase in surface exchange kinetics was observed for the materials aged in reducing conditions for 1000 hours. D^* and k^* in dual-phase ScSZ/LSCrF were on the order of 10^{-8} cm^2 s^{-1} and 10^{-8} cm s^{-1} respectively before and after aging up to 1000 hours. Oxygen surface exchange kinetics are increased by about one order of magnitude when performed in water vapor ($H_2{}^{18}O$) over dry oxygen. Examinations of the surface chemistry of as-prepared dual-phase ScSZ/LSCrF showed Cr depletion on the outer atomic surface of all samples, in addition to elevated surface fraction of Zr within ~10 nm of the sample surface.

Table of Contents

Table of Figures

List of Tables

1 Introduction

This chapter will detail the motivations of the project by elucidating the reliance on crude oil in the global energy mix, and compare and contrast the different technologies available for oxygen separation.

1.1 Role of Petroleum in Energy Security

The question of energy security is of paramount importance in any country's political and economic agenda. All countries rely on adequate, reliable and inexpensive sources of energy to achieve economic prosperity. The global dependency on fossil fuels remains an issue to resolve for developed countries, usually under the argument of reducing CO_2 emissions. While developed countries may achieve zero emission electricity generation within the next few decades, this cannot be said for developing countries who rely on fossil fuels heavily for their low cost, availability, and reliability.

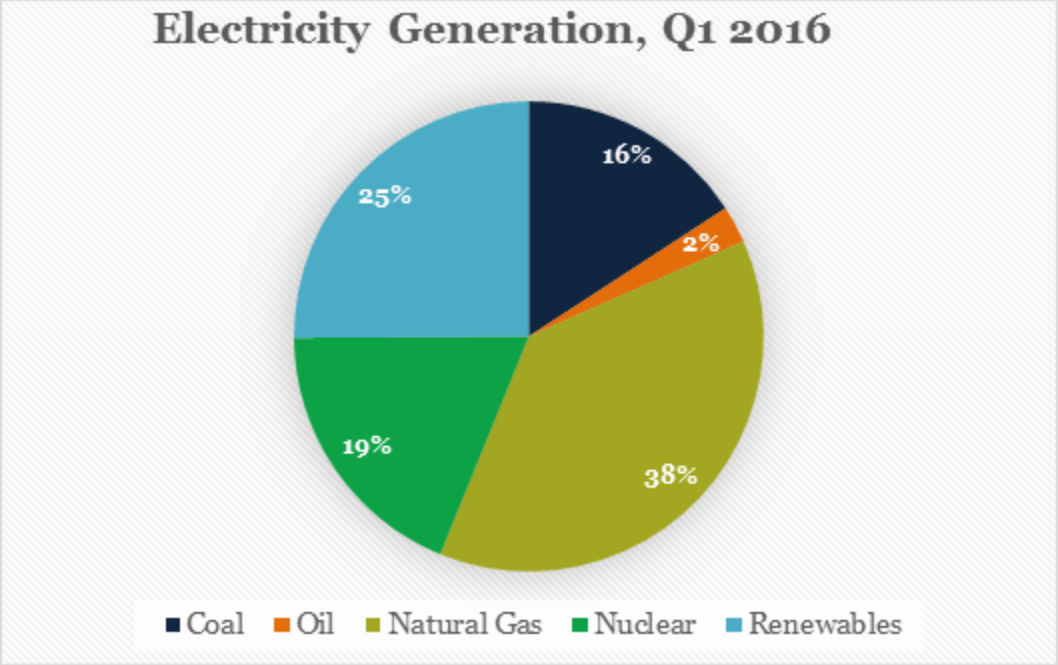

Figure 1.1: Primary sources of electricity generation in the United Kingdom, first quarter 2016 [1].

It is emphasized that there is a difference between *electricity generation* and *energy production*. Figure 1.1 shows the total electricity generation of the United Kingdom for the first quarter of 2016 [2]; Figure 1.2 shows the total energy production for the same time period [1]. Note that while oil constitutes only 2% of *electricity* generation in the UK in

the first quarter of 2016, it makes up 41% of *energy* production. This dichotomy results from the primary use of oil being for industrial and transportation purposes. A shift away from oil is easily achievable as a source of electricity generation, but highly challenging in overall energy production over the next decade.

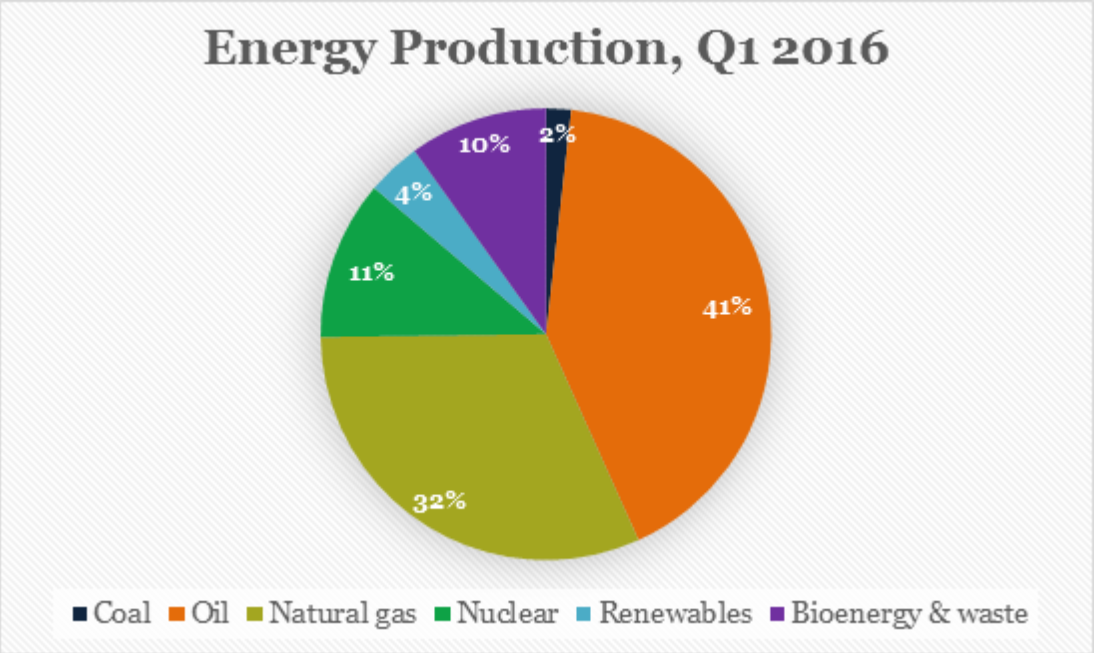

Figure 1.2: Primary sources of energy production in the United Kingdom, first quarter 2016 [1].

Crude oil as a natural resource possesses several characteristics that allow it to be employed throughout the world. It possesses high energy density per unit volume (~45 MJ/kg), is relatively abundant, and the extraction and transportation infrastructure is both well-known and in place, making it inexpensive for use as an energy source. However, high carbon emissions associated with its use, coupled with its non-renewability, have driven exploration of other energy forms to replace it as the primary source for transportation. Hydrogen-based technologies for transport (hydrogen-fueled cars) have begun to emerge on the market in recent years. Indeed, the recent push for large car companies to adopt fuel-cell or electric power technology shows promise that the automotive sector is attempting to shift away from fossil fuels, but these technologies are currently too expensive to implement with current technology without large subsidies from governmental bodies to offset their high production and infrastructure costs. For example, the Toyota Mirai, a hydrogen fuel cell car, will receive ¥2 million in subsidies (£13,500 as of August 1, 2017) from the Japanese government, reducing the effective cost

of the vehicle to ¥4.7 million (£32,200 as of August 1, 2017)[1]. The Mirai also receives a subsidy of $12,500 (£9,500 as of August 1, 2017) from the United States government[2], retailing at $57,500 (£43,500 as of August 1, 2017)[3]. In comparison, the 2017 Toyota Prius, a hybrid electric car, retails at $24,685[4], and the 2017 Toyota Corolla, a conventional petrol car, retails at $18,500[5], both vehicles requiring no subsidies. Until fuel cell technology for vehicles become viable on a cost basis without governmental support, petroleum crude oil will remain the dominant source of energy for transport for the foreseeable future.

However, substitutes for petroleum crude oil exist – in particular synthetic fuels derived from synthesis gas (syngas). Synthesis gas is a fuel gas mixture comprising primarily of hydrogen and carbon monoxide, and is used as an intermediate for creating synthetic petroleum through the Fischer-Tropsch process. A simplified reaction formula is shown in Equation 1.1:

$$(2n+1)\mathrm{H}_2 \; + \; n\mathrm{CO} \; \rightarrow \; \mathrm{C}_n H_{2n+2} + \; n\mathrm{H}_2\mathrm{O} \qquad (1.1)$$

where *n* is typically 10-20 for formation of synthetic fuels. Readers may refer to the summary of the Fischer-Tropsch process by DeKlerk et. al. [3] for more information.

Global demand for synthetic fuels rises on rising crude oil prices, or where economic/political uncertainty in oil-producing regions causes high volatility in prices. The generation of synthetic fuels, usually within a narrow cost range and annual production quota, may be of high interest to several administrations and governments, who value a more stable petroleum price for social/political/economic stability. Indeed, crude oil prices have been highly volatile in the past 50 years, as shown in Figure 1.3. In the 1970s, a brief revival of research into commercial-scale synthetic fuel production occurred when oil prices rose from $19.63 from July 1973 to $53.15 in January 1974 (a 171% increase over 6 months), and from $53.25 in January 1979 to $118.30 in May 1980 (a 122% increase over 5 months). Research stagnated when crude oil prices stabilized for the next two decades. In recent years, the price swings in oil since 2008 coupled with rising demand for a more stable crude oil price among oil-producing and oil-consuming countries has revived commercialization of synthetic fuel production.

[1] https://www.theguardian.com/technology/2014/nov/18/toyota-begin-selling-fuel-cell-cars-mirai
[2] http://mediarelations.cornell.edu/2014/11/18/toyota-mirai-needs-hydrogen-fuel-and-government-subsidies-to-survive/
[3] https://ssl.toyota.com/mirai/fcv.html
[4] https://www.toyota.com/prius/
[5] https://www.toyota.com/corolla/

Figure 1.3: Inflation-adjusted price of crude oil, 1946 to present (as of February 2017)[6].

1.2 *Syngas Production Methods*

The two main methods of syngas production for further refinement into synthetic fuels are gasification of coal and/or biomass, and steam reforming of natural gas. Gasification involves heating the reactants, consisting of the carbonaceous material, water and oxygen, to very high temperatures (~1500˚C) to produce syngas. A simplified schematic is shown in Figure 1.4. The simplified reaction of coal gasification is shown in Equation 1.2:

$$3C + H_2O + O_2 \rightarrow 3CO + H_2 \tag{1.2}$$

where C is the carbonaceous material. Impurities and contaminants in the carbonaceous material and water are typically removed by a scrubber prior to reaction with oxygen to produce syngas.

The oxygen used in coal gasification is predominantly obtained via cryogenic distillation of air (see Section 1.3). Significant energy input is required to bring the temperature of the

[6] http://www.macrotrends.net/1369/crude-oil-price-history-chart

distilled oxygen (–183°C) to the operating temperature, making the overall syngas production process for gasification more energy intensive and less efficient.

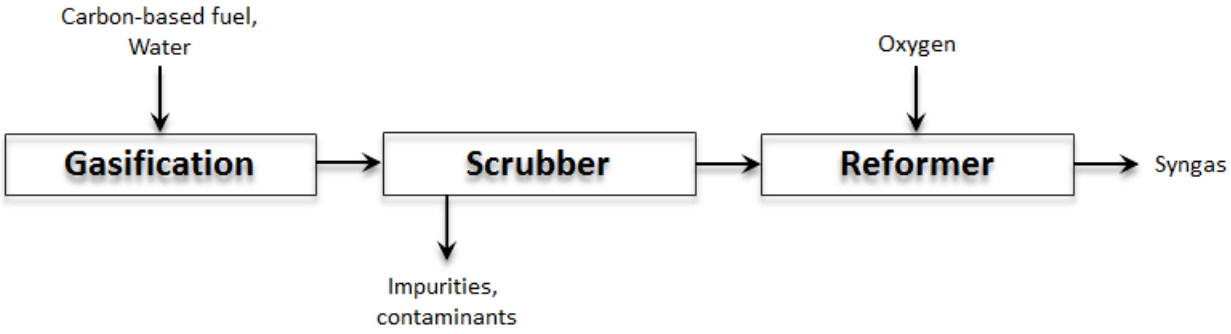

Figure 1.4: Simplified process schematic of syngas production by gasification.

Steam reforming of natural gas is a strongly endothermic process and would likewise be energy-intense and expensive. Natural gas (comprised mainly of methane) and steam are reacted in a chamber at elevated temperature (700-1100°C) and pressure (3-25 bar) in the presence of a catalyst (such as nickel) to produce syngas. The simplified reaction of methane steam reforming is shown in Equation 1.3:

$$CH_4 + H_2O \rightleftharpoons CO + H_2 \tag{1.3}$$

A water gas shift reaction occurs in both coal gasification and methane steam reforming, in which the carbon monoxide component of syngas reacts with steam to produce carbon dioxide and hydrogen, shown in Equation 1.4:

$$CO + H_2O \rightleftharpoons CO_2 + H_2 \tag{1.4}$$

The water gas shift reaction is desirable if the production of hydrogen (for example, in the hydrogen economy) is the aim, but it is detrimental for the purpose of syngas production.

1.3 Oxygen Separation Technologies

1.3.1 Current Technologies

To date, the two primary methods of oxygen separation from air are cryogenic distillation and pressure swing adsorption. In cryogenic distillation, high purity (>99%) oxygen is produced on an industrial scale by fractional distillation of air at low temperature and pressure [4]. Figure 1.5 shows a simplified schematic of the cryogenic method [5]. Air is compressed to between 4 to 10 atm and cooled to ambient temperature (~30°C). After contaminants such as H_2O, CO_2 and heavy hydrocarbons are removed by means of a

molecular sieve, the purified air enters the heat exchanger and is cooled to the liquefaction temperature (approximately –185˚C) in a low-pressure column. Of the three components in air, oxygen has the highest boiling point (–183˚C) and is collected in liquid form at the bottom of the column.

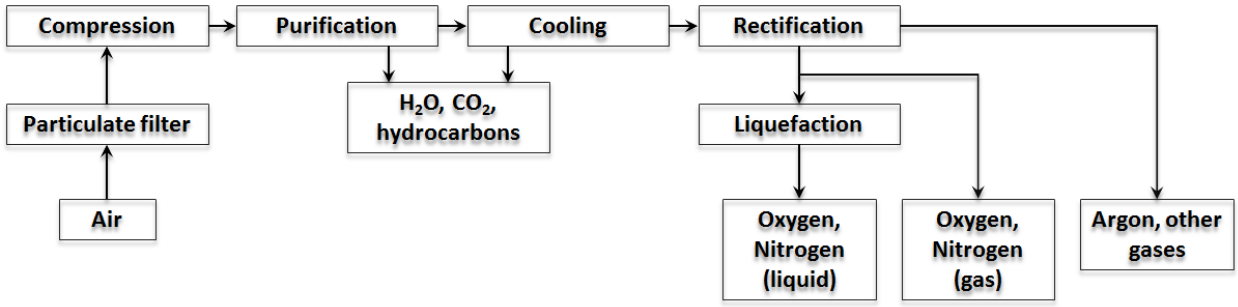

Figure 1.5: Schematic of cryogenic distillation for oxygen separation. Adapted from [6].

Pressure swing adsorption (PSA) involves the selective adsorption of nitrogen from air at high pressure using activated carbon or a molecular sieve (i.e. zeolite). A schematic is shown in Figure 1.6. Compressed air is fed through a vessel containing the molecular sieve upon contact, the nitrogen adsorbs on the sieve, allowing the oxygen to pass through relatively unimpeded. When the sieve is saturated with nitrogen, the pressure of the vessel is lowered from elevated pressure to ambient pressure, allowing the nitrogen to desorb from the sieve. The process does not provide continuous oxygen production during nitrogen desorption. However, operation of two vessels, where one is active and the other is desorbing nitrogen allows oxygen production to be continuous.

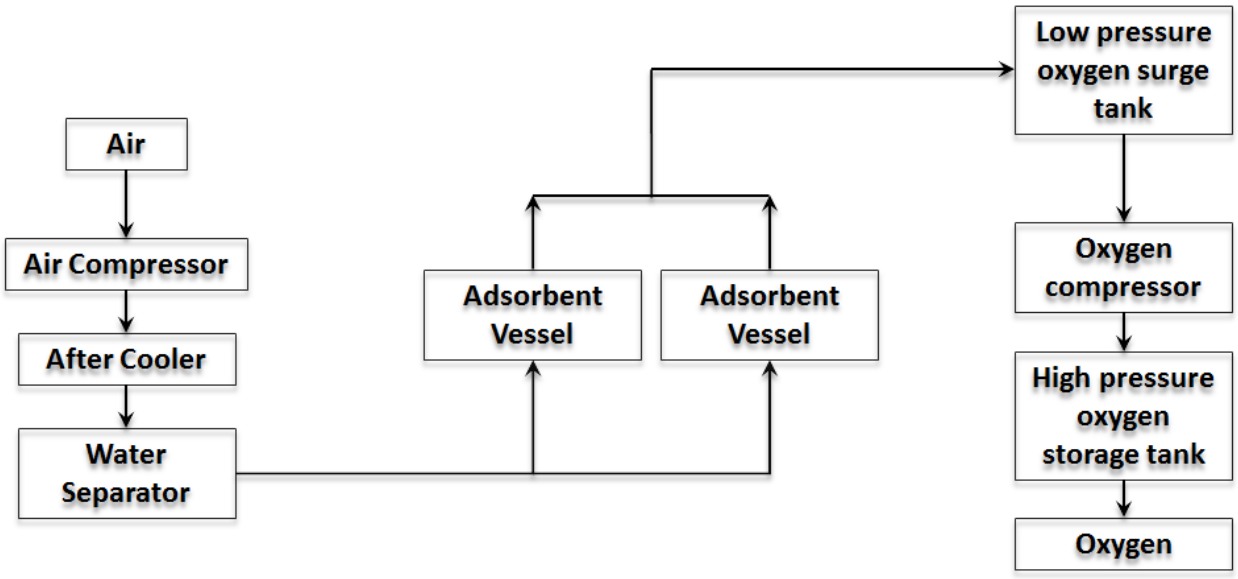

Figure 1.6: Schematic of pressure swing adsorption for oxygen separation. Adapted from [6].

1.3.2 Ceramic Oxygen Transport Membranes

Ceramic oxygen transport membranes (OTMs) can be used as industrial oxygen separators if the oxygen flux through the material under operating conditions is sufficiently high. The transport of oxygen through the membrane can occur from one of two driving forces: either from a difference in oxygen chemical potential (i.e. partial pressure), or from an external electrical potential applied across the membrane. A schematic is shown in Figure 1.7. Oxygen is transported in its ionic form, O^{2-}, across the membrane, and is accompanied by a flow of electrons migrating in the opposite direction to maintain electrical neutrality.

Table 1-1 summarizes the advantages and drawbacks of the three main oxygen separation technologies. Pressure swing adsorption, while less costly than cryogenic distillation, generates comparatively low-purity oxygen (90-95%) and operates in a batch (i.e. discontinuous) process, and is not suitable for large-scale oxygen separation for industrial applications [8]. In addition, it cannot be integrated into a combustion and/or gasification cycle. Cryogenic distillation produces high purity oxygen in a continuous process, but at high power consumption and low efficiencies [8]. For oxy-combustion and syngas production, integration of the cryogenic distillation process into an oxyfuel/integrated gasification combined cycle (IGCC) plant also has a large device footprint, high installment capital cost, large energy consumption, and reduces the total plant efficiency by 8–10% [6].

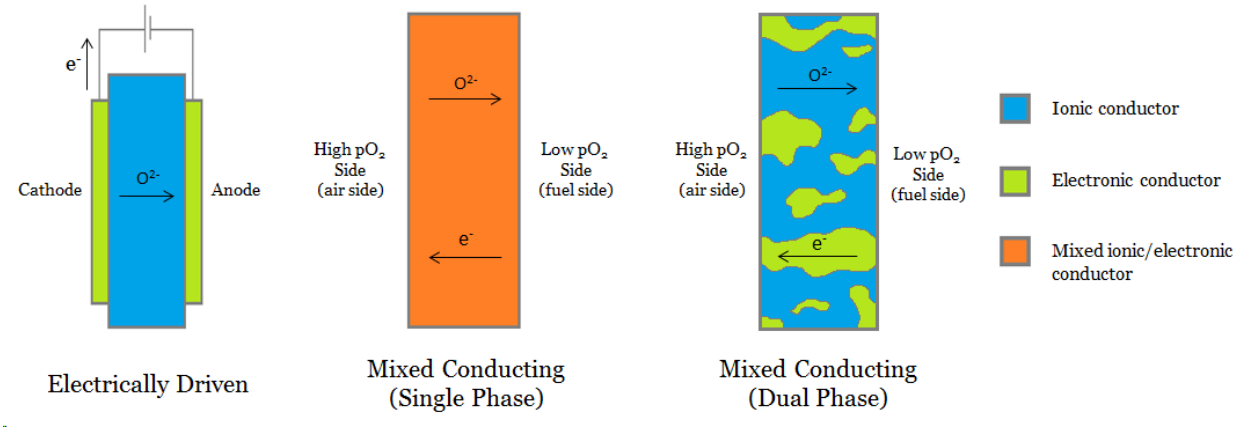

Figure 1.7: Types of ceramic oxygen transport membranes. Modified from [7].

Ceramic membranes for oxygen separation produce high purity oxygen (>99%) in a continuous single-step process, at lower capital and operating costs and power consumption than cryogenic distillation. In addition, heat recovery of the permeated oxygen gas stream is possible since the process operates at high temperature; integration in gasification/power cycles thus reduces power consumption of the overall plant significantly due to the elimination of the gas reheating step. Oxygen separation by ceramic membranes also requires less space and is fully scalable, making it the most advantageous technique for oxy-combustion and syngas production.

Table 1-1: Advantages and disadvantages of current oxygen separation techniques [4], [5], [9]–[12]. Modified from [6].

Types/Methods	Principle/Driving Force	Advantages	Disadvantages	Applications
Pressure swing adsorption	Adsorption/ desorption	• Less expensive • More efficient	• Low purity oxygen (90-95%) • Batch process (discontinuous oxygen flow) • Not applicable with integration with power or IGCC • Multiple stage separation process • Large space required	• Waste water treatment – wet oxidation • Chemical leaching for minerals extraction
Cryogenic distillation	Fractional distillation	• High purity oxygen (>99%)	• Higher capital cost (310-500 $US2008/kWe) & high energy consumption (245-670 kWh/t_{O2})	• Welding, medical, and petrochemical industries • Syngas production

			compared to ceramic membrane • Lower power production (409 MW), thermal efficiency (45.2% HHV), and higher electricity cost ($55.5/MWh) compared to ceramic membrane (when integrated with IGCC) • Integration of cryogenic distillation unit in a power plant results in effective energy demand of 235-250 kWh/t_{O2} • Multiple stage separation process • Large volume space required • Energy intensive • Lower efficiency compared to ceramic membrane • No heat recovery	• Oxy-combustion
Ceramic oxygen transport membrane (OTM)	Partial pressure gradient	• High purity oxygen (>99%) • Lower capital cost (260-295 $US2008/kWe) & lower energy consumption (100-655 kWh/t_{O2}) compared to cryogenic distillation • Higher power production (420 MW), thermal efficiency (46.5% HHV), and lower electricity cost ($51.9/MWh) compared to cryogenic distillation (when integrated with IGCC) • Integration of OTM unit in a power plant results in effective energy demand of 147 kWh/t_{O2} • Single stage separation process • Compact • Heat recovery	• Long-term sustainability • High oxygen flux	• Syngas production and oxy-combustion • Welding, medical and petrochemical industries

1.4 Summary

Global dependence on petroleum crude oil for energy applications is currently high and will remain so for the foreseeable future. Novel technologies attempting to penetrate into the market are currently not commercially viable without some form of state subsidy. In addition, the political stability of several oil-producing nations is being called into question and may cause oil production and prices to increase in volatility in the near future, which can be detrimental to the political/economic stability of other nations. It is thus desirable to develop a cost-effective and reliable method of liquid synthetic fuel production to ensure a large, stable, and accessible supply is in place to mitigate the risk of decreased crude oil supply. Of the technologies currently known, oxygen separation and transport using ceramic membranes are the optimal for use in synthesis gas production.

This thesis will determine the effects of exposure to various aging environments on the oxygen transport kinetics of dual-phase $Sc_{0.10}Ce_{0.01}Zr_{0.89}O_{2-\delta}/La_{0.8}Sr_{0.2}Cr_{0.5}Fe_{0.5}O_{3-\delta}$. The work will begin with analysis of the crystal structure and surface chemistry of the single phase components, $Sc_{0.10}Ce_{0.01}Zr_{0.89}O_{2-\delta}$ and $La_{0.8}Sr_{0.2}Cr_{0.5}Fe_{0.5}O_{3-\delta}$, with oxygen ion conductivity and oxygen self-diffusion experiments performed on $Sc_{0.10}Ce_{0.01}Zr_{0.89}O_{2-\delta}$. In addition, the crystal structure, microstructure, oxygen transport kinetics, and surface chemistry of the dual-phase material will be studied before and after aging. The effects of aging on dual-phase $Sc_{0.10}Ce_{0.01}Zr_{0.89}O_{2-\delta}/La_{0.8}Sr_{0.2}Cr_{0.5}Fe_{0.5}O_{3-\delta}$ observed in this thesis will clarify whether the dual-phase material is a viable candidate for use in oxygen transport membrane applications.

1.5 References

[1] I. MacLeay, "UK Energy Statistics, Q1 2016", *Department of Energy and Climate Change*, pp. 1–15, 2016.

[2] J. Druce, T. Ishihara, and J. Kilner, "Surface composition of perovskite-type materials studied by Low Energy Ion Scattering (LEIS)," *Solid State Ionics*, vol. 262, pp. 893–896, 2014.

[3] A. DeKlerk, "Fischer-Tropsch Process," *Kirk-Othmer Encyclopedia of Chemical Technology*. pp. 1–36, 2013.

[4] W. Schmidt, K. Kovak, W. Licht, and S. Feldman, "Managing Trace Contaminants in Cryogenic Air Separation," 2000.

[5] Siemens, "Use of Process Analytics in cryogenic Air Separation Plants," 2007.

[6] S. Gupta, M. Mahapatra, and P. Singh, “Lanthanum chromite based perovskites for oxygen transport membrane,” *Mater. Sci. Eng. R Reports*, vol. 90, pp. 1–36, 2015.

[7] J. Druce, “Mixed Conducting CGO-LSCF Composites for Oxygen Separation in Oxyfuelled Carbon Capture and Storage Systems,” August 2010.

[8] B. Belaissaoui, Y. Le Moullec, H. Hagi, and E. Favre, “Energy efficiency of oxygen enriched air production technologies: Cryogeny vs membranes,” *Energy Procedia*, vol. 63, pp. 497–503, 2014.

[9] S. Badwal and F. Ciacchi, “Ceramic Membrane Technologies for Oxygen Separation,” *Adv. Mater.*, vol. 13, no. 12–13, pp. 993–996, 2001.

[10] P. Dyer, R. Richards, S. Russek, and D. Taylor, “Ion transport membrane technology for oxygen separation and syngas production,” *Solid State Ionics*, vol. 134, pp. 21–33, 2000.

[11] S. Cooper, N. Frazier, and P. Urane, “Clean Coal Feasibility Study,” 2011.

[12] J. Da Costa, S. Smart, J. Motuzas, L. Shaomin, and D. Zhang, “State of Art (SOTA) Report on Dense Ceramic Membranes for Oxygen Separation from Air,” pp. 1–13, 2013.

2 Theory – Defects, Mass Transport, and Operation of Oxygen Transport Membranes

This chapter will outline the theory behind oxygen transport kinetics in metal oxide materials. The types of defects present in metal oxides and a notation to describe defect interactions in these materials is introduced. The different modes of oxygen diffusion in ionically conducting metal oxides is outlined, and oxygen bulk diffusion and surface exchange are defined within the context of this work. Finally, the mechanisms of oxygen transport during operation of oxygen transport membranes is discussed.

2.1 Defect Chemistry of Metal Oxides

Defects exist in all solid materials at temperatures above absolute zero, and adopt different forms. In solids, defects can be categorized by their dimensionality. Table 2-1 summarizes the types of defects most commonly present in a material. For the research conducted here, the point defect is most relevant to the defect chemistry and mass transport of the materials comprising the oxygen transport membrane.

Table 2-1: Types of common defects in solids.

Name of Defect	Dimensionality	Examples
Point defect	0	Vacancy, interstitial site
Line defect	1	Lattice dislocation
Planar defect	2	Grain boundary
Volume defect	3	Void/Pore, Aggregated point defects

2.1.1 Point Defects

Point defects are defects of zero-dimensionality – they do not extend long-range in any dimension. The main types of point defects are summarized in Figure 2.1. Vacancies arise when a site normally occupied by an atom is unoccupied, as shown in Figure 2.1a. Atomic

sites can also be occupied by impurity or dopant atoms, shown in Figure 2.1b. In oxygen transport membranes (as well as materials used in solid oxide fuel cells), the introduction of metal dopant ions of lower valence replaces cations comprising the base oxide, creating vacancies in the lattice to satisfy charge balance in the material – these vacancies serve as the primary sites of oxygen migration.

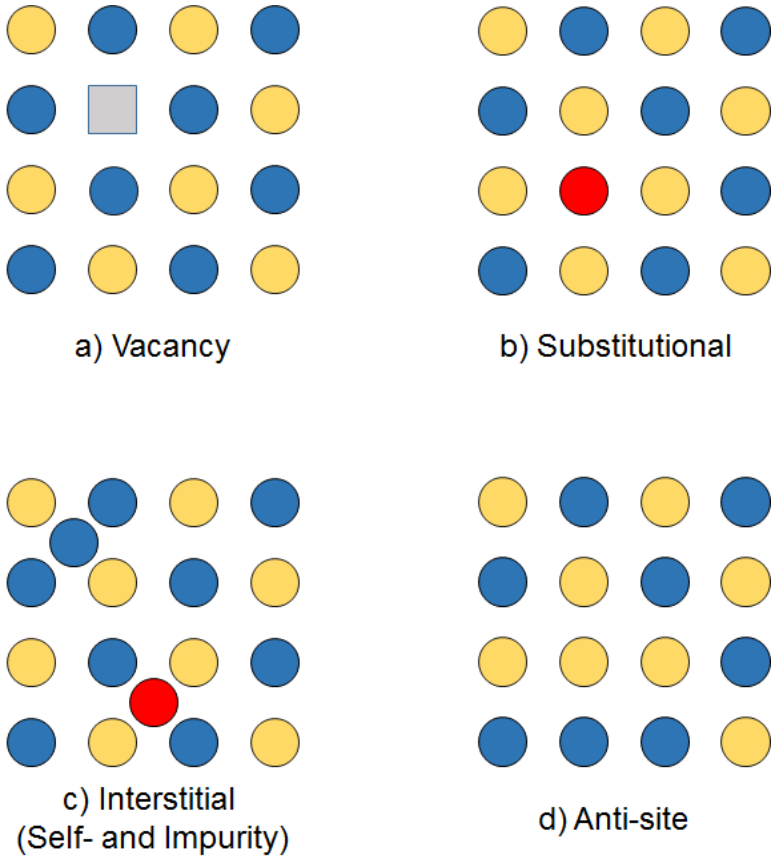

Figure 2.1: The main types of point defects in a binary oxide. Yellow circle = oxygen atom; Blue circle = metal atom; Red circle = dopant/impurity atom; Grey square = vacancy. Modified from [3].

In addition to substitutional sites, atoms can also occupy interstitial sites in the lattice, illustrated in Figure 2.1c. Occupation of interstitial sites, i.e. by oxygen (self-interstitial) or dopant (impurity interstitial), is only stable and likely to occur when the interstitial site size is comparable to the atom's radius, and if the packing energy of the crystal lattice is low. Diffusion along interstitial sites is predominant in materials such as $La_{2-x}Sr_xNiO_{4+\delta}$ [1] and $CeNbO_{4+\delta}$ [2] and present another method of oxygen migration through an oxide material. Anti-site defects also exist, shown in Figure 2.1d, when a cation occupies an anion site, or vice versa.

2.1.2 Kröger-Vink Notation

A notation of defects was devised by Kröger and Vink [4] in the 1950s. This notation describes a point defect in three parts; examples are shown in

Table 2-2. Using the form A_B^C, the main body of the notation *A* denotes the defect species which would occupy the lattice site, whether it be an ion, a vacancy (denoted V), an electron (denoted e) or an electron hole (denoted h). The subscript *B* denotes the ion which would normally occupy the lattice site. The superscript *C* denotes the difference in effective charge between the lattice ion *A* and the defect ion *B*. Dots and dashes represent positive and negative effective charges respectively, with crosses representing neutral effective charge.

Table 2-2: Examples of point defects described using Kröger-Vink notation.

Notation	Defect Description
La_{La}^{x}	A La atom sits on a La site. The difference in effective charge between the lattice ion and the defect ion is 0.
Sr_{La}'	Substitution of Sr (+2) atom into a La (+3) site. The difference in effective charge between the lattice ion and the defect ion is -1.
$V_O^{\bullet\bullet}$	Oxygen vacancy. The difference in effective charge between the lattice ion and the defect ion is +2.

Kröger-Vink notation can be used to construct defect equations, which is useful in expressing defect interactions of oxide materials. These defect interactions play a role in influencing the electrical properties of the oxygen transport membrane, as well as its two components, $Sc_{0.10}Ce_{0.01}Zr_{0.89}O_{1.79}$ and $La_{0.8}Sr_{0.2}Cr_{0.5}Fe_{0.5}O_{3-\delta}$.

2.1.3 Intrinsic and Extrinsic Defects

Intrinsic defects in a crystal are formed as a result of thermal energy in the surrounding environment, and are illustrated in Figure 2.2. Frenkel disorders involve the movement of an ion normally in a lattice site into an interstitial site. Frenkel defects are reserved for cation disorder; anion disorders of the Frenkel-type are termed anti-Frenkel. Schottky disorders involve the formation of cation and anion vacancies in the lattice in stoichiometric amounts; the ejected cation and anion species are then free to migrate through the lattice. In both disorder types, charge neutrality is maintained.

The dominant disorder type in an intrinsic crystal (i.e. no external dopant introduced in the material) is associated with the lowest energy. This depends on the crystal structure of the material. For fluorite materials such as $Sc_{0.10}Ce_{0.01}Zr_{0.89}O_{1.79}$, the lowest energy defect was estimated via atomistic simulations to be anti-Frenkel [5]. For perovskite materials such as $La_{0.8}Sr_{0.2}Cr_{0.5}Fe_{0.5}O_{3-\delta}$, interstitial formation is not energetically favourable due to lattice close packing, so Schottky disorder is dominant [6].

Extrinsic defects, in contrast, are not formed as a result of thermal disorder, but through the introduction of a secondary species that alters the defect population of the base material beyond its intrinsic disorder. These "dopant" species are responsible for the oxygen transport properties of electroceramics such as those used in the oxygen transport membrane and lead to desirable properties such as increased oxygen conductivity, chemical and thermal stability, and overall commercial viability.

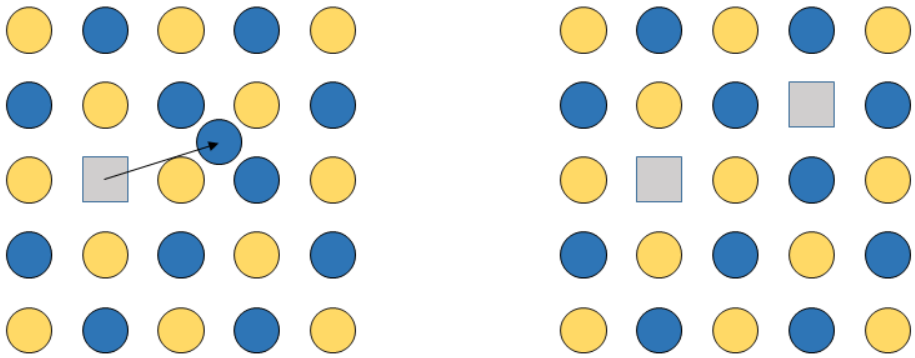

Figure 2.2: Two types of point defects in a crystal lattice. Modified from [3].

When a dopant such as Sc_2O_3 is incorporated into the parent ZrO_2 lattice, the following equilibrium equation expressed in Kröger-Vink notation is observed:

$$Sc_2O_3 \xrightarrow{ZrO_2} 2Sc'_{Zr} + 3O_O^x + V_O^{\bullet\bullet} \tag{2.1}$$

The introduction of a lower-valence dopant cation (Sc^{3+}) into the lattice (Zr^{4+}) induces an effective negative charge in the overall lattice. This charge imbalance is compensated either by electronic defects (such as electrons or electron holes), or ionic defects (such as oxygen vacancies). For Equation 2.1, the charge compensation from the substitution of Sc^{3+} cations in a ZrO_2 lattice is completed via the introduction of oxygen vacancies in a stoichiometric ratio of one vacancy formed for every two Sc^{3+} cation substitutions.

Oxygen transport occurs as a result of oxygen ion migration through the material using these vacancies as sites for diffusion.

2.2 Mass Transport

The operation of an oxygen transport membrane depends on the mass transport of species from one side of the membrane to the other (from high pO_2 to low pO_2). This section will introduce the concepts and methods of mass transport in an oxygen transport membrane, and will focus on oxygen diffusion in the solid state, oxygen reactions at the gas-membrane interfaces, and how the parameters derived from these two phenomena can provide information pertaining to the overall membrane performance.

2.2.1 Oxygen Diffusion

2.2.1.1 Fick's Laws

The diffusion of oxygen across an oxygen transport membrane can be described using Fick's laws of diffusion. Fick's first law, shown in Equation 2.2, states that at constant temperature and pressure, the flux of matter j across a material will be proportional to the concentration gradient $\frac{\partial C}{\partial x}$. The proportionality constant D is the diffusion coefficient or diffusivity, and is a function of the operating conditions (such as temperature and oxygen partial pressure) and the material's properties. The flux reduces the concentration gradient, and is denoted with a negative sign.

$$j = -D\frac{\delta C}{\delta x} \tag{2.2}$$

Equation 2.2 is valid only under steady-state conditions, when the concentration does not change over time. Variations in concentration over time, i.e. non-steady state conditions, can be described using Fick's second law, shown in Equation 2.3.

$$\frac{\delta C}{\delta t} = D\frac{\delta^2 C}{\delta x^2} \tag{2.3}$$

This equation can be solved analytically when appropriate boundary conditions are defined. A list of solutions have been compiled by Carslaw [7] and Crank [8]. The solutions to Equation 2.3 relevant to the work undertaken here will be discussed in Section 4.2.5.1.

2.2.1.2 Types of Diffusion Coefficients

There are several types of diffusion coefficients corresponding to the type of species undergoing diffusion, as well as the experimental conditions under which the measurement was made. For example, the vacancy diffusion coefficient D_V represents the diffusion of vacant sites of a particular species in the lattice, such as oxygen vacancies. The self-diffusion coefficient refers to the diffusion of ions within the lattice to adjacent vacant sites. The self-diffusion coefficient is dependent on the vacancy concentration according to Equation 2.4:

$$D_{self} = [V_O^{\bullet\bullet}]D_V \tag{2.4}$$

Equation 2.4 is applicable when the vacancy concentration in the lattice is sufficiently low that no interaction between vacancies occurs, in other words, that the oxygen vacancy diffusion coefficient is independent of $[V_O^{\cdot\cdot}]$.

Measurement of the self-diffusion coefficient is difficult due to the inability to distinguish the diffusing species (i.e. oxygen ions). Instead, a commonly accepted alternative involves the use and measurement of a chemically similar (or identical if an isotopic tracer is used) species to the species of interest. For example, the introduction of an oxygen tracer ($^{18}O_2$) as a representation of natural oxygen ($^{16}O_2$) self-diffusion in a material is the basis of the isotopic exchange depth profiling method outlined in Section 4.2.4, and the corresponding oxygen tracer self-diffusion coefficient D^* is taken to be an adequate substitute for oxygen self-diffusion. The introduction of a "correlation factor" f is required due to the nature of the measurement of tracer ions; when the tracer ion diffuses one step in the lattice, it leaves behind a vacancy, and there is a possibility that the tracer will diffuse back to its initial site, resulting in no discernable diffusion measured, despite two diffusion steps occurring (one forward, one back). Tracer diffusion measurements are thus less than the corresponding self-diffusion coefficients according to Equation 2.5. The correlation factor f is dependent on the crystal structure of the material, and has been estimated to be 0.65 for a simple cubic structure [9], and 0.69 for an ideal perovskite [10].

$$D^* = fD_{self} \tag{2.5}$$

The final type of diffusion coefficient is the chemical diffusion coefficient $\widetilde{D}$, which is measured under transient chemical potential gradients. Operation of the oxygen transport membrane in real-world applications occurs under significant oxygen partial pressure gradients, and oxygen diffusion would be driven by pO_2. However, the work undertaken here will not consider this type of diffusion coefficient, since studying the

oxygen transport kinetics of the dual-phase material using oxygen tracers involves the removal of pO_2 gradients to eliminate the influence of chemical diffusion $\widetilde{D}$ on the oxygen self-diffusion D^*.

Since the work here uses the isotope exchange depth profiling (IEDP) method to examine diffusion kinetics in the oxygen transport membrane, all references to a diffusion coefficient in this work are assumed to be oxygen tracer diffusion coefficients, unless otherwise stated.

2.2.1.3 Factors influencing the diffusion coefficient

Oxygen self-diffusion in metal oxides typically obey an Arrhenius-type law, shown in Equation 2.6, where E_a is the activation energy, R is the universal gas constant, T is the absolute temperature, and D_o is a pre-exponential term.

$$D = D_O \exp\left(-\frac{E_a}{RT}\right) \tag{2.6}$$

An expression of self-diffusion can be derived from random walk theory [9], [11] and is shown in Equation 2.7, where z is the number of equivalent adjacent sites, the number 6 is the number of directions an atom can jump in a three-dimensional structure, $[V_O^{\cdot\cdot}]_s$ is the mobile (i.e. active) oxygen vacancy fraction, a_O is the lattice parameter, and $v_O \exp\left(-\frac{\Delta G_m}{kT}\right)$ is the jump frequency of the migrating ion, which is a function of the free energy change of migration ΔG_m, the Boltzmann constant k, and the absolute temperature, T. ΔG_m can also be given as $\Delta G_m = \Delta H_m - T\Delta S_m$, where ΔH_m and ΔS_m are the enthalpy and entropy of migration respectively.

$$D = \frac{z}{6}[V_O^{\bullet\bullet}]_s f a_O^2 v_O \exp\left(-\frac{\Delta G_m}{kT}\right) \tag{2.7}$$

Combining Equations 2.6 and 2.7 yields an expression for D_o, shown in Equation 2.8. This equation assumes that the defect concentration is independent of temperature. For materials that exhibit variations in defect concentration with temperature (for example, oxygen vacancy formation with increasing temperature), Equation 2.8 would require a compensating temperature dependence term. In addition, the mobile oxygen vacancy fraction term $[V_O^{\bullet\bullet}]_s$ may not be linearly proportional to the diffusivity at higher defect concentrations, due to non-negligible probability of defect association and formation of comparatively immobile defect complexes.

$$D_O = \frac{z}{6}[V_O^{\bullet\bullet}]_s f a_O^2 v_O \tag{2.8}$$

2.2.2 Oxygen Surface Exchange

In addition to oxygen diffusion, the oxygen surface exchange, which is the transfer of oxygen at the gas-membrane interface, is another important factor in oxygen transport membranes. The overall reaction of oxygen incorporation from the gaseous phase onto the membrane surface is shown in Equation 2.9.

$$\frac{1}{2}O_{2\,(g)} + V_O^{\bullet\bullet} + 2e^- \rightleftharpoons O_O^x \tag{2.9}$$

This reaction is unlikely to proceed in a single step due to the high energy requirement [12]. Instead, a possible process for the overall oxygen reaction path may be divided into a number of possible reaction steps [13], [14] expressed in Kröger-Vink notation in Equations 2.10-2.14. The term $S_{(ad)}$ refers to a surface site available for adsorption, in this context a surface oxygen vacancy, and the subscript *"(ad)"* indicates the species is adsorbed on the surface. Molecular oxygen from the gas phase requires surface sites for adsorption (Equation 2.10) and electrons for dissociation into ionic oxygen (Equations 2.11-2.13). Incorporation of oxygen ions into the bulk lattice requires vacancies near the atomic surface, leaving behind surface sites available for adsorption (Equation 2.14).

$$O_{2\,(g)} + S_{(ad)} \rightleftharpoons O_{2\,(ad)} \tag{2.10}$$

$$O_{2\,(ad)} + e^- \rightleftharpoons O'_{2\,(ad)} \tag{2.11}$$

$$O'_{2\,(ad)} + e^- + S_{(ad)} \rightleftharpoons 2O'_{(ad)} \tag{2.12}$$

$$O'_{(ad)} + e^- \rightleftharpoons O''_{(ad)} \tag{2.13}$$

$$O''_{(ad)} + 2V_O'' \rightleftharpoons O_O^x + S_{(ad)} \tag{2.14}$$

The overall rate of oxygen surface exchange reaction can be represented by the surface exchange coefficient, k^*. This coefficient is estimated via the isotope exchange depth profiling (IEDP) technique (see Section 4.2.4), and related to the ^{18}O tracer flux via Equation 2.15, where C_g and C_s are the ^{18}O concentration in the gas and at the gas-solid interface.

$$jO_2 = k(C_g - C_s) \tag{2.15}$$

$$k = k_o \exp\left(-\frac{E_a}{RT}\right) \tag{2.16}$$

$$k = a_o m^{-\frac{1}{3}} [V_O^{\bullet\bullet}]^{\frac{2}{3}} v_e \exp\left(-\frac{\Delta H_e - T\Delta S_e}{RT}\right) \tag{2.17}$$

Like oxygen diffusion, oxygen surface exchange follows an Arrhenius-type dependence of temperature, shown in Equation 2.16. Kilner et al. derived an atomistic expression for the surface exchange coefficient [11], shown in Equation 2.17, where a_O is the lattice parameter, m is the number of oxygen sites per unit cell, $[V_O^{\bullet\bullet}]^{\frac{2}{3}}$ is the oxygen vacancy concentration at the surface, v_e is the exchange frequency, ΔH_e and ΔS_e are the enthalpy and entropy of surface exchange, and R and T the gas constant and absolute temperature respectively. The expression assumes a perfect surface, defined as a simple termination of the bulk, and ignores surface phenomena such as residual strains and impurity segregation.

Equations 2.7 and 2.17 are both functions of the oxygen vacancy concentration, $[V_O^{\bullet\bullet}]$. A plot of the surface exchange coefficient, k, against the self-diffusion coefficient, D^*, for several materials adopting the fluorite- [13] and perovskite- [11] crystal structures shows the two parameters are correlated, suggesting that the oxygen vacancy concentration plays a similar role in both phenomena. The correlation was found to be due to a linear relationship of the activation energy of surface exchange and bulk diffusion [15], which reinforces the role of oxygen vacancies in surface incorporation.

2.3 Operation of Oxygen Transport Membranes

An oxygen transport membrane functions as a fully-dense material separating two gas streams, which under operation, separates oxygen gas from air, reduces it into oxygen ions, O^{2-}, and transports it across the membrane. A schematic is shown in Figure 2.3. During operation, air from the high pO_2 side (feed side) of the membrane comes into contact with the membrane surface at elevated temperature (1000°C) and ambient pressure (3-5 psig), and undergoes a series of reactions outlined in Equations 2.10-2.14. Ionic oxygen then migrates through the membrane. The reaction of oxygen ions with a fuel (e.g. CH_4) on the low pO_2 side (permeate side) results in the formation of synthesis

gas, liberating electrons in the process. These electrons migrate in the opposite direction to the oxygen ions and participate in oxygen reduction on the feed side.

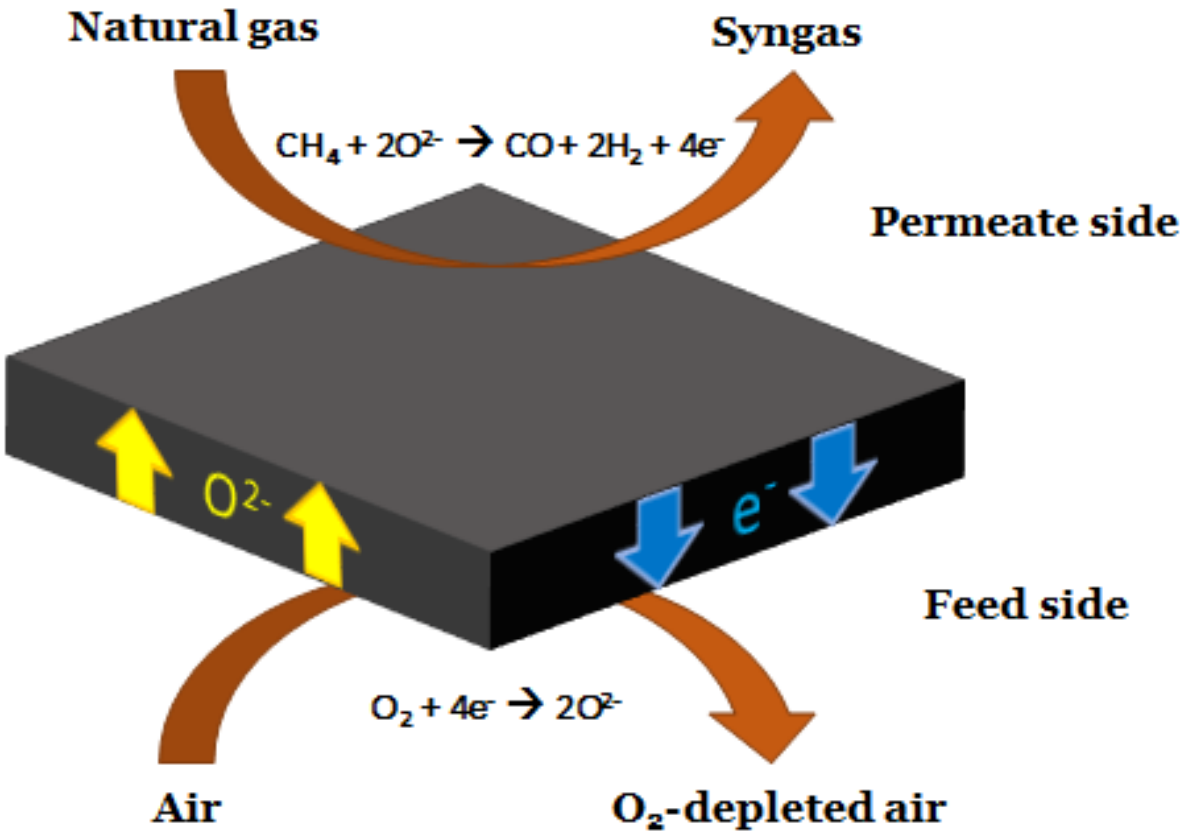

Figure 2.3: Schematic of working principle of oxygen transport membrane. Modified from [16].

The nature of oxygen migration can be represented by oxygen chemical potential gradients across the membrane. The main processes of oxygen migration in a partial pressure-driven membrane as a function of chemical potential are summarized in Figure 2.4, where μ denotes the chemical potential, and Δμ denotes the change in chemical potential. The main processes involve gas diffusion to the membrane surface ($\Delta\mu_{O_2}^{gas'}$), oxygen incorporation on the high pressure interface ($\Delta\mu_{O_2}'$), oxygen bulk diffusion ($\Delta\mu_{O_2}^{bulk}$), expulsion of oxygen in the low pressure interface ($\Delta\mu_{O_2}''$), and gas diffusion away from the membrane surface ($\Delta\mu_{O_2}^{gas''}$). The total chemical potential drop, $\Delta\mu_{O_2}^{tot}$, is the sum of these steps, expressed in Equation 2.18:

$$\Delta\mu_{O_2}^{tot} = \Delta\mu_{O_2}^{gas'} + \Delta\mu_{O_2}' + \Delta\mu_{O_2}^{bulk} + \Delta\mu_{O_2}'' + \Delta\mu_{O_2}^{gas''} \quad (2.18)$$

The gas diffusion steps are significantly more rapid than the other steps, and their chemical potential gradients correspondingly low such that they can be neglected. The remaining terms denote the processes of oxygen bulk diffusion and oxygen surface exchange. Depending on the reaction rate of each process, and the membrane parameters (i.e. thickness), one of these processes will be the limiting step in overall oxygen transport through the membrane. An explanation of diffusion-limited and surface exchange-limited transport will follow.

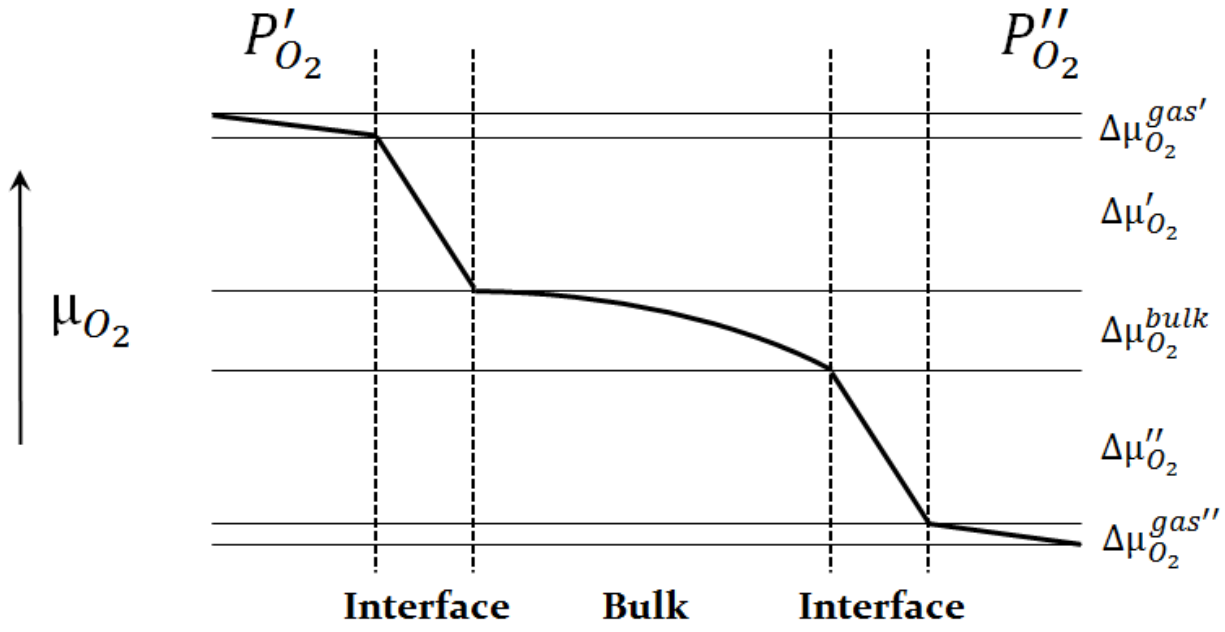

Figure 2.4: Schematic of the chemical potential gradients in a partial-pressure-driven oxygen transport membrane. Oxygen partial pressure at P'_{O_2} is higher than at P''_{O_2}. Adapted from [17].

2.3.1 Oxygen Flux – Diffusion Limited

If bulk diffusion of oxygen comprises the majority of the overall chemical potential drop across the membrane, and chemical potential drops of the surface reactions are negligible, the flux of oxygen is considered to be diffusion-limited. The oxygen flux, j_{O_2}, of an oxygen transport membrane operating in a chemical potential gradient is expressed in Equation 2.19, referred to as the Wagner equation [18].

$$j_{O_2} = -\frac{RT}{16F^2L}\int_{lnP'_{O_2}}^{lnP''_{O_2}} \frac{\sigma_{el}\sigma_{ion}}{\sigma_{el}+\sigma_{ion}}\, dlnP_{O_2} \tag{2.19}$$

where j_{O_2} represents the oxygen flux, σ_{el} and σ_{ion} are the electronic and ionic conductivities of the material respectively, R is the gas constant, T is the temperature, F is the Faraday constant, L is the membrane thickness, P'_{O_2} is the oxygen partial pressure on the feed (high pressure) side, and P''_{O_2} is the oxygen partial pressure on the permeate (low pressure) side.

If the electronic and ionic conductivities are independent of oxygen partial pressure, for example in very low oxygen partial pressure gradients, Equation 2.19 can be rewritten as Equation 2.20:

$$j_{O_2} = -\frac{RT}{16F^2L}\frac{\sigma_{el}\sigma_{ion}}{\sigma_{el}+\sigma_{ion}} ln\left(\frac{P''_{O_2}}{P'_{O_2}}\right) \tag{2.20}$$

Several observations can be made from Equation 2.20. First, the oxygen flux across a diffusion-limited oxygen transport membrane can be enhanced by increasing the temperature or by reducing the membrane thickness. In the latter case, a lower membrane thickness can be interpreted as lower resistance to diffusion of oxygen due to a reduction in the distance needed to travel through the membrane thickness. However, the thickness can only be lowered to a point where the oxygen flux is still diffusion-limited; further reduction of membrane thickness beyond this point will result in surface exchange-limited processes becoming dominant. This will be discussed in Section 2.3.2.

Second, increasing conductivity will also improve the oxygen flux. While an enhancement of the ionic conductivity resulting in increasing oxygen flux is somewhat intuitive, it is also interesting to note that improvements in both conductivities also raises the overall flux.

Finally, increasing the oxygen partial pressure gradient across the membrane improves the oxygen flux. This can be achieved by increasing the oxygen partial pressure at the feed side of the membrane (for example, by increasing the pressure of the feed air), or by decreasing the oxygen partial pressure at the permeate side (for example, by increasing the pressure of the permeate gas, or by applying a vacuum).

The transference number t_k for a charge-carrying species k can be a useful concept to understand, and represents the fraction of the total current the charge carrier is carrying. The transference numbers for ionic and electronic conduction are defined in Equation 2.21. For a purely ionic conducting material, the ionic transference number t_{ion} will be unity and the electronic transference number t_{el} will be zero, the reverse is true for a purely electronic conducting material.

$$t_{ion} = \frac{\sigma_{ion}}{\sigma_{ion} + \sigma_{el}} \quad \& \quad t_{el} = \frac{\sigma_{el}}{\sigma_{ion} + \sigma_{el}} \tag{2.21}$$

$$t_{ion} t_{el} (\sigma_{ion} + \sigma_{el}) = \frac{\sigma_{ion} \sigma_{el}}{\sigma_{ion} + \sigma_{el}} \tag{2.22}$$

The right-hand side of Equation 2.22, which appears in Equations 2.19 and 2.20, is defined as the ambipolar conductivity, σ_{amb}. In materials where the electronic conductivity is significantly higher than the ionic conductivity ($\sigma_{el} \gg \sigma_{ion}$, or $t_{el} \approx 1$), the ambipolar conductivity would be close to the ionic conductivity ($\sigma_{amb} \approx \sigma_{ion}$). This often applies to mixed conductors such as perovskite materials, where the mobility of electronic defects is significantly higher than those of ionic defects.

In materials where the ionic conductivity is significantly higher than the electronic conductivity ($\sigma_{el} \ll \sigma_{ion}$, or $t_{ion} \approx 1$), the relation between oxygen diffusivity and oxygen ionic conductivity can be expressed using the Nernst-Einstein equation:

$$\sigma_i = \frac{c_i (z_i e)^2 D_{self}}{kT} \tag{2.23}$$

where σ_i is the ionic diffusivity, c_i is the concentration of anion sites per unit volume, $z_i e$ is the charge of the ion, D_{self} is the self-diffusivity, k is the Boltzmann's constant, and T is the absolute temperature. This relation is applicable to purely ionic conductors such as single-phase 1Ce10ScSZ, where it is known that oxygen ionic conductivity is approximately equal to total ionic conductivity. Equation 2.23 is used to estimate the oxygen diffusion length of 1Ce10ScSZ in preparation for isotope exchange experiments by obtaining the oxygen ionic conductivity of the material from electrochemical impedance spectroscopy, which is outlined in Section 5.1.2.

2.3.2 Oxygen Flux – Surface Exchange Limited

It was mentioned in the previous section that reducing the thickness of an oxygen transport membrane will increase the oxygen flux. This holds true while the oxygen flux is diffusion-limited. However, below a certain thickness the oxygen flux will then be limited by surface reactions on the gas-membrane interface. In this case the oxygen flux becomes surface exchange-limited, and can be defined as a non-negligible decrease in oxygen chemical potential of the surface reactions during oxygen transport ($\Delta\mu'_{O_2}$ and $\Delta\mu''_{O_2}$ in Figure 2.4). At a critical thickness, also known as the critical length and defined as L_c, the

chemical potential drop from the bulk process is equal to that of the two surface processes (incorporation, expulsion), expressed in Equation 2.24.

$$\Delta\mu_{O_2}^{bulk} = \Delta\mu'_{O_2} + \Delta\mu''_{O_2} \tag{2.24}$$

The critical length L_c can be related to the parameters D^* and k, discussed in Sections 2.2.1 and 2.2.2, by Equation 2.25 [18]:

$$L_c = \frac{D^*}{k} = h^{-1} \tag{2.25}$$

When oxygen transport in a membrane is influenced by surface exchange kinetics as a result of the membrane thickness being below the critical length, the oxygen flux can be expressed as Equation 2.26, which is a modification of Equation 2.20 in which the flux is reduced by a factor $\frac{1}{1+2L_c/L}$ [3], where L is the membrane thickness.

$$j_{O_2} = -\frac{RT}{16F^2L}\frac{\sigma_{el}\sigma_{ion}}{\sigma_{el}+\sigma_{ion}} ln\left(\frac{P''_{O_2}}{P'_{O_2}}\right)\cdot \frac{1}{1+2L_c/L} \tag{2.26}$$

2.4 Summary

The various types of point defects, both intrinsic and extrinsic to the material, were discussed. Kröger-Vink notation was introduced to describe defect interactions. Mass transport in ionically conducting solids was discussed according to Fick's laws of diffusion, the different types of diffusion coefficients, and factors influencing diffusion in these materials. Oxygen bulk diffusion and surface exchange was introduced and expressed via atomistic expressions. Finally, the operation of an oxygen transport membrane was discussed with regard to oxygen chemical potential gradients, contrasting oxygen flux across the membrane as either diffusion-limited or surface exchange-limited, and relating the parameters D^* and k^* to the oxygen flux and conductivity of the membrane.

2.5 References

[1] S. Skinner and J. Kilner, "Oxygen diffusion and surface exchange in $La_{2-x}Sr_xNiO_{4+\delta}$," *Solid State Ionics*, vol. 135, no. 1–4, pp. 709–712, 2000.

[2] R. Packer, E. Tsipis, C. Munnings, V. Kharton, S. Skinner, and J. Frade, "Diffusion and conductivity properties of cerium niobate," *Solid State Ionics*, vol. 177, no. 19–25, pp. 2059–2064, 2006.

[3] J. Druce, “Mixed Conducting CGO-LSCF Composites for Oxygen Separation in Oxyfuelled Carbon Capture and Storage Systems,” no. August, 2010.

[4] F. Kröger and H. Vink, “Relations between the Concentrations of Imperfections in Crystalline Solids,” *Solid State Phys.*, no. Advances in Research and Applications, 1957.

[5] J. Fergus, “Doping and defect association in oxides for use in oxygen sensors,” vol. 8, pp. 4259–4270, 2003.

[6] A. Jones and M. Islam, “Atomic-Scale Insight into $LaFeO_3$ Perovskite: Defect Nanoclusters and Ion Migration,” *J. Phys. Chem. C*, vol. 112, pp. 4455–4462, 2008.

[7] H. Carslaw and J. Jaeger, “Conduction of heat in solids,” *Oxford Sci. Publ.*, 1986.

[8] J. Crank, *The Mathematics of Diffusion*. Clarendon Press, 1979.

[9] J. Kilner, “Fast oxygen transport in acceptor doped oxides,” *Solid State Ionics*, vol. 129, no. 1–4, pp. 13–23, Apr. 2000.

[10] T. Ishigaki, S. Yamauchi, K. Kishio, J. Mizusaki, and K. Fueki, “Diffusion of Oxide Ion Vacancies in Perovskite-Type Oxides,” *J. Solid State Chem.*, vol. 73, no. 1, pp. 179–187, 1988.

[11] J. Kilner, R. DeSouza, and I. Fullarton, “Surface exchange of oxygen in mixed conducting perovskite oxides,” *Solid State Ionics*, vol. 86–88, pp. 703–709, 1996.

[12] R. De Souza, “A universal empirical expression for the isotope surface exchange coefficients (k*) of acceptor-doped perovskite and fluorite oxides,” *Phys. Chem. Chem. Phys.*, vol. 8, pp. 890–897, 2006.

[13] P. Manning, J. Sirman, and J. Kilner, “Oxygen self-diffusion electrolytes and surface exchange studies of oxide having the fluorite structure,” *Solid State Ionics*, vol. 93, pp. 125–132, 1997.

[14] B. Boukamp, B. van Hassel, I. Vinke, K. De Vries, and A. Burggraaf, “The oxygen transfer process on solid oxide/noble metal electrodes, studied with impedance spectroscopy, dc polarization and isotope exchange,” *Electrochim. Acta*, vol. 38, no. 14, pp. 1817–1825, 1993.

[15] R. Merkle, J. Maier, and H. Bouwmeester, “A Linear Free Energy Relationship for Gas-Solid Interactions: Correlation between Surface Rate Constant and Diffusion Coefficient of Oxygen Tracer Exchange for Electron-Rich Perovskites,” no. 9, pp. 5069–5073, 2004.

[16] S. Gupta, M. Mahapatra, and P. Singh, “Lanthanum chromite based perovskites for

oxygen transport membrane," *Mater. Sci. Eng. R Reports*, vol. 90, pp. 1–36, 2015.

[17] Y. Lin, W. Wang, and J. Han, "Oxygen Permeation through Thin Mixed-Conducting Solid Oxide Membranes," vol. 40, no. 5, 1994.

[18] P. Gellings and H. Bouwmeester, *Handbook of Solid State Electrochemistry*. CRC Press, 1997.

3 Literature Review

The two sections of this chapter will focus on the two components comprising the $Sc_{0.10}Ce_{0.01}Zr_{0.89}O_{2-\delta}/(La_{0.8}Sr_{0.2})_{0.95}Cr_{0.5}Fe_{0.5}O_{3-\delta}$ (1Ce10ScSZ/LSCrF8255) oxygen transport membrane. In the first section, the properties of doped zirconia will be discussed. The rationale behind the use of Sc and Ce as dopants in ZrO_2 to form 1Ce10ScSZ will be explained. Focus is placed on the crystal phase stability and ionic conductivity of these materials. The mechanism governing ionic transport in this family of materials will also be examined.

In the second section, the properties of the $LaCrO_3$ family of materials will be discussed, as well as the suitability of various dopants in achieving properties necessary for membrane operation. Chemical stability of the $La_{1-x}Sr_xCr_{1-y}Fe_yO_{3-\delta}$ subset of materials will also be examined.

3.1 Introduction to $Sc_{0.10}Ce_{0.01}Zr_{0.89}O_{2-\delta}$ (1Ce10ScSZ)

Scandia-stabilized zirconia (referred to as ScSZ) is a category of ionically-conducting ceramic materials that are used in solid oxide fuel cells and oxygen transport membranes due to its high oxygen ion conductivity. The general formula of this family of materials is $Sc_{1-x}Zr_xO_{2-(x/2)}$, where x is the amount of Sc addition in mol%, with the dopant concentration expressed as a number preceding the composition. For example, Zr doped with 10mol% Sc would be written as 10ScSZ as well as $Sc_{0.10}Zr_{0.90}O_{1.95}$. Materials within the family with more than one dopant can be written similarly, for example 1Ce10ScSZ instead of $Sc_{0.10}Ce_{0.01}Zr_{0.89}O_{1.95}$.

3.1.1 Crystal Structure

Scandia-stabilized zirconia adopts the fluorite crystal structure, which is shown in Figure 3.1. Materials with this crystal structure have the general formula AB_2, where A is a cation, and B is an anion, with the oxidation state of the A cation bring twice that of the B anion. Several examples of materials adopting this structure include CaF_2, ZrO_2 and CeO_2. The cations occupy a face-centered cubic array in the unit cell, with the anions occupying the tetrahedral spaces between the cations.

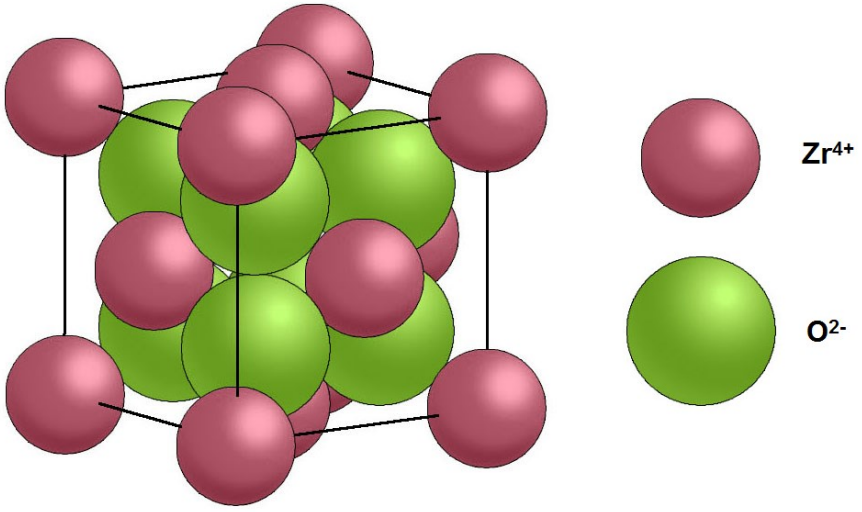

Figure 3.1: The fluorite crystal structure. Red spheres denote cations and green spheres denote anions. For ZrO_2, red and green spheres denote Zr^{4+} and O^{2-} ions respectively. Modified from [1].

Modification of the base ZrO_2 material via substitution of Zr^{4+} cations for other elements allows the material to adopt the properties required in a successful transport membrane, for example oxygen ionic conductivity, chemical stability, or processability. For ZrO_2, enhancement of the oxygen conductivity, which is of primary concern, is achieved by substitution of Zr^{4+} with cations of lower oxidation state (e.g. Sc^{3+}). This induces the formation of oxygen vacancies in the crystal lattice through which migration of oxygen ions is facilitated, giving the material its ionic conductivity. The defect reaction is shown in Equation 3.1.

$$Sc_2O_3 \xrightarrow{ZrO_2} 2Sc'_{Zr} + 3O_O^x + V_O^{\cdot\cdot} \tag{3.1}$$

A proposed phase diagram for the ZrO_2-Sc_2O_3 system was proposed by Ruh et. al. [2], shown in Figure 3.2. Pure ZrO_2 adopts a monoclinic crystal structure (denoted α_1 in Figure 3.2) at room temperature in air, and addition of Sc_2O_3 reveals that, the doped material assumes a tetragonal phase (denoted α_2' in Figure 3.2) between 5-8 mol% Sc_2O_3 content and various rhombohedral phases exist at compositions above ~9mol% Sc_2O_3 [2]. The rhombohedral phase, denoted as β, which exists at low temperatures in the range of 9-13 mol% Sc_2O_3, transforms into a cubic phase on heating to temperatures above 600˚C in air, which is relevant to oxygen transport membranes, which operate in the range of 1000˚C. This rhombohedral β phase, reported to be an ordered $Sc_2Zr_7O_{17}$ phase [3,4], exhibits considerably lower ionic conductivity than the cubic phase, which is attributed to poor oxygen vacancy ordering in the lattice [5].

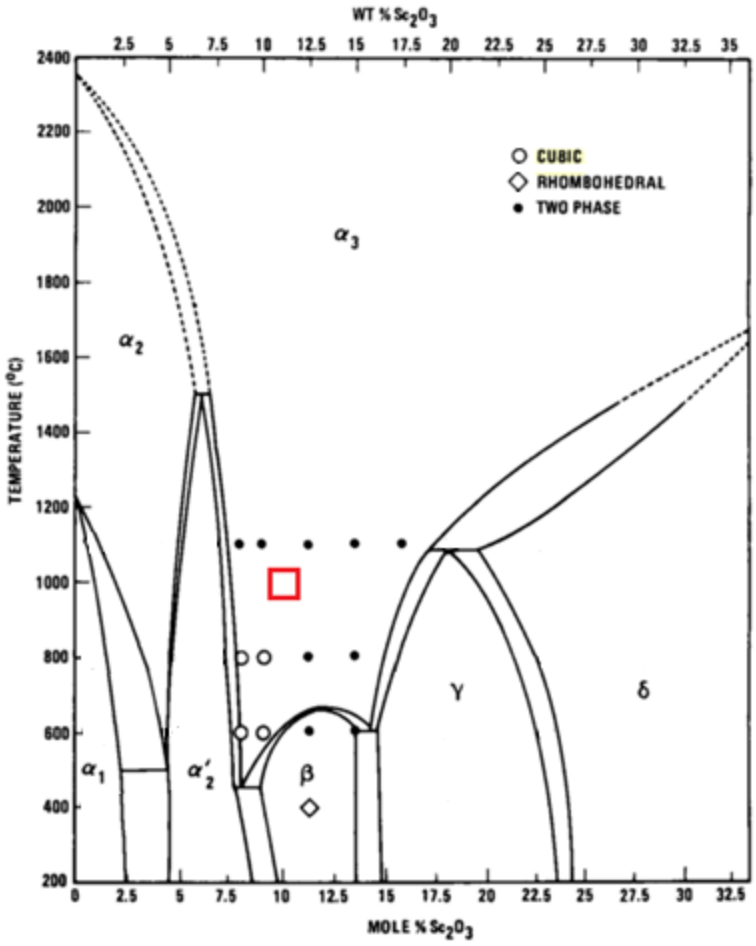

Figure 3.2: Proposed partial phase diagram for the ZrO_2-Sc_2O_3 system. Modified from Ruh et. al. [2]. Square denotes estimation of composition of 1Ce10ScSZ component used in this work and operating temperature investigated. Reprinted with permission from the Journal of the American Ceramic Society.

3.1.2 Defect Interactions in ScSZ

One of the conditions concerning oxygen ion conduction in non-stoichiometric oxides, examined by Mogensen et. al. [6] states that the oxide ion sites (i.e. oxygen vacancies) should have identical or very similar energy, making structures with cubic symmetry optimal. In addition, Mogensen et. al. [6] observe that the highest conductivities are obtained in lattices without strain, which occurs when the difference in ionic radius of the dopant and the parent ions is at a minimum; materials with lattices undistorted by strain also results in the highest concentrations and mobilities of oxide ion vacancies [6], further augmenting the conductivity.

The dopant concentration in the host material is another important parameter to consider. The presence of aliovalent cations induces the formation of oxygen vacancies in the crystal through which the materials' conductivity is derived. However, the maximum conductivity for the materials is achieved at a level of dopant above which the conductivity begins to decline. The occurrence of these conductivity maxima is attributed to defect associations, where at higher dopant concentrations (and thus higher oxygen vacancy concentrations) the oxygen vacancies in the material interact to form pairs or clusters [7]. Defect associates decrease the "free" vacancy concentration and themselves do not facilitate ionic conduction, making them detrimental to the materials' conductivity. The formation of dopant-vacancy associates such as $(Sc'_{Zr} - V_O^{\cdot\cdot})^{\cdot}$ and $(Sc'_{Zr} - V_O^{\cdot\cdot} - Sc'_{Zr})^{x}$ in 1Ce10ScSZ has been cited as a possible cause of conductivity degradation after aging at elevated temperature [8], [9].

Kilner et. al. [10], [11] discovered that these defect associations have an activation energy which is comprised of two parts: a migration enthalpy, and an association enthalpy. It was found that the migration enthalpy is less dependent on the size of the parent ion and more dependent on the crystal structure [10]. On the other hand, the association enthalpy is strongly dependent on the dopant ion size, as well as the ratio of the size of the dopant ion to the parent ion.

The nature and strength of defect associations in cubic-stabilized zirconia were further examined by Bogicevic et. al. [12], [13]. Analyses of yttria- and scandia-stabilized zirconia compounds attributed the magnitude of associations, from strongest to weakest, to be vacancy-vacancy > vacancy-dopant >> dopant-dopant. An investigation by Pietrucci et. al. [14] into the role of vacancy-vacancy interaction in oxide ionic conductivity using molecular dynamics simulations showed that the jump activation energy for mobile (single) vacancies were highly dependent on the location of other single vacancies, and that the most stable location for single vacancies is that of third nearest neighbor, which is corroborated by Bogicevic et. al. [12]. Molecular dynamics simulations were performed on 10ScSZ by Norberg et. al. [15] who also concluded that oxygen vacancies showed no significant preference to be nearest neighbor to either the Sc^{3+} dopant cation or the Zr^{4+} parent cation. The authors also found that vacancy-vacancy pairs have a strong tendency to form along the (111) direction rather than the (110) or (100) directions, indicating that significant repulsive forces exist between individual vacancies, which was observed and supported by both Bogicevic et. al. [12] and Pietricci et. al. [14]. This also is in line with the expectation that vacancies repel each other due to the +2 lattice-relative charge they possess. Marrocchelli et. al. [16] noted that vacancy-vacancy interactions appeared to be an intrinsic characteristic of the fluorite lattice that cannot be avoided, and that this type

of interaction is responsible for the existence of a maximum in the conductivity at dopant concentrations between 8-13mol% Sc.

Bogicevic et. al. [12] noted that the minimization of both the elastic and electronic interactions reduced the preference for vacancies to bind to dopant ions and thus the probability of vacancy-dopant interactions. These authors found that ionic conductivity of doped zirconias can be traced back to differences in the elastic component of vacancy-dopant interactions caused by mismatches in size between dopant and parent ions. To achieve high conductivity, this elastic component should be minimized; this is achieved by minimizing the difference in size between the dopant ion and the parent ion. The vacancy-dopant interaction is negligible in ScSZ since the Sc^{3+} cation (0.87 Å) is very close in size to the Zr^{4+} cation (0.84 Å), which manifests as higher conductivity behaviour for ScSZ compared to YSZ, where the Y^{3+} cation is much larger (1.02 Å). This would suggest that the ionic conductivity of ScSZ is superior to that of YSZ. Kim et. al. [17] came to a similar conclusion; by examining the effects of dopant size and ionic conductivity in ZrO_2, it was found that the smaller the difference between the dopant ion and the parent ion, the higher the conductivity. This conclusion was also supported by Marrocchelli et. al. [16], who also hypothesized that the weakness of the Sc-vacancy interaction in ScSZ confirmed that this material was likely to present the highest conductivity of the doped zirconias. The authors also asserted that among vacancy-dopant interactions, the elastic component (pertaining to the mismatch in ionic size) played a significantly larger role than the electronic component (pertaining to differences in effective charges between the vacancy and the dopant). Simoncic et. al. [18] discovered that the similar ionic radii resulted in the smallest extent of defect cluster formation, which decreased the vacancy mobility, indicating higher ionic conductivity. In addition, Kharton et. al. [19], [20] have found that alkaline earth metal dopant cations (for example Ca^{2+}) are much less effective than rare earth dopants, due to a higher tendency to form defect associates as well as lower stability of the cubic fluorite crystal structure.

In summary, it was found that vacancy-vacancy interactions in doped zirconia are relatively independent of the dopant species and appear to be an intrinsic property of the fluorite lattice. In contrast, vacancy-dopant interactions are primarily responsible for the variations in ionic conductivity in doped zirconia; conductivity can be improved by selecting a dopant cation which matches the radius of the parent ion. The Sc^{3+} dopant ion forms the closest match in size with the parent Zr^{4+} in ScSZ and was determined to possess the highest conductivity among doped zirconias.

3.1.3 Ionic Conductivity of ScSZ

Conductivity and phase stability of 7-13 mol% scandia-stabilized zirconia was examined by Haering et. al. [9], who focused on the material before and after annealing at 1000˚C for 1000 h. It was found that 10 mol% ScSZ (abbreviated as 10ScSZ) exhibited the highest ionic conductivity, but experienced partial phase transformation from cubic to dual cubic-rhombohedral after annealing [9], [21]–[23]. However, this transformation did not result in a decrease in ionic conductivity. It was observed that stabilized zirconia doped with less than 9 mol% Sc exhibited comparatively higher conductivity degradation after aging. This phenomenon was attributed to the nature of defect associates between the dopant ion and oxygen vacancies in the lattice. In the low dopant region (<10 mol% Sc) defect associates primarily adopt a dipole $(Sc'_{Zr} - V_O^{\cdot\cdot})^{\cdot}$ configuration, which upon aging, transform into a tripole $(Sc'_{Zr} - V_O^{\cdot\cdot} - Sc'_{Zr})^{x}$ configuration; the authors noted that this transformation was the main cause of the conductivity degradation. In contrast, defect associates in the high-dopant region (≥10 mol% Sc) were found to adopt the tripole configuration, and did not transform upon aging. As stated above, zirconia sufficiently doped with trivalent scandia did not exhibit a decrease in ionic conductivity after aging at 1000˚C for 1000 h. It was also observed that 10ScSZ undergoes a martensitic cubic ↔ rhombohedral phase transformation at a temperature of about 500˚C, coupled with a volume change of about 0.15%; this low volume change is due to the similarity in ion size between the dopant scandium ion and the parent zirconium ion. Finally, the addition of aluminum and titanium dopants in ScSZ did not exhibit any beneficial effect on the ionic conductivity or on the phase stability, which is also supported by Kharton et. al. [20].

The presence of the rhombohedral β phase in ScSZ implies that Sc by itself is unable to stabilize the cubic structure at ambient temperatures. In contrast, Y in YSZ materials is able to do so. Miller et. al. [24] examined this phenomenon and, using density functional theory, found that yttrium ions hold oxygen ions closer to their ideal lattice positions, making the lattice structure less susceptible to non-cubic ordering processes that are reported to cause degradation. However, the operating temperatures of oxygen transport membranes (~1000˚C) are well above the phase transition temperature (~600˚C), where ScSZ is fully cubic, so dopant selection was focused on achieving high ionic conductivity over crystal structure stabilization.

Oxygen diffusion studies were performed by Raj et. al. [25] on doped zirconia consisting of 2 mol% Y_2O_3 and 9 mol% Sc_2O_3 (abbreviated as 2Y9ScSZ). In this work the oxygen tracer diffusion coefficient D^* was determined using the isotopic exchange depth profiling method (IEDP) and Secondary Ion Mass Spectrometry (SIMS), detailed in Sections 4.2.4 and 4.2.5 respectively. The values of the tracer diffusion coefficient were

measured to be in the range of 10^{-8}–10^{-7} cm^2 s^{-1} in the exchange temperature range of 600-900°C. It was observed during SIMS analysis that the concentration of ^{18}O tracer was very low even after prolonged exchange times (1 h was used) to a point where the diffusion coefficients could not be reliably measured. For subsequent samples, a very thin layer of Ag (~20 nm) was sputter-coated onto the surface prior to the isotope exchange process. It was found by Kurumchin et. al. [26] that in an oxygen atmosphere the surface exchange of oxygen was accelerated by as much as a factor of 10^3 upon application of a silver or platinum layer; this layer is thought to participate in the surface exchange process by facilitating the dissociative adsorption of oxygen [25]. The application of the silver layer precluded the measurement of the surface exchange coefficient, k^*, and was estimated to be very low due to the absence of tracer oxygen in the non-applied specimen. The activation energies of 2Y9ScSZ, calculated from Arrhenius plots obtained from electrochemical impedance spectroscopy and DC conductivity measurements, were found to be 1.4 eV and 0.8 eV at T<600°C and T>600°C respectively, coinciding with the change in the crystal structure from cubic+rhombohedral below ~600°C to fully cubic above ~600°C as observed by other authors [9], [27], [28].

3.1.4 Ionic Conductivity of 1Ce10ScSZ

Ionic conductivity and aging behavior of 10 mol% Sc_2O_3-1 mol% CeO_2-ZrO_2 (abbreviated as 1Ce10ScSZ) was studied in-depth by Omar et. al. [27]–[31]. The co-dopant Ce cation stabilizes the cubic phase to ambient temperatures by suppressing the rhombohedral β phase, at the cost of slightly reduced ionic conductivity, when compared to the single-doped 10ScSZ [28]. Dasari et. al. [32] and Kumar et. al. [33] observed that 1 mol% Ce is the minimum amount to stabilize 1Ce10ScSZ into the cubic phase after sintering, with further Ce additions being detrimental to the ionic conductivity. 1Ce10ScSZ was observed to possess the highest conductivity of the co-doped zirconia compositions examined [29], which included Al_2O_3, Gd_2O_3, Ga_2O_3, Y_2O_3, and a separate study of MnO_2 doping by Yamaji et. al. [34]. Comparisons of conductivity values were also observed by Abbas et. al. [35], who noted that the conductivity of 1Ce10ScSZ was highest with the minimum amount of the ternary dopant (Ce) required to stabilize the cubic crystal phase at temperatures below the phase transition temperature, which was determined to be 1 mol% CeO_2 for 10ScSZ.

In the work of Omar et. al. [30], the ionic conductivity of 1Ce10ScSZ was examined using Electrochemical Impedance Spectroscopy after aging in oxidizing and reducing atmospheres at 600°C. It should be noted that Omar et. al. [30] is measuring the *total* conductivity of 1Ce10ScSZ using this technique, and taking the material to be a purely ionic conductor, equating the total conductivity calculated from impedance

measurements to be equal to the ionic conductivity. The material exhibited a conductivity loss of 6% after exposure to air for 3000 h, and a 20% loss after exposure to a 1%H_2O-9%H_2-90%N_2 gas mixture for 3000 h. The conductivity loss in the material aged in air was attributed to impurity or dopant segregation near the grain boundaries an increase increasing the grain boundary resistance [30]; The conductivity loss in the material aged in 1%H_2O-9%H_2-90%N_2 was associated with the reduction of dopant Ce^{4+} cations in the lattice to Ce^{3+}, which resulted in the higher concentration of oxygen vacancies, but created additional lattice elastic strain in the material (0.97 Å to 1.14 Å upon reduction from Ce^{4+} to Ce^{3+}) which trapped the vacancies [27], [29]. The increase in conductivity expected from increased oxygen vacancy concentration was less than the decrease in conductivity caused by the lower mobility of the vacancies from lattice strains in the material, resulting in lower ionic conductivity. The Ce dopant reduction from Ce^{4+} to Ce^{3+} causing lower total conductivity was also observed by Grosso et. al. [36] for the same material composition.

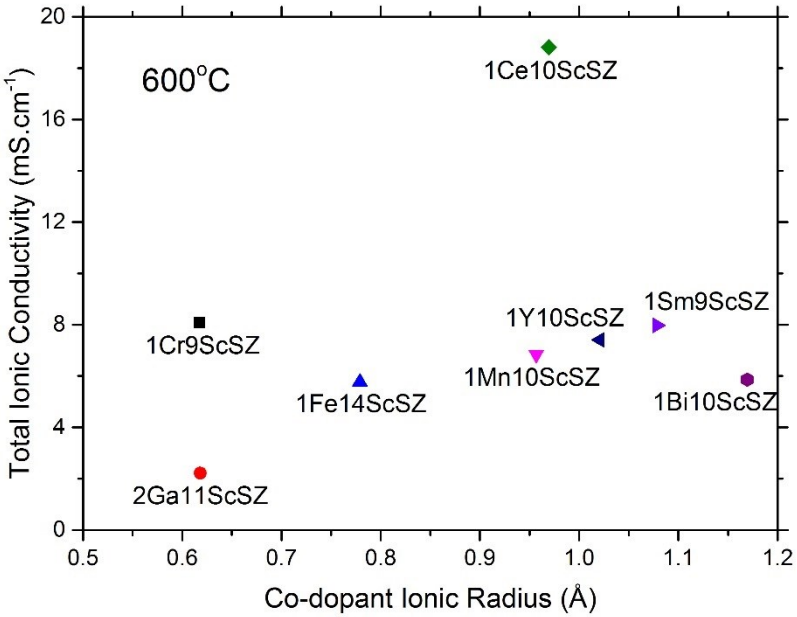

Figure 3.3: Selected total conductivity values in the literature at 600°C, plotted against the ionic radius of the co-dopant. All samples were measured in air. Modified from [28]. Reprinted with permission from the Journal of the American Ceramic Society.

Omar et. al. [28] also noted the relationship between the total ionic conductivity of co-doped 1M10ScSZ, where M is a dopant, and the ionic radius of the co-dopant, displayed in Figure 3.3. Of the selected materials, 1Ce10ScSZ shows the highest ionic conductivity.

Further, Omar et. al. [28] explored the conductivity degradation of Yb^{3+} co-dopant in 10ScSZ (i.e. 1Yb10ScSZ) and found that after aging for 1000 h at 600˚C in reducing atmosphere (1% H_2O, 99% H_2, $pO_2 \sim 10^{-28}$ atm), the ionic conductivity experienced a lower rate of degradation than 1Ce10ScSZ. The authors note that the conductivity degradation caused by reduction of Ce^4 to Ce^{3+} in 1Ce10ScSZ is absent in 1Yb10ScSZ since Yb^{3+} adopts the +3 oxidation state in oxide form. Therefore, the lattice strain observed in 1Ce10ScSZ trapping oxygen vacancies resulting in lower conductivity is not present in 1Yb10ScSZ. However, there is a relative lack of research in the literature on Yb compared to Ce as a ternary dopant, the latter of which is well-documented as a viable material for membrane applications [37]–[46].

Omar et. al. [27] attributed the difference in degradation rates between the oxidizing and reducing conditions primarily to the Ce co-dopant reduction phenomenon, which was easily observed by a change in color of the material from white to dark orange. The reduction process was observed to be incomplete after 3000 hours of aging time, evidenced by the colour gradient observed on the cross-sections of the samples. The authors noted that under both aging conditions, the rate of degradation was higher in the first 1000 hours of aging than in the subsequent 2000 hours, and that total conductivity thereafter degrades approximately linearly. Further work on the material [29] showed that re-oxidation of the 1Ce10ScSZ sample aged in reducing 9%H_2-1%H_2O-90%N_2 gas (600˚C, $pO_2 \sim 10^{-26}$ atm, Hour 0-3000) by subjecting the sample to air (600˚C, Hour 3000-5000) resulted in a slight gain in conductivity within the first 500 hours, which remained relatively unchanged for the next 1500 hours of continued exposure. The conductivity gain is attributed to the re-oxidation of Ce^{3+} to Ce^{4+}, which releases the lattice strain and increasing oxygen vacancy diffusion. This phenomenon was not fully reversible, as evidenced by the conductivity plateau reached after 500 hours of exposure to air, suggesting that lattice strains caused by Ce^{3+} dopant ions continues to impede oxygen vacancy diffusion in 1Ce10ScSZ.

Lee et. al. [47] also examined the electrical conductivity and phase stability of 1Ce10ScSZ. The material exhibited no phase transitions in the temperature range of 1250˚C-1550˚C, remaining in a cubic crystal structure over the entire temperature range. This composition of doped zirconia was found to possess significantly higher electrical conductivity than YSZ in the temperature range 300-1100˚C, and better long-term stability than any other ScSZ material. 1Ce10ScSZ was sintered in air for 1 hour in the temperature range 1250˚C-1550˚C in 50˚C increments. The grain sizes were found to increase from 0.5 μm to 12 μm as the sintering temperature increased from 1250˚C to 1550˚C. The normalized total conductivity measured by Electrochemical Impedance Spectroscopy at 1000˚C was approximately 30% lower in 1Ce10ScSZ with a grain size of

0.5 μm (1250˚C sintering temperature), than 1Ce10ScSZ with a grain size of 8 μm (1500˚C sintering temperature). The effects of the grain size on the total conductivity was also observed in previous YSZ studies by Gibson et. al. [48] and by Chen et. al. [49]. The smaller grain size results in a larger grain boundary volume, which has lower conductivity and higher activation energy for conduction [47]. This is corroborated by Shimonosono et. al. [50] who observed that, above the crystal phase transition point (>600˚C) the electrical conductivity of 10ScSZ decreases with decreasing grain size, which the authors attributed to a larger grain boundary volume. On the other hand, the electrical conductivity of 10ScSZ was observed to increase with decreasing grain size below the crystal transition temperature (<600˚C), but mainly due to an increasing fraction of the low-conductivity rhombohedral β phase. This suggests that below the phase transition temperature of ~600˚C, larger grains are undesirable due to the increased presence of the β phase. However, this implies that above the phase transition temperature and thus without the presence of any β phase, larger grains are desirable since large grain boundary volume reduces electrical conductivity.

Lee et. al. [47] observed a lower density in the samples at lower sintering temperatures (93% vs. 96%), although all samples sintered above 1350˚C in air achieved 95% of theoretical density or greater. Grosso et. al. [51] also observed that 1Ce10ScSZ achieves both full density (reported as >99% theoretical density) and full cubic stabilization at sintering temperatures above 1350˚C in air, and at longer holding times promotes the rhombohedral-to-cubic transition. This suggests that achievement of full density is relatively facile in 1Ce10ScSZ, requiring no specific conditions for sintering.

Sakai et. al. [52] recently published work on the determination of the oxygen tracer diffusion coefficient, D^*, and surface exchange coefficient, k^*, of 1Ce10ScSZ. The authors claim that D^* is higher in ScSZ oxides than in YSZ, with 1Ce10ScSZ exhibiting the highest D^* of the ScSZ samples, agreeing with ionic conductivity data in the literature. The authors observed a very high surface exchange coefficient in their experiments even at low temperatures (~500˚C), with k^* values higher than YSZ by a factor of 100. However, it was cautioned that the effect of water vapor pressure during the experiments, a determining factor in surface exchange kinetics in these materials, was unknown.

3.1.5 Summary of 1Ce10ScSZ Literature

Doped zirconia is reported in the literature to be a material possessing high oxygen ionic conductivity. The conductivity can be improved by choosing aliovalent dopants with ionic radii similar to the parent Zr^{4+} cation, such as Sc^{3+} [6], [12], [13]. It was found that 10 mol% Sc_2O_3 dopant concentration into ZrO_2 producing 10ScSZ possesses among the highest oxygen ion conductivities for doped zirconia materials in the literature [9]. The

addition of a co-dopant Ce cation improves the stability of the cubic crystal structure at room temperature, with 1 mol% CeO_2 being the lowest concentration to do so while achieving high conductivity [34]. The reduction of Ce cations from Ce^{4+} to Ce^{3+} in 1Ce10ScSZ reduces the total conductivity of the material due to oxygen vacancy trapping by lattice strains introduced by the larger Ce^{3+} cations [30]. A grain size of about 8 μm was also reported to achieve the highest total conductivity for 1Ce10ScSZ [47]. Finally, isotope exchange experiments were performed on 2Y9ScSZ [25] and 1Ce10ScSZ [52]. 2Y9ScSZ showed low oxygen surface kinetics without a Ag catalytic layer to improve oxygen surface exchange. A catalytic layer was not required to observe oxygen tracer diffusion in 1Ce10ScSZ, but the presence of water vapor during the experiment may have influenced the oxygen transport kinetics.

3.2 Introduction to $(La_{0.8}Sr_{0.2})_{0.95}Cr_{0.5}Fe_{0.5}O_{3-\delta}$ (LSCrF8255)

The material $La_{0.8}Sr_{0.2}Cr_{0.5}Fe_{0.5}O_{3-\delta}$ (abbreviated as LSCrF8255) possesses properties that are desirable for application in oxygen transport membranes. In particular, the mixed ionic-electronic conductive nature of these materials coupled with their relatively high chemical and mechanical stability in reducing environments may present an alternative to the more well-known $(La,Sr)(Co,Fe)O_{3-\delta}$ family for use in oxygen transport membrane technology.

3.2.1 Crystal Structure

The $(La,Sr)(Cr,Fe)O_{3-\delta}$ family of compounds adopts the general formula ABO_3, where A is an alkali, alkaline earth, or rare earth cation, B is a transition metal cation, and O is the oxygen anion. The unit cell, shown in Figure 3.4, depicts an ideal perovskite structure, which is cubic. A-site cations have 12-fold coordination with oxygen anions, and B-site cations have 6-fold coordination.

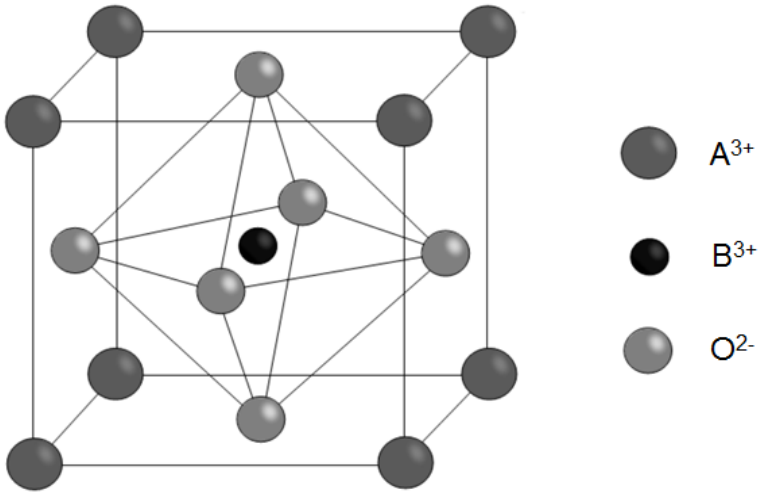

Figure 3.4: The ideal cubic perovskite crystal structure. Modified from [53].

The perovskite crystal structure retains its ideal cubic structure if the Goldschmidt tolerance factor *t*, expressed by the following equation, is between 0.75 and 1.0 [54]:

$$t = \frac{R_A + R_O}{\sqrt{2}\,(R_B + R_O)} \tag{3.2}$$

where R denotes the ionic radius, and the subscripts A, B, and O represent the A-site, B-site, and oxygen site respectively. If the ionic radii are highly mismatched, *t* will not be within the range under which the cubic structure is most stable, and will adopt other crystal structures. Ramos et al. [55] found via Rietveld refinement of XRD measurements that $La_{1-x}Sr_xCr_{0.2}Fe_{0.8}O_{3-\delta}$ does not adopt an idealized cubic perovskite structure, the authors observed that the level of A-site (Sr) dopant determines the crystal structure in this family of materials, with the orthorhombic (Pnma space group) structure being most preferable at $0 \leq x \leq 0.2$.

3.2.2 Suitability of Mixed Ionic-Electronic Perovskite Materials for Membrane Application

Extensive studies on mixed ionic-electronic conducting (MIEC) ceramic-based membranes for oxygen separation have been reviewed by Sunarso et. al. [56] and by Gupta et. al. [57]. A detailed list of the advantages and disadvantages of various perovskite oxides compiled and summarized by Gupta et. al. [57] are shown in Table 3-1.

Table 3-1: Advantages and disadvantages of various perovskite oxides [6], [10], [58]–[63]. Modified from [57]. Reprinted with permission from Materials Science and Engineering: R: Reports.

Perovskites	Ionic/electronic/mixed	Advantages	Disadvantages
Chromites	Predominantly electronic	• High stability ($0.21\text{-}10^{-22}$ atm at ~1000°C) • High electrical conductivity (0.6-1.0 S cm^{-1} at 1000 °C)	• Low ionic conductivity • Low density (<60%)
Ferrites	Mixed ionic-electronic	• High ionic (0.05 S cm^{-1} at 900°C) and electronic conductivity (~100 S cm^{-1} at 1000°C • High activity for oxygen reduction with oxygen flux (1.8×10^{-6} mol cm^{-2} s^{-1})	• High thermal expansion coefficient (23.8×10^{-6} K^{-1} for T > 600°C) • Decomposes into La_2O_3 and Fe in reducing atmosphere ($\leq 10^{-17}$ atm) at 1000°C • More prone to lattice structure distortion due to changes in valence states ($Fe^{3+}/Fe^{2+}/Fe^{4+}$)
Manganites	Predominantly electronic	• High electrical conductivity (83 S cm^{-1} at 800°C)	• Decomposes into La_2O_3 and MnO in reducing atmosphere ($\leq 10^{-15}$ atm) at 1000°C • Low ionic conductivity (1.1×10^{-7} S cm^{-1} at 900 °C)
Nickelates	Predominantly electronic	• Good electrical conductivity (~10 S cm^{-1} at 800°C) • High activity for oxygen reduction with oxygen flux ($\sim 1.6 \times 10^{-8}$ mol cm^{-2} s^{-1})	• Not stable and decomposes into La_2NiO_4 and NiO in reducing atmosphere ($<10^{-0.6}$) at 1000°C • Exolution of Ni metal when heavily doped (>50%)
Cobaltites	Mixed ionic-electronic	• High activity for oxygen reduction with oxygen flux ($0.3\text{-}3 \times 10^{-7}$ mol cm^{-2} s^{-1}) • High electronic conductivity (103 S cm^{-1} at 1000°C	• High thermal expansion coefficient (20×10^{-6} K^{-1}) • Decomposes into La_2CoO_4 and CoO in reducing atmosphere ($<10^{-7}$ atm) in reducing atmosphere at 1000°C • More prone to lattice structure distortion due to changes in valence states ($Co^{3+}/Co^{2+}/Co^{4+}$)

It has been found that in general, the perovskites are unstable within a large pO_2 range ($0.21\text{-}10^{-22}$ atm), undergoing decomposition in the highly reducing conditions expected during OTM operation, with the exception of lanthanum chromite, $LaCrO_3$. However,

undoped $LaCrO_3$ possesses negligible ionic conduction and low density, and so the introduction of dopants is necessary for suitable application in oxygen transport membranes. A-site dopants, such as Sr and Ca, are used to improve densification [57], while B-site dopants, comprising a wide variety of transition metals (Mn, Co, Fe, Ni, Ti, Al, Cu), are used to improve thermal and crystal structure stability [57]. The addition of both dopants enhances electrical conductivity, in particular A-site doping, where $LaCrO_3$ achieves ionic conduction, making it a mixed ionic-electronic conductor (MIEC).

3.2.2.1 Densification

Mori et. al. [64] found that in the material $La_{1-x}Sr_xCrO_3$ ($0.2 \leq x \leq 0.3$), the presence of Sr increased the density due to the formation of a $SrCrO_4$ phase, which is liquid above ~1256˚C. The density was observed to be ~65% at 1600˚C. $SrCrO_4$ formation aiding densification was also observed by Simner et. al. [65] for $(La_{0.7}Sr_{0.3})_xCrO_{3-\delta}$ ($0.95 \leq x \leq 1.05$), and by Ding et al. [66] for $La_{0.85}Sr_{0.15}CrO_{3-\delta}$, with both authors observing >80% density for their optimally prepared materials. However, these density values are insufficient for membrane application, which require >95% density. The addition of B-site dopants to $La(Sr)CrO_{3-\delta}$ further improves densification. In particular, the density of $La_{0.8}Sr_{0.2}Cr_{1-x}Fe_xO_{3-\delta}$ ($0.1 \leq x \leq 0.5$) was found to increase with increasing Fe-dopant, with measured density being ~97% of theoretical density observed at $x = 0.5$, that is, $La_{0.8}Sr_{0.2}Cr_{0.5}Fe_{0.5}O_{3-\delta}$. However, it was found that the amount of $SrCrO_4$ decreased as Fe-doping increased, despite increasing density. It was postulated by Gupta et. al. [57] that another mechanism that improved the material's density, namely the behaviour of Fe stabilizing the perovskite phase, was present.

3.2.2.2 Electrical Conductivity

The substitution of La^{3+} by a Sr^{2+} dopant in $La(Sr)CrO_{3-\delta}$ induced one of two charge compensation mechanisms, shown in Equations 3.3 and 3.4. The first, shown in Equation 3.3, involves the shift in oxidation state of a B-site ion from B_B^x to $B_B^\bullet$; in the case of $LaCrO_3$, from Cr^{3+} to Cr^{4+}. The second, shown in Equation 3.4, involves the stoichiometric formation of oxygen vacancies in the lattice upon doping. The method of charge compensation is dependent on the oxygen partial pressure; Equation 3.3 is favored in oxidizing atmospheres, while Equation 3.4 is preferred in reducing atmospheres.

$$La_{La}^x + Cr_{Cr}^x \xrightarrow{Sr} Sr'_{La} + Cr_{Cr}^\bullet \tag{3.3}$$

$$2La_{La}^x + O_O^x \xrightarrow{Sr} 2Sr'_{La} + V_O^{\bullet\bullet} + \frac{1}{2}O_2 \tag{3.4}$$

Increases in A-site (Sr) dopant concentration in LSCrF8255 under reducing conditions would result in increased oxygen vacancy concentration, [$V_O^{\bullet\bullet}$], and increased oxygen ion conductivity [57]. The shift in materials behaviour from a purely electronic conductor for $LaCrO_3$ to a mixed ionic-electronic conductor for $La(Sr)CrO_{3-\delta}$ also increases the active volume for oxygen migration within the membrane beyond the two-phase boundaries. Hayashi et. al. [63] determined the optimum oxygen deficiency to achieve maximum electrical conductivity for $A^{III}B^{III}O_3$ perovskites is 0.2, corresponding to the Sr dopant concentration of Sr in La in LSCrF8255. Khine et. al. [67] demonstrated that in simulated membrane operation conditions (950˚C, feed 5%O_2-Ar, permeate 5%CH_4-Ar) the presence of Sr in both $LaCrO_3$ and $LaFeO_3$ showed significant improvement of activity for syngas production, which was attributed to significantly increased mobility of lattice oxygen ions in the perovskite materials. Sfeir et. al. [68] determined, based on thermodynamic calculations based on the ideal solid solution model, that Sr-substituted $La(Sr)CrO_{3-\delta}$ decomposes into SrO and $LaCrO_3$ at a pO_2 of 1.6 x 10^{-26} atm. Similarly, Fe-substituted $LaCr(Fe)O_3$ decomposes into Fe metal and $LaCrO_3$ at a pO_2 of 1.3 x 10^{-23} atm. Both decompositions do not occur within the pO_2 range of 0.21-10^{-22} atm for oxygen transport membrane operation. Both substitution phenomena were also observed to improve catalytic activity for CH_4 oxidation, though the presence of Fe seems to facilitate the deposition of C on the surface.

Unlike the A-site ions, which are responsible for ionic conduction, B-site ions are responsible for electronic conduction, which occurs via B^{n+}-O-$B^{(n+1)+}$ conduction pairs [69]. Transition metals are able to adopt several valence states and so are applicable for electronic conduction. However, the effect of substitution of B-site Cr^{3+} ions for Fe^{3+} in $LaCr(Fe)O_3$ is less clear due to limited information [57]. Lü et al. have observed that for A-site deficient $(La_{0.75}Sr_{0.25})_{0.95}Cr_{1-x}Fe_xO_{3-\delta}$, where $0.3 < x < 0.4$, the prevailing oxidation state of Fe cations in the material in both oxidizing and reducing conditions is +3. This implies that electronic conduction in this material is primarily due to the Cr^{+3}/Cr^{+4} couple. X-ray diffraction analysis determined that the material adopts a rhombohedral (R-3c) structure, though the authors note that $La_{0.75}Sr_{0.25}Cr_{0.5}Fe_{0.5}O_{3-\delta}$ adopts an orthorhombic (Pbnm) structure. It was also speculated that rhombohedral ↔ orthorhombic phase transitions within the material may contribute to chemically induced strain upon redox cycling [70]. Finally, it was observed that while electronic conductivity in $(La_{0.75}Sr_{0.25})_{0.95}Cr_{1-x}Fe_xO_{3-\delta}$ decreased with increasing iron content, the reducibility of the material increases, and so would be considered a necessary detriment for the application of OTMs, which operate in highly reducing conditions.

Electrical conductivity of $La_{0.8}Sr_{0.2}Cr_{0.5}Fe_{0.5}O_{3-\delta}$ (LSCrF8255) was found by Wei et al. [71] to be 21.9 S cm^{-1} in oxidizing (air) atmosphere and 6.4 S cm^{-1} in reducing (5% H_2-Ar)

atmosphere at 800˚C, with the decrease in conductivity being attributed to a reduction in oxidation state of the B-site ions. It was also found by Wei et. al. [71] that as-prepared LSCrF adopts a rhombohedral (R-3c) crystal structure, with a slight increase in the unit cell volume after exposure to reducing conditions. The authors found that LSCrF8255 is chemically stable in reducing conditions up to $pO_2 \sim 10^{-20}$ atm.

3.2.2.3 Chemical Stability

Gupta et. al. [72] examined the effect of oxygen partial pressure on A-site deficient $(La_{0.8}Sr_{0.2})_{0.95}Cr_{0.7}Fe_{0.3}O_{3-\delta}$ (LSCrF8273) paired with 8YSZ acting as a dual-phase membrane material. It was observed that formation of an Fe oxide-enriched phase occurs in reducing atmospheres (Ar-3%H_2-3%H_2O) at elevated temperatures (1400˚C), with the chemical stability of the material decreasing with decreases in pO_2. Chemical and microstructural degradation was not observed in samples exposed to air for 80 h. In contrast, significant modification of the surface was identified on samples exposed to Ar-3%H_2-3%H_2O for 80 h. Examination of a symmetrical cell of configuration LSCrF8273-8YSZ/8YSZ/LSCrF8273-8YSZ under reducing conditions showed the formation of $SrZrO_3$ at the LSCrF/YSZ interfaces which was not present in oxidizing conditions (air). The authors attributed this phase formation to an increase in the polarization resistance of the cell in reducing atmospheres compared to oxidizing atmospheres.

Chemical stability of a dense dual-phase $Zr_{0.84}Y_{0.16}O_{1.92}/La_{0.8}Sr_{0.2}Cr_{0.5}Fe_{0.5}O_{3-\delta}$ composite hollow-fibre membrane was examined by Liu et. al. [73], who found that the membrane exhibited good chemical and microstructural stability after 500 h under an air/CO gradient at 950˚C. However, the asymmetric nature of the hollow-fibre membrane may introduce microstructural changes upon further operation. Asymmetric membranes of this composition were prepared by phase inversion tape casting by Zhang et. al. [74] and He et. al. [75] and were shown to possess high oxygen permeation fluxes and acceptable densities, but no examination of stability studies was performed.

3.2.3 Summary of LSCrF8255 Literature

$LaCrO_3$ perovskite materials were found to be stable within the oxygen partial pressure range 0.21-10^{-22} atm. However, their low density and negligible ionic conduction require the use of dopants to improve the properties of the material for oxygen transport membrane operation [57]. The addition of Sr dopant on the A-site improves the ionic conductivity of the material, making $La(Sr)CrO_{3-\delta}$ a mixed ionic-electronic conductor. The addition of Sr and Fe dopants in $La(Sr)Cr(Fe)O_{3-\delta}$ were found to raise the density of the material [64]–[66], with the density of $La_{0.8}Sr_{0.2}Cr_{0.5}Fe_{0.5}O_{3-\delta}$ (LSCrF8255) observed to be ~97% [57]. $(La_{0.75}Sr_{0.25})_{0.95}Cr_{1-x}Fe_xO_{3-\delta}$, where $0.3 < x < 0.4$ was found to adopt a

rhombohedral (R-3c) crystal structure, but an orthorhombic (Pbnm) crystal structure at x = 0.5. The rhombohedral ↔ orthorhombic transitions caused by B-site concentration variations within the material may contribute to chemically induced strain upon redox cycling [70]. YSZ/LSCrF8273 was observed to possess lower chemical stability in reducing conditions than in oxidizing conditions, evidenced by the formation of $SrZrO_3$ on the surface and formation of iron oxide in the bulk under Ar-3%H_2-3%H_2O at 1400˚C but not under air [72]. In addition, $SrZrO_3$ and iron oxide formation were not observed on YSZ/LSCrF8255 under air/CO gradient at 950˚C [73].

3.3 Summary

Literature of the materials comprising the oxygen transport membranes studied in this work, the fluorite ionic-conducting phase 1Ce10ScSZ and the perovskite mixed ionic-electronic-conducting phase LSCrF8255, was reviewed.

The fluorite ionic-conducting material 1Ce10ScSZ was found to exhibit among the highest ionic conductivity of the doped zirconias, which was attributed to the similarity in size between the dopant Sc^{3+} and the parent Zr^{4+} ions. 1Ce10ScSZ did not exhibit significant degradation after aging for up to 3000 h, although expansion of the reduced Ce^{3+} dopant ion, evidenced by dark orange regions observed, may exacerbate residual stresses over longer aging periods. Preparation of 1Ce10ScSZ to achieve properties (i.e. density) adequate for further study was relatively facile. Oxygen surface exchange at elevated temperatures (~700˚C) was found to be very low without a catalytic surface layer (Ag or Pt) or minimal presence of water.

Of the perovskites examined in the literature, it was found that only lanthanum chromites, $LaCrO_3$, were chemically stable within a high temperature (~1000˚C) and oxygen partial pressure range (0.21-10^{-22} atm) necessary for oxygen transport membrane operation. The addition of A-site Sr dopants significantly improved the ionic conductivity of the predominantly electronically-conducting $LaCrO_3$, making it a mixed ionic-electronic material. The addition of both A-site Sr dopants and B-site dopants improved the density of the material; it was found that LSCrF8255 exhibited >95% of theoretical density, making it acceptable for membrane use. The high iron content in LSCrF8255 was observed to decrease electronic conductivity but was also found to improve its stability in highly reducing conditions. Tests performed on 8YSZ/LSCrF8273 showed the material is less stable in reducing conditions than in air as observed by formation of $SrZrO_3$ and iron oxide phases under Ar-3%H_2-3%H_2O at 1400˚C but not under air at the same temperature. However, $SrZrO_3$ and iron oxide formation were not observed on YSZ/LSCrF8255 under air/CO gradient at 950˚C.

3.4 References

[1] P. Stoffer, "Introduction to Geology," 2015. [Online]. Available: http://geologycafe.com/class/chapter3.html. [Accessed: 06-May-2017].

[2] R. Ruh and H. Garrett, "The System Zirconia-Scandia," *J. Am. Ceram. Soc.*, vol. 60, pp. 399–403, 1977.

[3] S. Badwal and J. Drennan, "Microstructure/conductivity relationship in the scandia-zirconia system," *Solid State Ionics*, vol. 53–56, pp. 769–776, 1992.

[4] S. Badwal, F. Ciacchi, and D. Milosevic, "Scandia-zirconia electrolytes for intermediate temperature solid oxide fuel cell operation," *Solid State Ionics*, vol. 136–137, pp. 91–99, 2000.

[5] I. Takao, I. Tsunekazu, and T. Yukimichi, "Structural phase transition and ion conductivity in $0.88ZrO_2$–$0.12Sc_2O_3$," *Solid State Ionics*, vol. 57, pp. 153–157, 1992.

[6] M. Mogensen, D. Lybye, N. Bonanos, P. V. Hendriksen, and F. W. Poulsen, "Factors controlling the oxide ion conductivity of fluorite and perovskite structured oxides," *Solid State Ionics*, vol. 174, no. 1–4, pp. 279–286, 2004.

[7] J. Kilner, "Fast oxygen transport in acceptor doped oxides," *Solid State Ionics*, vol. 129, no. 1–4, pp. 13–23, 2000.

[8] J. Janek, M. Martin, and K. Becker, "Physical chemistry of solids--the science behind materials engineering.," *Phys. Chem. Chem. Phys.*, vol. 11, no. 17, p. 3010, 2009.

[9] C. Haering, A. Roosen, H. Schichl, and M. Schnoller, "Degradation of the electrical conductivity in stabilised zirconia system Part II: Scandia-stabilised zirconia," *Solid State Ionics*, vol. 176, no. 3–4, pp. 261–268, 2005.

[10] J. Kilner and R. Brook, "A study of oxygen ion conductivity in doped non-stoichiometric oxides," *Solid State Ionics*, vol. 6, pp. 237–252, 1982.

[11] J. Kilner, "Fast Anion Transport in Solids," *Solid State Ionics*, vol. 8, pp. 201–207, 1983.

[12] A. Bogicevic and C. Wolverton, "Nature and strength of defect interactions in cubic stabilized zirconia," *Phys. Rev. B*, vol. 67, no. 24106, pp. 1–13, 2003.

[13] A. Bogicevic, C. Wolverton, G. Crosbie, and E. Stechel, "Defect ordering in aliovalently doped cubic zirconia from first principles," *Phys. Rev. B*, vol. 64, no. 1, pp. 1–14, 2001.

[14] F. Pietrucci, M. Bernasconi, A. Laio, and M. Parrinello, "Vacancy-vacancy

interaction and oxygen diffusion in stabilized cubic ZrO_2 from first principles," *Phys. Rev. B*, vol. 78, no. 94301, pp. 1–7, 2008.

[15] S. Norberg, S. Hull, I. Ahmed, S. Eriksson, D. Marrocchelli, P. Madden, P. Li, and J. Irvine, "Structural Disorder in Doped Zirconias, Part I: The $Zr_{0.8}Sc_{0.2-x}Y_xO_{1.9}$ ($0.0 \leq x \leq 0.2$) System," *Chem. Mater.*, vol. 23, pp. 1356–1364, 2011.

[16] D. Marrocchelli, P. Madden, S. Norberg, and S. Hull, "Structural Disorder in Doped Zirconias, Part II: Vacancy Ordering Effects and the Conductivity Maximum.," *Chem. Mater.*, vol. 23, no. 6, pp. 1365–1373, 2011.

[17] D. Kim, "Lattice Parameters, Ionic Conductivities, and Solubility limits in Fluorite-Structure MO_2 Oxide Solid Solutions," *J. Am. Ceram. Soc.*, vol. 72, no. 8, pp. 1415–1421, 1989.

[18] P. Simoncic and A. Navrotsky, "Systematics of Phase Transition and Mixing Energetics in Rare Earth, Yttrium, and Scandium Stabilized Zirconia and Hafnia," *J. Am. Ceram. Soc.*, vol. 90, no. 7, pp. 2143–2150, 2007.

[19] V. Kharton, E. Naumovich, and A. Vecher, "Research on the electrochemistry of oxygen ion conductors in the former Soviet Union. I. ZrO_2-based ceramic materials," *J. Solid State Electrochem.*, vol. 3, no. 2, pp. 61–81, 1999.

[20] V. Kharton, F. Marques, and A. Atkinson, "Transport properties of solid oxide electrolyte ceramics: a brief review," *Solid State Ionics*, vol. 174, no. 1–4, pp. 135–149, 2004.

[21] J. Dixon, L. LaGrange, U. Merten, C. Miller, and J. Porter, "Electrical Resistivity of Stabilized Zirconia at Elevated Temperatures," *J. Electrochem. Soc.*, vol. 110, p. 276, 1963.

[22] D. Strickler and W. Carlson, "Electrical Conductivity in the ZrO_2-Rich Region of Several M_2O_3—ZrO_2 Systems," *J. Am. Ceram. Soc.*, vol. 69, pp. 2–5, 1965.

[23] D. Hohnke, "Ionic conduction in doped oxides with the fluorite structure," *Solid State Ionics*, vol. 5, no. C, pp. 531–534, 1981.

[24] S. Miller, B. Dunlap, and A. Fleischer, "Cation coordination and interstitial oxygen occupancy in co-doped zirconia from first principles," *Solid State Ionics*, vol. 227, pp. 66–72, 2012.

[25] E. Raj, A. Atkinson, and J. Kilner, "Oxygen diffusion studies on $(Y_2O_3)_2(Sc_2O_3)_9(ZrO_2)_{89}$," *Solid State Ionics*, vol. 180, no. 14–16, pp. 952–955, 2009.

[26] E. Kurumchin, "An isotope exchange study of the behaviour of electrochemical systems," *Solid State Ionics*, vol. 42, no. 3–4, pp. 129–133, 1990.

[27] S. Omar and N. Bonanos, "Ionic conductivity ageing behaviour of 10 mol.% Sc_2O_3–1 mol.% CeO_2–ZrO_2 ceramics," *J. Mater. Sci.*, vol. 45, no. 23, pp. 6406–6410, 2010.

[28] S. Omar, W. Bin Najib, W. Chen, and N. Bonanos, "Electrical Conductivity of 10 mol% Sc_2O_3-1 mol% M_2O_3-ZrO_2 Ceramics," *J. Am. Ceram. Soc.*, vol. 95, no. 6, pp. 1965–1972, 2012.

[29] S. Omar, W. Najib, and N. Bonanos, "Conductivity ageing studies on 1M10ScSZ (M^{4+} = Ce, Hf)," *Solid State Ionics*, vol. 189, no. 1, pp. 100–106, 2011.

[30] S. Omar, A. Belda, A. Escardino, and N. Bonanos, "Ionic conductivity ageing investigation of 1Ce10ScSZ in different partial pressures of oxygen," *Solid State Ionics*, vol. 184, no. 1, pp. 2–5, 2011.

[31] S. Omar, W. Najib, W. Chen, and N. Bonanos, "Ionic conductivity of co-doped Sc_2O_3-ZrO_2 ceramics," *Funct. Mater.*, vol. 289, pp. 289–293, 2012.

[32] H. Dasari, J. Ahn, K. Ahn, S. Park, J. Hong, H. Kim, K. Yoon, J. Son, H. Lee, and J. Lee, "Synthesis, sintering and conductivity behavior of ceria-doped Scandia-stabilized zirconia," *Solid State Ionics*, vol. 263, pp. 103–109, 2014.

[33] A. Kumar, A. Jaiswal, M. Sanbui, and S. Omar, "Oxygen-Ion Conduction in Scandia-Stabilized Zirconia-Ceria Solid Electrolyte (xSc_2O_3–$1CeO_2$–$(99 - x)ZrO_2$, $5 \leq x \leq 11$)," *J. Am. Ceram. Soc.*, vol. 8, no. 38652, pp. 1–8, 2016.

[34] K. Yamaji, H. Kishimoto, M. Brito, T. Horita, H. Yokokawa, M. Shimazu, K. Yashiro, T. Kawada, and J. Mizusaki, "Effect of Mn-doping on stability of Scandia stabilized zirconia electrolyte under dual atmosphere of solid oxide fuel cells," *Solid State Ionics*, vol. 247–248, no. July 2012, pp. 102–107, 2013.

[35] H. Abbas, C. Argirusis, M. Kilo, H. Wiemhöfer, F. Hammad, and Z. Hanafi, "Preparation and conductivity of ternary scandia-stabilised zirconia," *Solid State Ionics*, vol. 184, no. 1, pp. 6–9, 2011.

[36] R. Grosso, M. Bertolete, I. Machado, R. Muccillo, and E. Muccillo, "Ionic conductivity and phase stability of spark plasma sintered scandia and ceria-stabilized zirconia," *Solid State Ionics*, vol. 230, pp. 48–51, 2013.

[37] J. Joo, K. Yun, J. Kim, Y. Lee, C. Yoo, and J. Yu, "Substantial Oxygen Flux in Dual-Phase Membrane of Ceria and Pure Electronic Conductor by Tailoring the Surface," *ACS Appl. Mater. Interfaces*, p. 150701120954008, 2015.

[38] J. Joo, K. Yun, Y. Lee, J. Jung, C. Yoo, and J. Yu, "Dramatically Enhanced Oxygen Fluxes in Fluorite-Rich Dual-Phase Membrane by Surface Modification," 2014.

[39] J. Joo, G. Park, C. Yoo, and J. Yu, "Contribution of the surface exchange kinetics to

the oxygen transport properties in $Gd_{0.1}Ce_{0.9}O_{2-\delta}$–$La_{0.6}Sr_{0.4}Co_{0.2}Fe_{0.8}O_{3-\delta}$ dual-phase membrane," *Solid State Ionics*, vol. 253, pp. 64–69, 2013.

[40] X. Zhu, Q. Li, Y. Cong, and W. Yang, "Syngas generation in a membrane reactor with a highly stable ceramic composite membrane," *Catal. Commun.*, vol. 10, no. 3, pp. 309–312, 2008.

[41] X. Zhu, M. Li, H. Liu, T. Zhang, Y. Cong, and W. Yang, "Design and experimental investigation of oxide ceramic dual-phase membranes," *J. Memb. Sci.*, vol. 394–395, pp. 120–130, 2012.

[42] I. Kagomiya, T. Iijima, and H. Takamura, "Oxygen permeability of nanocrystalline $Ce_{0.8}Gd_{0.2}O_{1.9}$–$CoFe_2O_4$ mixed-conductive films," *J. Memb. Sci.*, vol. 286, no. 1–2, pp. 180–184, 2006.

[43] P. Seeharaj, A. Berenov, E. Raj, R. Rudkin, and A. Atkinson, "Mixed-conducting LSC/CGO composites for passive oxygen separation membranes," *Solid State Ionics*, vol. 192, no. 1, pp. 638–641, 2011.

[44] Y. Lin, S. Fang, D. Su, K. Brinkman, and F. Chen, "Enhancing grain boundary ionic conductivity in mixed ionic–electronic conductors," *Nat. Commun.*, vol. 6, p. 6824, 2015.

[45] J. Yi, Y. Zuo, W. Liu, L. Winnubst, and C. Chen, "Oxygen permeation through a $Ce_{0.8}Sm_{0.2}O_{2-\delta}$–$La_{0.8}Sr_{0.2}CrO_{3-\delta}$ dual-phase composite membrane," *J. Memb. Sci.*, vol. 280, no. 1–2, pp. 849–855, 2006.

[46] B. Wang, J. Yi, L. Winnubst, and C. Chen, "Stability and oxygen permeation behavior of $Ce_{0.8}Sm_{0.2}O_{2-\delta}$–$La_{0.8}Sr_{0.2}CrO_{3-\delta}$ composite membrane under large oxygen partial pressure gradients," *J. Memb. Sci.*, vol. 286, no. 1–2, pp. 22–25, 2006.

[47] D. Lee, W. Kim, S. Choi, J. Kim, H. Lee, and J. Lee, "Characterization of ZrO_2 co-doped with Sc_2O_3 and CeO_2 electrolyte for the application of intermediate temperature SOFCs," *Solid State Ionics*, vol. 176, no. 1–2, pp. 33–39, 2005.

[48] I. Gibson, G. Dransfield, and J. Irvine, "Sinterability of commercial 8 mol% yttria-stabilized zirconia powders and the effect of sintered density on the ionic conductivity," *J. Mater. Sci.*, vol. 33, pp. 4297–4305, 1998.

[49] X. Chen, K. Khor, S. Chan, and L. Yu, "Influence of microstructure on the ionic conductivity of yttria-stabilized zirconia electrolyte," *Mater. Sci. Eng. A*, vol. 335, no. 1–2, pp. 246–252, 2002.

[50] T. Shimonosono, H. Kimura, and Y. Sakka, "Effect of grain size on electrical properties of scandia-stabilized zirconia," *J. Ceram. Soc. Japan*, vol. 118, no. 1383, pp. 1038–1043, 2010.

[51] R. Grosso and E. Muccillo, “Sintering, phase composition and ionic conductivity of zirconia–scandia–ceria,” *J. Power Sources*, vol. 233, pp. 6–13, 2013.

[52] T. Sakai, J. Hyodo, M. Ogushi, A. Inoishi, S. Ida, and T. Ishihara, “Evaluation of isotope diffusion coefficient and surface exchange coefficient of ScSZ series oxide by oxygen isotope exchange method,” *Solid State Ionics*, vol. 301, pp. 156–162, 2017.

[53] J. Druce, “Mixed Conducting CGO-LSCF Composites for Oxygen Separation in Oxyfuelled Carbon Capture and Storage Systems,” 2010.

[54] P. Gellings and H. Bouwmeester, *Handbook of Solid State Electrochemistry*. CRC Press, 1997.

[55] T. Ramos, M. Carvalho, L. Ferreira, M. Cruz, and M. Godinho, “Structural and Magnetic Characterization of the Series $La_{1-x}Sr_xFe_{0.8}Cr_{0.2}O_{3-d}$ (x = 0.2, 0.4, 0.6 and 0.8),” *Chem. Mater.*, vol. 18, no. 16, pp. 3860–3865, 2006.

[56] J. Sunarso, S. Baumann, J. M. Serra, W. A. Meulenberg, S. Liu, Y. S. Lin, and J. C. Diniz da Costa, “Mixed ionic–electronic conducting (MIEC) ceramic-based membranes for oxygen separation,” *J. Memb. Sci.*, vol. 320, no. 1–2, pp. 13–41, 2008.

[57] S. Gupta, M. Mahapatra, and P. Singh, “Lanthanum chromite based perovskites for oxygen transport membrane,” *Mater. Sci. Eng. R Reports*, vol. 90, pp. 1–36, 2015.

[58] J. Richter, P. Holtappels, T. Graule, T. Nakamura, and L. Gauckler, “Materials design for perovskite SOFC cathodes,” *Monatshefte für Chemie - Chem. Mon.*, vol. 140, no. 9, pp. 985–999, 2009.

[59] R. De Souza and M. Martin, “An atomistic simulation study of oxygen-vacancy migration in perovskite electrolytes based on LaGaO3,” *Monatshefte fur Chemie*, vol. 140, no. 9, pp. 1011–1015, 2009.

[60] M. Cherry, M. Islam, and C. Catlow, “Oxygen Ion Migration in Perovskite-Type Oxides,” *Journal of Solid State Chemistry*, vol. 118, no. 1. pp. 125–132, 1995.

[61] Y. Tsuru, M. Shimazu, M. Shiono, and M. Morinaga, “Evaluation of linear thermal expansion coefficients of perovskite oxides using ab-initio molecular dynamics with small cell sizes for materials design,” *Jpn. J. Appl. Phys.*, vol. 49, no. 4 PART 1, pp. 0457011–0457015, 2010.

[62] S. Taniguchi and M. Aniya, “Relationship Between Thermal Expansion, Ionic Conduction and Ionicity in Perovskite-Type Oxides,” *Integr. Ferroelectr.*, vol. 115, no. 1, pp. 18–24, 2010.

[63] H. Hayashi, “Structural consideration on the ionic conductivity of perovskite-type oxides,” *Solid State Ionics*, vol. 122, no. 1–4, pp. 1–15, 1999.

[64] M. Mori, Y. Hiei, and N. Sammes, "Sintering behavior of Ca- or Sr-doped $LaCrO_3$ perovskites including second phase of $AECrO_4$ (AE = Sr , Ca) in air," *Solid State Ionics*, vol. 135, pp. 743–748, 2000.

[65] S. Simner, J. Hardy, J. Stevenson, and T. Armstrong, "Sintering of non-stoichiometric strontium doped lanthanum chromite," *J. Mater. Sci. Lett.*, vol. 19, no. 10, pp. 863–865, 2000.

[66] X. Ding, Y. Liu, L. Gao, and L. Guo, "Effects of cation substitution on thermal expansion and electrical properties of lanthanum chromites," *J. Alloys Compd.*, vol. 425, no. 1–2, pp. 318–322, 2006.

[67] M. Khine, L. Chen, S. Zhang, J. Lin, and S. Jiang, "Syngas production by catalytic partial oxidation of methane over $(La_{0.7}A_{0.3})BO_3$ (A = Ba, Ca, Mg, Sr, and B = Cr or Fe) perovskite oxides for portable fuel cell applications," *Int. J. Hydrogen Energy*, vol. 38, no. 30, pp. 13300–13308, 2013.

[68] J. Sfeir, P. Buffat, P. Möckli, N. Xanthopoulos, R. Vasquez, H. Mathieu, J. Van herle, and K. Thampi, "Lanthanum Chromite Based Catalysts for Oxidation of Methane Directly on SOFC Anodes," *J. Catal.*, vol. 202, no. 2, pp. 229–244, 2001.

[69] J. ten Elshof, H. Bouwmeester, and H. Verweij, "Oxidative coupling of methane in mixed-conducting perovskite membrane reactor," *Appl. Catal. A Gen.*, vol. 130, no. 2, pp. 195–212, 1995.

[70] M. Lü, E. Tsipis, J. Waerenborgh, A. Yaremchenko, V. Kolotygin, S. Bredikhin, and V. Kharton, "Thermomechanical, transport and anodic properties of perovskite-type $(La_{0.75}Sr_{0.25})_{0.95}Cr_{1-x}Fe_xO_{3-d}$," *J. Power Sources*, vol. 206, pp. 59–69, 2012.

[71] T. Wei, X. Zhou, Q. Hu, Q. Gao, D. Han, X. Lv, and S. Wang, "A high power density solid oxide fuel cell based on nano-structured $La_{0.8}Sr_{0.2}Cr_{0.5}Fe_{0.5}O_{3-\delta}$ anode," *Electrochim. Acta*, vol. 148, pp. 33–38, 2014.

[72] S. Gupta, H. Sabarou, Y. Zhong, and P. Singh, "Phase evolution and electrochemical performance of iron doped lanthanum strontium chromite in oxidizing and reducing atmosphere," *Int. J. Hydrogen Energy*, pp. 2–11, 2016.

[73] J. Liu, T. Liu, W. Wang, J. Gao, and C. Chen, "$Zr_{0.84}Y_{0.16}O_{1.92}$–$La_{0.8}Sr_{0.2}Cr_{0.5}Fe_{0.5}O_{3-\delta}$ dual-phase composite hollow fiber membrane targeting chemical reactor applications," *J. Memb. Sci.*, vol. 389, pp. 435–440, 2012.

[74] Y. Zhang, R. Yuan, Z. He, J. Gao, and C. Chen, "Phase inversion tape casting and oxygen permeation properties of supported planar $Zr_{0.84}Y_{0.16}O_{1.92}$–$La_{0.8}Sr_{0.2}Cr_{0.5}Fe_{0.5}O_{3-\delta}$ composite membrane," *Solid State Ionics*, pp. 8–12, 2016.

[75] W. He, J. Liu, C. Chen, and M. Ni, "Oxygen permeation modeling for

$Zr_{0.84}Y_{0.16}O_{1.92}$–$La_{0.8}Sr_{0.2}Cr_{0.5}Fe_{0.5}O_{3-\delta}$ asymmetric membrane made by phase-inversion," *J. Memb. Sci.*, vol. 491, pp. 90–98, 2015.

4 Materials and Methods

This chapter will detail the materials used in this work, including synthesis, processing, and preparation prior to and after experimental analysis. The experimental methods and techniques will also be reviewed, with emphasis placed on the analysis techniques more relevant to this work.

4.1 Materials Preparation

4.1.1 Preliminary Powder Characterization

Powders of $Sc_{0.10}Ce_{0.01}Zr_{0.89}O_{2-\delta}$ (1Ce10ScSZ) and $(La_{0.8}Sr_{0.2})_{0.95}Cr_{0.5}Fe_{0.5}O_{3-\delta}$ (LSCrF8255) were obtained from Daiichi Kigenso Kagaku Kogyo (DKKK) Co. Ltd and Praxair Specialty Ceramics Inc. respectively.

In addition to the expected oxides in stoichiometric proportions, trace amounts of other oxides were detected, including Fe_2O_3, SiO_2 and Na_2O. Other elements including Al_2O_3, TiO_2 and CaO were below the detection limits of the analysis. All trace elements were less than 0.01%. The average particle size D_{50} of both powders was quoted as being 0.58 μm. Analysis on the LSCrF8255 powders provided by Praxair Specialty Ceramics Inc. showed that the particles exhibited an average particle size of 0.90 μm after ball-milling in ethanol solution for 24 h. X-ray diffraction data provided with the samples indicated that the powders adopted an orthorhombic structure and Pbnm space group.

The sponsor of this work, Praxair Inc., performed further ball-milling of the powders, reducing the average particle size of both powders to D_{50} = 0.30 μm. In addition, a polymer binding agent was added to both powders to facilitate the formation of fully dense samples upon sintering.

4.1.2 Powder Preparation, Pressing and Sintering

Samples of 1Ce10ScSZ were prepared at Imperial College by uniaxially pressing the powders (2 tonne load) in a cylindrical stainless steel die with a diameter of 12.8 mm. One gram of powder added to the die was sufficient to create a disc-shaped 'green' sample approximately 2 mm in thickness. An alumina crucible was lined with as-received powder, where the samples were placed. Samples of LSCrF8255 were prepared in the same manner, with a separate crucible used to prevent cross-contamination. Samples were sintered in ambient air at 1450°C for 6 hours with a heating and cooling rate of 10°C/min. Sintered samples of 1Ce10ScSZ were 9.6 mm in diameter and 2.4 mm in thickness.

Preparation of dual-phase 1Ce10ScSZ/LSCrF8255 powders was achieved by mixing the two single-phase powders in a 50/50 vol% ratio (approximately 55/45 wt% ratio) and ball-milling in ethanol for 24 h. The powder was allowed to dry in ambient air, after which dual-phase samples were prepared using the same method as the single-phase samples described above.

Samples of 1Ce10ScSZ and LSCrF8255 were also prepared externally by Praxair Inc. Samples were pressed uniaxially at 5,000 psi (~35 MPa) and then isostatically at 28,000 psi (~193 MPa). The samples were sintered in air at 1400˚C for 6 hours.

4.1.3 Sample Aging

The dual-phase 1Ce10ScSZ/LSCrF8255 samples prepared externally were exposed to two aging periods, under three separate aging conditions. The first batch of samples were aged at 1000°C for 300 hours in ambient air, 4% H_2-96% N_2, and 5% H_2-95% CO_2. It was expected that under operating conditions, the materials would be exposed to air (pO_2 ~ 0.21 atm) on the feed side, and a syngas mixture of approximately 5% H_2-95% CO_2 (pO_2 ~ 10^{-11} atm) on the permeate side. The aging condition of 4% H_2-96% N_2 (pO_2 ~ 10^{-18} atm) was chosen to test the stability of the material under highly reducing conditions. The aging conditions on the second batch of samples were identical to that of the first batch, with the only exception being that the materials were left exposed to aging conditions for 1000 hours.

Table 4-1: Aging parameters for dual-phase 1Ce10ScSZ/LSCrF8255 samples used in this work.

1Ce10ScSZ/LSCrF8255 Sample #	Aging Time	Aging Condition
1	0 h	N/A
2	300 h	1000˚C, ambient air
3	300 h	1000˚C, 4%H_2-96%N_2
4	300 h	1000˚C, 5%H_2-95%CO_2
5	1000 h	1000˚C, ambient air

6	1000 h	1000˚C, 4%H_2-96%N_2
7	1000 h	1000˚C, 5%H_2-95%CO_2

4.1.4 Density Measurements

Highly-dense samples are a requirement for meaningful measurements of the oxygen transport kinetics via Isotope Exchange Depth Profiling (Section 4.2.4), as open porosity in samples act as short circuits for diffusion. It has been shown that open porosity is eliminated if the density of the samples is 95% or greater of theoretical density [1]. To determine the experimental density of a sintered sample, the Archimedes method was used, where the weight of the sample in air and in distilled water was measured. Using Equation 4.1 the experimental density was calculated:

$$\rho_{exp} = \frac{W_{air} \bullet \rho_{H2O,t}}{W_{air} - W_{H2O,t}} \tag{4.1}$$

where ρ_{exp} is the experimental density, W_{air} is the weight of the sample in ambient air, $W_{H2O,t}$ is the weight of the sample in water at a given temperature, and $\rho_{H2O,t}$ is the density of water at a given temperature. The theoretical density of the sample can be determined if the crystal structure and lattice parameters of the material are known. In particular, the theoretical density of the material is the total mass of a species *i* in a unit cell of the material divided by the volume of the unit cell, as shown in Equation 4.2:

$$\rho_{theo} = \frac{\Sigma_i(N_i \bullet M_i)}{V_{cell} \bullet N_A} \tag{4.2}$$

where ρ_{theo} is the theoretical density, N_i is the number of atoms of a species *i* per unit cell, M_i is the molar mass of the species *i*, V_{cell} is the volume of the unit cell, and N_A is Avogadro's number.

4.1.5 Preparation for Isotope Exchange Depth Profiling

Samples with densities greater than 95% of theoretical density were subsequently prepared for oxygen isotopic (^{18}O) exchange measurements. Samples were polished to a "mirror finish" to reduce the effect of surface roughness on experimental results. The polishing process remains constant for all samples in this work, and any future references to "polished" samples will have undergone this method, outlined below:

1. A sintered sample was adhered to a cylindrical brass stub, by heating the stub to ~180˚C on a hot plate and applying a resin to the stub surface. The sintered dense sample was placed on this resin-covered surface.
2. Silica glass slides cut to appropriate shapes were adhered to the resin-covered surface to prevent the stub from tilting during polishing. For ease of polishing, the glass slides should ideally be close to the height (thickness) of the sample and cover as much of the stub surface as possible. The stub is then taken off the hot plate and allowed to cool to room temperature.
3. With the sample and glass slide firmly set on the stub surface, the sample was ground at 300 RPM using P600 (~30 μm particle size), P800 (~22 μm) and P1200 (~15 μm) grade silicon carbide paper until the sample and glass slides were flush with each other.
4. The sample was polished at 300 RPM using diamond polishing media of particle size 6 μm, 3 μm, 1 μm and ¼ μm using a 'Struers RotoPol-15 Autopolisher'. The brass stub was mounted on the autopolisher and a constant 20 N of force was applied to the stub during polishing. The duration of polishing was increased at progressively finer particle sizes, from ~15 minutes for 6 μm to ~30 minutes for ¼ μm.
5. The sample was removed from the stub by heating the stub to ~180 ˚C. The sample was then cleaned using acetone, isopropanol and distilled water using an ultrasonic bath.

Once polished, the sample was sectioned using a low-speed diamond saw. The sample was adhered onto a silica glass slide in the manner described for the polishing stub outlined above, allowed to cool, and placed into the saw. The sample was removed from the glass slide via re-application of heat, and cleaned using acetone, isopropanol and distilled water using an ultrasonic bath as outlined above.

4.2 Analysis Technique Background

This section will detail the analysis techniques used in this work. The primary question to be addressed for this project is the effect of prolonged exposure to simulated operating conditions on the self-diffusion behaviour of ionic oxygen in 1Ce10ScSZ/LSCrF8255 in the absence of any chemical gradient. Total conductivity of single-phase 1Ce10ScSZ was performed by Electrochemical Impedance Spectroscopy (Section 4.2.3). Oxygen transport kinetics of single-phase 1Ce10ScSZ and dual-phase 1Ce10ScSZ/LSCrF8255 was performed using Isotope Exchange Depth Profiling (IEDP – Section 4.2.4) coupled with Secondary Ion Mass Spectrometry (SIMS – Section 4.2.5). Examination of the surface chemistry of the materials before and after aging was performed using Low Energy Ion Scattering

(LEIS – Section 4.2.6) and X-ray Photoelectron Spectroscopy (XPS – Section 4.2.7). The understanding of bulk properties such as the crystal structure and microstructure were also performed via X-ray Diffraction (XRD – Section 4.2.1) and Secondary Electron Microscopy (SEM – Section 4.2.2) respectively.

4.2.1 X-ray Diffraction (XRD)

The wavelengths of X-ray radiation are comparable to the spacing between planes of atoms in a crystal. In specific situations, scattering of X-rays upon interaction with electron clouds surrounding atoms in a crystal will result in constructive interference. This phenomenon is described by Bragg's Law [2], shown in Equation 4.3,

$$\lambda = 2d_{hkl}\sin\theta_{hkl} \tag{4.3}$$

where λ is the X-ray wavelength, d_{hkl} is the d spacing of the plane with index hkl, and θ_{hkl} is the angle of incidence of the X-ray. A schematic of Bragg's Law is shown in Figure 4.1.

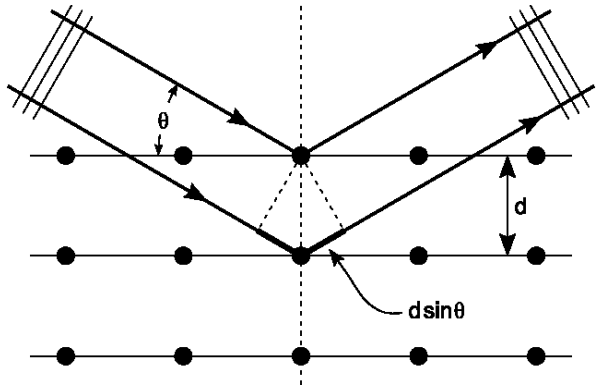

Figure 4.1: Schematic of Bragg's Law illustrating the condition for constructive interference[7].

The unique combination of a material's crystal structure and d-spacing acts as a "fingerprint" for the material, allowing for comparisons between materials with similar diffraction patterns. One database with x-ray diffraction information on the materials relevant to this work is the Inorganic Crystal Structure Database (ICSD) [3]. Experimental diffraction patterns of the materials in this work were initially compared with those with the same composition in this database to confirm the material's crystal phase properties.

Further information can be obtained by refining the parameters of an appropriate structural model until the difference of the diffraction patterns between the theoretical and experimental models is minimized. The theoretical model thus describes the

[7] http://photonicswiki.org/index.php?title=X-ray_Diffraction

experimental model sufficiently well that parameters extracted from the theoretical model are viewed as an analog to the experimental model. This process is called 'Rietveld refinement', and was proposed by Hugo Rietveld [4]. The Rietveld refinement technique was used to determine the crystal phases present in the materials and to confirm whether the crystal structure is in agreement with that displayed in the literature.

Measurement of X-ray diffraction patterns for the starting powders was performed on a Bruker D2 Phaser diffractometer (Billerica, Massachusetts, US) operating at 20 mV and 10 mA producing Cu-K_α radiation (λ = 1.5406 Å). X-rays generated via a copper target consist of Cu-$K_{\alpha 1}$, Cu-$K_{\alpha 2}$, and Cu-K_β wavelengths, so a monochromator was equipped to the instrument to remove the Cu-K_β component.

Diffraction patterns were obtained between 20 and 90 degrees two-theta, with a step size of 0.034° 2θ per data point, and a data collection duration of 0.5 seconds. Rietveld refinement was performed on the single phase materials using the FullProf Suite software [5].

4.2.2 Scanning Electron Microscopy

Electron microscopy is a type of microscopy that uses a focused beam of high energy electrons (1-30 keV) [6] as the illumination source. Since the wavelength of electrons are several orders of magnitude lower than that for visible light, electron microscopy is capable of resolving significantly smaller details on a specimen compared to optical microscopes. Conventional electron microscopes are capable of detecting secondary electrons (SE), backscattered electrons (BSE) and characteristic x-rays, each providing specific information about the material.

Secondary electrons are low-energy electrons (< 50 eV) emitted from the sample resulting from inelastic scattering interactions with the electron beam. The escape depth for SE is typically 5-50 nm [7] and is affected by the accelerating voltage of the electron beam, and the angle of incidence relative to the specimen. Secondary electron images provide surface topography differences and contain no chemical information.

Backscattered electrons are electrons that are elastically scattered upon interaction with electron clouds surrounding the atoms of a material. Atoms with larger numbers of electrons (i.e. larger atomic number Z) have a larger scattering cross-section and thus have higher probability of elastic collisions. In this regard, contrast in backscattered electron images is proportional to the chemical composition of the specimen, with elements of higher Z number appearing brighter and those with lower Z number appearing darker. Thus, backscattered electrons retain much of the initial kinetic energy

after interaction and thus are significantly more energetic than secondary electrons. The escape depth of backscattered electrons is approximately 1-5 μm, so chemical information using BSE images is obtained up to this depth.

Energy-dispersive X-ray spectroscopy (EDX) involves the use of the electron beam to induce characteristic X-ray emission. An incident electron from the electron beam interacts with the electron cloud in an atom, promoting ground-state electrons into higher states, leaving behind electron holes. These electron holes are subsequently filled by electrons from a higher state, and the difference in energies is emitted in the form of X-rays. The characteristic energies of these X-rays are directly related to the elements present and thus can be used for elemental or chemical analysis of a specimen. Escape depths of characteristic X-rays are greater than that of backscattered electrons (> 1-5 μm), so EDX analyses performed in this work are considered to be examinations of the bulk chemical distribution of the material.

The sintered materials were prepared for SEM observation by grinding and polishing as outlined in Section 4.1.5.Preparation for Isotope Exchange Depth Profiling Prior to SEM examinations, samples were sputter-coated in a thin conducting layer of gold to counter the effects of charging on the material. Samples were mounted on the sample holder via double-sided carbon tape. Secondary electron micrographs were obtained using a LEO Gemini 1525 FEG-SEM manufactured by Carl Zeiss Ltd operating in vacuum (~10^{-6} mbar) at approximately 5 keV accelerating voltage. Energy-dispersive X-ray spectroscopy was performed on a JSM6400 SEM manufactured by JEOL (Akishima, Tokyo, Japan) with 20 keV accelerating voltage operating in vacuum (10^{-4} mbar).

4.2.3 Electrochemical Impedance Spectroscopy

Information on the conductivity of a sample can be obtained by measuring its impedance over a wide range of frequencies. A voltage is applied to a cell (consisting of the sample and the electrodes applied to both sample sides) of known dimensions and simple geometry, and the alternating current response is observed. The voltage V is represented as:

$$V = V_o e^{i\omega t} \tag{4.4}$$

where V_o is the amplitude of the voltage, ω is the angular frequency and t is the time constant. The resultant current passing through the sample is thus:

$$I = I_o e^{i(\omega t + \phi)} \tag{4.5}$$

where ϕ is the phase angle. The impedance (Z) of the cell can be obtained from:

$$Z = \frac{V}{I} = \frac{V_o e^{-i\phi}}{I_o} = |Z|e^{-i\phi} \tag{4.6}$$

where |Z|, displayed in Figure 4.2, is the absolute magnitude of the impedance of the cell. Impedance can be split into real and imaginary components:

$$Z = Z' - iZ'' \tag{4.7}$$

where Z' is the real component of impedance = $Z_o\cos\phi$, and Z'' is the imaginary component of impedance = $-Z_o\sin\phi$. A Nyquist plot can be created by plotting -Z'' against Z', which at varying frequency, produces a semicircle; an idealized Nyquist plot is shown in Figure 4.2.

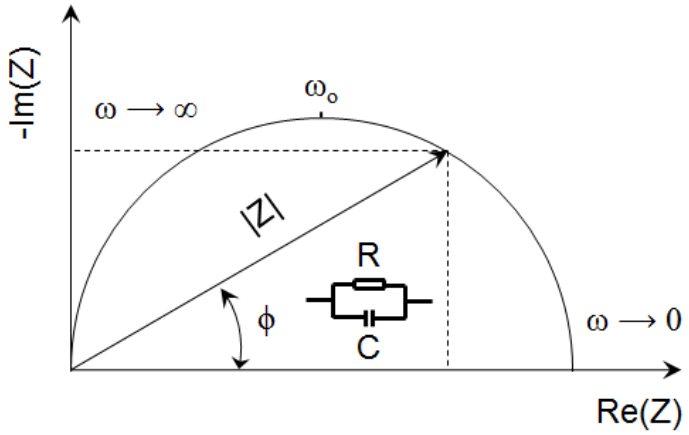

Figure 4.2: Idealized Nyquist plot represented by RC element. Adapted from [8].

Interpretation of the Nyquist plot can be done by attributing each semicircle, which represents a region of a ceramic sample, to an equivalent circuit element, usually an RC element (a resistance and capacitance in parallel). The characteristic relaxation time or time constant, τ, for each RC element is given by:

$$\tau = RC \tag{4.8}$$

The resistance is obtained from the Nyquist plot via the intercepts of the semicircle with the Z' axis; the capacitance is obtained from the equation:

$$\omega_o RC = 1 \tag{4.9}$$

where ω_o is the angular frequency at the maximum amplitude on the -Z'' axis of the Nyquist plot. The characteristic frequency f_{max} of the RC element can be represented as:

$$f_{max} = \frac{\omega_o}{2\pi} = \frac{1}{2\pi RC} \tag{4.10}$$

Experimental impedance spectra will differ from the ideal model in several ways, and can be represented by other equivalent circuit models. Equivalent circuit models exist for phenomena such as electrolyte resistance, double layer capacitance, constant phase elements (CPE), polarization resistances, charge transfer resistances, and Warburg impedance.

In impedance measurements of electroceramics, double layer capacitance often manifests itself away from ideality; the "imperfect capacitor" phenomenon can be interpreted using a constant phase element (CPE) equivalent circuit, and manifests on a Nyquist plot as a depressed semicircle [9]. Several phenomena exhibit CPE behavior, including sample surface roughness, inhomogeneous surface reaction rates, or non-uniform current distribution across the electrode-electrolyte interface.

For electroceramics, characteristic frequencies are adequately separated for the bulk, grain boundary and electrode responses. For a ceramic sample, which can be represented as a parallel plate capacitor with area A, separation between the plates l, and a medium of permittivity ε' between the plates, the capacitance is given by:

$$C = \varepsilon' e_o \frac{A}{l} \tag{4.11}$$

where ε' is the dielectric constant of the material, e_o is the permittivity of free space, 8.854 x 10^{-14} F cm^{-1}, A is the cross-sectional area of the sample, and l is the length (thickness) of the sample. Irvine et al. proposed interpretations of the phenomena responsible based on the magnitude of the capacitance of a material and assigned the phenomena to the corresponding arc in a Nyquist plot [10], summarized in Table 4-2.

In this work, electrochemical impedance spectroscopy was employed primarily to determine the conductivity of 1Ce10ScSZ at elevated temperatures to estimate a diffusion length in preparation for isotopic exchange experiments (see Section 4.2.4). The technique was not performed on single-phase LSCrF8255 due to the inability of the technique to differentiate between ionic and electronic conductivity.

Table 4-2: Capacitance values and their possible interpretations [10].

Capacitance (F/cm^2)	Phenomenon Responsible
10^{-12}	bulk
10^{-11}	minor, second phase
10^{-11}-10^{-8}	grain boundary
10^{-10}-10^{-9}	bulk ferroelectric
10^{-9}-10^{-7}	surface layers
10^{-7}-10^{-5}	sample-electrode interface
10^{-4}	electrochemical reactions

4.2.4 Measurement of Oxygen Self-Diffusion – Isotope Exchange Depth Profiling (IEDP)

Isotopic Exchange Depth Profiling (IEDP), developed by Kilner et. al. [11], utilizes isotopically labelled oxygen as a tracer in measuring the rates of oxygen self-diffusivity and surface exchange in oxide materials. A schematic is illustrated in Figure 4.3. This is possible due to the significantly lower natural abundance of the ^{17}O and ^{18}O isotopes relative to the ^{16}O isotope, as illustrated in

Table 4-3, allowing for any elevated concentration of the isotope fraction in the material above the natural abundance to be evident. The isotope exchange technique employs thermal anneals in controlled oxygen atmospheres enriched with ^{17}O or ^{18}O to introduce a tracer diffusion profile within an oxide material. This technique is performed in conjunction with Secondary Ion Mass Spectrometry (SIMS – see Section 4.2.5) in measuring oxygen tracer self-diffusion in oxide materials.

Table 4-3: Atomic mass and natural abundance of the stable oxygen isotopes [12].

Isotope	Atomic Mass (amu)	Natural Abundance (%)

^{16}O	15.995	99.762
^{17}O	16.999	0.038
^{18}O	17.999	0.200

In this work ^{18}O was used as the oxygen tracer, as ^{17}O has a very similar mass to the hydroxyl species $^{16}O^{1}H$ which is likely to be present in the SIMS measurement chamber. The atomic mass of ^{18}O is similar to that of water, $H_2{}^{16}O$, but due to the high vacuum environment of the SIMS chamber, the presence of detected $H_2{}^{16}O$ species during measurement is minimal. In both cases, SIMS possesses sufficient mass resolution to be able to differentiate between the masses of species of very similar mass. However, the $^{17}O/^{16}O^{1}H$ ratio, which may differ by as little as 0.01 amu, may introduce errors in the number counts of the oxygen isotope. To avoid this, all isotopic experiments were performed using ^{18}O as the oxygen tracer.

A schematic of the isotope exchange apparatus is shown in Figure 4.3. The sample is placed in the exchange chamber in contact with the silica (quartz) "boat". The exchange chamber is connected to several gas streams (^{16}O, ^{18}O, and N_2 gas) controlled via valves, and to a turbomolecular pump capable of reaching high vacuum (< 10^{-7} mbar) in the chamber. A tube furnace is mounted on a rail which is "rolled" onto the sample area during the experiment. A thermocouple is attached to the apparatus in close proximity to the silica boat, in order to determine the temperature of the sample during the experiment. Data on the temperature, oxygen partial pressure, and experimental duration are outputted to a data-logging computer throughout the exchange experiment. The residual gas analyzer (RGA) attached to the apparatus can be used to determine the concentration of the gas species, in particular the isotopic fraction of tracer oxygen ^{18}O relative to the total oxygen fraction (^{16}O+^{18}O). However, a more accurate method to determine the isotopic ratio is to oxidize a piece of silicon in the isotopically enriched gas atmosphere and analyze the oxide layer formed using SIMS.

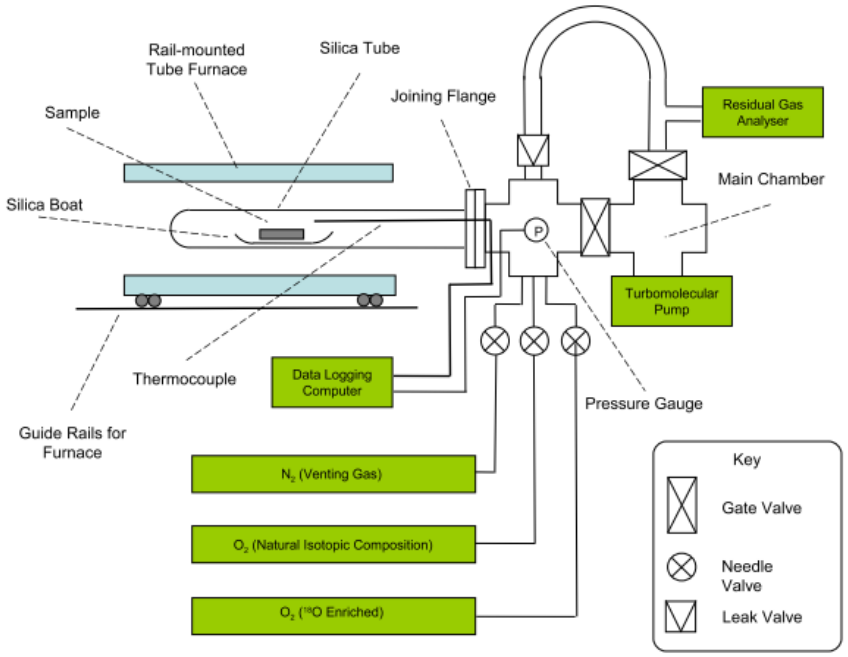

Figure 4.3: Schematic of oxygen isotope exchange apparatus. Figure courtesy of J. Druce [13].

The isotopic exchange technique relies on several assumptions in order to produce meaningful results. It is assumed that the behaviour of ^{16}O and ^{18}O is identical, in that ionic diffusion of both species in the oxide material is the same. In addition, the material has to be sufficiently dense that open porosity is eliminated. If a material possesses open porosity, diffusing oxygen ions within the material at elevated temperatures may recombine to form oxygen gas at a pore boundary, travel in gaseous form through the pore, and dissociate at the opposite end. Samples with open porosity will have higher perceived oxygen tracer concentrations and diffusion lengths not representative of the oxygen transport kinetics in the sample. The introduction of tracer species should be made along a constant diffusion front at the gas-solid interface, which is affected by the surface roughness of the material. Prior to isotope exchange, the material is polished to ensure a more constant front for diffusion of tracer species at the sample surface.

Prior to isotope exchange experiments, it is useful to estimate the diffusion length of the material. The diffusion length, L_D, is a measure of the distance the tracer has diffused into the material, and is related to the diffusivity of a material via Equation 4.12 [14],

$$L_D = 2\sqrt{D_{T,P} t_e} \tag{4.12}$$

where $D_{T,P}$ is the diffusivity at a specific temperature and oxygen partial pressure, t_e is the total time of exchange (i.e. ^{18}O exposure duration). The knowledge of the diffusion length determines which of the two experimental procedures for isotope exchange experiments are appropriate, as summarized in Table 4-4.

Table 4-4: Summary of approximate limits for depth profile and linescan analysis techniques in isotope exchange.

	Depth Profile (μm)	Linescan (μm)
Minimum diffusion length	0.1	10
Maximum diffusion length	5	300

The diffusion length must fall into one of these two ranges. For depth profile measurements and analyses, the minimum diffusion length measurable is ~0.1 μm, and the maximum length is restricted to the point where the sputter-induced roughness at the base of the crater reduces analysis depth resolution [15]. For linescans, the minimum diffusion length is dependent on the maximum lateral resolution of the SIMS instrument, which is approximately 60 nm [16]. The maximum diffusion length depends on the maximum analysis area of the SIMS instrument, which is 500 μm. However, the diffusion profile must also include the profile reaching the background ^{18}O concentration, so a more practical maximum length is ~300 μm. It should be noted that if the SIMS instrument possesses the ability to accurately join multiple scanned areas during analysis, then the maximum diffusion length for linescans can be significantly greater.

Figure 4.4 outlines the experimental procedure for isotope exchange, which is split into two segments. The first "pre-anneal" step is performed using research-grade $^{16}O_2$ (99.999% purity, BOC Ltd.) at a determined temperature, T, and oxygen partial pressure, pO_2. The objective of this step is to chemically equilibrate the material in the exchange conditions, that is, to equilibrate the number of oxygen species, ensuring that the exchange step is purely an exchange and does not introduce a chemical potential gradient. The pre-anneal step is typically performed for 3-10 times the duration of the second "exchange" step, in order to ensure the region of the material through which oxygen tracer ions undergo self-diffusion is in chemical equilibrium.

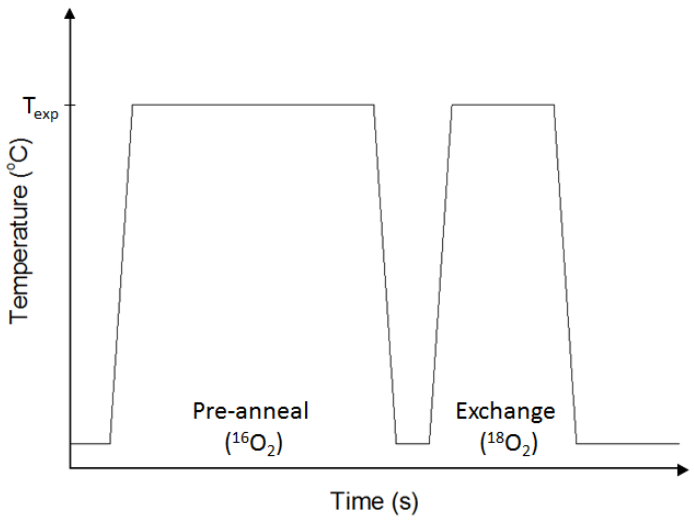

Figure 4.4: Typical temperature/time profile for an isotope exchange experiment performed in this work.

The exchange step involves the substitution of the ^{16}O environment with isotopically enriched ^{18}O (99.9% purity) introduced at the same temperature and oxygen partial pressure. The ^{18}O is stored in a reservoir containing a molecular sieve, which in addition to keeping the oxygen tracer gas free of moisture, allows for recovery of ^{18}O after the experiment using liquid nitrogen. Prior to the introduction of ^{16}O or ^{18}O, the isotope exchange chamber is evacuated to high vacuum ($< 10^{-7}$ mbar) to reduce the presence and effect of impurities in the chamber environment.

Preparation of samples for depth profile analysis on the SIMS instrument is carried out according to the procedure outlined in Section 4.1.5. For linescan analyses, further sample preparation is required prior to SIMS analysis, which is shown in Figure 4.5. After isotope exchange, a sample intended for linescan analysis via SIMS is sectioned using a low-speed diamond saw and the polished surfaces of the two halves are adhered together. This new surface, perpendicular to the original polished surface, is itself polished according to the procedure outlined in Section 4.1.5. This cross-section is analyzed using SIMS.

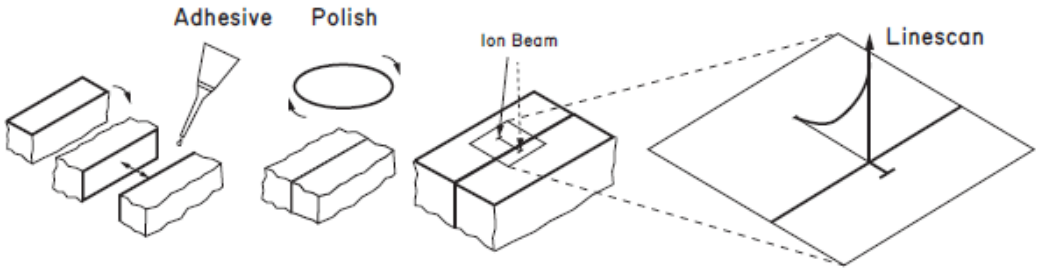

Figure 4.5: A schematic diagram showing sample preparation for linescan analyses, showing the resultant diffusion profile generated. Adapted from [17].

Several potential sources of error are apparent during the isotope exchange experiment. First, as shown in Figure 4.3, the furnace is in a horizontal orientation, and is intended to "roll on" into the sample area. Inside this furnace there is a "hot zone", a region of uniform temperature at the centre of the furnace, which was measured to be approximately 25 mm in length with a temperature variation of ±1°C. Second, the temperature indicator of the furnace may not be the same as the temperature of the hot zone, so the thermocouple installed in the chamber next to the sample is used. For the duration of the experiment, the thermocouple is positioned to be as near to the sample as possible, typically ~10 mm away, and within the hot zone. This ensures that the temperature to which the sample is exposed is accurately displayed by the thermocouple.

The temperature/time profile shown in Figure 4.4 is an idealized scenario of the sample's exposure during the exchange experiment. In reality, when the furnace is removed from the sample area and the sample cools, the initial temperature closely resembles the idealized scenario. However, as the chamber environment approaches ambient (i.e. room) temperature, the cooling rate decreases exponentially. Oxygen self-diffusion, while still occurring at elevated temperatures immediately after the initial cooling step, is considered to be minimal below a certain temperature. In the case of the ionically-conducting 1Ce10ScSZ phase, a significant increase in activation energy was observed below 600°C (see Figure 5.4, Section 5.1.2), which would decrease oxygen migration in the material below this temperature. Since the sample cools below this temperature within 5 seconds of cooling after 30 minutes of exchange time, it is taken that tracer diffusion occurring after cooling does not contribute significantly to the overall measurement.

4.2.5 Measurement of Oxygen Self-Diffusion – Secondary Ion Mass Spectrometry (SIMS)

Secondary Ion Mass Spectrometry (SIMS) is a technique allows examination of the chemical composition of a material with high chemical sensitivity, depth resolution and mass resolution. The high mass resolution of the technique grants the capability to distinguish between isotopes of the same element in a material, which is beyond other chemical analysis techniques such as energy dispersive x-ray spectroscopy (EDX). When used in conjunction with isotopic exchange experiments, SIMS can be used to examine the chemical nature and isotopic behaviour of a surface for the purpose of understanding oxygen transport in ceramic materials.

SIMS involves the bombardment of the sample with high energy primary ions (0.1-20 keV) [19]. The energy of the primary ions results in the destruction of the surface region producing a wide variety of particles, including monoatomic and polyatomic particles from the surface, electrons, and reflected primary ions. Ions from the surface liberated by the primary ion source, termed secondary ions, are extracted and detected using mass spectrometry. A simplified schematic illustration is shown in Figure 4.6.

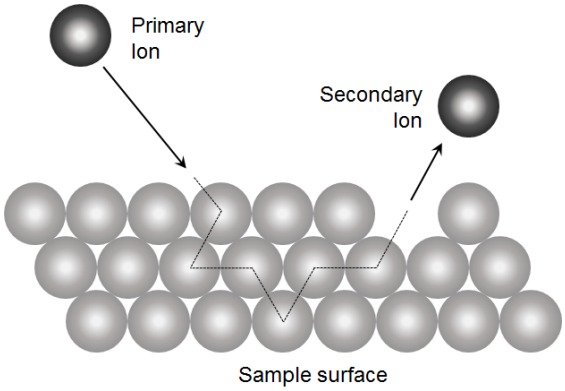

Figure 4.6: Schematic representation of collision event leading to the formation of secondary ions in SIMS. Energy from the primary ion is transferred to the sample surface and distributed between atoms (grey lines) leading to expulsion of secondary ion(s). Modified from [19].

The secondary ion yield is defined by Equation 4.13,

$$I_s^m = I_p C_m y_m \alpha^{\pm} \eta \tag{4.13}$$

where I_s^m is the secondary ion current (yield) of species m, I_p is the primary ion current, C_m is the surface concentration, y_m is the sputter yield, $\alpha^{\pm}$ is the probability of ionization, and η is the transmission efficiency of the analysis system.

Equation 4.13 shows that the measured secondary ion count I_s^m is directly proportional to the concentration C_m, which implies that quantification of species is relatively simple to make. However, quantification is far from simple. In particular, the ionization probability $\alpha^{\pm}$ is dependent on the distribution of ions in the sample analysis area. Quantitative measurements via SIMS depend not only on individual ions analyzed in an oxide material, but also the surrounding matrix of ions, which are referred to as 'matrix effects'. The use of standard materials, one for each element of interest in the sample material, enables data quantification, but are difficult and time-consuming to produce. For this work, relative quantification of the oxygen isotopic fraction was used to measure tracer diffusion profiles. Since oxygen isotopes are chemically identical, they possess the same ionization probability $\alpha^{\pm}$. With the other parameters in Equation 4.13 being identical, the secondary ion yield I_s^m of ^{16}O and ^{18}O can be determined and compared, and the isotopic ratio ($^{16}O/^{18}O$) extracted directly from the SIMS data.

The mass analyzer used in this work was a Time-of-Flight (TOF) SIMS[5] developed by ION-TOF GmbH (Münster, Germany). A schematic is shown in Figure 4.7. The analysis ion gun is a Bi^+ Liquid Metal Ion Gun (LMIG) operated at very low currents (~0.3 pA) to ensure the analysis ion dose has a negligible effect on the sample surface. The sputter ion gun is a Cs^+ ionization source (~150 nA) and is used primarily to reveal subsequent atomic layers for analysis in the SIMS chamber. Extracted secondary ions generated by the analysis ion gun are decelerated and reflected via an electrostatic ion mirror, and then accelerated via an electric field to give all ions the same kinetic energy. The ions are allowed to drift freely to the ion detector, which is a known distance from the mirror. In this configuration, heavier ions would take longer to reach the detector as explained by the equation of kinetic energy ($E_k = \frac{1}{2}mv^2$). The mass-to-charge ratio is calculated from the "time-of-flight" of the ion. In this configuration, the TOF-SIMS is able to measure the mass-to-charge ratios of all ions simultaneously.

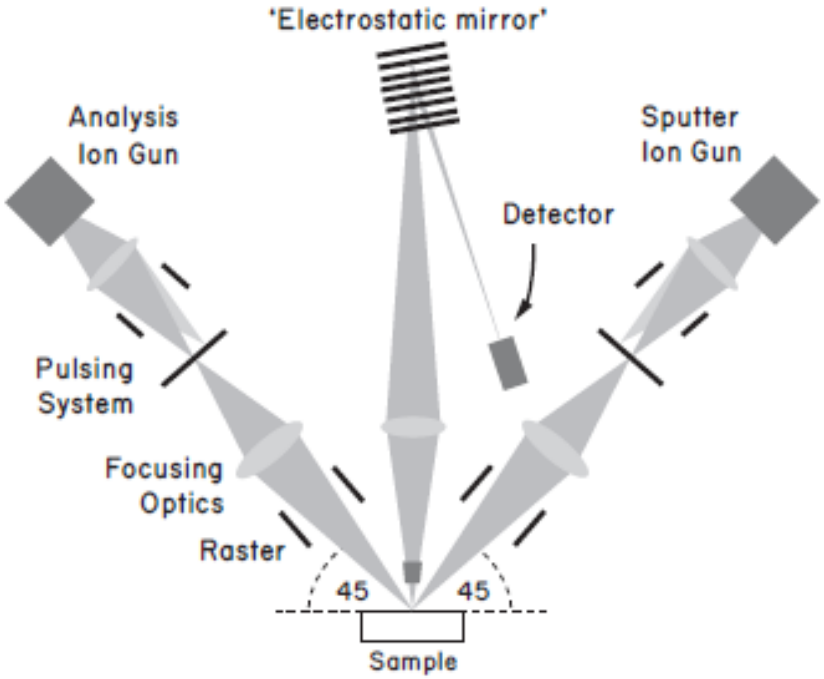

Figure 4.7: Schematic of the TOF-SIMS[5] including the analysis and sputter ion guns and electrostatic mirror. Figure courtesy of M. Niania [17].

The TOF-SIMS employs very short pulses of primary ions in order to prevent detector saturation and to increase mass resolution [20]. There are two methods to generate pulses, which are summarized in Figure 4.8. The first involves "bunching" the ions via a condenser to reduce the ion pulse duration (from ~20 ns to ~0.5 ns), but significantly increase the ion current. This mode results in the highest mass resolution and secondary ion count, at the cost of reducing lateral resolution. The second involves "chopping" a pulse of longer duration (~100 ns) into several bursts (~15 ns each) to further reduce the primary ion yield. This results in lower secondary ion yield and mass resolution but is necessary for analysis of samples with very high ionization rates leading to detector saturation. These modes of operation are termed "High Current Bunched Mode" (HCBM) and "Burst Alignment" (BA) by the ION-TOF manufacturers.

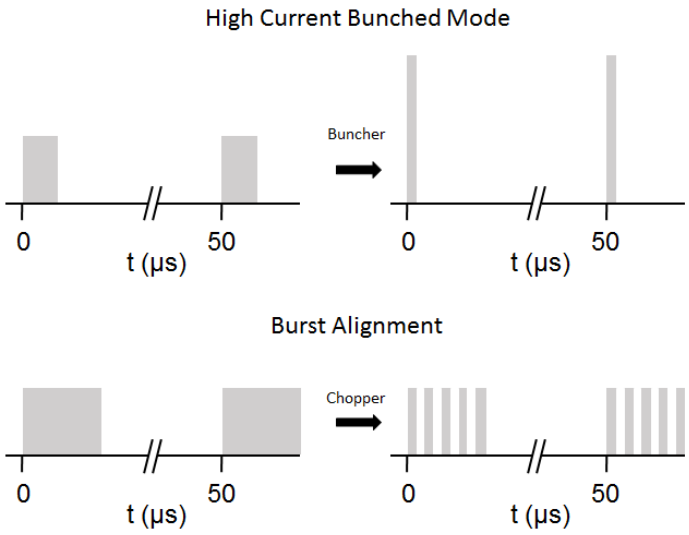

Figure 4.8: A schematic diagram displaying the characteristics for the primary analysis beam for the TOF-SIMS[5] instrument used in this work. Adapted from [17].

In this work, TOF-SIMS measurements were primarily performed on samples for 'linescan' analysis using BA mode to obtain tracer diffusion profiles of 1Ce10ScSZ single-phase and 1Ce10ScSZ/LSCrF8255 dual-phase samples. Measurements were also performed on samples for 'depth profile' analysis using HCBM mode on 1Ce10ScSZ/LSCrF8255 samples to determine the elemental distribution within ~1 μm of the sample surface.

4.2.5.1 Diffusion Data Analysis

In "The Mathematics of Diffusion" [21], Crank solves Fick's second law of diffusion in a semi-infinite medium for a series of boundary conditions, shown in Equation 4.14,

$$\begin{aligned} C'(x,t) &= \frac{C(x,t) - C_{bg}}{C_g - C_{bg}} \\ &= erfc\left(\frac{x}{2\sqrt{D^* t}}\right) \\ &- \left[exp\left(\frac{k^* x}{D^*} + \frac{k^{*2} t}{D^*}\right) \times erfc\left(\frac{x}{2\sqrt{D^* t}} + k^* \sqrt{\frac{t}{D^*}}\right)\right] \end{aligned} \tag{4.14}$$

where $C'(x,t)$ is the isotopic fraction at a given position x and time t normalized to the isotopic fraction in the annealing gas C_g and background isotopic fraction C_{bg}, D^* is the

tracer (^{18}O) self-diffusion coefficient, and k^* is the (^{18}O) tracer surface exchange coefficient. A typical oxygen tracer diffusion profile of this type is illustrated in Figure 4.9.

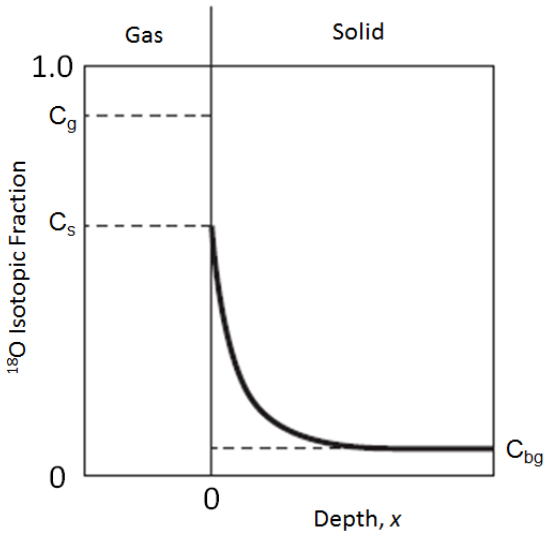

Figure 4.9: Illustration of a typical oxygen tracer diffusion profile. Modified from [17].

Data analysis of oxygen tracer profiles was performed using "TraceX", a Matlab-based program developed by S. Cooper [22] of Imperial College London. The program applies Equation 4.14 to fit the experimental oxygen tracer profile obtained via SIMS to one generated by the program by varying the coefficients of oxygen tracer diffusion D^* and surface exchange k^*. For a specific exchange duration t, ^{18}O isotopic fraction C_g, and background ^{18}O isotopic fraction C_{bg}, D^* and k^* of the generated profile is extracted, which is taken as an adequate representation of the experimental profile. Details of the profile generation, fitting process, and data extraction can be found in the Appendix section of reference [22].

4.2.6 Measurement of Surface Chemistry: Low Energy Ion Scattering (LEIS)

Low Energy Ion Scattering (LEIS) is a surface-sensitive technique that analyzes the chemical composition of the outermost atomic layer of a material. An illustration is shown in Figure 4.10. A sample is bombarded with low energy (0.5-10 keV) noble gas ions (He^+, Ne^+, or Ar^+) at a fixed incident angle α. Binary collisions between the primary ion (of mass m_1 and energy E_o) and an atom on the sample surface (of mass m_2) result in primary ions backscattering at an angle θ.

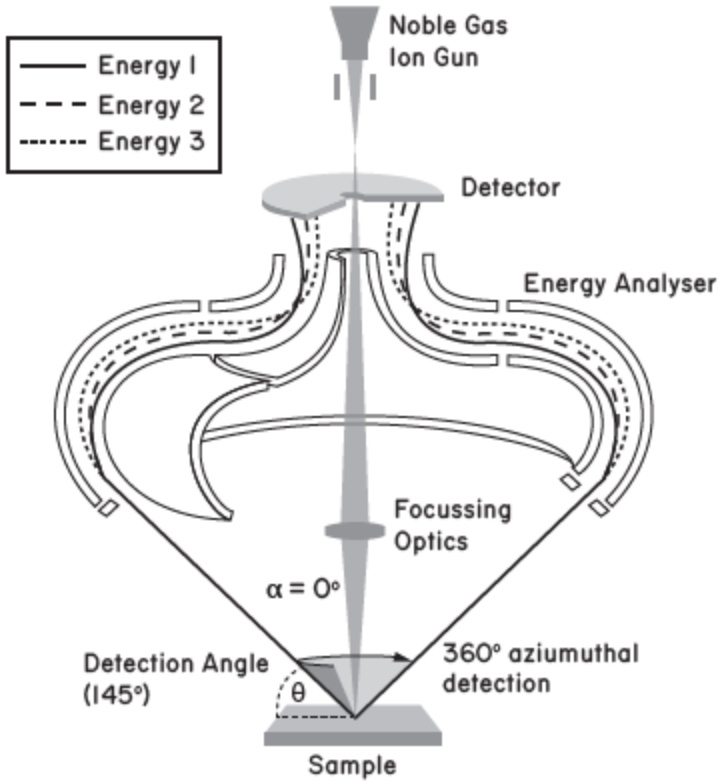

Figure 4.10: Schematic of the detector used in the Qtac[100] LEIS instrument showing beam incident angle and ion detection. Figure courtesy of M. Niania [17].

The relationship between the initial energy E_o and final energy E_f of the primary ion allows for the calculation of the mass of the target ion from conservation of energy and momentum, which is shown in Equation 4.15:

$$E_f = \left(\frac{cos\theta \pm \sqrt{\left(\frac{m_2}{m_1}\right)^2 - sin^2\theta}}{1 + \frac{m_2}{m_1}} \right) \bullet E_o \tag{4.15}$$

The LEIS technique is capable of very high surface sensitivity due to the ease of neutralization of the noble gas ions. Any subsequent collisions with atomic layers beyond the outermost surface will significantly increase the probability of neutralization and thus will be undetected. For this reason, binary peaks in a typical LEIS spectrum are considered to be representative of the outermost atomic layer. In some instances, however, primary ions undergoing multiple collisions within the sample can be "re-ionized" upon exiting the surface and thus be detected. These backscattered ions, having lost energy from multiple inelastic interactions, typically appear as 'background' or 'tail' signals in a LEIS spectrum.

The measurement of the atomic surface of a sample using LEIS is primarily affected by sample surface roughness and surface contamination. Surface roughness causes "shadowing" [21, 22], where backscattered ions are neutralized on roughness edges that would not occur if the sample was relatively flat. This results in reduced signal detection and is of particular concern for elements with low detectable concentrations on the atomic surface. Surface contamination occurs as a result of exposure to ambient environments, i.e. when transferring the sample into the LEIS instrument for examination. The contaminants form a monolayer coating the exposed surface and inhibits the LEIS analysis beam resulting in significant or total signal loss. The contaminants are easily removable in the LEIS chamber via the use of atomic oxygen or very low sputter ion doses.

Unlike SIMS, LEIS is considered to be free from matrix effects [25], and thus can be employed to obtain quantitative chemical composition of the atomic surface. However, like SIMS, absolute quantification requires the use of well-defined spectra of each element of interest, which is beyond the scope of this project. Instead, qualitative information on the composition of the atomic surface will be obtained for each of the single- and dual-phase materials and compared with each other.

The LEIS instrument used in this work is a Qtac^{100} manufactured by ION-TOF GmbH (Münster, Germany), which is claimed by the company to possess 3000 times higher sensitivity than conventional LEIS instruments [26]. The instrument is equipped with dual analysis/sputter beams allowing depth profiles to be performed during examination. The instrument is also equipped to use different sources of primary ions. In this work, He^+ (3 keV) and Ne^+ (5 keV) were used for analyzing sample surfaces. LEIS spectra generated from He^+ constituted an overview "survey" spectra of the outer surface and could ascertain the presence of surface impurities (such as sodium, magnesium, aluminum or silicon). LEIS spectra generated from Ne^+ are employed to separate peaks at higher mass species typically observed in the He^+ spectra.

He^+ survey spectra were collected from samples after the surface was subject to a very low dose of sputter ions. The beam analysis area was a square 1 mm x 1 mm area. Depth profiles were performed using a 1 keV Ar^+ sputter gun with a square beam sputter area of 1.5 mm x 1.5 mm. The analysis was then moved to a fresh area of the sample and spectra were collected using Ne^+ ions of analysis area 1 mm x 1 mm. Depth profiles were performed on this area per the conditions stated above.

4.2.7 Measurement of Surface Chemistry: X-ray Photoelectron Spectroscopy (XPS)

Like LEIS, X-ray Photoelectron Spectroscopy is a technique capable of extracting chemical information of a material with very high depth resolution. XPS possesses lower information depth and detection ranges, ostensibly rendering the technique inferior to LEIS. However, the main advantage of XPS is the ability to obtain information on the chemical bonding of elements on the near-surface, defined to be ~10 nm from the sample surface, which is beyond the capabilities of SIMS and LEIS. XPS can also acquire quantitative information on a sample surface without the use of material standards.

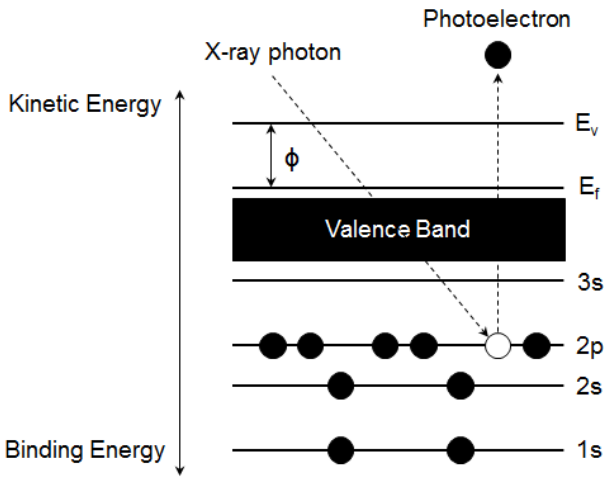

Figure 4.11: Illustration of the photoelectric effect. Photoelectrons are ejected from the core shells of an atom if the photon energy exceeds the binding energy of the electron.

X-ray Photoelectron Spectroscopy is based on the photoelectric effect. An illustration is shown in Figure 4.11. When an X-ray beam is directed onto a sample surface the energy of the X-ray photons is absorbed by the electrons of an atom. If the energy of an X-ray photon is higher than the binding energy of an electron, the electron is ejected from the atom. The probability of detection of photoelectrons is highest at the surface and diminishes with depth into a material, giving the technique its high surface sensitivity, which is typically 1-10 nm from the surface. Characteristic binding energies associated with the photoelectrons of an element can be determined from the X-ray photon energy and the kinetic energy of the photoelectron, according to Equation 4.16:

$$E_b = h\nu - (E_k + \phi) \tag{4.16}$$

where E_b is the binding energy of the photoelectron, $h\nu$ is the X-ray photon energy, E_k is the kinetic energy of the photoelectron, and ϕ is the work function, which is the energy expended to bring the photoelectron from the surface to the detector. Since ϕ is

compensated by the instrument, it is presumed that in XPS measurements the sum of the binding and kinetic energies of the photoelectron are equal to the energy of the X-ray photon.

In addition to photoelectrons, the emission of Auger electrons will also appear as peaks on a typical spectrum. A schematic of Auger electron emission is illustrated in Figure 4.12. The liberation of a photoelectron by an X-ray photon may result in an electron from a higher core shell level dropping into the lower-state shell, releasing energy in the process. This energy can manifest as X-rays or as Auger electrons. The detection of Auger electrons in XPS is characterized by peaks with fixed positions in the XPS spectrum. In this work, Auger peaks measured during XPS did not overlap with any elements comprising the material and were thus ignored.

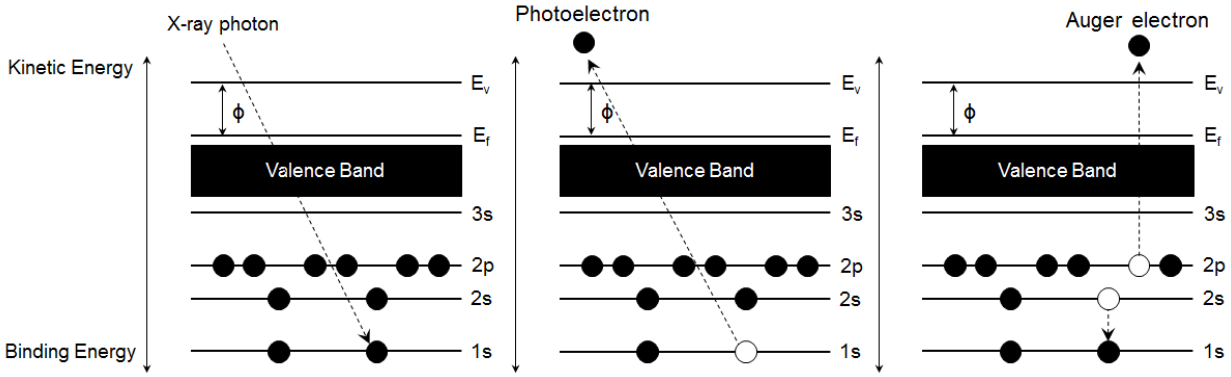

Figure 4.12: Schematic of process of Auger electron emission in X-ray photoelectron spectroscopy. The kinetic energy of Auger electrons is independent of the x-ray photon energy and will appear in the same peak position in a XP spectrum.

Detection of photoelectrons in XPS is commonly performed using a Concentric Hemisphere Analyzer. An illustration is shown in Figure 4.13. This type of analyzer consists of two hemispheres through which photoelectrons travel to reach the detector. In this configuration, photoelectrons emitted from the sample surface pass through an electrostatic lens, which acts as a focus. This increases the counting statistics of the measurement. The photoelectrons enter the hemispheres with a range of kinetic energies. The hemispheres reduce this range of energies to allow only electrons with a particular kinetic energy, called the pass energy, to reach the detector, with other electrons being neutralized. The pass energy is then varied (for example, from 0 to 1350 eV) to obtain a XPS spectrum.

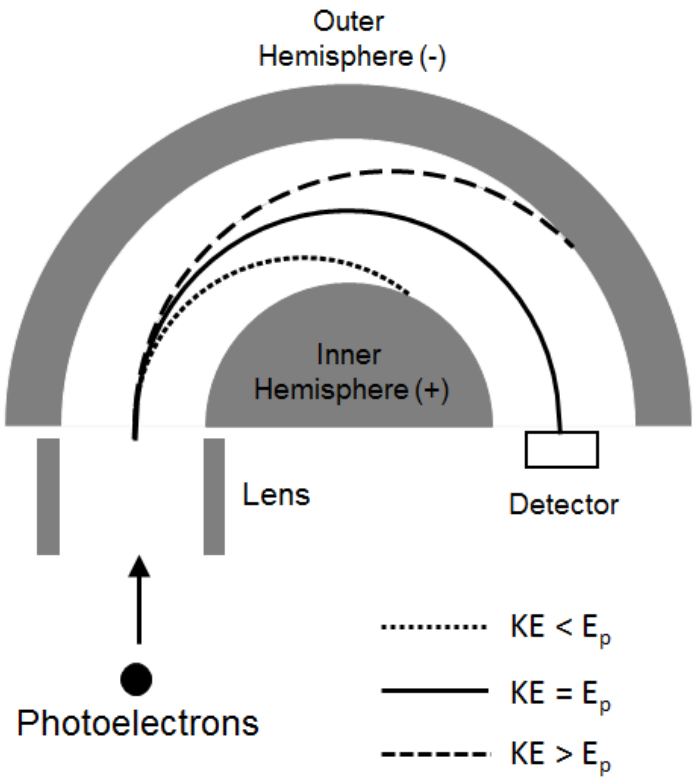

Figure 4.13: Illustration of Concentric Hemisphere Analyzer commonly used in XPS [27]. In this configuration, detection of photoelectrons is restricted to a particular kinetic (binding) energy, or Pass Energy (E_p). An XPS spectrum is obtained by measuring an E_p range across the analysis area.

The binding energy of a core electron of an element can vary depending on the chemical bonding of that element. This phenomenon manifests as shifts in elemental peak position in an XPS spectrum. These shifts can provide information about the chemical state of a material, including the oxidation state of elements on the surface. For example, the binding energy of the Cr 2p peak in pure Cr metal is 574 eV, but 576 eV in Cr_2O_3 [28]. While the peak positions are easily resolvable by the instrument, there may be peak overlaps if both states are present on the surface, which would require peak fitting to attempt to resolve the two (or more) peak signals.

The area of peaks in XPS spectra contain information on the chemical stoichiometry of the surface and can be used to perform quantitative analysis. The atomic concentration C_i of element i can be calculated according to Equation 4.17 [29]:

$$C_i = \frac{A_{ij}/S_i}{\sum A_i/S_i} \tag{4.17}$$

where A_{ij} is the area of peak j of element i, and S_i is the sensitivity factor, which is a function of the photoionization cross-section of core electrons in an atom and the length of the inelastic mean free path, and have been catalogued for most elements [30].

XPS was performed using a K-Alpha+™ X-ray Photoelectron Spectrometer (XPS) System manufactured by Thermo Fisher Scientific™ (Waltham, Massachusetts, US) equipped with a MXR3 Al-K_α monochromated X-ray source ($h\nu$ = 1486.6 eV). The X-ray gun power was set to 72 W (6 mA and 12 kV). Binding energy calibration was made using the Au $4f_{7/2}$ (84.01 eV), Ag $3d_{5/2}$ (368.20 eV) and Cu $2p_{3/2}$ (932.55 eV) peaks. Charge compensation was achieved using the FG03 flood gun using a combination of low energy electrons and the ion flood source.

Survey scans were acquired from photoelectrons with binding energies between 0 and 1350 eV, with a pass energy of 200 eV, a 0.5 eV step size and 500 milliseconds (50 ms x 10 scans) dwell times, to ensure sufficient energy resolution of measured photoelectrons while maintaining high count rate, all within acceptable time constraints. High resolution spectra of the Zr 3d, Sc 2p, and La 3d peaks were acquired using the appropriate energy range for the expected peaks as obtained from the NIST database [28], with a 20 eV pass energy, a 0.1 eV step size and 1 second (50ms x 20 scans = 1000 ms) dwell times to ensure sufficient energy resolution and photoelectron counts. The pass energy was lowered to 10 eV for high-resolution scans performed on the Sr 3d, Cr 2p, and Fe 2p peaks to increase the energy resolution while keeping the count rate to acceptable levels. The duration of the high-resolution scan for the Ce 4d peak was increased from 20 scans to 50 scans, resulting in a total dwell time of 2.5 s (50ms x 50 scans = 2500 ms).

Samples were prepared by adhering the sample onto double-sided carbon tape and analysed at an electron take-off angle perpendicular to the surface with respect to the analyser. The vacuum pressure during the measurement was $\leq 1 \times 10^{-8}$ mbar.

CasaXPS software was used for data interpretation, with guidance from Dr. Ignacio Villar-Garcia of Imperial College London. Two-point-linear or Shirley background subtractions were employed depending on the background shape. Peaks were fitted using GL(30) lineshapes, a combination of a Gaussian (70%) and Lorentzian (30%). All XPS spectra were charge-corrected by setting the value of the C 1s peak, which represents the signal for the C-C bond, to 285 eV.

4.3 Summary

The techniques outlined in this chapter comprised the methods by which the materials were synthesized and examined. The first section outlined the processes of preparing the

samples relevant to this work, including preparation and sintering conditions of powders, aging parameters and justifications, and preparation for Isotope Exchange Depth Profiling examination. The second section discussed the techniques used to understand the behaviour of the relevant materials, from characterization of materials using X-ray Diffraction, Secondary Electron Microscopy/Energy Dispersive X-ray Spectroscopy and Electrochemical Impedance Spectroscopy, to examination of oxygen tracer diffusion kinetics via Isotope Exchange Depth Profiling coupled with Secondary Ion Mass Spectrometry, to elucidation of the surface chemistry via Low Energy Ion Scattering and X-ray Photoelectron Spectroscopy. The parameters used in this work were also stated. The techniques described in this chapter will be used to better understand the behaviour of the 1Ce10ScSZ/LSCrF8255 dual-phase membrane as well as its single-phase constituents for application in syngas production.

4.4 References

[1] W. Kingery, *Introduction to Ceramics*. 1977.

[2] B. Cullity, "Elements of X-Ray Diffraction," *Phys. Today*, vol. 10, no. 3, pp. 50–51, 1957.

[3] F. Karlsruhe, "Inorganic Crystal Structure Database," *Leibnitz Institute for Information Infrastructure*.

[4] H. Rietveld, "A profile refinement method for nuclear and magnetic structures," *J. Appl. Crystallogr.*, vol. 2, no. 2, pp. 65–71, 1969.

[5] T. Roisnel and J. Rodríguez-Carvajal, "WinPLOTR: a Windows tool for powder diffraction patterns analysis," *Mater. Sci. Forum*, pp. 1–6, 2001.

[6] J. Goldstein, D. Newbury, P. Echlin, D. Joy, C. Lyman, E. Lifshin, L. Sawyer, and J. Michael, *Scanning Electron Microscopy and X-ray Microanalysis*, 3rd ed. 2003.

[7] B. Hafner, "Scanning Electron Microscopy Primer," *University of Minnesota-Twin Cities*, 2015. .

[8] J. Liu, "Mass Transport and Electrochemical Properties of $La_2Mo_2O_9$ as a Fast Ionic Conductor," 2010.

[9] E. Barsoukov and J. Macdonald, *Impedance Spectroscopy*. 2005.

[10] J. Irvine, D. Sinclair, and A. West, "Electroceramics: Characterization by Impedance Spectroscopy," *Adv. Mater.*, vol. 2, no. 3, pp. 132–138, 1990.

[11] J. Kilner, B. Steele, and L. Ilkov, "Oxygen self-diffusion studies using negative-ion

secondary ion mass spectrometry (SIMS)," *Solid State Ionics*, vol. 12, no. C, pp. 89–97, 1984.

[12] J. Meija, T. Coplen, M. Berglund, W. Brand, P. De Bièvre, M. Gröning, N. Holden, J. Irrgeher, R. Loss, T. Walczyk, and T. Prohaska, "Atomic weights of the elements 2013 (IUPAC Technical Report)," *Pure Appl. Chem.*, vol. 88, no. 3, pp. 265–291, 2016.

[13] J. Druce, "Mixed Conducting CGO-LSCF Composites for Oxygen Separation in Oxyfuelled Carbon Capture and Storage Systems," 2010.

[14] R. Chater, S. Carter, J. Kilner, and B. Steele, "Development of a novel SIMS technique for oxygen self-diffusion and surface exchange coefficient measurements in oxides of high diffusivity," *Solid State Ionics*, vol. 56, pp. 859–867, 1992.

[15] R. De Souza, "Ionic transport in acceptor-doped perovskites," 1996.

[16] ION-TOF, "TOF-SIMS 5 Brochure." pp. 1–7.

[17] M. Niania, "In-Situ Analysis of $La_{0.6}Sr_{0.4}Co_{0.2}Fe_{0.8}O_{3-\delta}$ Surface in Ambient Temperatures," 2016.

[18] T. Sakai, J. Hyodo, M. Ogushi, A. Inoishi, S. Ida, and T. Ishihara, "Evaluation of isotope diffusion coefficient and surface exchange coefficient of ScSZ series oxide by oxygen isotope exchange method," *Solid State Ionics*, vol. 301, pp. 156–162, 2017.

[19] S. Fearn, *An Introduction to Time-of-Flight Secondary Ion Mass Spectrometry (ToF-SIMS) and its Application to Materials Science*. 2015.

[20] G. van Tendeloo, *Handbook of Microscopy*, 2nd ed. New York, 1997.

[21] J. Crank, *The Mathematics of Diffusion*. Clarendon Press, 1979.

[22] S. Cooper, "Quantifying the Transport Properties of Solid Oxide Fuel Cell Electrodes," 2015.

[23] W. Jansen, A. Knoester, A. Maas, P. Schmit, A. Kytokivi, A. Denier, and H. Brongersma, "Influence of compaction and surface roughness on low-energy ion scattering signals," *Surf. Interface Anal.*, vol. 36, no. 11, pp. 1469–1478, 2004.

[24] G. Nelson, "Influence of surface roughness on the intensity of elastically scattered low-energy noble-gas ions," *J. Appl. Phys.*, vol. 47, no. 4, pp. 1253–1255, 1976.

[25] J. Druce, N. Simrick, T. Ishihara, and J. Kilner, "'Imaging' LEIS of micro-patterned solid oxide fuel cell electrodes," *Nucl. Instruments Methods Phys. Res. Sect. B Beam Interact. with Mater. Atoms*, vol. 332, pp. 261–265, 2014.

[26] ION-TOF, “Quantitative elemental characterisation of the top atomic layer.”

[27] “Instrumentation: The ‘what?’, the ‘how?’ but especially the ‘why?’ of an X-ray photoelectron spectrometer,” in *UCL-ICL XPS Summer School*, 2015.

[28] A. Naumkin, A. Kraut-Vass, S. Gaarenstroom, and C. Powell, “NIST X-ray Photoelectron Spectroscopy Database, Version 4.1.” 2012.

[29] “X-ray Photoelectron Spectroscopy,” *Statler College of Engineering, West Virginia University*, 2015. [Online]. Available: https://web.statler.wvu.edu/~wu/mae649/xps.pdf. [Accessed: 12-Jun-2017].

[30] M. Seah, I. Gilmore, and S. Spencer, “Quantitative XPS: I. Analysis of X-ray photoelectron intensities from elemental data in a digital photoelectron database,” *J. Electron Spectros. Relat. Phenomena*, vol. 120, no. 1–3, pp. 93–111, 2001.

[31] I. Gilmore and J. Vickerman, *Surface Analysis – The Principal Techniques 2nd Edition*. 2009.

[32] J. Kilner, S. Skinner, and H. Brongersma, “The isotope exchange depth profiling (IEDP) technique using SIMS and LEIS,” *J. Solid State Electrochem.*, vol. 15, no. 5, pp. 861–876, 2011.

5 Properties of Single-Phase 1Ce10ScSZ and LSCrF8255

This chapter details the characterization of the single-phase components of the dual-phase oxygen transport membrane. The crystal structure information for single-phase $Sc_{0.10}Ce_{0.01}Zr_{0.89}O_{2-\delta}$ (1Ce10ScSZ) and $(La_{0.8}Sr_{0.2})_{0.95}Cr_{0.5}Fe_{0.5}O_{3-\delta}$ (LSCrF8255) was determined. In addition, the surface chemistry for the two single-phase materials was elucidated. Finally, oxygen transport kinetics were determined for single-phase 1Ce10ScSZ due to its role as the primary medium through which oxygen ions migrate.

5.1 Characterization of 1Ce10ScSZ

Characterization of $Sc_{0.10}Ce_{0.01}Zr_{0.89}O_{2-\delta}$ (1Ce10ScSZ) in this work involves the determination of the crystal structure via X-ray diffraction, the ionic conductivity and oxygen diffusion kinetics via Electrochemical Impedance Spectroscopy and Isotopic Exchange Depth Profiling coupled with Secondary Ion Mass Spectrometry (IEDP-SIMS) respectively, and the surface chemistry via Low Energy Ion Scattering (LEIS) and X-ray Photoelectron Spectroscopy (XPS).

5.1.1 Crystal Structure

The X-ray diffraction pattern measured for the as-received 1Ce10ScSZ powder is shown in Figure 5.1. Rietveld refinement was performed on the pattern with the understanding that there are two crystal phases present in the bulk material, cubic (Fm-3m) and rhombohedral (R-3), with the peak positions for the two phases labelled under the diffraction pattern. The difference of the Rietveld refinement to the experimental data is also shown. Output data from the refinement shows that the 1Ce10ScSZ powder exhibits ~40 mol% rhombohedral crystal phase with the remainder adopting the cubic phase. The theoretical density of 10Sc1CeSZ was determined from the refinement data to be 5.71 g cm^{-3}, in agreement with the literature value of 5.71 g cm^{-3} for both cubic [1] and rhombohedral [2] 1Ce10ScSZ.

The lattice parameters extracted from the refinement were a=b=c=5.0919(1) Å; α=β=γ=90° for the cubic phase and a=b=3.5793(3) Å, c=8.9535(9) Å; α=β=90°, γ=120° for the rhombohedral phase. The lattice parameter of the cubic phase is in agreement with previous work reported by Itoh et. al. [3] but is not in agreement with that reported by Omar et. al. [4], who found the lattice parameter to be 5.0956(1) $Å^3$. However, the lattice parameter obtained from 1Ce10ScSZ in the work of Itoh et. al. [3] was determined using

Rietveld refinement of XRD patterns generated from synchrotron X-rays. In contrast, the lattice parameter of 1Ce10ScSZ was estimated by Omar et. al. [4] using the Nelson-Riley extrapolation method [5]. It is thus taken that the lattice parameter of 1Ce10ScSZ is closer in value to the value determined by Itoh et. al. [3]. The lattice parameter of the rhombohedral phase is slightly different from the value calculated by Fujimori et. al. [2], who calculated the lattice parameters to be a=b=3.5615(6) Å , c=9.0187(9) Å; α=β=90°, γ=120°. However, Fujimori et. al. [2] performed the Rietveld refinement and lattice parameter calculation on 10ScSZ. The presence of Ce in 1Ce10ScSZ may be the reason between the discrepancy between the two rhombohedral lattice parameters. Comparing the lattice volumes between the rhombohedral phase in 1Ce10ScSZ in this work and that of 10ScSZ in the work of Fujimori et. al. [2] we observe a larger volume for 1Ce10ScSZ than for 10ScSZ (99.339 $Å^3$ vs. 99.070 $Å^3$), which is consistent with the presence of the larger Ce^{4+} dopant relative to the Zr^{4+} parent (0.97 Å vs 0.84 Å).

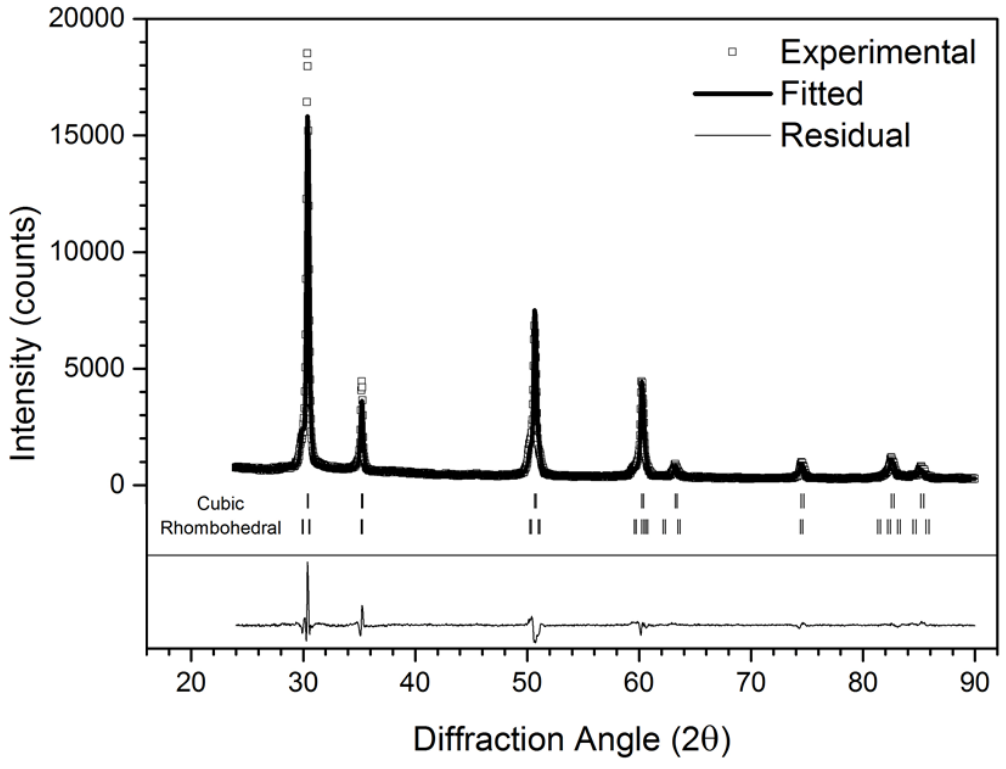

Figure 5.1: Experimental X-ray diffraction pattern of 1Ce10ScSZ (open squares) with fitted Rietveld refinement (solid line). Peak positions for the cubic (top) and rhombohedral

(bottom) crystal phases are labelled under the pattern. Residual of Rietveld refinement fit to experimental data is shown at the bottom of the figure.

Figure 5.2 compares the X-ray diffraction patterns of an as-prepared 1Ce10ScSZ sample sintered at 1450°C in ambient air for 6 hours with a reference sample of 1Ce9ScSZ [3] ($Sc_{0.09}Ce_{0.01}Zr_{0.90}O_{2-\delta}$) sintered in air at 1500°C for 6 hours. The stabilization effect of ZrO_2 into the cubic phase was not fully achieved in the powder 1Ce10ScSZ sample in Figure 5.1, as evidenced by the presence of the rhombohedral phase, but is fully stabilized upon sintering, evidenced by the absence of the rhombohedral phase in the diffraction pattern of the experimental 1Ce10ScSZ sample in Figure 5.2. This may be due to the ability of the Sc and Ce dopants to achieve mobility within the material under elevated temperatures, allowing better homogeneity of the dopants during sintering and enhancing stability into the cubic phase.

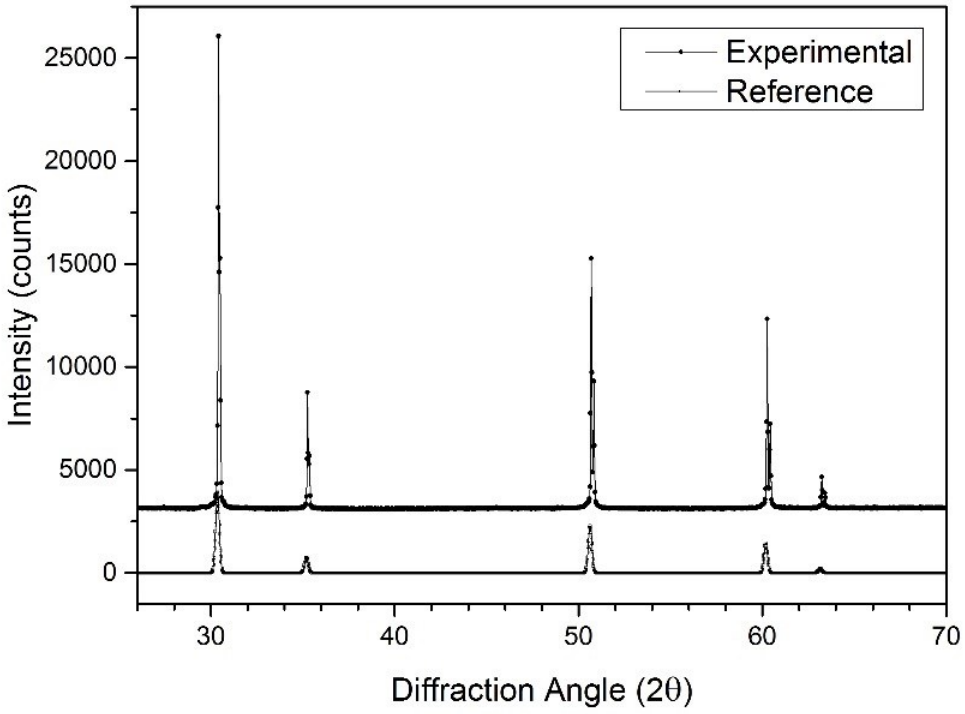

Figure 5.2: X-ray diffraction pattern of sintered 1Ce10ScSZ sample (top), compared to reference 1Ce9ScSZ [3] obtained from the CDS-ICSD database [6] (bottom). The rhombohedral phase is absent in the experimental 1Ce10ScSZ samples, suggesting that

exposure to sintering conditions (1450°C in ambient air for 6 hours) increases stability of the cubic crystal structure at room temperature.

5.1.2 Conductivity and Ionic Transport

The conductivity of 1Ce10ScSZ over a range of temperatures can be determined using Electrochemical Impedance Spectroscopy by observing the magnitude of the real component of the impedance of the bulk and grain boundary contributions of the material. The sum total of these contributions is the resistance of the material, which is converted to the resistivity using the sample dimensions, and inverted to produce the conductivity. This conductivity value is used in the work primarily to ascertain the appropriate conditions for isotopic exchange experiments.

At temperatures above 450°C, it was observed that the bulk and grain boundary contributions to the overall resistivity, which were discrete below this temperature, became convoluted. The bulk and grain contributions became unresolvable above 550°C, above which the semicircle plots for the bulk and grain boundary contributions to the impedance became so small they disappeared. It is thus unlikely that resistivity contributions can be examined at a simulated operating temperature of 1000°C, however, the total resistivity of the sample can still be obtained.

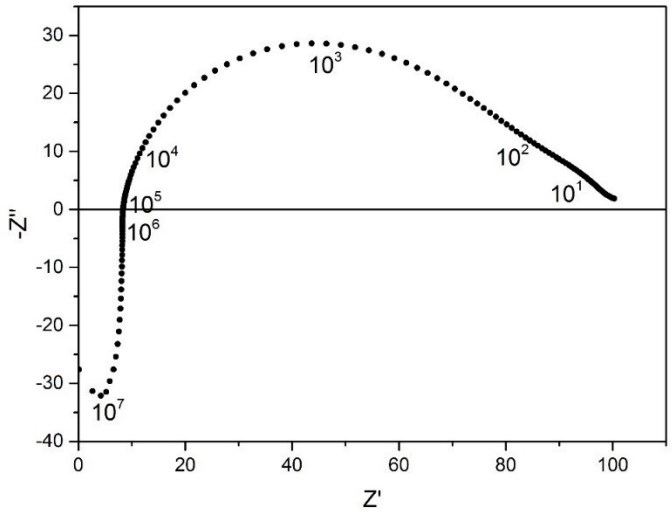

Figure 5.3: Nyquist plot of 1Ce10ScSZ performed in air at 800°C, with frequency decades 10^7-10^1 Hz indicated. The semicircle shown corresponds to the sample-electrode interface.

The bulk and grain boundary contributions to the impedance are unresolvable at this temperature.

Figure 5.3 shows the Nyquist plot of a 1Ce10ScSZ sample measured at 800˚C over a frequency range from 1 MHz to 1 Hz. The peak capacitance of the semicircle shown in the figure is on the order of 10^{-7}-10^{-5} F, corresponding to the sample-electrode interface [7]. The total ohmic resistance of the system was measured from Figure 5.3 to be 8.4 ohms. Factoring the contribution of the resistance of the experimental setup (i.e. platinum wire mesh, FRA connections, etc.) which was measured to be approximately 6.0 ohms, and the dimensions of the sample (thickness 2.23 mm, radius 10.0 mm), resistivity values for the sample were taken from 400˚C to 850˚C in 25˚C intervals. The conductivity values were obtained by taking the reciprocal of the resistivity values.

Figure 5.4 shows an Arrhenius plot of 1Ce10ScSZ over the temperature range 400˚C to 850˚C. A change in activation energy was observed for the material at ~600˚C, which is likely a result of a change in crystal structure from dual-phase cubic-rhombohedral to single-phase cubic. The activation energy was determined to be 1.30 eV and 0.72 eV below and above the phase transition temperature respectively, corresponding with higher (oxygen) ion conduction above the transition temperature.

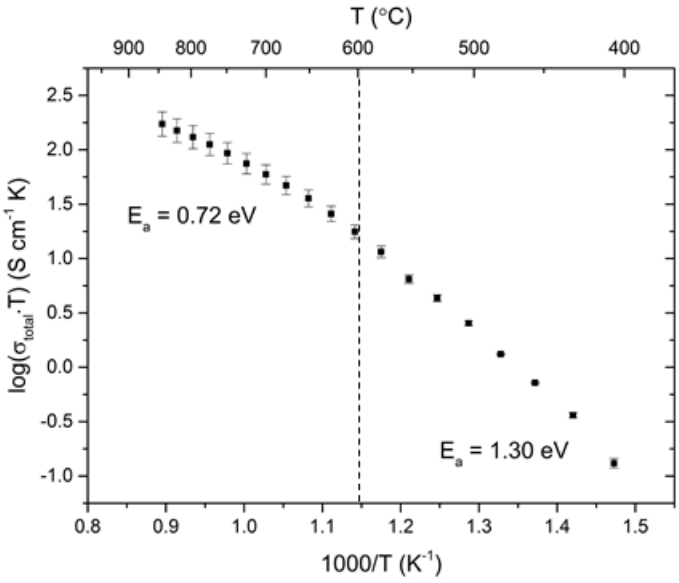

Figure 5.4: Arrhenius plot of 1Ce10ScSZ indicating that a decrease in activation energy was observed at temperatures above 600˚C, likely corresponding to a crystal phase transition from two-phase cubic-rhombohedral to single-phase cubic.

Conversion of the conductivity value obtained for 1Ce10ScSZ into a self-diffusivity value is performed using the Nernst-Einstein equation, expressed by Equation 2.23. The self-

diffusion coefficient D_{self} is then used in the determination of the estimated diffusion length of the material by using Equation 4.12. It was determined that the diffusion length at 800˚C for 30 minutes would be on the order of ~100 μm. Therefore, secondary ion mass spectrometry measurements on isotopically exchanged samples would require the "linescan" analysis configuration (see Table 4.5).

Isotopic Exchange Depth Profiling (IEDP) experiments were performed on as-sintered 1Ce10ScSZ samples after preparing the sample via the procedure outlined in Section 4.1.5. For the IEDP experiment, samples were exchanged in $^{18}O_2$ (isotopic ratio ~95%) at 800˚C for 30 minutes (pO_2 = 200 mbar) after annealing in $^{16}O_2$ at the same temperature for 5 hours. The sample was then prepared for linescan analysis via SIMS as outlined in Figure 4.7.

Upon analysis of the ^{18}O tracer diffusion profile via SIMS, it was observed that the exchange of ^{18}O was absent beyond the background concentration, i.e. isotope exchange did not take place in detectable amounts. Subsequently, a thin coating (thickness ~40 nm) of platinum was applied to the polished surface of the 1Ce10ScSZ sample prior to oxygen isotope exchange. It was reported that platinum accelerated oxygen exchange when applied onto the surface of doped zirconia materials by a factor of 10^2-10^3 [8]. This is likely achieved by increasing catalytic activity at the surface, increasing the kinetics of the oxygen reduction reaction. However, the surface exchange coefficient obtained from extraction of the oxygen transport kinetic parameters using Crank's solution for diffusion in a semi-infinite medium no longer corresponds to a 1Ce10ScSZ surface and so does not represent the oxygen surface kinetics of the material.

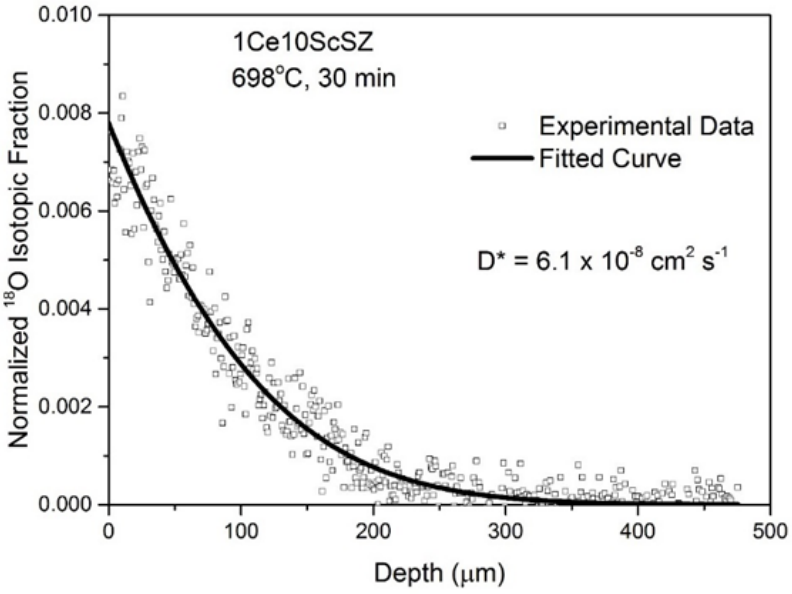

Figure 5.5: Normalized isotopic oxygen profile and fitted curve of Pt-coated (~40 nm) 1Ce10ScSZ annealed in $^{18}O_2$ at 700˚C for 30 mins (pO_2 = 200 mbar). The surface exchange coefficient k* is invalidated due to the presence of the platinum coating.

Figure 5.5 shows a normalized oxygen isotope exchange depth profile obtained from Secondary Ion Mass Spectrometry (IEDP-SIMS) for a Pt-coated 1Ce10ScSZ sample exposed to an $^{18}O_2$ environment at 698˚C for 30 minutes (pO_2 = 200 mbar) after annealing in $^{16}O_2$ for 5 hours at the same temperature and pO_2. Even with the addition of the platinum coating catalyzing the surface for oxygen surface exchange, the elevated oxygen fraction at the surface of the material is only marginally enhanced, achieving a normalized ^{18}O isotopic fraction of ~0.8%. This deviates from the work reported by Raj et. al. [9] which shows that the addition of the silver catalyst on the surface significantly improves the normalized isotopic fraction (from near-zero to ~65%).

Sakai et. al. [10] recently performed isotope exchange experiments on 1Ce10ScSZ, whose results are slightly different from the work reported here. In their work, 1Ce10ScSZ was annealed in $^{18}O_2$ at 711˚C for 30 mins (pO_2 = 200 mbar) after exposure to $^{16}O_2$ at the same temperature and oxygen partial pressure for ~5 hours. The oxygen isotope exchange profile showed a normalized isotopic fraction of ~4% for the material, about 5 times the value obtained in this work. Sakai et. al. did not require surface catalysis to improve oxygen incorporation in 1Ce10ScSZ, and thus were able to extract the self-diffusion and surface exchange coefficients from the fit of the diffusion profile, which were determined to be $D^* = 1.1 \times 10^{-7}$ cm^2 s^{-1} and $k^* = 2.1 \times 10^{-7}$ cm s^{-1} respectively. The diffusion coefficient

obtained in this work is in reasonable agreement with Sakai's results (6.1×10^{-8} vs. 1.1×10^{-7} $cm^2\ s^{-1}$), however the low oxygen incorporation of the material observed in this work meant that surface exchange coefficients between this work and the work of Sakai et. al. [10] could not be compared.

The surface exchange kinetics of 1Ce10ScSZ obtained in this work and in the work of Sakai et al. [10] were not in agreement. In this work, surface incorporation of oxygen in the material was found to be so low that the surface required catalysis to promote surface exchange. The normalized surface concentration of the tracer oxygen ^{18}O in surface-catalyzed 1Ce10ScSZ observed in this work was significantly lower than that of uncatalyzed 1Ce10ScSZ in the work of Sakai et. al. One possible reason for the discrepancy is the presence of water in the chamber during isotope exchange. Sakai et. al. [10] observed a water vapor pressure from *in-situ* hygroscopic measurements of 6-13 Pa (0.06-0.13 mbar) during isotope exchange. Therefore, the concentration of water in the gas mixture during the exchange process in Sakai's work would be 300-650 ppm, with the assumption that the oxygen partial pressure of the chamber during isotope exchange (200 mbar) is equal to the total chamber pressure.

The vapor pressure was not measured in isotope exchange experiments in this work, so a comparison cannot be made. However, the isotope exchange system used in this work houses the $^{18}O_2$ tracer gas in a molecular sieve (Type 5Å) comprised of a zeolite material with a very high affinity for water. The moisture level in the $^{18}O_2$ gas is estimated to be at levels below 20 ppm by volume [11], which is significantly lower than the $^{18}O_2$ used in the work of Sakai et. al. [10]. Furthermore, isotope exchange of uncatalyzed 1Ce10ScSZ at 900°C for 45 mins (pO_2 = 200 mbar) also showed negligible elevated ^{18}O surface fraction, suggesting that the presence of water has a significantly stronger effect on oxygen surface exchange than an increase in temperature.

5.1.3 Surface Chemistry

The surface chemistry of 1Ce10ScSZ was analyzed using Low Energy Ion Scattering (LEIS) and X-ray Photoelectron Spectroscopy (XPS), outlined in Sections 4.2.6 and 4.2.7 respectively. As outlined in Chapter 4, the two techniques were used in conjunction to better understand the chemical composition at the surface, with LEIS offering atomic-scale depth resolution and XPS providing more reliable chemical quantification within several atomic layers (< 10 nm).

5.1.3.1 LEIS Analysis – Outer Atomic Surface

The surface of 1Ce10ScSZ was analyzed via LEIS with two primary objectives in mind. First, are the elements comprising the material present at the first few atomic layers, and in what amounts? The latter part of this question will only be answered on a qualitative basis, as the quantification of elemental composition requires reference samples of all relevant elements (ZrO_2, Sc_2O_3 and CeO_2), which was not performed in this work due to time constraints. Second, does the elemental distribution of specific elements change significantly further away from the surface? To answer this question, sputtering was performed on the material until the LEIS signal reached a steady state, i.e. no significant change in the LEIS spectrum with further sputtering was observed.

Figure 5.6 shows a series of overlapped LEIS spectra of the surface of a 1Ce10ScSZ sample. The sample was sintered from powders provided by Daiichi Kigenso Kagaku Kogyo (DKKK) Co. Ltd (refer to Section 4.1.1) at 1450˚C in air for 6 hours. The surface was then polished to a ¼ µm mirror finish as outlined in Section 4.1.5. Initial analysis of the surface (3 keV $^4He^+$ analysis beam) showed a very weak signal, which was caused by a carbon-based layer adsorbed on the sample surface from exposure to the environment. This layer was removed by sputtering the surface with a very low sputter dose (~10^{15} ions cm^{-2}) of noble gas ions (1 keV $^{40}Ar^+$). Analyses of the 1Ce10ScSZ surface after dose densities of 1.1, 2.0 and 3.1 x 10^{15} ions cm^{-2} were applied to the analysis area showed that all relevant elements were present on the surface. The presence of impurities was also observed, and are comprised of a combination of (Na, Mg, Al, Si) oxides, likely originating from a combination of the sintering process or from the 1Ce10ScSZ powder precursors.

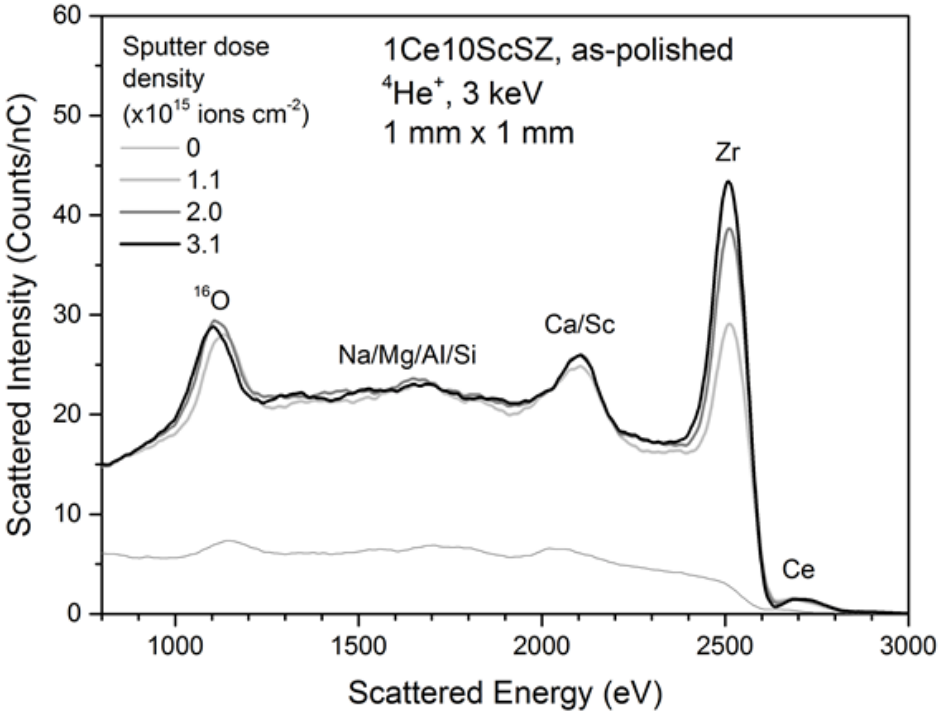

Figure 5.6: Low Energy Ion Scattering spectrum for 1Ce10ScSZ, using a 3 keV He^+ primary ion analysis beam. The surface is initially coated with a carbon-based layer from exposure to the environment. Upon removal of the layer via low sputter dosage (dose density 1.1 x 10^{15} ions cm^2), the chemical elements (and impurities) are immediately present.

The Sc peak in the spectrum potentially contains a contribution from Ca, which is a common contaminant in stabilized zirconia materials. Deconvolution of peak signals is typically performed by increasing the energy of the primary beam or by using noble gas ions of higher mass [12]. However, the Ca and Sc signal peaks are convoluted even with optimal resolution of the Qtac LEIS instrument (analysis beam $^{20}Ne^+$, 10 keV). Therefore, Ca and Sc on the atomic surface cannot be adequately resolved with LEIS. The presence of Ce was also detected by LEIS, which is an anomaly given that the concentration in the bulk (~1 mol%) would be below the detection limit of the LEIS instrument. This suggests that Ce segregates to the surface of single-phase 1Ce10ScSZ. The effects of Ce segregation are discussed in Chapter 8.

Sputtering is one of several methods to clean samples for LEIS analysis. de Ridder et. al. [13] analyzed the effects of eight different cleaning methods for yttria-stabilized zirconia YSZ, and devised a method which consists of annealing the sample in high vacuum and elevated temperature (300°C) in combination with oxidation using atomic oxygen, which

minimizes surface contamination coverage without affecting the surface structure. This technique was not adopted in this work due to the incapability of performing the cleaning procedure *in-situ* prior to analysis. de Ridder et. al. [13] notes that excluding the technique devised in his work, surface cleaning via sputtering is acceptable if the sputter dose is low, which was defined as < 10^{16} $^{4}He^{+}$ or < 10^{15} $^{20}Ne^{+}$ ions cm^{-2}, although the dose density for the use of $^{40}Ar^{+}$ was not specified.

de Ridder et. al. also found that the ratio of O signal to (Y, Zr) signal for the normalized LEIS yield in YSZ was at unity if the material was cleaned via sputtering, compared to there being a significantly elevated O signal relative to (Y, Zr) signal when cleaning methods such as atomic oxidation, UHV annealing, and plasma oxidation were adopted. Unsurprisingly, it was found that performing oxidation of the carbon-based layer on the atomic surface introduces oxygen via adsorption, affecting the surface chemistry. To summarize, surface cleaning by sputtering *at low dose densities* can be applied without significantly affecting the surface structure.

Several scenarios can be interpreted from the presence of Ca/Sc on the atomic surface. The most likely scenario is that the Ca/Sc peak comprises primarily Sc, with the two peaks adopting similar ratios on the surface as in the bulk. However, de Ridder et. al. [14] showed that bulk impurities such as SiO_2, CaO and Na_2O segregate to the outermost surface layer of YSZ until they completely cover the surface. They also note that YSZ samples require very low impurity levels (< 10 ppm) to ensure impurities will not fully cover the surface [14]. While 1Ce10ScSZ likely does not adopt this behaviour, since peak signals were observed in the LEIS spectrum, it should be noted that the removal of the carbon-based layer via sputtering may have inadvertently affected the detection of Ca on the outermost layer. However, one would expect Ca to be present in the carbon-based layer if this were the case, but no such signal was detected. Therefore, it is unlikely that Ca is present in large amounts within the carbon-based layer.

Another scenario would be that Ca comprises a majority of the convoluted Ca/Sc signal due to significant surface segregation from the bulk. This is also unlikely since if this were the case, the Ca would reduce the signal of the entire spectrum instead of just the single Sc signal. The final scenario would be that both Ca and Sc are present in non-negligible amounts on the outer surface. This is the most likely case since the Ca/Sc peak width is larger than that of the single Zr or O peak signals, suggesting the presence of two concurrent signals.

The Zr signal in the spectrum was observed to be reduced at the atomic surface, but the signal rapidly increases with increasing sputter dose density. This suggests that zirconium

oxide may be deficient on the atomic surface that equilibrates towards stoichiometric values into the bulk material. The detection of Ce on the outer atomic surface was also observed, which as stated above, was an anomaly. The Zr and Ce signals were further analyzed using a 5 keV $^{20}Ne^+$ analysis beam and depth profiling the area ($^{40}Ar^+$, 1 keV) until the two signals reached a steady state, shown in Figure 5.7. The Zr signal was observed to be below steady state up to a dose density of 5 x 10^{15} ions cm^{-2}, corresponding to an estimated depth of ~2 nm, after which minimal deviations were evident. The Ce signal was above its steady state intensity up to a dose density of 30 x 10^{15} ions cm^{-2}, an estimated depth of ~6 nm. Further depth profiling up to 110 x 10^{15} ions cm^{-2} showed no significant deviation from the steady state for both signals.

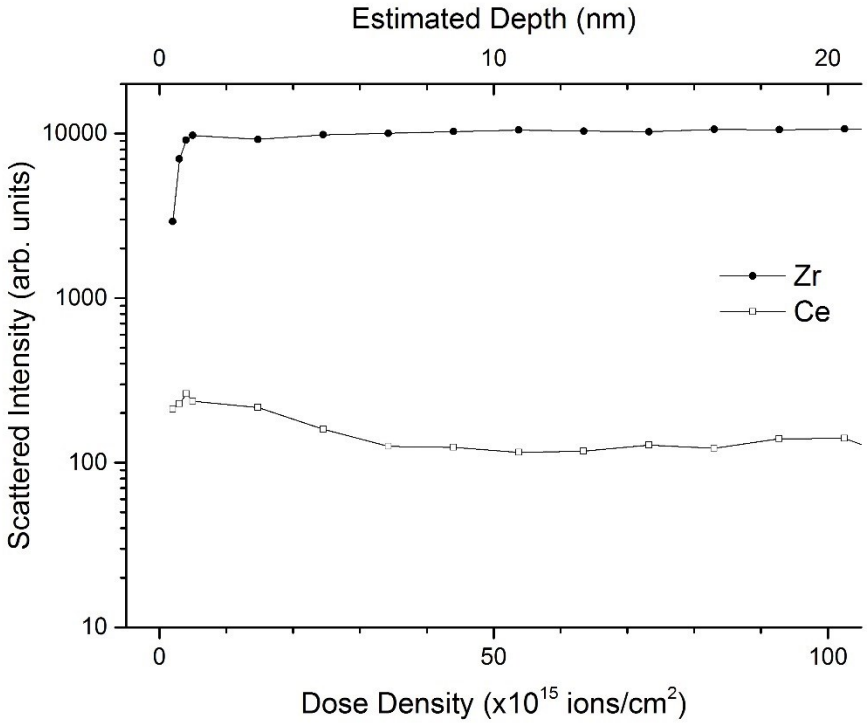

Figure 5.7: LEIS depth profile of Zr and Ce in 1Ce10ScSZ using a 5 keV $^{20}Ne^+$ analysis beam. Sputtering was performed using 1 keV $^{40}Ar^+$. Top x-axis denotes the estimated depth sputtered into the material.

Finally, the background signal of the spectra observed in Figure 5.6 is characteristic of LEIS measurements on oxide materials using a $^4He^+$ analysis beam. This is due to the neutralization and re-ionization of primary He^+ ions upon interaction with an oxygen anion prior to its escape into the detector, and is discussed in more detail in Section 5.2.1.1. This phenomenon is not observed when heavier noble gas ions (Ne^+, Ar^+) are used for analysis since these interactions do not occur. The background signal complicates

quantification of surface chemical composition and would need to be removed. However, quantification is beyond the scope of the work done in this work. For more information on background subtraction and quantification of elements using LEIS, readers are encouraged to read the work of Brongersma et. al. [15].

5.1.3.2 XPS analysis – Near-Surface Chemical Composition

Surface chemical analysis of 1Ce10ScSZ using XPS was performed with three primary objectives in mind. First, does the chemical composition of the material differ significantly from information obtained in the LEIS? While both techniques are extremely surface-sensitive, ultimate (i.e. atomic-scale) resolution cannot be achieved in XPS, which only achieves depth resolutions of ~3-10 nm. Therefore, we define the XPS depth resolution range of ~10 nm as the "near-surface" of the material. Second, does the chemical composition of the near-surface agree with the expected bulk stoichiometry of 1Ce10ScSZ? Third, does the chemical composition differ after 1Ce10ScSZ is exposed to aging conditions expected under operating conditions?

The surfaces of all three 1Ce10ScSZ samples were not modified or cleaned prior to XPS measurements, and care was taken to avoid contact with the analysis surface. It was determined that the carbon-based layer that forms on the surface of 1Ce10ScSZ samples in contact with ambient air is on the order of a few atomic layers thick (~ 1 nm). Unlike LEIS, where the presence of the carbon-based layer almost completely obscures the LEIS spectrum, photoelectrons are emitted from the sample to within ~10 nm of the surface, so surface chemical information via XPS will be detected even with the carbon-based layer present. The presence of the carbon-based layer is partly beneficial in XPS analysis as calibrations of the XP spectra are performed using the C 1s peak.

Figure 5.8 shows the X-ray Photoelectron spectrum of as-prepared and aged 1Ce10ScSZ. Two 1Ce10ScSZ samples were separately exposed to air and a 5%H_2-95%CO_2 syngas mixture, respectively. The conditions were chosen to simulate static conditions of the oxygen transport membrane during operation. Zr and Sc were present on the near-surface, up to a resolution of ~10 nm, manifesting as the Zr 3d and Sc 2p peaks. No Ce signal (Ce 4d) was observed on the unaged and aged-5%H_2-95%CO_2 1Ce10ScSZ samples.

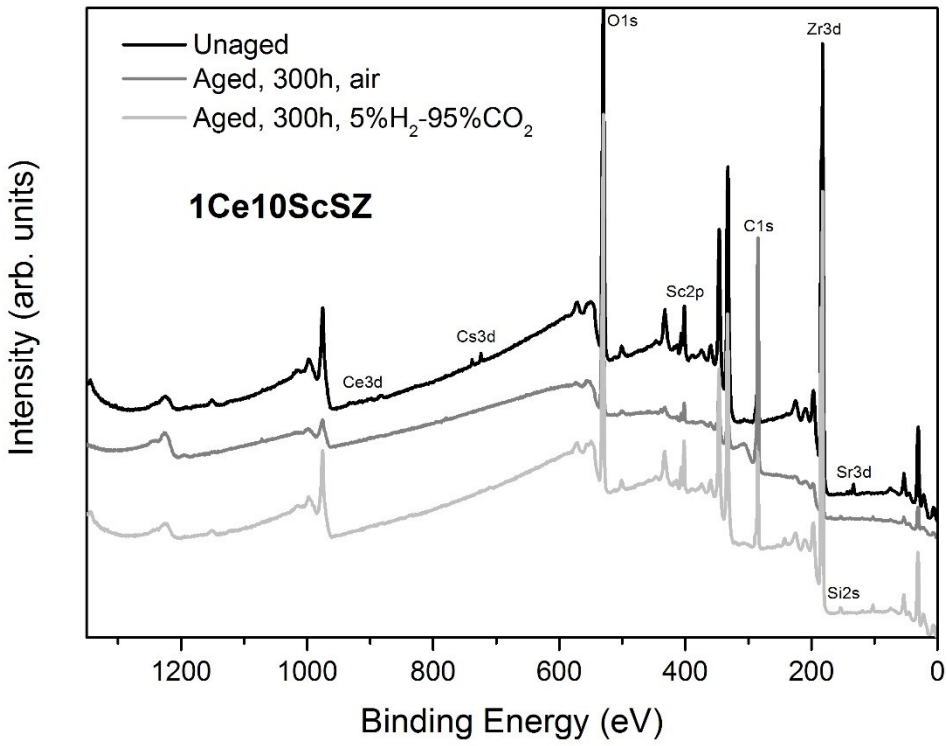

Figure 5.8: X-ray Photoelectron survey spectra of as-prepared and aged (1000°C, 300 h) 1Ce10ScSZ obtained using an Al Kα monochromated X-ray source (hν = 1486.6 eV).

In addition to the expected elements, impurity signals were also observed, in particular Si, Sr and Cs. The Si 2s peak was observed for the two aged 1Ce10ScSZ samples but was absent in the unaged sample. Si is a common contaminant on the surfaces of zirconia materials and was also observed on the outer surface via LEIS, outlined in Section 5.1.3.1. The converse was true for the Sr 3d peak, which was present in the unaged sample but not in the two aged samples. The Sr contamination was likely introduced to the surface of the unaged sample externally, possibly from exposure to equipment in contact with perovskite materials containing Sr. Cs 3d was also observed in the unaged sample surface, which may have been introduced in a previous SIMS experiment on the material.

Table 5-1 summarizes the quantification of the 1Ce10ScSZ sample surface analyzed via XPS. Quantification was performed on the peak intensity of the Zr3d5/2, Sc2p and Ce3d peaks labelled in Figure 5.8 after background subtraction was applied. For all three samples, the chemical composition at the sample surface was in agreement with the expected bulk stoichiometry. This suggests that the surface elemental composition of 1Ce10ScSZ is relatively stable under the expected operating conditions of the oxygen

transport membrane. However, it was observed that the 1Ce10ScSZ sample aged in air displayed slightly elevated concentrations of Sc at the near-surface. This may cause de-stabilization of the cubic crystal phase in 1Ce10ScSZ in regions where the material is Sc-deficient. The segregation of Sc to the near-surface may result in the formation of a rhombohedral γ phase, which is stable at ~15mol% Sc_2O_3 at temperatures below 600˚C [16], coupled with lower crystal stabilization into the cubic phase in the Sc-deficient regions. The reduction in the volume of the cubic crystal phase in the material as a result of the increased volume of the rhombohedral γ phase is likely to result in a significant degradation of oxygen incorporation and conductivity in 1Ce10ScSZ.

Table 5-1: Semi-quantitative results of chemical composition of 1Ce10ScSZ surface via X-ray Photoelectron Spectroscopy. Ideal bulk concentrations are indicated. B.D.L indicates the concentration is 'below detection limit' of the instrument.

	Ideal Bulk	Unaged	Aged 300 h, air	Aged 300 h, 5%H_2-95%CO_2
Zr	89	88.1	86.5	88.2
Sc	10	11.7	13.5	11.8
Ce	1	0.2	B.D.L	B.D.L

The detection of the Ce signal was also observed for the un-aged material, which was near the detection limit of the instrument. Shard et. al. [17] found that the majority of elements in a material are detectable in XPS around the 1 at% to 0.1 at% range, with detection limits as high as 0.01 at% for heavy elements in a light element matrix. Shard et al. [17] also estimated that the detection limit for an XPS instrument using Al Kα radiation for trace Ce in a matrix of Zr and O to be 0.01 at% and 0.03 at% respectively. However, it was noted that the material must be homogeneously distributed in pure elemental matrices with no contaminant overlayers, both of which is not the case for 1Ce10ScSZ. The effects of inhomogeneity and surface contamination on the detection limit were not mentioned. Therefore, it is difficult to verify whether Ce was in reality detected on the near-surface since the detection limit could be above 1 at%, which is above the bulk concentration of Ce in 1Ce10ScSZ. However, quantification results show that the Ce concentration is lower than that expected in the bulk, which is ~1 at%.

Surface chemical results obtained via LEIS hypothesize that the presence of Ce is likely elevated on the outer atomic surface of 1Ce10ScSZ since the ideal bulk concentration of Ce (1 mol%) is below the detection limit of the Qtac LEIS instrument. In contrast, XPS

examination of the chemical composition of the near-surface of 1Ce10ScSZ suggests that Ce is deficient within this region of the material. Therefore, it is conjectured that cerium in 1Ce10ScSZ may preferentially segregate from the near-surface to the outer atomic surface during the sintering procedure (the only time where the material is exposed to sufficiently high temperatures for non-negligible cationic mobility). The areas of the material that are Ce-deficient would likely experience less complete stabilization into the cubic phase as it was observed that 10ScSZ adopts a two-phase cubic-rhombohedral structure at temperatures below 600°C. However, the expected environment of the oxygen transport membrane under operating conditions (~1000°C) will eliminate this issue entirely.

5.1.4 Summary

The crystal structure, oxygen transport kinetics and surface chemistry of 1Ce10ScSZ was examined. The material exhibits a dual cubic-rhombohedral crystal structure in its powder form that is reduced to a single cubic phase upon sintering into a dense sample. Electrochemical impedance spectroscopy and IEDP-SIMS experiments have determined the material to exhibit high oxygen ionic conductivity. IEDP-SIMS experiments further discovered that the oxygen surface exchange kinetics of 1Ce10ScSZ was sufficiently low that a catalytic layer was required to enhance oxygen incorporation. Examination of the surface of 1Ce10ScSZ showed that the relevant elements were present on both the outer and near-surface. Potential segregation of Ce was observed on the outer surface, in addition to Zr deficiency. Impurities (Na, Mg, Si, Al, possibly Ca) were also observed on the outer surface. The semi-quantification of elemental chemistry on the near-surface of 1Ce10ScSZ showed a deficiency of Ce within the first ~10 nm of the material. In addition, an elevated Sc signal was detected after 1Ce10ScSZ was aged in air (1000°C, 300 h).

5.2 Characterization of LSCrF8255

Characterization of $(La_{0.8}Sr_{0.2})_{0.95}Cr_{0.5}Fe_{0.5}O_{3-\delta}$ (denoted LSCrF8255) was performed using X-ray diffraction to determine the crystal structure, and the surface chemistry was examined via Low Energy Ion Scattering (LEIS) and X-ray Photoelectron Spectroscopy (XPS). With the understanding that LSCrF8255 functions primarily as the electronically-conducting phase in the oxygen transport membrane, efforts were focused on elucidation of the surface chemistry. As a result, conductivity measurements via Electrochemical Impedance Spectroscopy and IEDP-SIMS on LSCrF8255 were omitted from this work. Information on the conductivity of LSCrF8255 can be found in the work by Z. Shen [18] of Imperial College London, and can be read in conjunction with the work reported here.

5.2.1 Crystal Structure

The x-ray diffraction pattern measured for the as-received LSCrF8255 powder and the Rietveld refinement fit to the data is shown in Figure 5.9. No secondary-phases were observed, which was in contrast to the work done by Wei et. al. [21] on LSCrF8255 who observed minor phases of strontium chromate, $SrCrO_4$, which disappeared when the material was exposed to reducing conditions. However, Wei et. al. [21] sintered their LSCrF8255 powders in air at 850˚C for 4 hours, a significantly lower temperature than the conditions in the work reported here (1450˚C in air for 6 hours), which may affect the solubility of $SrCrO_4$ into the perovskite structure during the sintering process.

The orthorhombic crystal structure observed in this work differs from that reported by Lü et. al. [22], who determined the structure of $(La_{0.75}Sr_{0.25})_{0.95}Cr_{1-x}Fe_xO_{3-\delta}$, x = 0.3 –0.4 after sintering in 1200˚C for 10 hours adopted a single-phase rhombohedral (R-3c) crystal structure. Lü et. al. [22] postulated that the higher symmetry of the rhombohedral structure of $(La_{0.75}Sr_{0.25})_{0.95}Cr_{1-x}Fe_xO_{3-\delta}$, x = 0.3 –0.4 compared to the orthorhombic structure of $La_{0.75}Sr_{0.25}Cr_{0.5}Fe_{0.5}O_{3-\delta}$ was due to the higher concentration of Cr^{3+}/Cr^{4+} cations, which have smaller radii than Fe^{3+}/Fe^{4+} cations. Wei et. al. [21] reported a rhombohedral (R-3c) crystal structure for LSCrF8255, but the lattice parameters were slightly different (a = 5.4848 Å; b = 5.5136 Å; c = 7.7810 Å), suggesting this is actually an orthorhombic crystal structure.

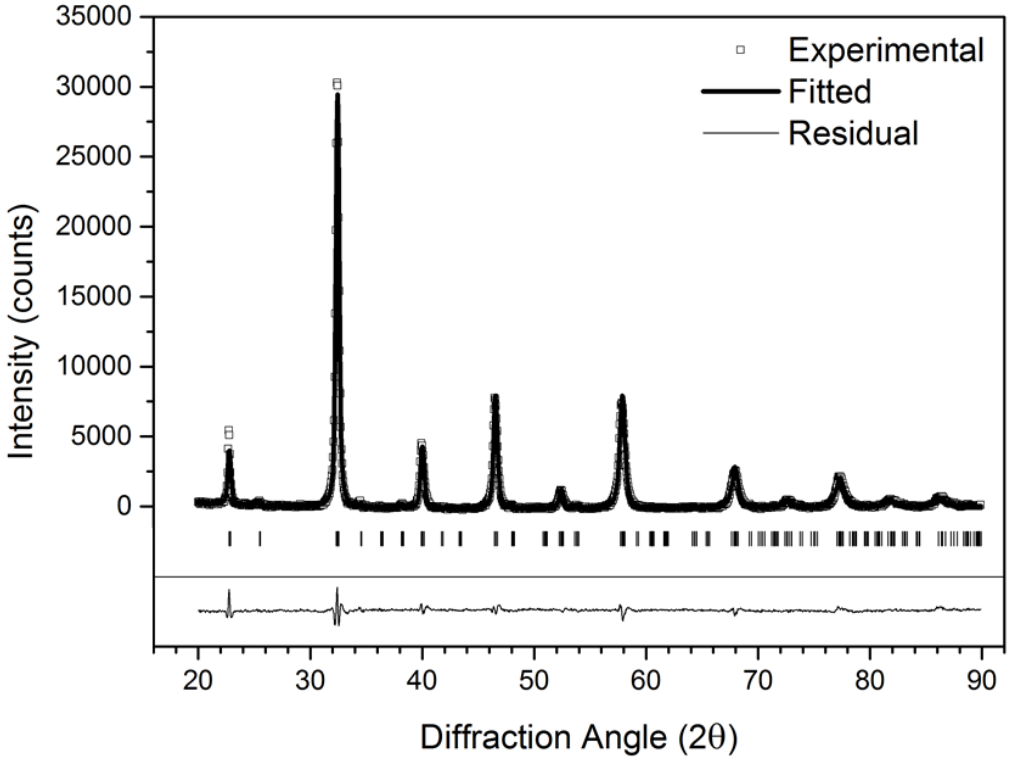

Figure 5.9: Experimental X-ray diffraction pattern of LSCrF8255 (open squares) with fitted Rietveld refinement (solid line). Peak positions for the orthorhombic crystal phase is labelled under the pattern. Residual of Rietveld refinement fit to experimental data is shown at the bottom of the figure.

Ramos et. al. [19] determined that the orthorhombic crystal structure in the perovskite material $La_{1-x}Sr_xCr_{0.2}Fe_{0.8}O_{3-\delta}$ was dependent on the degree of A-site doping, i.e. the substitution of Sr^{2+} cations into La^{3+} sites. At x = 0.2, $La_{1-x}Sr_xCr_{0.2}Fe_{0.8}O_{3-\delta}$ adopted a highly distorted orthorhombic structure that transformed into a rhombohedral (R-3cH) structure at $x \geq 0.4$. Ramos et. al. determined the cell volume of $La_{0.6}Sr_{0.4}Cr_{0.2}Fe_{0.8}O_{3-\delta}$ (LSCrF6428) to be 354.02 $Å^3$, significantly larger than that of LSCrF8228, which was 239.10 $Å^3$.

The presence of multiple crystal phases as a result of elevated concentrations of Sr in certain areas of the material may cause internal residual strain, and could impact the long-term phase stability of the material. This is especially evident on the surface of perovskite materials, where literature studies have reported the segregation of Sr to the surface in $La_{1-x}Sr_xCo_{1-y}Fe_yO_{3-\delta}$ [23]–[27] and $La_{1-x}Sr_xCr_{1-y}Mn_yO_{3-\delta}$ [28]–[31] after exposure to elevated temperatures. Segregation of Sr to the surface could also result in deficiency of

strontium from within the bulk, resulting in a reduced active volume for ionic conduction in the Sr-depleted regions due to lower oxygen vacancy concentration in these regions. Despite the role of LSCrF8255 in the dual-phase membrane as an electronic conductor, the effect of a reduced active volume for ionic conduction in the membrane bulk may reduce the overall conductivity of the dual-phase membrane.

5.2.2 Surface Chemistry

Like 1Ce10ScSZ, the surface chemistry of LSCrF8255 was analyzed using Low Energy Ion Scattering (LEIS) and X-ray Photoelectron Spectroscopy (XPS), outlined in Sections 4.2.6 and 4.2.7 respectively. As stated above, LEIS enables atomic-scale depth resolution and XPS provides more reliable chemical quantification within several atomic layers (~10 nm). The techniques were used together to ascertain the surface chemical structure of the mixed conductor perovskite material LSCrF8255.

5.2.2.1 LEIS Analysis – Outer Atomic Surface

Analysis of the outer atomic surface of LSCrF8255 via LEIS aimed to achieve two primary objectives. The first objective sought to determine whether the elements comprising the material were present in the first few atomic layers, and whether they are in approximate stoichiometric amounts. The elemental presence was determined on a qualitative basis, as quantification of elemental composition requires reference samples of all relevant elements (La_2O_3, SrO, Cr_2O_3, Fe_2O_3), which was not performed in this work. The second objective was to determine whether the elemental distribution of specific elements changes significantly on moving further away from the outer surface. Sputtering was employed on the material to uncover further atomic layers into the depth of the material.

Figure 5.10 shows a LEIS spectrum of the surface of a LSCrF8255 sample. The material was sintered from powders provided by Praxair Specialty Ceramics Inc. (refer to Section 4.1.1) at 1450˚C in air for 6 hours. The surface was then polished to a ¼ μm mirror finish as outlined in Section 4.1.5. Like the LEIS spectrum for 1Ce10ScSZ, the initial outer layer is comprised of a carbon-based layer that obscures the total surface signal. Upon application of a very low dose (~10^{15} ions cm^{-2}) of sputter ions (1 keV $^{40}Ar^{+}$) this layer was removed. The signal for the expected elements was immediately evident on the outer surface after dose densities of 0.9 and 2.0 x 10^{15} ions cm^{-2} were applied. At first glance, the peak intensities appear to agree with the ideal bulk stoichiometry. The presence of impurities (Na, Mg, Al, Si, Ca) was also detected on the outer surface of LSCrF8255. Finally, the peak signals for Cr and Fe were convoluted under the analysis conditions used here.

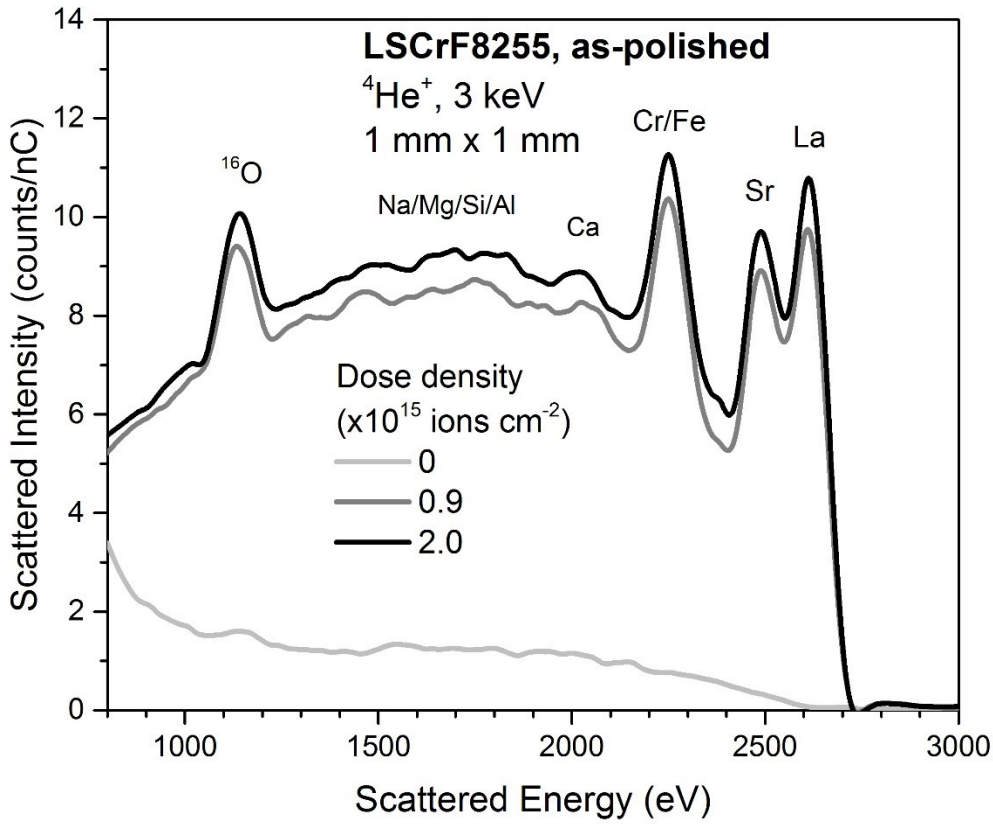

Figure 5.10: Low Energy Ion Scattering spectrum for LSCrF8255, obtained using a 3 keV He^+ primary ion analysis beam. The surface was initially covered with a carbon-based layer from exposure to the environment that obscures the entire spectral signal. Upon removal of the layer via low sputter dosage, the chemical elements (and impurities) are immediately present. The strong background signal likely denotes the high concentration of sub-surface oxygen anions [15].

The background signal observed in Figure 5.10 is a result of the elevated concentration of oxygen ions in the sub-surface of LSCrF8255. This background is characteristic of LEIS analysis of oxide materials using a He^+ primary analysis ion [15]. Three main possibilities for interactions to occur between the He^+ primary ion and sample surface atoms are shown in Figure 5.11. The scattering of the primary noble gas ion upon interaction with a sample atom on the outer surface (Figure 5.11a) has a low probability of neutralization, maintaining its charged state. The charged He^+ ion will thus be detected by the energy analyzer. Conversely, primary noble gas ions that penetrate the outer surface and undergo collision with sub-surface sample atoms (Figure 5.11b) will have a significantly higher probability of neutralization and will not be detected. However, sub-surface

interaction causing neutralization can be followed by an interaction with a surface atom (Figure 5.11c) on its trajectory out of the material. Interactions of this nature where the surface atom is an anion such as oxygen may re-ionize the primary ion as it exits the sample. In this case, the primary ion has undergone multiple backscattered collisions in the sample and will have lost energy, but will still be detected by the energy analyzer. The background observed in LEIS spectra using $^{4}He^{+}$ as the primary analysis beam is eliminated with the use of heavier noble gas ions for LEIS analysis such as $^{20}Ne^{+}$ and $^{40}Ar^{+}$.

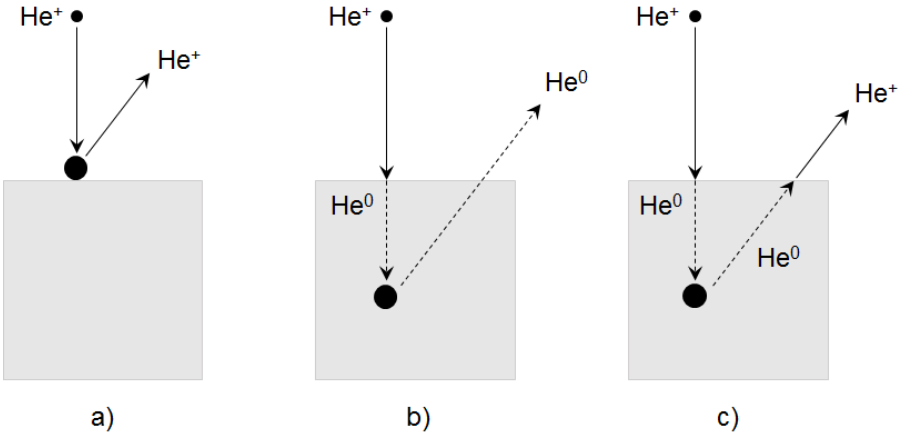

Figure 5.11: Illustration of three possibilities for the interaction between a He^{+} primary ion and the sample surface. a): He^{+} ion is backscattered from the outer surface of the sample. b): He^{+} ion penetrates beyond the outer surface, and is neutralized. Upon exit, the primary ion is not detected by the energy analyzer. c): He^{+} ion penetrates beyond the outer surface, and is neutralized. Upon exit, interaction with another sample ion (such as oxygen) re-ionizes the primary ion, which is detected by the energy analyzer, although at lower energy. Modified from [12].

The use of heavier noble gas ions is also used to increase the energy resolution of the LEIS instrument, allowing the deconvolution of peak signals in the spectrum. Deconvolution of the Cr and Fe peaks in the LEIS spectrum of LSCrF8255 was performed by utilizing a 5 keV $^{20}Ne^{+}$ analysis beam. The LEIS spectrum is shown in Figure 5.12. A pristine surface was chosen on the LSCrF8255 surface for this analysis. Area analysis was performed after sputter doses ($^{40}Ar^{+}$, 1 keV) of 0, 1.0 and 5.0 x 10^{15} ions cm^{-2} were applied.

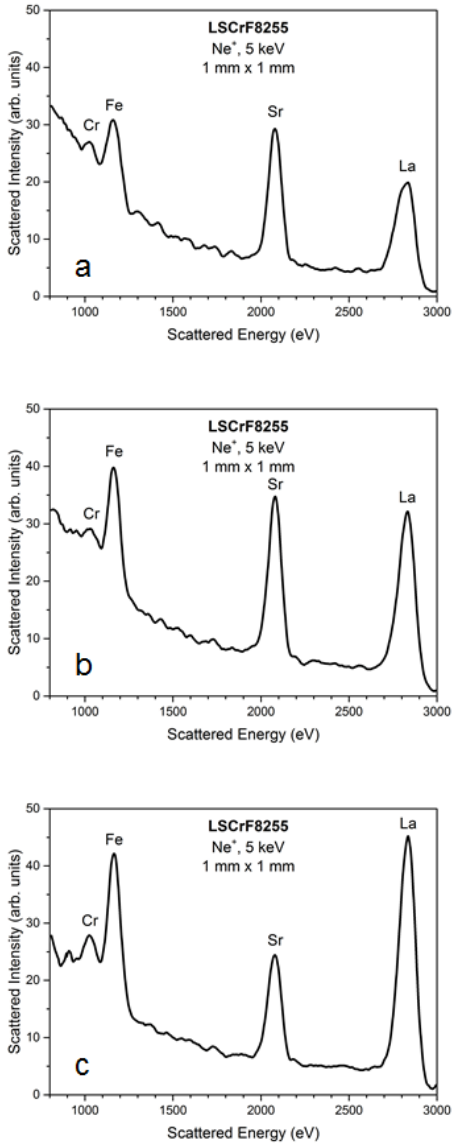

Figure 5.12: LEIS spectra of LSCrF8255, using a $^{20}Ne^{+}$ primary analysis beam. Sputter dose density using a sputter beam ($^{40}Ar^{+}$, 1 keV) of 0 (top), $1.0x10^{15}$ ions cm^{-2} (middle), and $5.0x10^{15}$ ions cm^{-2} (bottom) was applied to the analysis area. The Sr signal was observed to be strong at the outer layer but reverted towards stoichiometric fraction with further sputtering. The Cr signal was observed to be significantly weaker than the Fe signal on the outer atomic layers of LSCrF8255.

The presence of the carbon-based layer did not obscure the signal generated from the 5 keV $^{20}Ne^{+}$ primary ions. The analysis of the LSCrF8255 outer surface and subsequent atomic layers using 5 keV $^{20}Ne^{+}$ primary ions as shown in Figure 5.12 revealed two main pieces of information. First, the Sr signal on the outer surface (Figure 5.12a) was

significantly elevated, with the signal appearing stronger than the La signal. This deviates significantly from the expected ideal bulk stoichiometry, where the La : Sr ratio of LSCrF8255 is 4 : 1. Application of a sputter dose of 5.0 x 10^{15} ions cm^{-2} showed the peak signals of La and Sr reverting back towards the expected bulk stoichiometric composition.

It was hypothesized by Druce et. al. [32] that for the $A^{3+}B^{3+}O_3$ family of perovskite materials, of which LSCrF8255 is a part of, where an alkaline earth metal (e.g. Sr) is substituting for the trivalent A-site cation (e.g. La^{3+}) that the divalent alkaline earth metal segregates very strongly to the outer atomic layer, in an attempt to terminate in an AO (SrO) plane. This phenomenon was not observed in LSCrF8255, although it is noted that the material analyzed was not exposed to annealing temperatures similar to that performed in the work of Druce et. al. [32]. However, surface segregation of Sr in $La_{0.6}Sr_{0.4}Co_{0.2}Fe_{0.8}O_{3-\delta}$ was found by Hansen et. al. [33] to be suppressed by the introduction of A-site deficiency to the material. Therefore, it is possible that A-site deficiency introduced in $(La_{0.8}Sr_{0.2})_{0.95}Cr_{0.5}Fe_{0.5}O_{3-\delta}$ may suppress Sr segregation in the material.

Second, the Cr peak signal was significantly lower than the Fe signal at each sputter depth. This deviates significantly from the expected Cr : Fe ratio in the ideal bulk stoichiometry of LSCrF8255, which is 1 : 1. In addition, at increasing sputter depths, the Fe signal increases at a significantly faster rate than the Cr signal. This suggests that Cr is deficient within the first few atomic layers of LSCrF8255. As a result of the absence of Cr, the composition of the surface of LSCrF8255 may be closer to lanthanum strontium ferrite $La_{1-x}Sr_xFeO_{3-\delta}$ (LSF).

LSF possesses higher mixed ionic-electronic conductivity and oxygen reduction activity than LSCrF, but has significantly higher thermal expansion coefficients (23.8 x 10^{-6} C^{-1}, T ≥ 600˚C vs. 11.2 x 10^{-6} C^{-1}, 27 ˚C ≤ T ≤ 1097˚C). In addition, increasing iron content was found to be correlated with decreasing electronic conductivity, which was attributed to lower hole conduction in the Fe-rich regions [22]. This phenomenon was pronounced in reducing conditions and at higher Fe concentrations. Increasing iron content also tends to increase chemical expansion of the material. Finally, LSF is chemically unstable in reducing atmospheres, decomposing into La_2O_3 and Fe at $pO_2 \leq 10^{-17}$ atm at 1000˚C [34]. This makes it incompatible in OTM operations, where the thermal expansion coefficient must be similar to that of the ScSZ phase (TEC of $Zr_{0.80}Sc_{0.19}Al_{0.02}O_{1.90}$ = 10.9 x 10^{-6} C^{-1}, 30˚C ≤ T ≤ 1000˚C [35]) and maintain chemical stability in partial pressure conditions of the permeate side of the membrane of $pO_2 \leq 10^{-22}$ atm.

5.2.2.2 XPS analysis – Near-Surface Chemical Composition

Figure 5.13 shows the XPS spectrum of un-aged LSCrF8255 and LSCrF8255 exposed to simulated static operating conditions of the OTM (air; 5%H_2-95%CO_2) obtained using an Al Kα monochromated X-ray source (hν = 1486.6 eV). The surface was exposed to the sintering temperature (1450°C, 6 h) and in the case of the aged samples, further exposed to air or a gas mixture comprised of 5%H_2-95%CO_2 (pO_2 ~ 10^{-11} atm) at 1000°C for 300 h (1 atm total pressure).

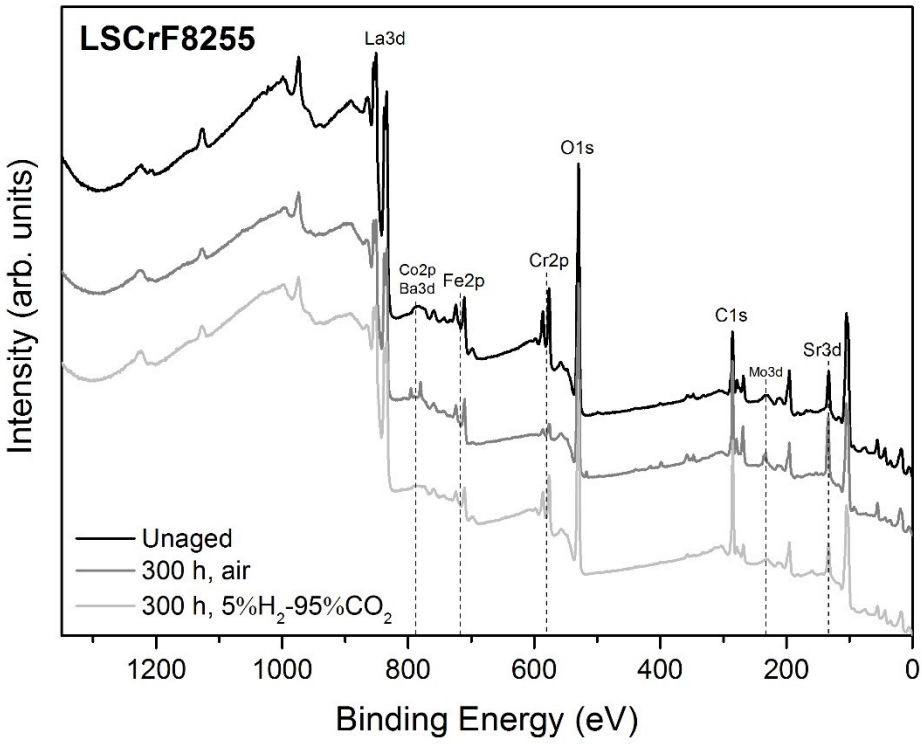

Figure 5.13: X-ray Photoelectron Spectrum of as-prepared and aged (1000°C, 300 h) LSCrF8255 using an Al Kα monochromated X-ray source (hν = 1486.6 eV).

Table 5-2 summarizes the quantification of the LSCrF8255 sample surface analyzed via XPS. Quantification was performed on the intensity of La3d5/2, Sr3d5/2, Cr2p3/2 and Fe2p3/2 peak signals, with the relative sensitivity factor appropriately adjusted to represent the total peak signal, with the ideal bulk stoichiometry of LSCrF8255 included for reference. LSCrF8255 exhibits Sr surface segregation after exposure to air at elevated temperatures, as shown by the un-aged and air-aged samples (bearing in mind that

samples were exposed to air at elevated temperatures during sintering). Prolonged exposure to air shows the depletion of Cr from the near-surface as well as further Sr surface segregation. Exposure to 5%H_2-95%CO_2 shows a strong Cr signal in the near-surface and Sr depletion compared to the un-aged sample.

Table 5-2: Semi-quantitative results of chemical composition of LSCrF8255 surface via X-ray Photoelectron Spectroscopy. Samples were exposed to i) air; ii) 5%H_2-95%CO_2 at 1000˚C for 300 h at atmospheric pressure.

Element	Ideal Bulk (%)	Unaged (%)	Aged 300 h, air (%)	Aged 300 h, 5%H_2-95%CO_2 (%)
La	40	32.0	38.4	39.2
Sr	10	29.6	35.8	15.1
Cr	25	25.6	9.4	32.9
Fe	25	12.8	16.4	12.8

The observation and quantification of the Sr and Cr concentration at the near-surface via XPS suggests that exposure of LSCrF8255 to oxidizing conditions promotes Sr surface segregation, in contrast to exposure to reducing conditions which discourages it. This may be of some concern in prolonged OTM operation as over time, Sr segregation to the air side (pO_2 = 0.21 atm) and Cr segregation to the fuel side ($pO_2 \leq 10^{-22}$ atm) may result in destabilization of LSCrF8255 by several mechanisms, including secondary phase formation, instability of the crystal structure, reduction in density, and inhomogeneous elemental distribution within the bulk material, resulting in losses in ionic or electronic conductivity and thus in overall oxygen transport.

The Fe signal was observed to be below the expected stoichiometric values for all three samples. This could be a result of the tendency of Fe to migrate to the outer surface as was observed in the LEIS measurements. It was found by Wei et. al. [21] that the measured density of $La_{0.8}Sr_{0.2}Cr_{1-x}Fe_xO_{3-\delta}$ (sintered in air at 1400˚C for 4 hours) increased with increasing Fe dopant, from 84% density at x = 0.1 (LSCrF8291) to 97% at x = 0.5 (LSCrF8255).

Finally, impurities of Ba and Co, as well as Mo were found within the detection limit of the instrument to the analysis depth (~10 nm). The Ba3d/Co2p dual peak observed on Figure 5.13: X-ray Photoelectron Spectrum of as-prepared and aged (1000˚C, 300 h) LSCrF8255 using an Al Kα monochromated X-ray source (hν = 1486.6 eV).Figure 5.13 is determined to be Ba, due to the presence of $Ba4d_{3/2}$ and $Ba4d_{5/2}$ doublet peaks (BE ~ 95 eV and 90 eV respectively) in the low-energy XPS spectrum, but not the $Co3p_{1/2}$ and $Co3p_{3/2}$ peaks (BE ~ 60 eV). However, the formation of secondary phases on the surface or in the bulk, with properties detrimental to ionic/electronic conductivity, cannot be ruled out. The analysis of such secondary phases is beyond the scope of this work.

5.2.3 Summary

The crystal structure and surface chemistry of LSCrF8255 was examined. The material exhibits a single-phase orthorhombic crystal structure in its sintered form, with no secondary phases observed in the as-prepared (un-aged) material. Examination of the surface of as-prepared (un-aged) LSCrF8255 showed Sr excess and Cr deficiency on the outer surface. Sr excess was also observed in the near-surface (~10 nm) of the material, as well as Fe deficiency. LSCrF8255 exhibited Sr excess and Cr deficiency at the near-surface upon exposure to air (1000˚C, 300 h) and Sr deficiency and Cr excess upon exposure to 5%H_2-95%CO_2 (1000˚C, 300 h). The Fe content was below stoichiometric values prior to and after aging. The minor presence of impurities (Ba, Co, Mo) was also observed on the near-surface.

5.3 Conclusions

$Sc_{0.10}Ce_{0.01}Zr_{0.89}O_{2-\delta}$ (1Ce10ScSZ) achieves a single cubic phase at elevated temperatures, and possesses acceptably high oxygen ionic conductivity. However, the oxygen surface exchange kinetics of 1Ce10ScSZ was observed to be minimal without the presence of a catalytic layer to improve oxygen incorporation. Examination of the surface of 1Ce10ScSZ showed that the relevant elements were present on both the outer and near-surface, with Ce excess, Zr deficiency, and impurities (Na, Mg, Si, Al, possibly Ca) observed on the outer atomic surface. Ce deficiency within the first ~10 nm of the material was also observed. In addition, elevated Sc signal was detected after 1Ce10ScSZ was aged in air (1000˚C, 300 h).

$(La_{0.8}Sr_{0.2})_{0.95}Cr_{0.5}Fe_{0.5}O_{3-\delta}$ (LSCrF8255) achieves a single-phase orthorhombic crystal structure at elevated temperatures, with no secondary phases observed in the as-prepared (un-aged) material. Sr excess and Cr deficiency was observed on the outer surface. Sr excess and Fe deficiency was also observed on the near-surface (~10 nm) of the material. LSCrF8255 exhibited Sr excess and Cr deficiency at the near-surface upon exposure to air

(1000°C, 300 h) and Sr deficiency and Cr excess upon exposure to 5%H_2-95%CO_2 (1000°C, 300 h). The Fe content was measured to be below stoichiometric values prior to and after aging. The minor presence of impurities (Ba, Co, Mo) was also observed on the near-surface.

This chapter attempts to examine the oxygen transport kinetics of single-phase 1Ce10ScSZ, and the surface chemical compositions of both single-phase 1Ce10ScSZ and LSCrF8255. The next chapter (Chapter 6) discusses the oxygen transport kinetics and surface chemistry of the dual-phase 1Ce10ScSZ/LSCrF8255 material, and the effects of aging in simulated operating conditions on these two parameters.

5.4 References

[1] S. Omar, A. Belda, A. Escardino, and N. Bonanos, "Ionic conductivity ageing investigation of 1Ce10ScSZ in different partial pressures of oxygen," *Solid State Ionics*, vol. 184, no. 1, pp. 2–5, 2011.

[2] H. Fujimori, M. Yashima, M. Kakihana, and M. Yoshimura, "Structural Changes of Scandia-Doped Zirconia Solid Solutions: Rietveld Analysis and Raman Scattering," *J. Am. Ceram. Soc.*, vol. 81, pp. 2885–2893, 1998.

[3] T. Itoh, M. Mori, M. Inukai, H. Nitani, T. Yamamoto, T. Miyanaga, N. Igawa, N. Kitamura, N. Ishida, and Y. Idemoto, "Effect of annealing on crystal and local structures of doped zirconia using experimental and computational methods," *J. Phys. Chem. C*, vol. 119, no. 16, pp. 8447–8458, 2015.

[4] S. Omar and N. Bonanos, "Ionic conductivity ageing behaviour of 10 mol% Sc_2O_3–1 mol% CeO_2–ZrO_2 ceramics," *J. Mater. Sci.*, vol. 45, no. 23, pp. 6406–6410, 2010.

[5] J. Nelson and D. Riley, "An experimental investigation of extrapolation methods in the derivation of accurate unit-cell dimensions of crystals," *Cavendish Lab. Cambridge*, pp. 160–177, 1944.

[6] D. Fletcher, R. McMeeking, and J. Parkin, "The United Kingdom Chemical Database Service," vol. 36, pp. 746–749, 1996. Available at http://cds.rsc.org/

[7] J. Irvine, D. Sinclair, and A. West, "Electroceramics: Characterization by Impedance Spectroscopy," *Adv. Mater.*, vol. 2, no. 3, pp. 132–138, 1990.

[8] E. Kurumchin, "An isotope exchange study of the behaviour of electrochemical systems," *Solid State Ionics*, vol. 42, no. 3–4, pp. 129–133, 1990.

[9] E. Raj, A. Atkinson, and J. Kilner, "Oxygen diffusion studies on $(Y_2O_3)_2(Sc_2O_3)_9(ZrO_2)_{89}$," *Solid State Ionics*, vol. 180, no. 14–16, pp. 952–955, 2009.

[10] T. Sakai, J. Hyodo, M. Ogushi, A. Inoishi, S. Ida, and T. Ishihara, "Evaluation of isotope diffusion coefficient and surface exchange coefficient of ScSZ series oxide by oxygen isotope exchange method," *Solid State Ionics*, vol. 301, pp. 156–162, 2017.

[11] R. Chater, "Oxygen self-diffusion and surface exchange measurements of the polycrystalline oxide $(La_{0.8}Sr_{0.2})(Cr_{0.2}Fe_{0.8})O_{3-d}$ using Secondary Ion Mass Spectrometry," 2014.

[12] J. Kilner, S. Skinner, and H. Brongersma, "The isotope exchange depth profiling (IEDP) technique using SIMS and LEIS," *J. Solid State Electrochem.*, vol. 15, no. 5, pp. 861–876, 2011.

[13] M. de Ridder, R. van Welzenis, and H. Brongersma, "Surface cleaning and characterization of yttria-stabilized zirconia," *Surf. Interface Anal.*, vol. 33, no. 4, pp. 309–317, 2002.

[14] M. de Ridder, A. Vervoort, R. Van Welzenis, and H. Brongersma, "The limiting factor for oxygen exchange at the surface of fuel cell electrolytes," *Solid State Ionics*, vol. 156, pp. 255–262, 2003.

[15] H. Brongersma, M. Draxler, M. Deridder, and P. Bauer, "Surface composition analysis by low-energy ion scattering," *Surf. Sci. Rep.*, vol. 62, no. 3, pp. 63–109, 2007.

[16] R. Ruh and H. Garrett, "The System Zirconia-Scandia," *J. Am. Ceram. Soc.*, vol. 60, pp. 399–403, 1977.

[17] A. Shard, "Detection limits in XPS for more than 6000 binary systems using Al and Mg Kα X-rays," *Surf. Interface Anal.*, no. February, pp. 175–185, 2014.

[18] Z. Shen, "Mass Transport in Mixed-Conducting LSCrF-ScSZ Dual Phase Composites for Oxygen Transport Membrane Applications," Imperial College London, 2017.

[19] T. Ramos, M. Carvalho, L. Ferreira, M. Cruz, and M. Godinho, "Structural and Magnetic Characterization of the Series $La_{1-x}Sr_xFe_{0.8}Cr_{0.2}O_{3-d}$ (x=0.2, 0.4, 0.6 and 0.8)," *Chem. Mater.*, vol. 18, no. 16, pp. 3860–3865, 2006.

[20] R. Shannon and C. Prewitt, "Effective Ionic Radii in Oxides and Fluorides," *Acta Crystallogr. Sect. B Struct. Sci. Cryst. Eng. Mater.*, vol. III, no. 1454, pp. 925–946, 1967.

[21] T. Wei, X. Zhou, Q. Hu, Q. Gao, D. Han, X. Lv, and S. Wang, "A high power density solid oxide fuel cell based on nano-structured $La_{0.8}Sr_{0.2}Cr_{0.5}Fe_{0.5}O_{3-\delta}$ anode," *Electrochim. Acta*, vol. 148, pp. 33–38, 2014.

[22] M. Lü, E. Tsipis, J. Waerenborgh, A. Yaremchenko, V. Kolotygin, S. Bredikhin, and

V. Kharton, "Thermomechanical, transport and anodic properties of perovskite-type $(La_{0.75}Sr_{0.25})_{0.95}Cr_{1-x}Fe_xO_{3-d}$," *J. Power Sources*, vol. 206, pp. 59–69, 2012.

[23] H. Ding, A. Virkar, M. Liu, and F. Liu, "Suppression of Sr surface segregation in $La_{1-x}Sr_xCo_{1-y}Fe_yO_{3-\delta}$: A First Principles Study," *Phys. Chem. Chem. Phys.*, pp. 489–496, 2012.

[24] S. Kim and G. Choi, "Stability of LSCF electrode with GDC interlayer in YSZ-based solid oxide electrolysis cell," *Solid State Ionics*, vol. 262, pp. 303–306, 2014.

[25] J. Druce, T. Ishihara, and J. Kilner, "Surface composition of perovskite-type materials studied by Low Energy Ion Scattering (LEIS)," *Solid State Ionics*, vol. 262, pp. 893–896, 2014.

[26] J. Joo, K. Yun, J. Kim, Y. Lee, C. Yoo, and J. Yu, "Substantial Oxygen Flux in Dual-Phase Membrane of Ceria and Pure Electronic Conductor by Tailoring the Surface," *ACS Appl. Mater. Interfaces*, 2015.

[27] M. Niania, "In-Situ Analysis of $La_{0.6}Sr_{0.4}Co_{0.2}Fe_{0.8}O_{3-\delta}$ Surface in Ambient Temperatures," 2016.

[28] J. ten Elshof, H. Bouwmeester, and H. Verweij, "Oxidative coupling of methane in a mixed-conducting perovskite membrane reactor," *Appl. Catal. A Gen.*, vol. 130, no. 2, pp. 195–212, 1995.

[29] R. DeSouza and J. Kilner, "Oxygen transport in $La_{1-x}Sr_xMn_{1-y}Co_yO_{3+-delta}$ perovskites, Part II. Oxygen surface exchange," *Solid State Ionics*, vol. 126, pp. 153–161, 1999.

[30] S. Gupta, Y. Zhong, M. Mahapatra, and P. Singh, "Processing and electrochemical performance of in oxidizing and reducing atmospheres," *Int. J. Hydrogen Energy*, pp. 1–11, 2015.

[31] J. Sfeir, P. Buffat, P. Möckli, N. Xanthopoulos, R. Vasquez, H. Mathieu, J. Van Herle, and K. Thampi, "Lanthanum Chromite Based Catalysts for Oxidation of Methane Directly on SOFC Anodes," *J. Catal.*, vol. 202, no. 2, pp. 229–244, 2001.

[32] J. Druce, H. Téllez, M. Burriel, M. Sharp, L. Fawcett, S. Cook, D. McPhail, T. Ishihara, H. Brongersma, and J. Kilner, "Surface termination and subsurface restructuring of perovskite-based solid oxide electrode materials," *Energy Environ. Sci.*, vol. 7, pp. 3893–3599, 2014.

[33] K. Hansen and K. Hansen, "A-site deficient $(La_{0.6}Sr_{0.4})_{1-s}Fe_{0.8}Co_{0.2}O_{3-\delta}$ perovskites as SOFC cathodes," *Solid State Ionics*, vol. 178, pp. 1379–1384, 2007.

[34] S. Gupta, M. Mahapatra, and P. Singh, "Lanthanum chromite based perovskites for oxygen transport membrane," *Mater. Sci. Eng. R Reports*, vol. 90, pp. 1–36, 2015.

[35] F. Tietz, “Thermal Expansion of SOFC Materials,” *Ionics*, vol. 5, pp. 129–139, 1999.

6 Properties of Dual-Phase $Sc_{0.10}Ce_{0.01}Zr_{0.89}O_{2-\delta}$ / $(La_{0.8}Sr_{0.2})_{0.95}Cr_{0.5}Fe_{0.5}O_{3-\delta}$ Oxygen Transport Membrane Material

This chapter examines the dual-phase $Sc_{0.10}Ce_{0.01}Zr_{0.89}O_{2-\delta}/(La_{0.8}Sr_{0.2})_{0.95}Cr_{0.5}Fe_{0.5}O_{3-\delta}$ (1Ce10ScSZ/LSCrF8255) oxygen transport membrane material, following the analysis of the single-phase components examined in the previous chapter. The dual-phase material is comprised of a 50/50 vol. % mixture of each phase as outlined in Section 4.1.2. The effects on 1Ce10ScSZ/LSCrF8255 composites from exposure to three separate static conditions (air, 4% H_2-96% N_2, 5% H_2-95% CO_2) at two aging durations (300 hours, 1000 hours) will be examined, with emphasis on the crystal structure, oxygen transport kinetics, and surface chemistry of the material. In addition, the effects of oxygen transport kinetics of the material under water vapor environment will be discussed.

6.1 Effects of Aging (300 hours) on 1Ce10ScSZ/LSCrF8255

The properties of dual-phase 1Ce10ScSZ/LSCrF8255 from exposure to three separate static conditions (air, 4%H_2-96%N_2, 5%H_2-95%CO_2) at 1000˚C for 300 hours will be examined and compared to the unaged material. Characterization will be performed for the four samples via X-ray diffraction and secondary electron microscopy. The oxygen transport kinetics of 1Ce10ScSZ/LSCrF8255 will be examined using isotopic exchange depth profiling combined with secondary ion mass spectrometry. The surface chemistry of the outer atomic layer and the near-surface (within ~10 nm) will be studied using low energy ion scattering and X-ray photoelectron spectroscopy respectively, with relative elemental quantification of the near-surface via XPS also performed.

6.1.1 Characterization of 1Ce10ScSZ/LSCrF8255

6.1.1.1 X-ray Diffraction

The X-ray diffraction pattern of dual-phase 1Ce10ScSZ/LSCrF8255 is shown in Figure 6.1. The X-ray analysis was performed on the material after mixing the single-phase components to achieve a 50/50 vol. % (~45/55 wt %) ratio, and sintering at 1450˚C in air for 6 hours yielding dense samples. All peak signals present on the single-phase 1Ce10ScSZ (Figures 5.1 and 5.2) and single-phase LSCrF8255 (Figures 5.9 and 5.10) were

present in dual-phase 1Ce10ScSZ/LSCrF8255, suggesting that both components retain their respective crystal structures (1Ce10ScSZ: cubic fluorite; LSCrF8255: orthorhombic perovskite) when mixed together and exposed to sintering temperatures. The structural stability of the dual-phase material is also evidenced by the absence of any peak signals other than the component single-phases, within the 2-theta resolution and X-ray intensities generated by the instrument. This means that formation of long-range ordered secondary phases in 1Ce10ScSZ/LSCrF8255 was not observed after sintering.

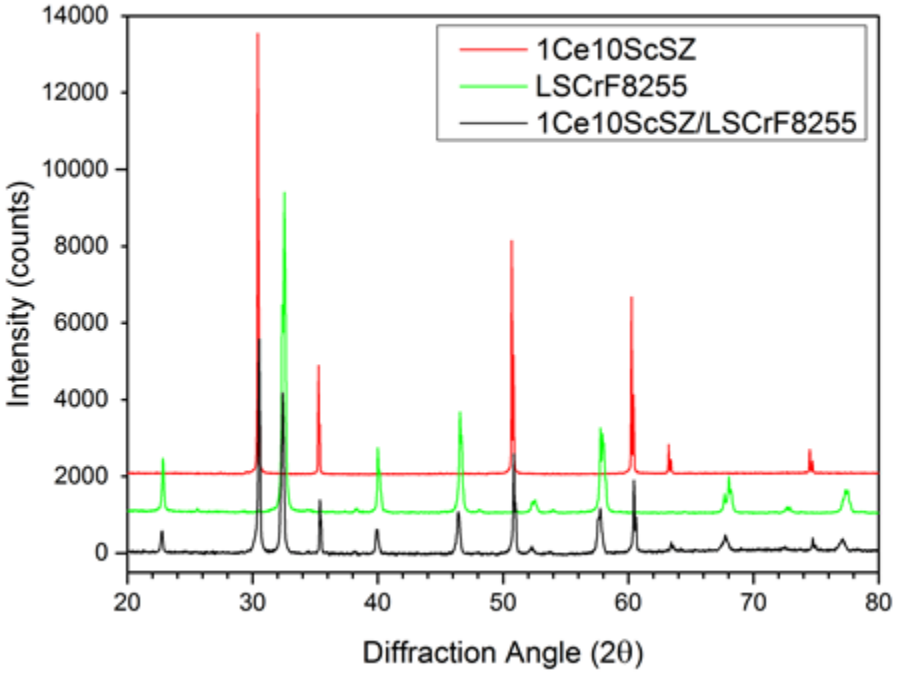

Figure 6.1: X-ray diffraction pattern of 1Ce10ScSZ/LSCrF8255 dual-phase membrane (black) superimposed with diffraction pattern of single-phase 1Ce10ScSZ (red) and single-phase LSCrF8255 (green). All diffraction peaks of the single-phase components were present in the XRD pattern of the dual-phase material. A shift in peak position in the overall 1Ce10ScSZ/LSCrF8255 pattern was observed.

However, a shift in peak positions of the X-ray diffraction pattern in the dual-phase 1Ce10ScSZ/LSCrF8255 material was observed. The peaks representing the 1Ce10ScSZ single-phase component in 1Ce10ScSZ/LSCrF8255 (black line in Figure 6.1) are shifted to higher 2-theta values compared to the standalone single-phase 1Ce10ScSZ material (green line in Figure 6.1). Conversely, the peaks representing the LSCrF8255 single-phase component in 1Ce10ScSZ/LSCrF8255 are shifted to lower 2-theta values compared to the standalone single-phase LSCrF8255 material (red line in Figure 6.1). Joo et. al. [1] observed

a similar phenomenon in a $Ce_{0.9}Gd_{0.1}O_{2-\delta}/La_{0.6}Sr_{0.4}Co_{0.2}Fe_{0.8}O_{3-\delta}$ (CGO/LSCF) dual-phase membrane sandwiched between two layers of LSCF, which was attributed to the diffusion of La and Sr from the LSCF layers into the CGO/LSCF composite. Although the experimental setup of the work here does not include the analogous scenario of layers of LSCrF8255 sandwiching the 1Ce10ScSZ/LSCrF8255 material, inter-diffusion of La and Sr may still have occurred as a result of the contact between the un-sintered sample and the 1Ce10ScSZ/LSCrF8255 powder lining the crucible during sintering (see Section 4.1.2). Shaula et. al. [2] observed that inter-diffusion of cations between the phases does not significantly affect the electronic conductivity of the dual-phase material, but lowers the ionic conductivity with increasing interaction between phases.

This may translate into several possible phenomena in dual-phase 1Ce10ScSZ/LSCrF8255. Lower ionic conductivity in the bulk material as a result of cation inter-diffusion translates into lower oxygen diffusivity. Since La^{3+} or Sr^{2+} ions are unlikely to sit in oxygen vacancy sites of the fluorite 1Ce10ScSZ structure despite having similar ionic radii ($r_{O^{2-}}$= 1.38 Å, $r_{La^{3+}}$, 1.36 Å, $r_{Sr^{2+}}$= 1.44 Å [3]) due to the difference in ion charge, they may segregate in the grain boundaries of 1Ce10ScSZ. This may inhibit oxygen diffusion along grain boundaries in 1Ce10ScSZ, although the large grain sizes of the material (1-5 μm) results in a comparatively low grain boundary volume, so the effect of cation grain boundary segregation on overall oxygen transport may be limited. More saliently, the migration of A-site cations away from LSCrF8255 would destabilize the perovskite phase over prolonged exposure at elevated temperatures. Cation inter-diffusion in LSCrF8255 over long operating durations may result in loss of percolation of the perovskite phase across the membrane thickness, resulting in membrane failure.

Figure 6.2 shows the X-ray diffraction patterns of 1Ce10ScSZ/LSCrF8255 after exposure to three aging conditions. The materials were subject to air, 4% H_2-96% N_2, and 5% H_2-95 %CO_2 at 1000˚C and atmospheric pressure for 300 hours. The oxygen partial pressures of 4% H_2-96% N_2 and 5% H_2-95% CO_2 were calculated to be ~ 10^{-18} atm and pO_2 ~ 10^{-11} atm respectively. The XRD patterns were obtained *ex-situ* from the aging environment, in air at ambient conditions. The unaged 1Ce10ScSZ/LSCrF8255 diffraction pattern is added to Figure 6.2 for reference.

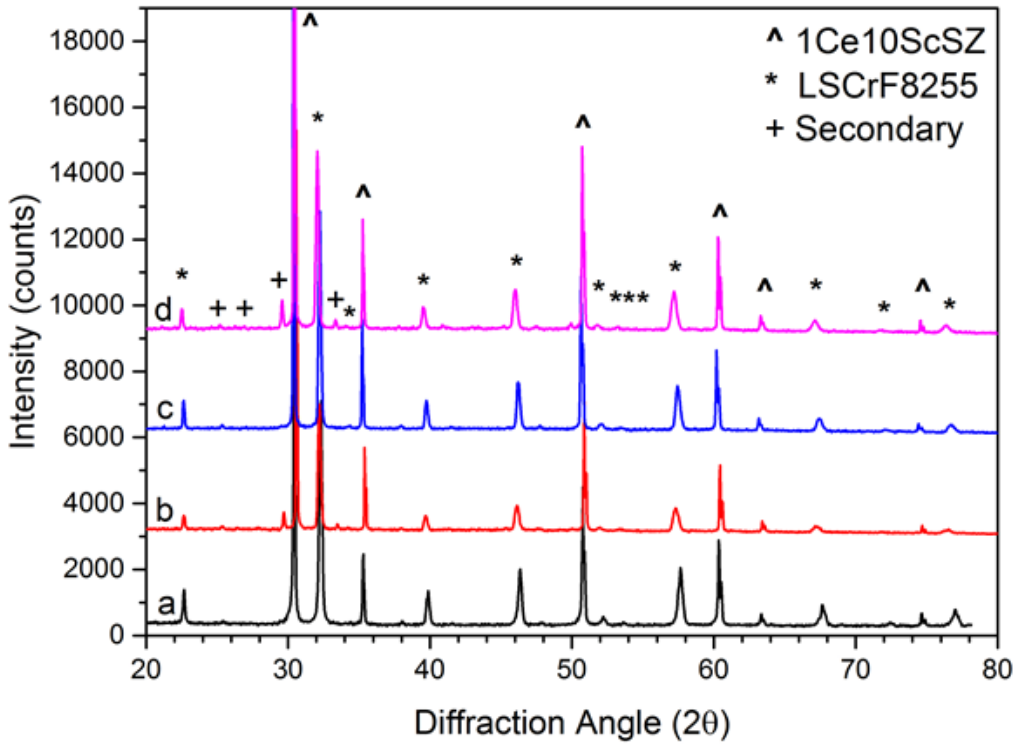

Figure 6.2: X-ray diffraction patterns of 1Ce10ScSZ/LSCrF8255 dual-phase membranes before and after aging for 300 hours. From bottom to top: a) unaged; b) aged in air at 1000˚C for 300 h; c) aged in 4% H_2-96% N_2 ($pO_2 \sim 10^{-18}$ atm) at 1000˚C for 300 h; d) aged in 5% H_2-95% CO_2 ($pO_2 \sim 10^{-11}$ atm) at 1000˚C for 300 h. Aging atmospheres were 1 atm. The formation of a secondary phase hypothesized to be $SrCrO_4$ [4] was found in samples b) and d).

It was observed that both 1Ce10ScSZ and LSCrF8255 components maintain their crystal structures after 300 hours of aging. The material exposed to 4% H_2-96% N_2 (Figure 6.2c) did not experience any significant change in its diffraction pattern when compared to the unaged material (Figure 6.2a). This suggests that the 1Ce10ScSZ/LSCrF8255 dual-phase material is chemically stable at highly reducing conditions, which corroborates the work done by Gupta et. al. [5]. However, the formation of a $SrCrO_4$ secondary phase was observed for the materials subject to air and 5% H_2-95% CO_2 (Figure 6.2b and d respectively). The presence of this secondary phase was also observed by He et. al. [6] who exposed LSCrF8255 powders to undiluted hydrogen gas ($pO_2 < 10^{-28}$ atm) for 30 hours, but it was claimed as an unknown phase, and no further discussions were made. The presence of $SrCrO_4$ was observed by Mori et. al. [7] to enhance densification in Sr-doped $LaCrO_3$ materials. However, the thermal expansion coefficient of $SrCrO_4$ was found

to be 17.5 x 10^{-6} $^{\circ}C^{-1}$ in the temperature range 50°C ≤ T ≤ 1000°C [7], which is higher than the 11.2 x 10^{-6} $^{\circ}C^{-1}$ observed for LSCrF8255 [5], which may contribute to mechanical stresses in the perovskite phase under prolonged operation.

It is known that $SrCrO_4$ formation is common in $La_{0.6}Sr_{0.4}Co_{0.2}Fe_{0.8}O_{3-\delta}$ materials due to its susceptibility to Cr poisoning [8], [9]. However, the formation of $SrCrO_4$ in these materials is due to the interaction between Sr at the outer surface of this material and Cr from the environment, in the form of Cr-containing vapors. In the case of LSCrF8255, chromium exists in oxide form as the B-site cation in the perovskite material. However, the relationship between the presence of Cr in the bulk material as a primary component and the formation of strontium chromate phases under prolonged operating conditions is unclear.

However, Wei et. al. [10] examined the crystal structure of single-phase LSCrF8255 and determined that $SrCrO_4$ dissolves into the perovskite at sintering temperatures above 1200°C. Since the material was sintered at 1450°C in this work, the presence of $SrCrO_4$ secondary phases would not be expected. Similarly, Oishi et. al. [11] found that $(La_{0.75}Sr_{0.25})Cr_{0.5}Fe_{0.5}O_{3-\delta}$ decomposes into $(La,Sr)_2FeO_4$ and FeO at $pO_2 \sim 10^{-20}$ atm and 900°C as a result of the tendency for the material to form oxygen vacancies for charge balance, resulting in reduced B-site cations ($Fe^{3+} \rightarrow Fe^{2+}$). The correlation in this work between the formation of $SrCrO_4$ on LSCrF8255 and the aging conditions used is unclear, as it was absent in the material aged in 4% H_2-96% N_2, which is significantly more reducing than 5% H_2-95% CO_2 ($pO_2 \sim 10^{-18}$ atm vs 10^{-11} atm), but present in the sample aged in air.

6.1.1.2 Secondary Electron Microscopy

Figure 6.3 shows the microstructure of 1Ce10ScSZ/LSCrF8255 before and after aging for 300 hours in the three atmospheric conditions specified above. Samples were polished to a ¼ µm mirror finish as outlined in Section 4.1.5, and coated with a thin Cr layer (~5 nm) to eliminate sample charging during examination.

The microstructures of all four samples was observed to be dense, with very few scattered pores. This suggests that aging for 300 hours at elevated temperatures and varying partial pressures does not significantly affect the density of dual-phase 1Ce10ScSZ/LSCrF8255. The dual-phase membrane also exhibits high coherence between the two components of the material, evidenced by the absence of porous regions in the boundaries between the two phases. The thermal expansion coefficients of the two phases are similar (see Chapter 5), so interphase strain is minimized at elevated temperatures. This suggests good interfacial stability between 1Ce10ScSZ and LSCrF8255 in the dual-phase membrane.

Aggregation of the components was observed for all four dual-phase samples. Inhomogeneity of the two phases comprising the membrane is considered to be one of the most undesirable traits of the membrane, likely resulting in reduced oxygen flux through the membrane due to lower degrees of percolation for each phase, as well as increased probability of the presence of "bottleneck" regions within the membrane that would restrict the migration of charge carriers. This is especially prominent for the 1Ce10ScSZ phase, as oxygen ion migration through the membrane is considered to be the limiting factor in the overall oxygen transport kinetics. Very high inhomogeneity may also result in inability of either component phase to achieve percolation, leading to mechanical failure.

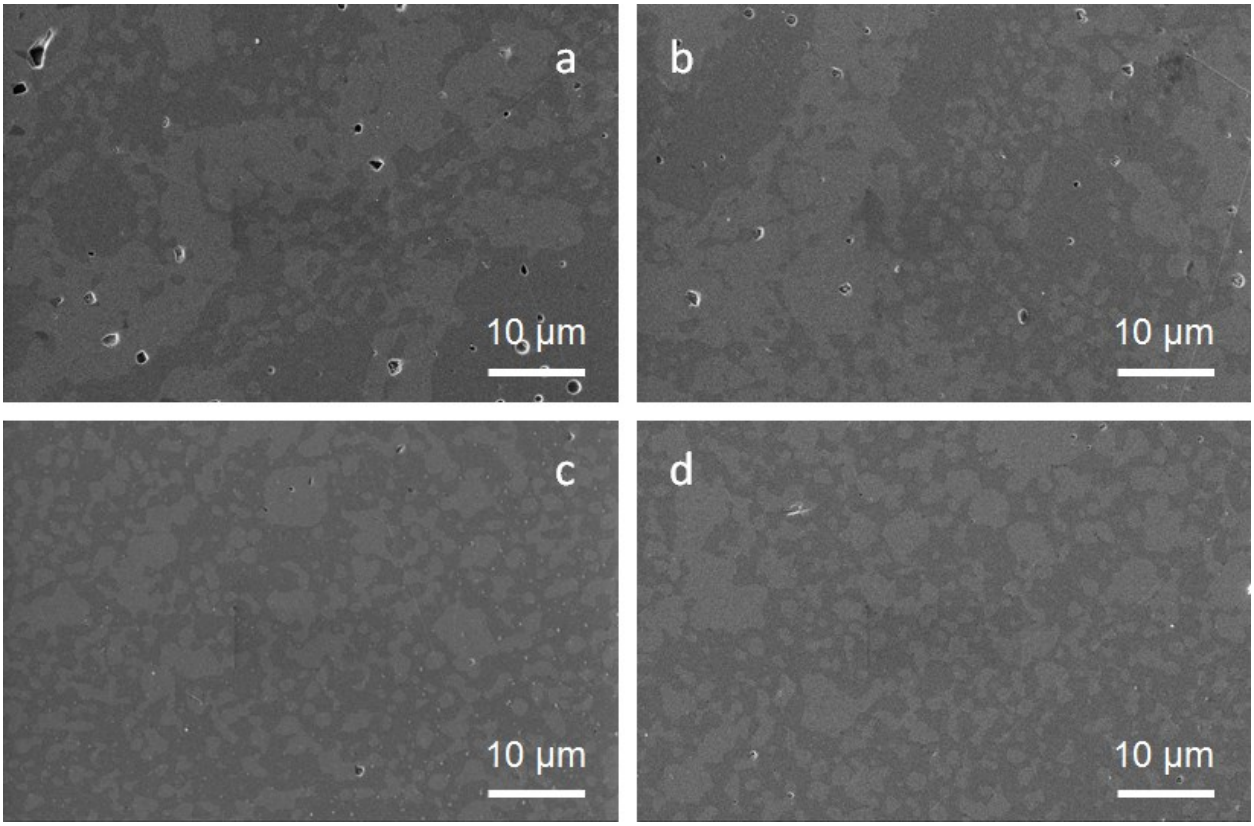

Figure 6.3: Secondary electron micrographs (SEI) of dual-phase 1Ce10ScSZ/LSCrF8255, magnification 5000x. Legend: a) unaged; b) aged in air at 1000˚C for 300 h; c) aged in 4% H_2-96% N_2 ($pO_2 \sim 10^{-18}$ atm) at 1000˚C for 300 h; d) aged in 5% H_2-95% CO_2 ($pO_2 \sim 10^{-11}$ atm) at 1000˚C for 300 hours. The dark phase represents 1Ce10ScSZ, the bright phase represents LSCrF8255.

6.1.2 Oxygen Transport Kinetics of Dual-Phase 1Ce10ScSZ/LSCrF8255

Isotopic Exchange Depth Profiling/Secondary Ion Mass Spectrometry (IEDP-SIMS) experiments were performed for the four 1Ce10ScSZ/LSCrF8255 samples discussed above.

The oxygen self-diffusion coefficient D^* and the surface exchange coefficient k^* extracted from the fit to the experimental data will be compared to determine the effects of aging on the oxygen transport kinetics of the material.

6.1.2.1 Isotopic Exchange Depth Profiling/Secondary Ion Mass Spectrometry of 1Ce10ScSZ/LSCrF8255

The oxygen self-diffusion profiles determined by IEDP-SIMS of dual-phase 1Ce10ScSZ/LSCrF8255 are shown in Figure 6.4. The materials were exposed to the aging conditions prior to isotope exchange experiments. Samples were prepared according to the procedure for isotope exchange outlined in Section 4.1.5. Samples were exposed to ^{18}O (isotopic ratio ~51%) at ~800˚C for 30 minutes (pO_2 = 200 mbar) after equilibration in an ^{16}O environment at the same temperature and pO_2 for 5 hours. Exchanged samples were prepared for the "linescan" sample configuration in SIMS analysis, outlined in Section 4.2.4.

The experimental oxygen tracer profile obtained via SIMS was fitted to the solution for diffusion in a semi-infinite medium [12] using a Matlab-based program developed by Cooper [13] as outlined in Section 4.2.5.1. The oxygen transport kinetic parameters were extracted from the fitted diffusion profile to the experimental data and are summarized in Table 6-1.

The self-diffusion coefficients D^* of 1Ce10ScSZ/LSCrF8255 were calculated from the fitted diffusion profile to be 3.5 (±0.3) x 10^{-8} cm^2 s^{-1} for the unaged sample, 2.3 (±0.3) x 10^{-8} cm^2 s^{-1} for the sample aged in air at 1000˚C for 300 hours, 2.4 (±0.3) x 10^{-8} cm^2 s^{-1} for the sample aged in reducing 4% H_2-96% N_2 at 1000˚C for 300 hours, and 4.2 (±0.3) x 10^{-8} cm^2 s^{-1} for the sample aged in reducing 5% H_2-95% CO_2 at 1000˚C for 300 hours. The self-diffusion coefficient D^* of the aged samples did not differ significantly from the self-diffusion coefficient of the unaged sample, with all four samples possessing D^* on the order of 10^{-8} cm^2 s^{-1}. This suggests that the self-diffusion kinetics of 1Ce10ScSZ/LSCrF8255

were relatively unaffected by exposure to the selected aging environments at elevated temperatures over this length of time.

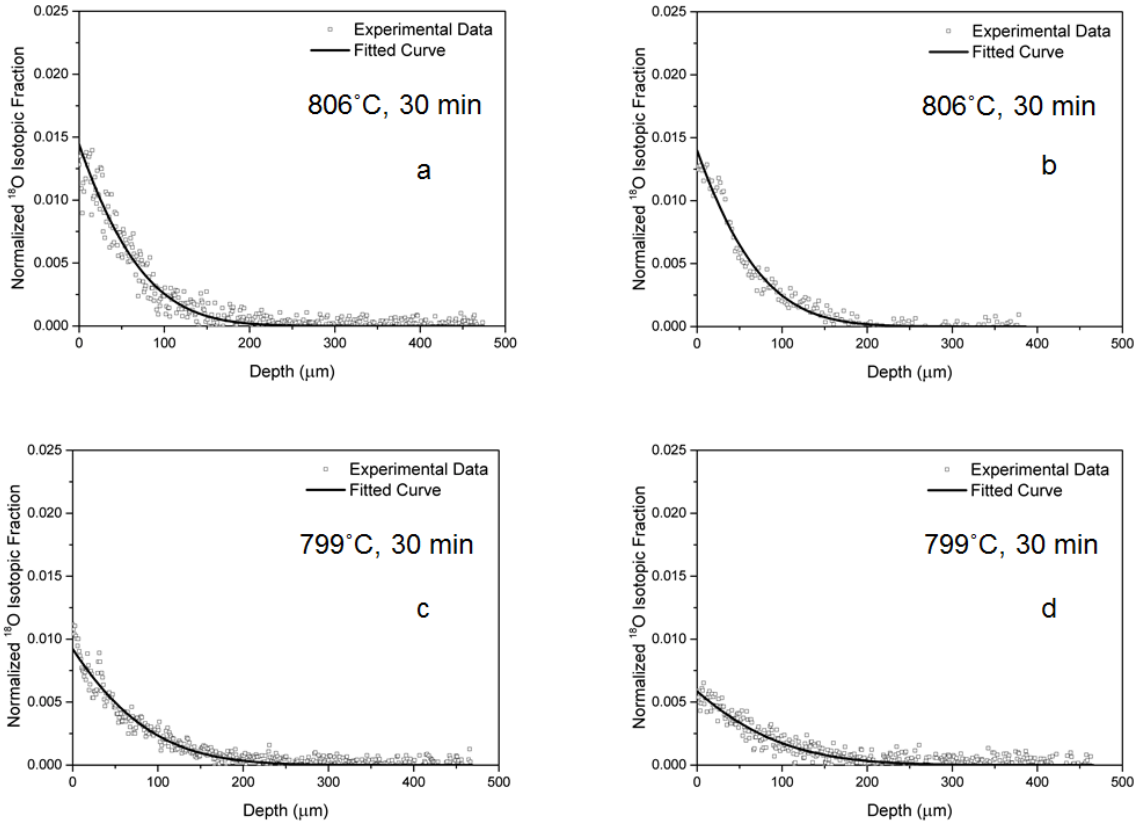

Figure 6.4: Normalized isotopic fraction depth profiles of 1Ce10ScSZ/LSCrF8255 dual-phase membrane before and after aging at 1000˚C for 300 hours. Legend: a) unaged; b) aged in air; c) aged in 4% H_2-96% N_2; d) aged in 5% H_2-95% CO_2. Samples were annealed in ^{18}O environment (pO_2 = 200 mbar) at ~800˚C for 30 minutes after equilibrating in ^{16}O environment at the same temperature and pO_2 for 5 hours.

The surface exchange coefficients k^* of 1Ce10ScSZ/LSCrF8255 were calculated from the fitted diffusion profile to be 3.6 (±0.5) x 10^{-8} cm^2 s^{-1} for the unaged sample, 4.5 (±0.4) x 10^{-8} cm^2 s^{-1} for the sample aged in air at 1000˚C for 300 hours, 4.7 (±0.4) x 10^{-8} cm^2 s^{-1} for the sample aged in reducing 4% H_2-96% N_2 at 1000˚C for 300 hours, and 2.5 (±0.5) x 10^{-8} cm^2 s^{-1} for the sample aged in reducing 5% H_2-95% CO_2 at 1000˚C for 300 hours. As with the self-diffusion coefficients, the effect of aging on 1Ce10ScSZ/LSCrF8255 was not observed to significantly influence oxygen surface exchange kinetics, with all k^* values remaining on the order of 10^{-8} cm s^{-1} compared to the unaged sample. Like D^*, k^* of the

dual-phase 1Ce10ScSZ/LSCrF8255 does not appear to be significantly affected by exposure to the selected aging environments at elevated temperatures over this length of time.

Table 6-1: Oxygen transport kinetic parameters extracted from fitted curve of diffusion profile for 1Ce10ScSZ/LSCrF8255 dual-phase membrane before and after aging (300 hrs). Samples were annealed in ^{18}O environment (200 mbar, 800˚C) for 30 minutes after equilibrating in ^{16}O environment at the same temperature and pO_2 for 5 hours.

	Oxygen self-diffusion coefficient, D* ($cm^2\ s^{-1}$)	Oxygen surface exchange coefficient, k* ($cm\ s^{-1}$)
Unaged	3.5 (±0.3) x 10^{-8}	3.6 (±0.5) x 10^{-8}
Aged (1000˚C, 300 h, air)	2.3 (±0.3) x 10^{-8}	4.5 (±0.4) x 10^{-8}
Aged (1000˚C, 300 h, 4% H_2-96% N_2)	2.4 (±0.3) x 10^{-8}	4.7 (±0.4) x 10^{-8}
Aged (1000˚C, 300 h, 5% H_2-95% CO_2)	4.2 (±0.3) x 10^{-8}	2.5 (±0.5) x 10^{-8}

It is known that 1Ce10ScSZ, which primarily functions as the oxygen ion conductor in the dual-phase material, possesses comparatively low oxygen incorporation to the point that steps to catalyze the surface were required to analyze the transport kinetics (see Section 5.1.2.2). In contrast, isotope exchange experiments on LSCrF8255 performed by Shen [14] showed that the material exhibits very high oxygen surface exchange kinetics, achieving near-full saturation of ^{18}O (i.e. 100% normalized isotopic fraction) at the surface, but low diffusion kinetics. This suggests that LSCrF8255 serves two primary functions in the dual-phase membrane: the first as an electronic conductor, and the second as the preferred phase for oxygen incorporation into the material.

It was observed in the aged samples that a decrease in D^* occurred in conjunction with an increase in k^* when compared to the unaged sample. The samples exposed to air and 4% H_2-96% N_2 atmosphere exhibited this phenomenon, with the sample exposed to 5% H_2-95% CO_2 atmosphere exhibited the opposite effect (increased D^*, decreased k^*). However, low oxygen tracer incorporation of dual-phase 1Ce10ScSZ/LSCrF8255 was observed regardless of exposure to aging conditions. Normalized ^{18}O isotopic fraction

near the surface of the material was observed to be ~1% above the background fraction for all four samples, with the elevated isotopic fraction varying very slightly between samples.

No correlation was observed between the formation of the $SrCrO_4$ secondary phase in the samples aged in air and in 5% H_2-95% CO_2 atmosphere, and their corresponding oxygen transport kinetics, which suggests that the presence of this phase has negligible effect on the oxygen transport kinetics of the material. It is possible, however, under longer aging durations in these environments, that secondary phases not limited to the one observed continue to evolve, contributing to the degradation of the material.

6.1.2.2 IEDP-SIMS Summary

The effects of aging on the oxygen transport kinetics of dual-phase 1Ce10ScSZ/LSCrF8255 were examined. The self-diffusion and surface exchange coefficients were all found to be on the order of 10^{-8} cm^2 s^{-1} and 10^{-8} cm s^{-1} respectively. The effects of aging in air, 4% H_2-96% N_2 and 5% H_2-95% CO_2 at 1000˚C for 300 hours on the oxygen transport kinetics were observed to be minimal. Low incorporation of elevated ^{18}O isotopic fraction was observed, similar to that observed for single-phase 1Ce10ScSZ, which suggests the elevated presence of this component on the surface.

6.1.3 Surface Chemistry

The surface chemistry of dual-phase 1Ce10ScSZ/LSCrF8255 was examined using Low Energy Ion Scattering and X-ray Photoelectron Spectroscopy. As with the surface analysis for the single-phase components, the techniques were employed in tandem to ascertain the surface chemical composition of the material, with LEIS examining the chemistry of the outer atomic surface and XPS allowing a semi-quantitative analysis of the near-surface (~10 nm).

6.1.3.1 Low Energy Ion Scattering – Outer Atomic Surface Chemistry

The outer atomic surface of dual-phase 1Ce10ScSZ/LSCrF8255 was first examined via Low Energy Ion Scattering using a $^4He^+$ 3 keV primary ion, with sputtering dose densities (1 keV $^{40}Ar^+$) up to 10.0 x 10^{15} ions cm^{-2} applied to the analysis area. The LEIS spectrum generated is shown in Figure 6.5. In contrast to the single-phase samples, where samples were polished prior to LEIS analysis, the sample surface of all four dual-phase samples was unmodified. This was to preserve the effects of aging on the surface chemical composition of the materials. The sample was wrapped in Al foil used to protect the sample surface from contamination.

As with the single-phase components, the LEIS signal generated from the low energy $^{4}He^{+}$ ions was obscured by the presence of a carbon-based layer [15], which upon removal via sputtering, reveals peak signals representing the material surface. At first glance, all relevant peak signals are present on the outer atomic surface, but the convolution of multiple peak signals as a result of inadequate energy resolution makes it difficult to verify this.

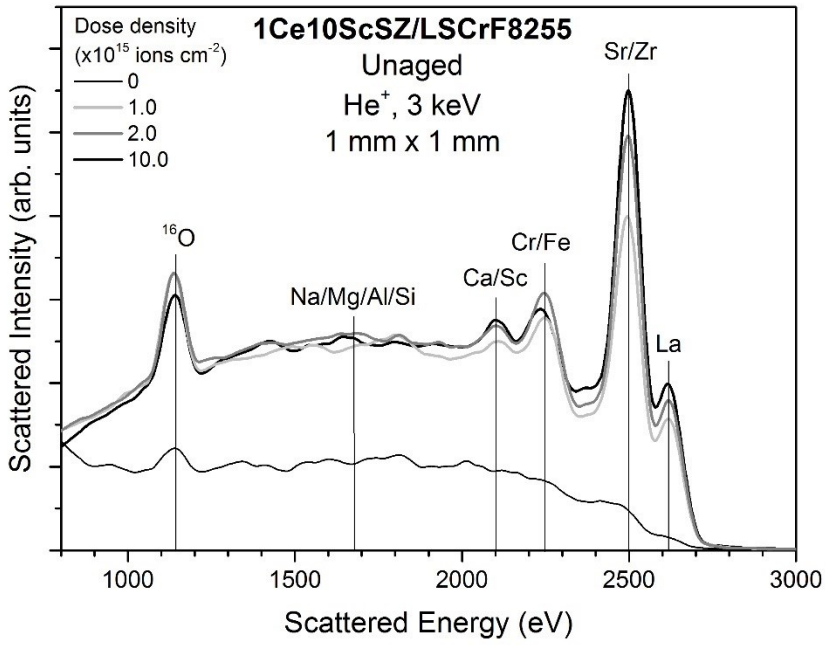

Figure 6.5: LEIS spectrum ($^{4}He^{+}$, 3 keV) of 1Ce10ScSZ/LSCrF8255. Sputter dose densities up to 10.0 x 10^{15} ions cm^{-2} using a sputter beam ($^{40}Ar^{+}$, 1 keV) were applied to the analysis area. All element peak signals appear to be present, but significant convolution of peak signals complicates further analysis. Na/Mg/Al/Si impurities on the outer surface appear to be reduced in presence for 1Ce10ScSZ/LSCrF8255 compared to its two single-phase constituents. Vertical lines are added to guide the eye.

The presence of Na/Mg/Al/Si impurities on the outer surface of the dual-phase material was compared to that for the single-phase components. The peak intensity of the impurity Na/Mg/Al/Si signals for dual-phase 1Ce10ScSZ/LSCrF8255 shown in Figure 6.5 appears to be lower than the single-phase components, summarized in Figure 6.6. The absence of these impurities can be attributed to the dissolution of Na/Mg/Al/Si oxides into the perovskite LSCrF8255 lattice, which improves the oxygen surface exchange kinetics of the 1Ce10ScSZ component [16].

Peak deconvolution was performed using $^{20}Ne^+$ 5 keV primary ions for analysis. The examination was performed on a fresh surface from the previous area. For this analysis, no sputtering was performed on the surface. Instead, the measurement was kept running until the dose density of the primary ions on the surface reached 1 x 10^{15} ions cm^{-2}, the estimated dose required to displace one atomic layer of the sample surface. The process was repeated for the three 1Ce10ScSZ/LSCrF8255 aged samples. The LEIS spectra of the first and last analysis points (at 0 and 1.0 x 10^{15} ions cm^{-2}) of all four samples is compiled and summarized in Figure 6.7. The background signal of the $^{20}Ne^+$ ions, which is the result of the detection of charged secondary ions ejected from the sample during analysis, was subtracted from the spectra.

The Sr/Zr peak signal on dual-phase 1Ce10ScSZ/LSCrF8255 in Figure 6.5 can be compared to the Zr signal and Sr signal on single-phase 1Ce10ScSZ and LSCrF8255 respectively, shown in Figure 6.6. The evolution of the Sr/Zr peak intensity in Figure 6.5 is in closer agreement with the Zr peak signal observed in 1Ce10ScSZ than the Sr peak signal observed in LSCrF8255 after sputter dose densities up to 2.0 x 10^{15} ions cm^{-2} were applied, exhibiting a more gradual increase in peak intensity between 1.0 and 2.0 x 10^{15} ions cm^{-2}. In addition, the Ca/Sc peak in 1Ce10ScSZ/LSCrF8255 also exhibits increasing peak intensity after sputtering, which was not observed in the Ca peak in single-phase LSCrF8255.

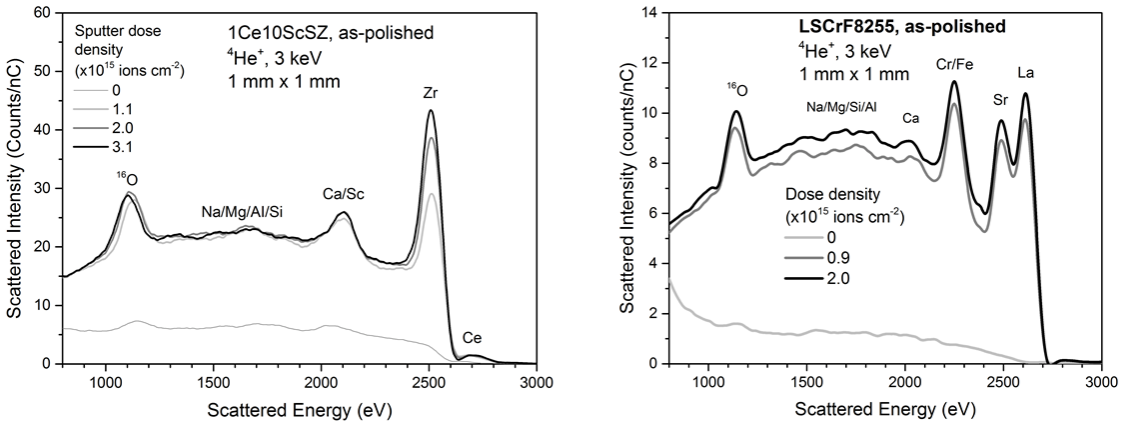

Figure 6.6: Comparison of $^4He^+$ LEIS spectra for single-phase 1Ce10ScSZ and LSCrF8255.

LEIS analysis of the outer surface of unaged 1Ce10ScSZ/LSCrF8255 showed lower presence of Na/Mg/Al/Si impurities than either single-phase component, which is attributed to a surface cleaning mechanism where the impurities are incorporated into the perovskite LSCrF8255 lattice and disappear from the outer surface. This was observed

by Shen [14] on a sample of single-phase 1Ce10ScSZ and LSCrF8255 which were fused together by heat treatment. The surface of the 1Ce10ScSZ phase on this sample after isotope exchange in $^{18}O_2$ at 900˚C for 1 hour was examined via LEIS ($^4He^+$, 3 keV) and compared to single-phase 1Ce10ScSZ exposed to the same conditions. The LEIS spectrum showed a Na/Mg/Al/Si peak in single-phase 1Ce10ScSZ but no such peak in the fused 1Ce10ScSZ/LSCrF8255 sample, suggesting the presence of the LSCrF8255 component in the dual-phase material aids in the removal of these impurities from the surface. It is expected that the removal of these impurities from the surface of dual-phase 1Ce10ScSZ/LSCrF8255 improves the overall surface exchange kinetics of the material.

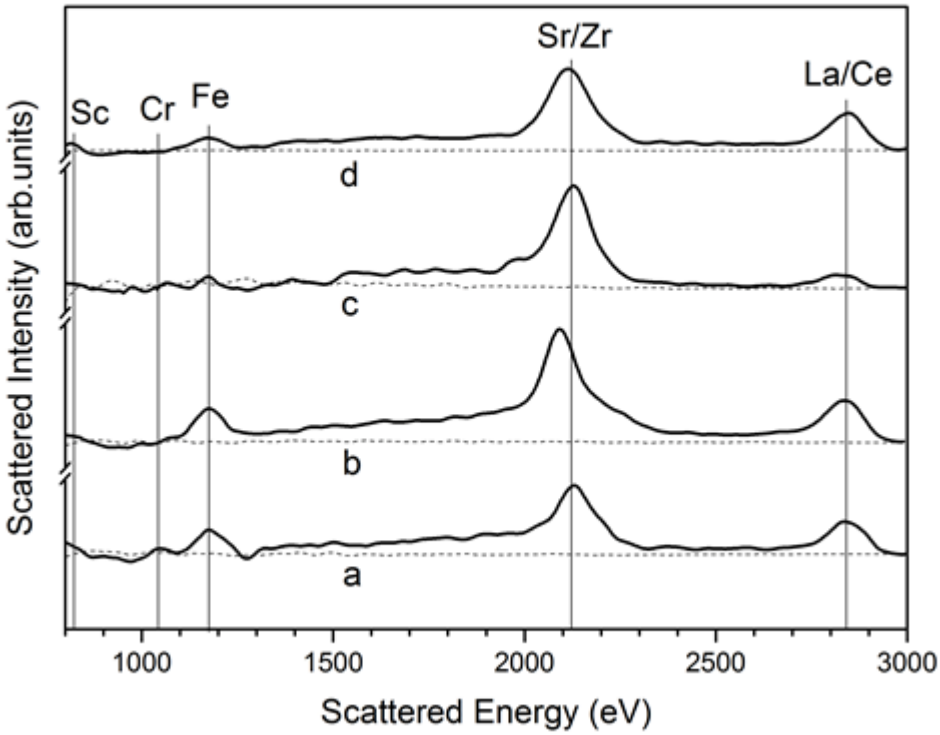

Figure 6.7: LEIS spectra ($^{20}Ne^+$, 5 keV) of 1Ce10ScSZ/LSCrF8255 before and after aging for 1000˚C for 300 hours. From bottom to top: a) unaged; b) aged in air; c) aged in 4% H_2-96% N_2; d) aged in 5% H_2-95% CO_2. Dotted line represents initial measurement; solid line represents measurement performed after primary ion dose density of $1x10^{15}$ ions cm^{-2} was reached. Vertical lines are added to guide the eye.

The deconvolution of Cr and Fe in the LEIS spectra using 5 keV $^{20}Ne^+$ ions shown in Figure 6.7 shows the absence of Cr on the outer atomic surface of 1Ce10ScSZ/LSCrF8255. This is in agreement with the surface chemical analysis of the single-phase LSCrF8255

component detailed in Section 5.2.2.1. The effect of Cr deficiency was outlined in Section 5.2.2.1 in that the outer surface of single-phase LSCrF8255 is likely to be lanthanum strontium ferrite, possessing higher oxygen kinetic activity but lower mechanical and chemical stability. In addition, the presence of Fe on the outer atomic surface also appears to be deficient for the materials aged in 4% H_2-96% N_2 (Figure 6.7c) and 5% H_2-95% CO_2 (Figure 6.7d) compared to the unaged material (Figure 6.7a) and the material aged in air (Figure 6.7b). This suggests that the Fe content on the outer surface may be diminished under reducing conditions. However, it is premature to attribute the aging conditions under reducing environments as the cause of the depleted Fe signal observed on the outer surface of the dual-phase samples.

The depletion of all peak signals except for Sr/Zr for dual-phase 1Ce10ScSZ/LSCrF8255 aged in 4% H_2-96% N_2 for 300 hours (Figure 6.7c) suggests one of two possibilities. On the one hand, the Sr/Zr peak is comprised predominately of the Zr element, which would imply that the 1Ce10ScSZ phase is prevalent on the outer surface. On the other hand, the Sr/Zr peak is comprised mainly of the Sr element, caused by strong Sr segregation covering the rest of the material. In both cases, this would likely result in significantly reduced oxygen surface exchange in the material.

The Sr/Zr peak shape for the material aged in air (Figure 6.7b) may indicate Sr segregation, although without higher energy resolution to deconvolute the two signals, it is not possible to confirm this claim. Attempts to deconvolute the Sr/Zr and La/Ce peaks using the highest energy resolution offered by the Qtac LEIS instrument ($^{40}Ar^+$ primary ion, 10 keV) were unsuccessful. Using these analysis settings, it is calculated from the SurfaceLab 6 analysis software developed by ION-TOF GmbH (Münster, Germany) that the peak signal for the natural isotopes of Sr and Zr (^{87}Sr, ^{89}Zr) would be approximately 1662 and 1741 eV respectively. Deconvolution of the La/Ce peak was also unsuccessful as, the peak signals for the natural isotopes of La and Ce (^{139}La, ^{140}Ce) appear at 3398 and 3426 eV respectively, with full deconvolution of peaks roughly achieved at a peak separation of ~100 eV. However, it is expected that the peak signal comprises mainly the element La due to the comparatively low concentration of Ce in the ideal bulk stoichiometry of 1Ce10ScSZ/LSCrF8255. However, since the presence of Ce was observed on the outer surface for single-phase 1Ce10ScSZ (Figure 5.6, Chapter 5), it cannot be ruled out that a minor Ce peak signal could be present in a convoluted La/Ce LEIS peak signal.

6.1.3.2 LEIS Summary

The surface chemical composition of the outer atomic surface of dual-phase 1Ce10ScSZ/LSCrF8255 was examined before and after aging at 1000°C for 300 hours. The presence of Na/Mg/Al/Si impurities on the outer surface was reduced compared to its

single-phase constituents likely as a result of a surface cleaning mechanism where the impurities are dissolved into the LSCrF8255 phase. Peak evolution of the signal of the unaged 1Ce10ScSZ/LSCrF8255 sample suggests that the outer surface layer was comprised of an elevated surface fraction of 1Ce10ScSZ. All relevant elements appear to be on the outer atomic layer of the material, but due to multiple peak convolutions, it is unclear whether this is the case. It was not possible to deconvolute the Sr/Zr or La/Ce peaks using the current instrument setup.

Deconvolution of the Cr and Fe peaks shows that Cr is absent on the surface of dual-phase 1Ce10ScSZ/LSCrF8255 before and after aging for 300 hours. In addition, the Fe signal is depressed in the samples aged in 4% H_2-96% N_2 and 5% H_2-95% CO_2. A hypothesis suggesting a tendency for the element to avoid the outer surface under reducing conditions was made. Finally, possible Sr segregation was observed on the air-aged sample, but could not be clearly determined due to the inability to adequately deconvolute the Sr/Zr peak signal.

6.1.3.3 X-ray Photoelectron Spectroscopy – Near-Surface Chemistry and Quantification

The X-ray photoelectron survey spectra of dual-phase 1Ce10ScSZ/LSCrF8255 before and after aging for 300 hours in the three conditions (air, 4% H_2-96% N_2 and 5% H_2-95% CO_2) are shown in Figure 6.8. As with the LEIS analysis in the preceding section, the surface was unmodified after sintering and aging prior to XPS examination.

The XPS survey spectra show at first glance the presence of all relevant elements within ~10 nm of the surface of the dual-phase 1Ce10ScSZ/LSCrF8255 before and after aging for 300 hours. It was observed that the sample aged in 4% H_2-96% N_2 at 1000˚C for 300 h (Sample c) exhibited a decrease in Sr content at the near-surface. This is consistent with the hypothesis made in Section 5.2.2.2 that exposure to reducing conditions causes Sr depletion on the outer surface of single-phase LSCrF8255. However, it was observed that the Sr content was not significantly diminished for the dual-phase material exposed to 5% H_2-95% CO_2, for which the same aging conditions caused the depletion of Sr in single-phase LSCrF8255. The oxygen partial pressure of the 4% H_2-96% N_2 environment was calculated to be approximately seven orders of magnitude lower than for 5% H_2-95% CO_2 ($pO_2 \sim 10^{-18}$ atm vs $pO_2 \sim 10^{-11}$ atm). This phenomenon could be attributed to the presence of the 1Ce10ScSZ component in discouraging Sr surface segregation of the LSCrF8255 component in the dual-phase material under reducing conditions.

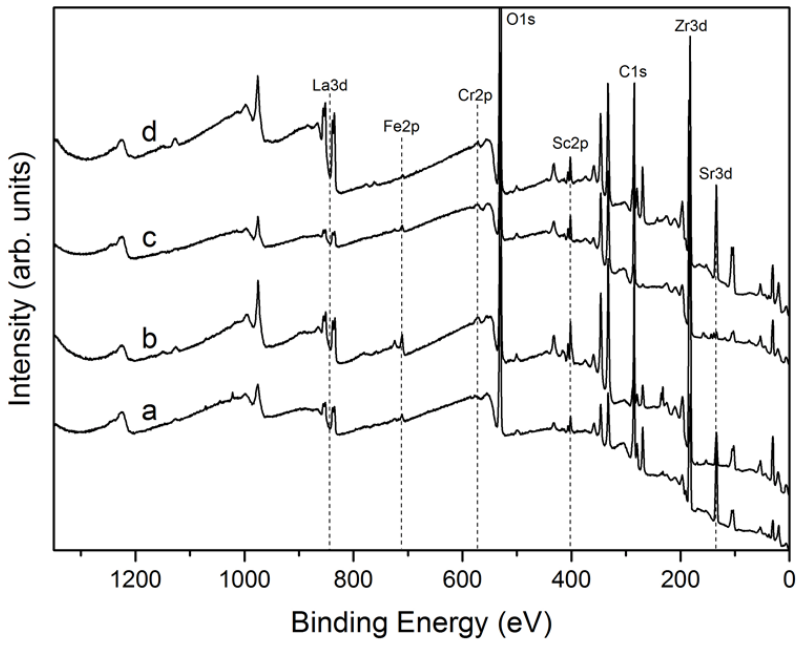

Figure 6.8: X-ray Photoelectron Survey Spectra of 1Ce10ScSZ/LSCrF8255 dual-phase membrane. From bottom to top: a) unaged; b) aged in air at 1000˚C for 300 hours; c) aged in 4% H_2-96 %N_2 at 1000˚C for 300 hours; d) aged in 5% H_2-95% CO_2 at 1000˚C for 300 hours. Dotted lines are included to facilitate viewing.

Wei et. al. [6] observed a similar phenomenon in YSZ/$La_{0.8}Sr_{0.2}Cr_{0.5}Fe_{0.5}O_{3-\delta}$ (YSZ composition not specified), in which the degradation was seen in single-phase LSCrF8255 but not in dual-phase YSZ/LSCrF8255. They speculated that the transport processes of LSCrF8255 operating as a standalone material differs from LSCrF8255 as a component in a dual-phase material. As a single phase, LSCrF8255 undergoes both ionic and electronic conduction, but as a component in a dual-phase material, where the other component is primarily an oxide ion conductor, LSCrF8255 would function primarily as the electronic conductor [6]. Mixed conduction in the single-phase LSCrF8255 was hypothesized to induce severe stress on the crystal lattice, which could lead to accelerated degradation.

Figure 6.9 to Figure 6.15 show high-resolution X-ray photoelectron spectra of the component elements of dual-phase 1Ce10ScSZ/LSCrF8255 before and after aging for 300 hours. XPS spectra were taken for the Zr 3d, Sc 2p, La 3d, Sr 3d, Cr 2p and Fe 2p peak signals. Peak signals for the Ce 4d peak was not detected in any of the high-resolution spectra, and was omitted. The relative concentration of the elements comprising the dual-phase membrane before and after aging were calculated by determining the

intensity of the peaks and factoring in the relative sensitivity factor of each element, and is summarized in Figure 6.16.

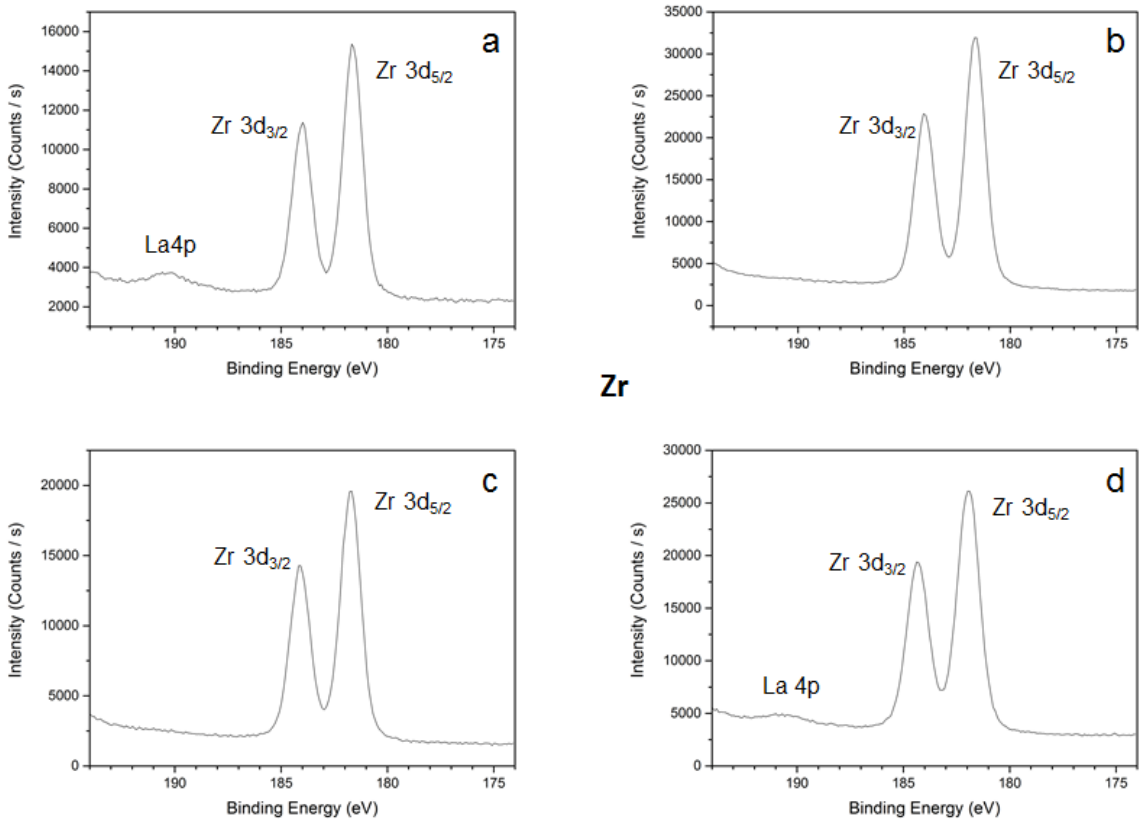

Figure 6.9: Zr $3d_{3/2}$ and Zr $3d_{5/2}$ peaks from high-resolution XPS measurement of 1Ce10ScSZ/LSCrF8255 dual-phase membrane. Legend: a) unaged; b) aged in air at 1000˚C for 300 h; c) aged in 4% H_2-96% N_2 at 1000˚C for 300 h; d) aged in 5% H_2-95% CO_2 at 1000˚C for 300 h. No effects were observed after aging. A peak at ~191 eV binding energy denoting the La 4p signal was observed in Samples a and d. Minimal changes in the peak shape and position were observed after aging for 300 hours.

The peak signals for Zr $3d_{3/2}$ and Zr $3d_{5/2}$ shown in Figure 6.9 show minimal change in shape or position after aging for 300 hours. The shape and position of the peaks indicates that Zr in the dual-phase material exists as an oxide, likely to be ZrO_2, with no presence of Zr metal (BE ~ 179 eV) or sub-oxide ZrO (BE ~ 180 eV) observed within ~10 nm of the surface. The La 4p peak signal was also observed in the XPS spectra for the unaged sample (Figure 6.9a) and the sample aged in 5% H_2-95% CO_2 (Figure 6.9d).

The peak signals for Sc $2p_{1/2}$ and Sc $2p_{3/2}$ shown in Figure 6.10 also show no change in shape and position. The Sc $2p_{3/2}$ peak position was observed to be at BE ~ 402 eV,

corresponding to the peak signal for Sc_2O_3 [17]. The absence of Sc $2p_{3/2}$ peak signals at BE ~ 398 eV and BE ~ 403 eV suggests that metallic Sc or hydrated ScOOH is not present within the near-surface [17]. A N 1s peak was observed on the sample aged in air (Sample b) which may have been an environmental contaminant introduced in the near-surface prior to analysis. Nitrogen could also be introduced as a result of exposure to high concentration of N_2 in air at elevated temperatures, but this was not observed on the sample aged in 4% H_2-96% N_2 (Sample c).

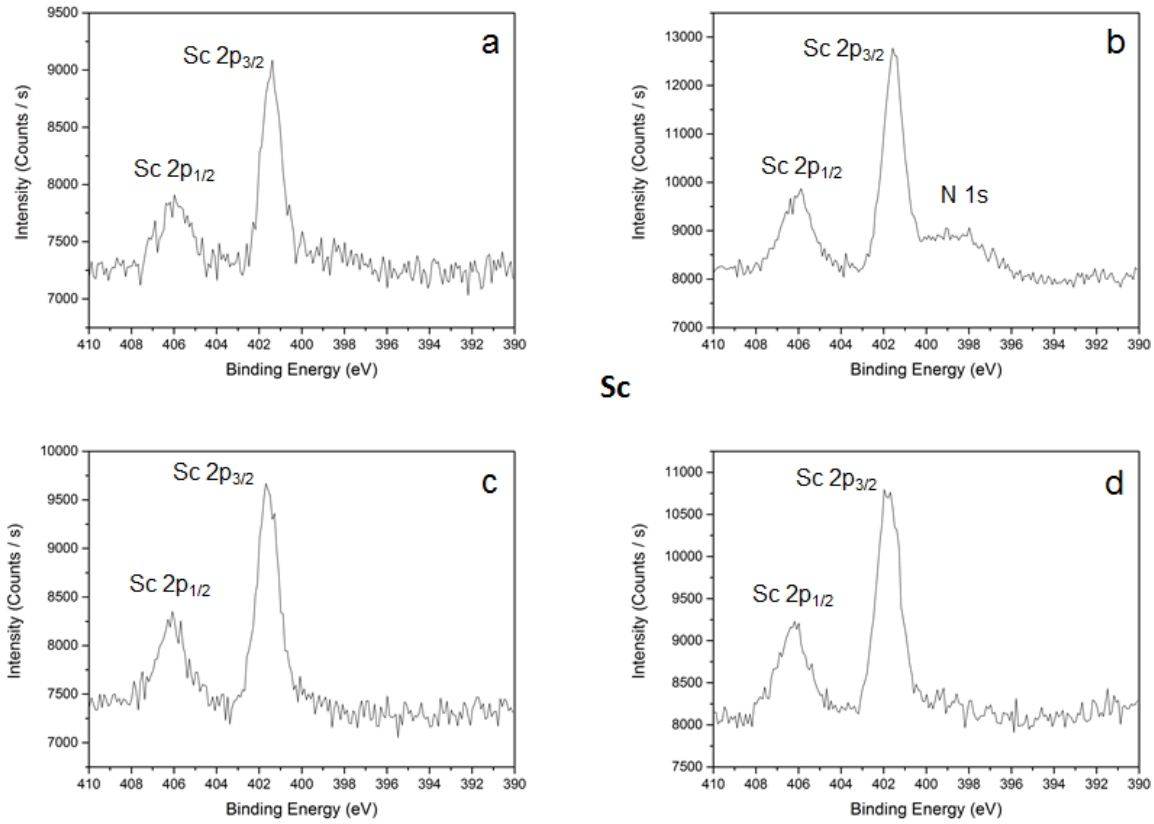

Figure 6.10: Sc $2p_{1/2}$ and Sc $2p_{3/2}$ peaks from high-resolution XPS measurement of 1Ce10ScSZ/LSCrF8255 dual-phase membrane. Legend: a) unaged; b) aged in air at 1000°C for 300 h; c) aged in 4% H_2-96% N_2 at 1000°C for 300 h; d) aged in 5% H_2-95% CO_2 at 1000°C for 300 h. Minimal effects were observed after aging.

The peak signals for La $3d_{3/2}$ and La $3d_{5/2}$ shown in Figure 6.11 exhibit multiplet splitting due to the interaction of unpaired 3d electrons in the La atom with core 2p electrons [18]. In addition to the shape and position of the peak, the difference in binding energy of a multiplet peak can provide information on the nature of the compound in the near-surface region of the specimen. In this case, the difference in binding energy between the two peaks comprising the La $3d_{5/2}$ peak in Figure 6.11 is ~3.9 eV for all four samples,

suggesting that the La compound that is predominant in the near-surface of dual-phase 1Ce10ScSZ/LSCrF8255 is lanthanum hydroxide, $La(OH)_3$ [19]. The shape of the peak also suggests the presence of $La(OH)_3$ in the near-surface [19]. Lanthanum oxide La_2O_3 reacts readily and spontaneously with water vapor at room temperature to form $La(OH)_3$.

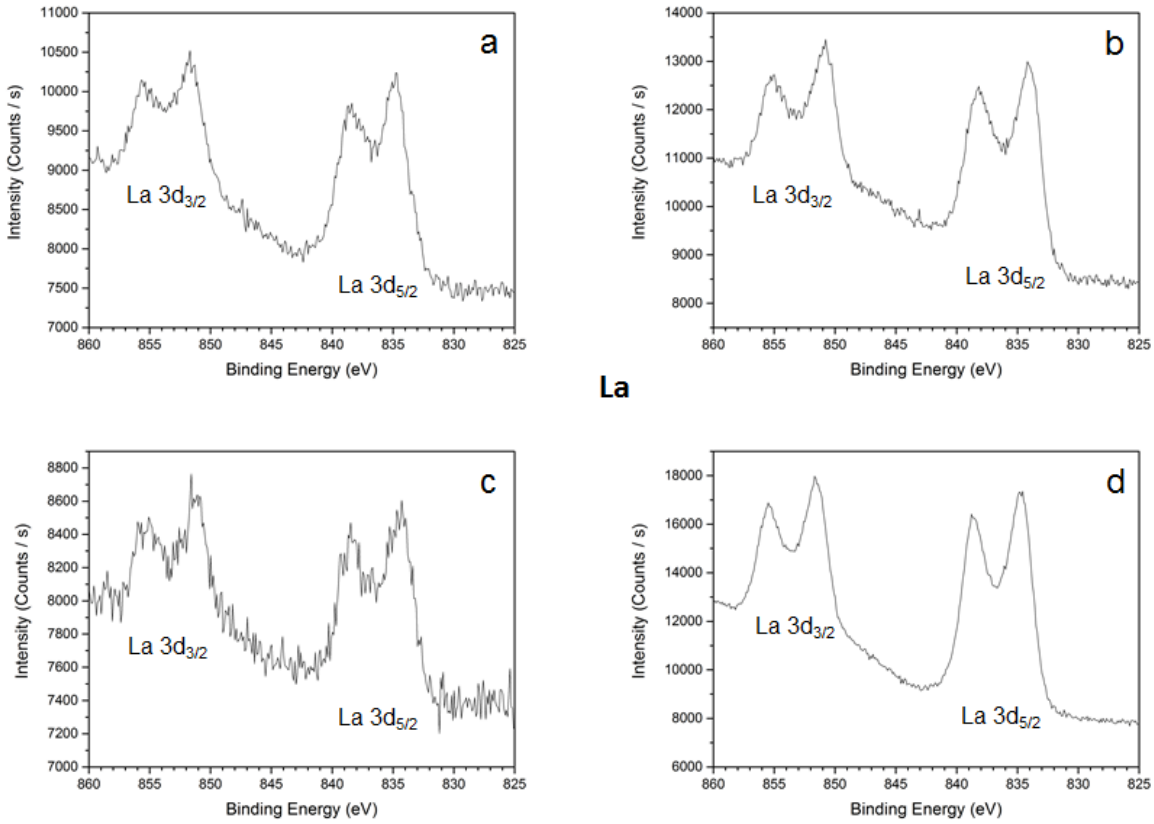

Figure 6.11: La $3d_{3/2}$ and La $3d_{5/2}$ peaks from high-resolution XPS measurement of 1Ce10ScSZ/LSCrF8255 dual-phase membrane. Legend: a) unaged; b) aged in air at 1000°C for 300 h; c) aged in 4% H_2-96% N_2 at 1000°C for 300 h; d) aged in 5% H_2-95% CO_2 at 1000°C for 300 h. The peak shape and the magnitude of multiplet splitting for the La $3d_{5/2}$ peak suggests that La exists in hydroxide form $La(OH)_3$ on the near-surface of 1Ce10ScSZ/LSCrF8255 [19] regardless of aging conditions.

However, lanthanum hydroxide decays into lanthanum oxyhydroxide, LaOOH, at temperatures above 330°C which then decomposes into lanthanum oxide La_2O_3 upon further heating [20]. Therefore, exposure to ambient air over prolonged periods, i.e. during transport and storage prior to XPS analysis, may cause La on the surface to exist purely in hydroxide form. However, it is expected that under operating conditions at elevated temperatures (1000°C) that lanthanum adopts the oxide compound in the dual-phase material.

Determining the relative concentrations of La_2O_3 and $La(OH)_3$ on the near-surface via XPS is challenging, as the peak shapes are very similar. In addition, the analysis of the La satellite peak signals such as La 4f, La 5s, and La 5p in conjunction with the main La 3d signal is necessary to clarify the presence of each compound in the material. The counting statistics of the satellite peaks was too low in the experiment performed here to allow this comparison to be made; only the presence of the La 4p coincidentally detected near the high-resolution Zr scan seen in Figure 6.9.

The effects of the material's transport kinetics as a result of the presence of lanthanum hydroxide on the near-surface of 1Ce10ScSZ/LSCrF8255 is unclear. Sakai et. al. [21] notes that in strontium-doped lanthanum chromite materials, the stability of Sr^{2+} ions in the perovskite structure is higher than that of La^{3+} ions, resulting in the precipitation of lanthanum oxide being favored over strontium oxide. It is implied in the work of Sakai et. al. [21] that this phenomenon exists in the bulk material. However, if lanthanum oxide precipitation occurs at the near-surface, it may react with water vapor in the ambient environment, forming $La(OH)_3$. Degradation of the dual-phase material is accelerated with $La(OH)_3$ due to the accompaniment of a volume change with the formation of this phase. The material may attempt to counterbalance the volume change through the migration of species or by the adoption of B-site cations towards a preferred oxidation state. In the worst case, the volume change may facilitate the delamination of LSCrF8255 with 1Ce10ScSZ in the dual-phase material leading to de-coupling of the two phases and ultimately failure of the membrane.

The peak signals for Sr $3d_{3/2}$ and Sr $3d_{5/2}$ shown in Figure 6.12 show a deficiency of Sr signal in the sample aged in 4% H_2-96% N_2 (Sample c) compared to the other samples. Zn impurity was also observed in the sample aged in 4% H_2-96% N_2. Sr deficiency in reducing conditions as observed in Sample c is consistent with the hypothesis made in Section 5.2.2.2 that exposure of LSCrF8255 to reducing conditions inhibits Sr surface segregation. However, it is unclear why this phenomenon was not observed in the sample aged in 5% H_2-95% CO_2 (Sample d).

The reaction of SrO in CO_2 atmosphere may result in the formation of $SrCO_3$ on the material surface. This is of particular concern for the sample aged in 5% H_2-95% CO_2 (Sample d). Peak fitting of the Sr $3d_{3/2}$ and Sr $3d_{5/2}$ peaks performed via CasaXPS software to the experimental data of Sample d in Figure 6.12, shown in Figure 6.13, showed a good fit when one of the two Sr compounds, either SrO or $SrCO_3$, was presumed to be present on the near-surface. Peak fits performed on Samples a and b of Figure 6.12 produced similar results. A peak fit was not performed on Sample c due to poor counting statistics.

A Zn peak signal was observed for Sample c, which may have been introduced as a surface contaminant prior to analysis.

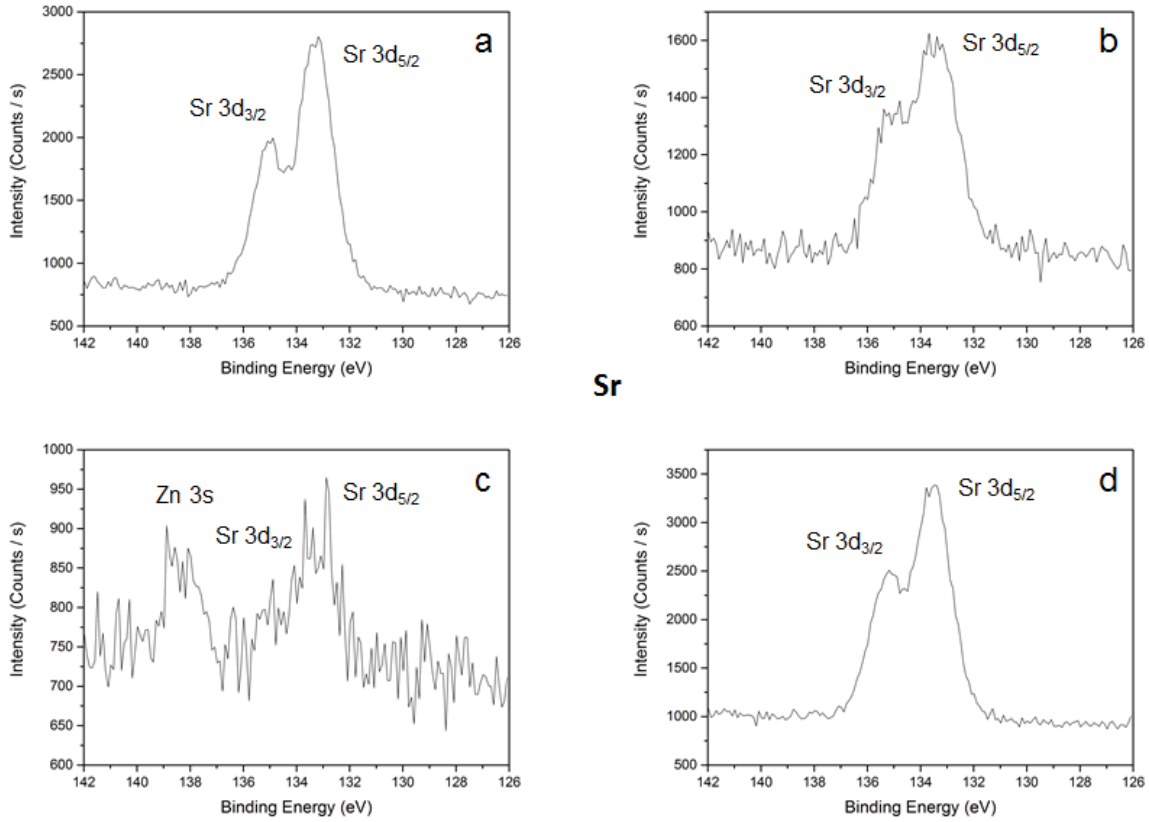

Figure 6.12: Sr $3d_{3/2}$ and Sr $3d_{5/2}$ peaks from high-resolution XPS measurement of 1Ce10ScSZ/LSCrF8255 dual-phase membrane. Legend: a) unaged; b) aged in air at 1000˚C for 300 h; c) aged in 4%H_2-96%N_2 at 1000˚C for 300 h; d) aged in 5%H_2-95%CO_2 at 1000˚C for 300 h. The Sr peak signal is significantly reduced when exposed to 4%H_2-96%N_2 (Sample c), with a Zn impurity peak also observed.

The peak fit of Sr $3d_{3/2}$ and Sr $3d_{5/2}$ peaks for both $SrCO_3$ and SrO did not generate an appropriate fit to any of the experimental data, suggesting that the presence of both strontium compounds on the near-surface of the dual-phase material is unlikely. The single Sr compound present in the near-surface of dual-phase 1Ce10ScSZ/LSCrF8255 appears to be $SrCO_3$, evidenced by the peak position of the Sr $3d_{5/2}$ peak at 133.4 eV [19]. It is known that SrO reacts readily with CO_2 present in ambient conditions to form $SrCO_3$. The presence of $SrCO_3$ acts as an insulating layer for the oxygen reduction reaction at the surface [22], and would have a detrimental effect on the oxygen transport of dual-phase 1Ce10ScSZ/LSCrF8255.

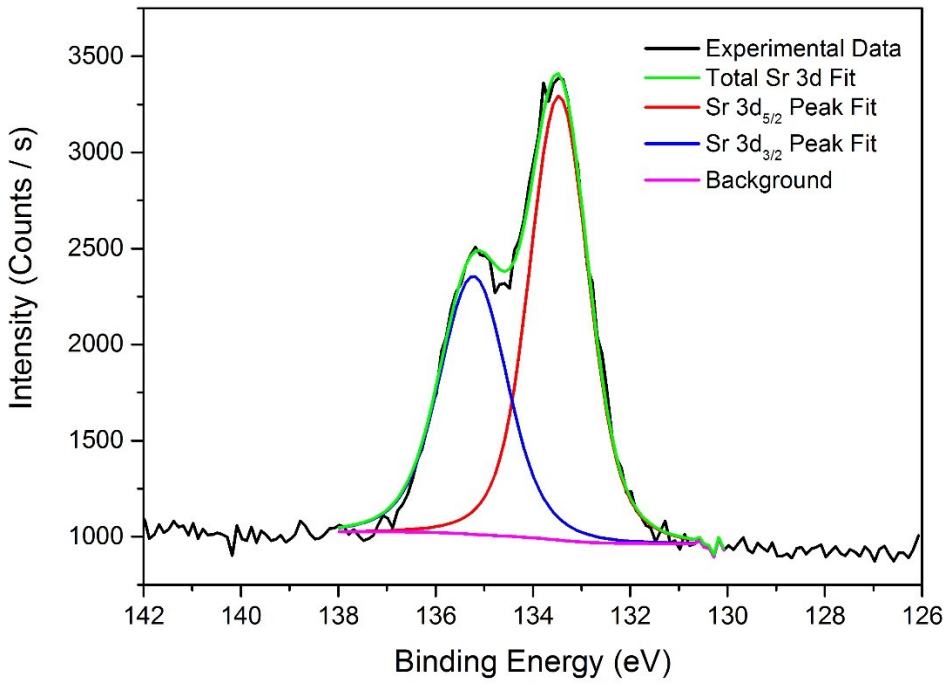

Figure 6.13: Sr 3d peak fit for 1Ce10ScSZ/LSCrF8255 aged in in 5%H_2-95%CO_2 at 1000°C for 300 h (Figure 6.12, Sample d). The presence of a single Sr compound on the near-surface of the dual-phase material is more likely than the presence of two compounds due to the accuracy of the peak fit. The compound present was identified to be $SrCO_3$ due to the position of the Sr $3d_{5/2}$ peak at 133.4 eV [19].

The peak signals for Cr $2p_{1/2}$ and Cr $2p_{3/2}$ shown in Figure 6.14 were observed to be mostly absent from high-resolution XPS scans. This is consistent with the absence of Cr observed on the outer surface of dual-phase 1Ce10ScSZ/LSCrF8255 as examined by LEIS outlined in Section 6.1.3.1. The LEIS and XPS results together show Cr is depleted in the surface region of dual-phase 1Ce10ScSZ/LSCrF8255. Due to the low signal-to-noise ratio of the high-resolution XPS scan, it was not possible to determine the oxidation state of Cr in the LSCrF8255 component of the dual-phase material. Peak signals for the Cr $2p_{1/2}$ and Cr $2p_{3/2}$ peaks of Cr_2O_3 exist at BE ~ 584 eV and BE ~ 575 eV respectively, shown with vertical lines in Figure 6.14.

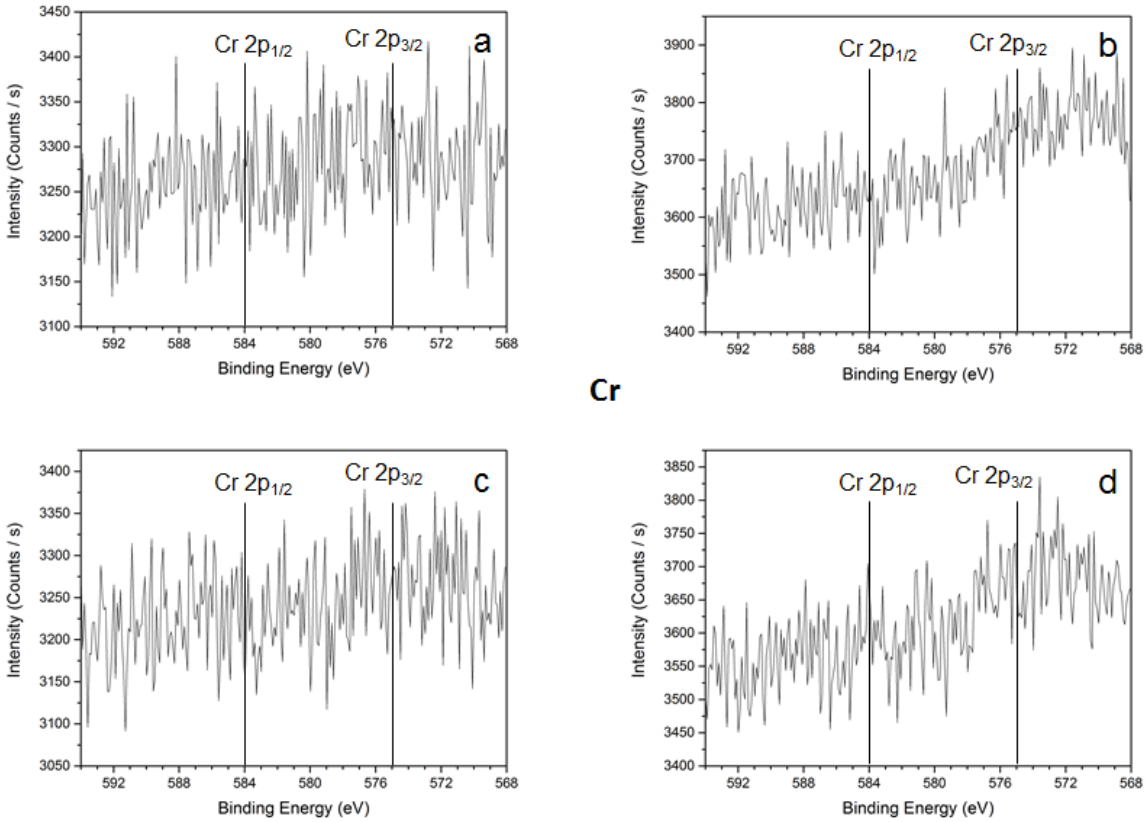

Figure 6.14: Cr $2p_{1/2}$ and Cr $2p_{3/2}$ peaks from high-resolution XPS measurement of 1Ce10ScSZ/LSCrF8255 dual-phase membrane. Legend: a) unaged; b) aged in air at 1000˚C for 300 h; c) aged in 4% H_2-96% N_2 at 1000˚C for 300 h; d) aged in 5% H_2-95% CO_2 at 1000˚C for 300 h. Vertical lines denote expected peak positions of the Cr $2p_{1/2}$ and Cr $2p_{3/2}$ signals for Cr (III) oxide [23].

As was mentioned in Chapter 5, the depletion of Cr on the surface may result in the presence of lanthanum strontium ferrite, LSF, which possesses higher mixed ionic-electronic conductivity and oxygen reduction activity than LSCrF, but has a significantly higher thermal expansion coefficient (23.8×10^{-6} C^{-1}, $T \geq 600$˚C). A key criterion of the dual-phase membrane requires the thermal expansion coefficient to be within the range of $9.5\text{-}12.0 \times 10^{-6}$ K^{-1} [5]. This causes the regions where Cr is depleted to be incompatible with adjacent 1Ce10ScSZ regions. Under prolonged operating conditions, the mismatch in thermal expansion may cause significant residual stresses in the dual-phase material, and may lead to delamination of the LSF phase from the surface of the membrane.

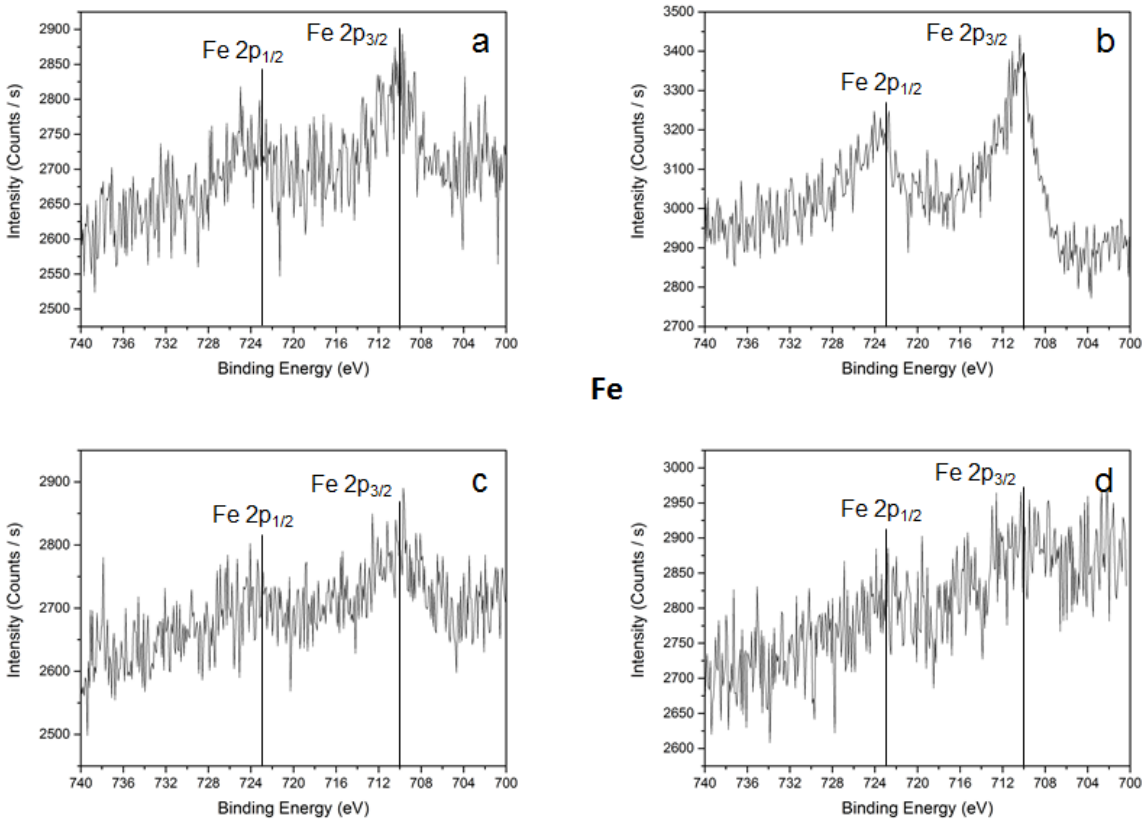

Figure 6.15: Fe $2p_{1/2}$ and Fe $2p_{3/2}$ peaks from high-resolution XPS measurement of 1Ce10ScSZ/LSCrF8255 dual-phase membrane. Legend: a) unaged; b) aged in air at 1000˚C for 300 h; c) aged in 4%H_2-96%N_2 at 1000˚C for 300 h; d) aged in 5%H_2-95%CO_2 at 1000˚C for 300 h. Vertical lines denote expected peak positions of the Fe $2p_{1/2}$ and Fe $2p_{3/2}$ signals for Fe_2O_3 [23].

The peak signals for Fe $2p_{1/2}$ and Fe $2p_{3/2}$ shown in Figure 6.15 show relatively low concentrations of Fe in the near-surface of 1Ce10ScSZ/LSCrF8255. The peaks are evident for the sample aged in air (Sample b), but were nearly absent for the sample aged in 4% H_2-96% N_2 and 5% H_2-95% CO_2. The peak positions for Fe $2p_{1/2}$ and Fe $2p_{3/2}$ of Fe_2O_3 are at BE ~ 722 eV and BE ~ 710 eV respectively, shown with vertical lines in Figure 6.15. The peak shape and position of the XPS spectra of Sample b in Figure 6.15 closely resembles the high-resolution Fe 2p XPS spectra of Fe_2O_3 or FeOOH performed by Grosvenor et. al. [24]. However, the resolution of Fe XPS spectra is too low to distinguish the oxide species of Fe in the analyzed samples.

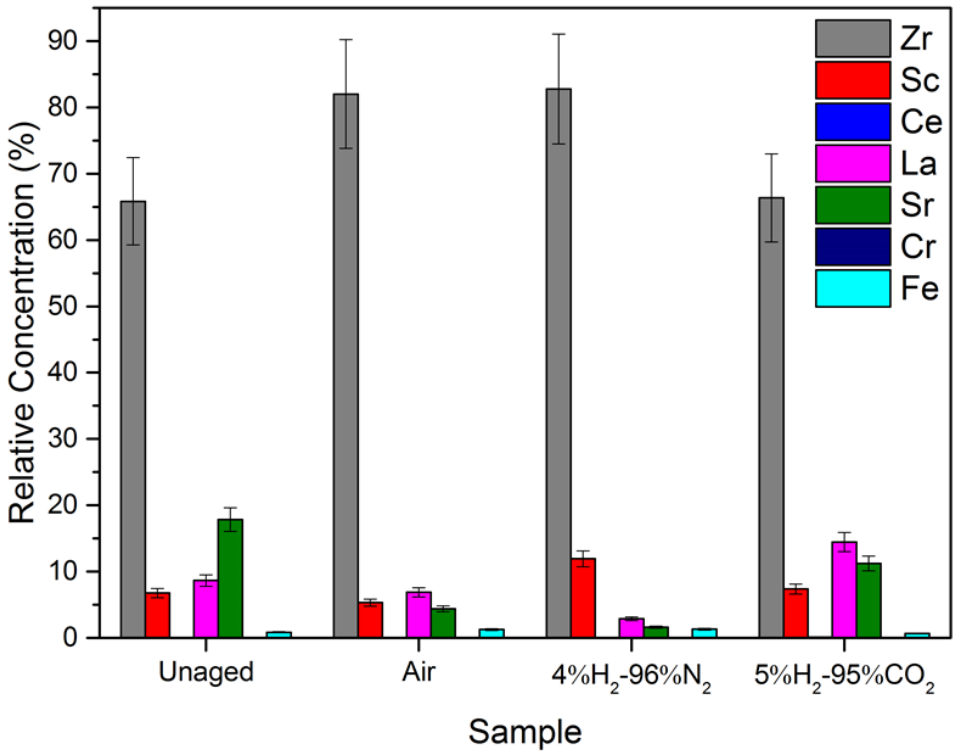

Figure 6.16: Relative concentration of component elements in the near-surface (~10 nm) of 50/50 vol% 1Ce10ScSZ/LSCrF8255 dual-phase membrane after aging for 300 h obtained from high-resolution XPS spectra. The relative concentration of Zr is significantly elevated in the near-surface (~10 nm) of the dual-phase material. In addition, the presence of Cr and Fe is depleted within this region. Finally, the Sr concentration was observed to be elevated for the unaged sample, but reverted towards expected bulk Sr:La ratio after aging.

Figure 6.16 and Table 6-2 summarize the relative concentration at the near-surface of the elements comprising dual-phase 1Ce10ScSZ/LSCrF8255 aged for 300 hours. To obtain the relative concentration, the raw peak areas of each element obtained from high-resolution XPS spectra were integrated for each of the four samples and divided by the appropriate relative sensitivity factor (RSF) of the element peak signal found in the CasaXPS database [25]. The RSF-factored peak areas were summed and taken to be 100% of the relative concentration of each sample, with each element representing a percentage of the total relative concentration.

Calculation of the relative concentration of dual-phase 1Ce10ScSZ/LSCrF8255 shows that the near-surface (~10 nm) of the material is dominated by the presence of Zr, comprising

more than 60% of the relative elemental concentration within this region. The relative Sc concentration is similarly elevated from bulk stoichiometric concentration. In contrast, the concentration of B-site cations Cr and Fe in the near-surface was significantly below the expected bulk stoichiometric concentration, with the Cr signal being undetected under the experimental setup for all four samples. This was consistent with the low concentrations of Cr observed on the outer atomic surface of 1Ce10ScSZ/LSCrF8255 as detailed in Section 6.1.3.1.

The La concentration was also observed to be below the ideal bulk stoichiometry within the near-surface of the material. In addition, the Sr:La ratio was observed to be above unity for the unaged sample, but reverted toward the ideal bulk stoichiometry of 0.25 for all three aged samples. This could be attributed to the re-incorporation of Sr cations back into the LSCrF8255 lattice, or the volatilization and removal of Sr from the sample surface upon exposure to elevated temperatures (1000˚C). An elevated Sr concentration observed on the unaged sample as well as on the sample aged in 5% H_2-95% CO_2 suggests that Sr re-incorporation is possible.

Table 6-2: Relative concentration of component elements in near-surface (~10 nm) of 50/50 vol% 1Ce10ScSZ/LSCrF8255 dual-phase membrane before and after aging for 300 h obtained from high-resolution XPS spectra. The phrase "B.D.L" denotes signal was below the detection limit of the XPS instrument.

Element	Ideal Bulk Stoichiometry (%)	Unaged (%)	Aged Air (%)	Aged 4%H_2-96%N_2 (%)	Aged 5%H_2-95%CO_2 (%)
Zr	44.5	65.8	82.0	82.8	66.4
Sc	5.0	6.8	5.3	11.9	7.4
Ce	0.5	B.D.L	B.D.L	B.D.L	B.D.L
La	20.0	8.7	6.9	2.9	14.4
Sr	5.0	17.8	4.4	1.7	11.2

Cr	12.5	B.D.L	B.D.L	B.D.L	B.D.L
Fe	12.5	0.9	1.3	0.7	1.4

The strong presence of Zr on the near-surface may support the claim that the outer atomic surface of dual-phase 1Ce10ScSZ/LSCrF8255 discussed in Section 6.1.3.1 is also Zr-rich, despite the inability to deconvolute the Sr/Zr peak in the LEIS spectra as discussed in Section 6.1.3.1. In addition, the high Zr content on the surface supports the low elevated oxygen surface fraction observed for dual-phase 1Ce10ScSZ/LSCrF8255 observed in the isotopic exchange measurements and discussed in Section 5.1.2.2 for single-phase 1Ce10ScSZ. The combination of elevated Zr presence and deficiency of Cr and Fe in the near-surface could result in significantly reduced electronic conduction during the oxygen surface exchange process, thereby reducing the rate of oxygen surface incorporation into the material.

6.1.3.4 XPS Summary

X-ray photoelectron spectra were obtained for the dual-phase 1Ce10ScSZ/LSCrF8255 material aged for 300 hours in three conditions (air, 4% H_2-96% N_2 and 5% H_2-95% CO_2) and compared to the unaged material. Analysis of the high-resolution XPS spectra showed the absence of Ce and Cr from the near-surface (~10 nm) of all four samples. The shape and energy separation of the La$3d_{5/2}$ peak suggests that La exists as a hydroxide, $La(OH)_3$. Peak fitting of the Sr signal shows that Sr likely exists as $SrCO_3$ within the near-surface, with the presence of other strontium compounds (such as SrO) deemed to be unlikely. The oxidation state of Fe is estimated to be +3 based on the position of the Fe $2p_{3/2}$ peak [24]. Relative quantification of the high-resolution XPS spectra shows the concentration of elements comprising single-phase 1Ce10ScSZ (Zr, Sc) is significantly elevated on the near-surface of dual-phase 1Ce10ScSZ/LSCrF8255 compared to the ideal bulk stoichiometry, corresponding to a deficiency of the concentration of the elements comprising single-phase LSCrF8255 (La, Sr, Cr, Fe). However, Sr concentration was observed to be elevated from ideal bulk stoichiometric values in the near-surface region for the sample aged in 5% H_2-95% CO_2 as well as in the unaged sample. In addition, the Sr:La ratio was observed to be above unity for the unaged sample, but reverted toward the ideal bulk stoichiometry for the three aged samples.

6.1.4 Summary of the Effects of Aging (300 hrs) on 1Ce10ScSZ/LSCrF8255

The effects of aging in three environments (air, 4% H_2-96% N_2 and 5% H_2-95% CO_2) at 1000˚C for 300 hours on dual-phase 1Ce10ScSZ/LSCrF8255 was not observed to significantly affect the oxygen transport kinetics of the material. The microstructure remained relatively unchanged after 300 hours of aging. The formation of a secondary phase, possibly $SrCrO_4$, was observed for the materials aged in air and in 5% H_2-95% CO_2, but its presence had a negligible effect on the oxygen transport kinetics of the material. Oxygen self-diffusion coefficients D^* and surface exchange coefficients k^* were observed to be on the order of 10^{-8} cm^2 s^{-1} and 10^{-8} cm s^{-1} respectively for all four samples. The normalized isotopic fraction at the surface of all four samples was low, similar to the low oxygen surface incorporation exhibited by single-phase 1Ce10ScSZ observed in the previous chapter. Relative quantification of the near-surface (~10 nm) of dual-phase 1Ce10ScSZ/LSCrF8255 showed a significant presence of Zr and Sc, suggesting a disproportionally high phase fraction of 1Ce10ScSZ within this region, which is consistent with the low isotopic fraction observed for the dual-phase material.

Relative quantification also shows the depletion of La, Cr and Fe on the near-surface for all four samples of dual-phase 1Ce10ScSZ/LSCrF8255 compared to bulk stoichiometric values. The absence of Cr was also observed on the outer atomic surface. The presence of Fe was also observed to be deficient on the outer surface in the samples aged in reducing conditions (4% H_2-96% N_2 and 5% H_2-95% CO_2) compared to the unaged and air-aged samples. However, Fe was deficient on the near-surface for all four samples. Finally, possible Sr segregation on the outer atomic surface was observed for dual-phase 1Ce10ScSZ/LSCrF8255 aged in air, corresponding to a Sr deficiency within the near-surface. The Sr:La ratio was observed to be significantly elevated for the unaged sample, but reverted toward the ideal bulk stoichiometry for the three aged samples.

6.2 Effects of Aging (1000 hours) on 1Ce10ScSZ/LSCrF8255

The effects of exposure to three separate static conditions (air, 4% H_2-96% N_2, 5% H_2-95% CO_2) at 1000˚C for 1000 hours on the oxygen transport kinetics and surface chemistry of dual-phase 1Ce10ScSZ/LSCrF8255 after will be examined and compared to the unaged material. Analysis of these samples is similar to those aged for 300 hours outlined in the previous section. Characterization will be performed via X-ray diffraction and secondary electron microscopy. The oxygen transport kinetics will be examined using Isotopic Exchange Depth Profiling/Secondary Ion Mass Spectrometry. Additional IEDP/SIMS experiments will be performed in water vapor environment to examine the

effect of water on oxygen transport kinetics. The surface chemistry of the outer atomic layer and the near-surface (within ~10 nm) will be studied using low energy ion scattering and X-ray photoelectron spectroscopy respectively, with relative elemental quantification of the near-surface via XPS also performed.

6.2.1 Characterization of 1Ce10ScSZ/LSCrF8255

6.2.1.1 X-ray Diffraction

Figure 6.17 shows the X-ray diffraction patterns of 1Ce10ScSZ/LSCrF8255 after exposure to air, 4% H_2-96% N_2, or 5% H_2-95% CO_2 at 1000°C and atmospheric pressure for 1000 hours. As in the previous measurements, XRD patterns were obtained *ex-situ* from the aging environment, in air at ambient conditions. The unaged 1Ce10ScSZ/LSCrF8255 diffraction pattern is added to Figure 6.17 for reference.

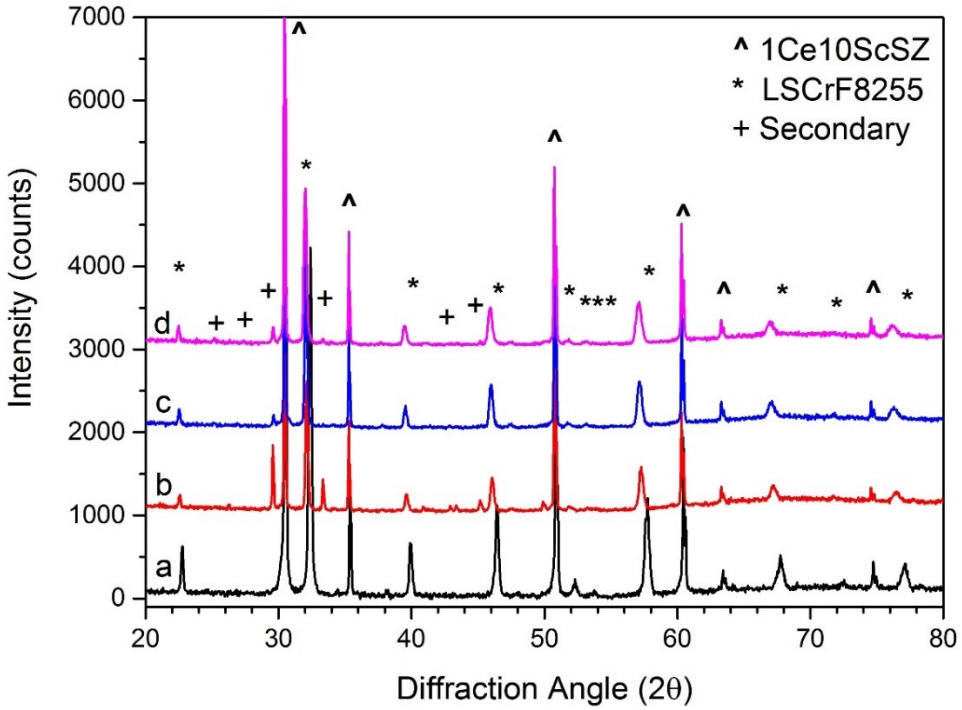

Figure 6.17: X-ray diffraction pattern of 1Ce10ScSZ/LSCrF8255 dual-phase membrane before and after aging at 1000°C for 1000 hours. From bottom to top: a) unaged; b) aged in air; c) aged in 4% H_2-96% N_2 ($pO_2 \sim 10^{-18}$ atm); d) aged in 5% H_2-95% CO_2 ($pO_2 \sim 10^{-11}$ atm). Aging atmospheres were 1 atm. The formation of a secondary phase hypothesized to be $SrCrO_4$ [4] was found in all three aged samples.

It was observed that both components of the dual-phase material maintain their respective crystal structure after 1000 hours of aging. The diffraction pattern of the 1Ce10ScSZ component in dual-phase 1Ce10ScSZ/LSCrF8255 does not change significantly after 1000 hours of aging, which suggests high chemical stability of this phase in the dual-phase material. On the other hand, partial decomposition of the LSCrF8255 phase was observed after 1000 hours of aging, as evidenced by the evolution of a secondary diffraction pattern and shifts in the LSCrF8255 diffraction pattern (marked as an asterisk * in Figure 6.17) towards smaller diffraction angles after exposure to aging environments. The diffraction pattern of the secondary phase is similar among the aged samples, and is likely comparable to that observed for the samples aged for 300 hours outlined in Section 6.1. Therefore, it is hypothesized that the phase formed in the 1Ce10ScSZ/LSCrF8255 samples aged for 1000 hours is strontium chromate, $SrCrO_4$. The presence of this secondary phase in all three aged samples suggests that its formation is independent of oxygen partial pressure in the environment, within a range of $pO_2 \sim 0.21 - 10^{-18}$ atm.

6.2.1.2 Secondary Electron Microscopy

The backscattered electron micrographs of dual-phase 1Ce10ScSZ/LSCrF8255 after aging at 1000˚C for 1000 hours are shown in Figure 6.18.The materials were polished to ¼ µm mirror finish as outlined in Section 4.1.5, and a gold coating (~5 nm) was applied to the polished surface prior to SEM/EDX analysis to minimize sample charging.

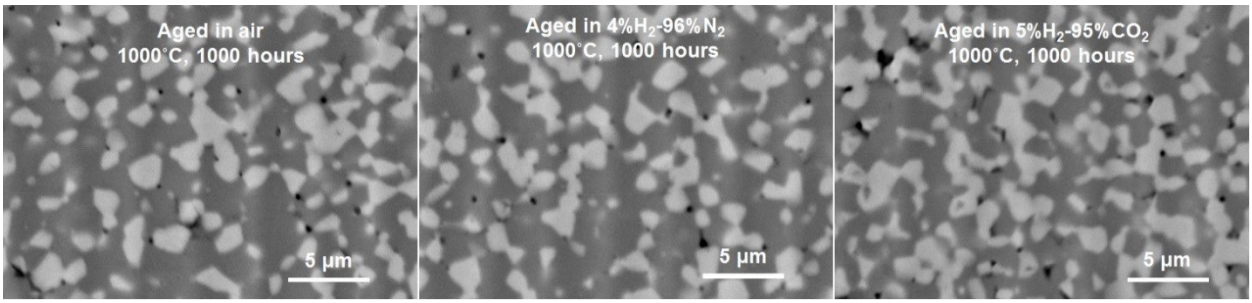

Figure 6.18: Backscattered electron micrographs of dual-phase 1Ce10ScSZ/LSCrF8255 aged for 1000 hours. Left: aged in air; Centre: aged in 4% H_2-96% N_2; Right: aged in 5% H_2-95% CO_2. Dark phases denote 1Ce10ScSZ component; bright phases denote LSCrF8255 component.

The two phases of the material were observed to be highly distributed, suggesting the material maintains high homogeneity after 1000 hours aging in environments (air, 4%H_2-96%N_2, 5%H_2-95%CO_2) at elevated temperatures. In addition, reaction between the two phases was observed to be minimal due to the absence of phases appearing at the interphase boundaries between the two components. However, pores on the polished surfaces were observed, appearing as black dots on the micrographs. The pores could

have formed as a result of sample polishing, due to the high strain induced by the polishing paper on the material surface. In all three samples the pore concentration and average pore size is relatively low, which suggests the material maintains mechanical stability after 1000 hours of aging.

6.2.2 Oxygen Transport Kinetics

6.2.2.1 Dry Oxygen (^{18}O)

The oxygen self-diffusion profiles determined by Isotope Exchange Depth Profiling and Secondary Ion Mass Spectrometry (IEDP-SIMS) of dual-phase 1Ce10ScSZ/LSCrF8255 after aging for 1000 hours is shown in Figure 6.19. The material was exposed to the aging conditions prior to isotope exchange experiments. Samples were prepared according to the procedure for isotope exchange outlined in Section 4.1.5. Samples were exposed to ^{18}O (isotopic ratio ~51%) at ~800˚C for 30 minutes (pO_2 = 200 mbar) after equilibration in ^{16}O environment at the same temperature and pO_2 for 5 hours. Exchanged samples were prepared for the "linescan" sample configuration in SIMS analysis, outlined in Section 4.2.4.

The experimental oxygen tracer profile obtained via SIMS was fitted to the solution for diffusion in a semi-infinite medium [12] using a Matlab-based program developed by S. Cooper [13] as outlined in Section 4.2.5.1. The oxygen transport kinetic parameters were extracted from the fitted diffusion profile to the experimental data and are summarized in Table 6-3.

The oxygen diffusion profiles for dual-phase 1Ce10ScSZ/LSCrF8255 after aging for 1000 hours are similar to those after aging for 300 hours shown in Figure 6.4. Under both aging conditions, low oxygen incorporation and relatively high oxygen penetration was observed, which is similar to the oxygen transport kinetics of the single-phase 1Ce10ScSZ component of the dual-phase material.

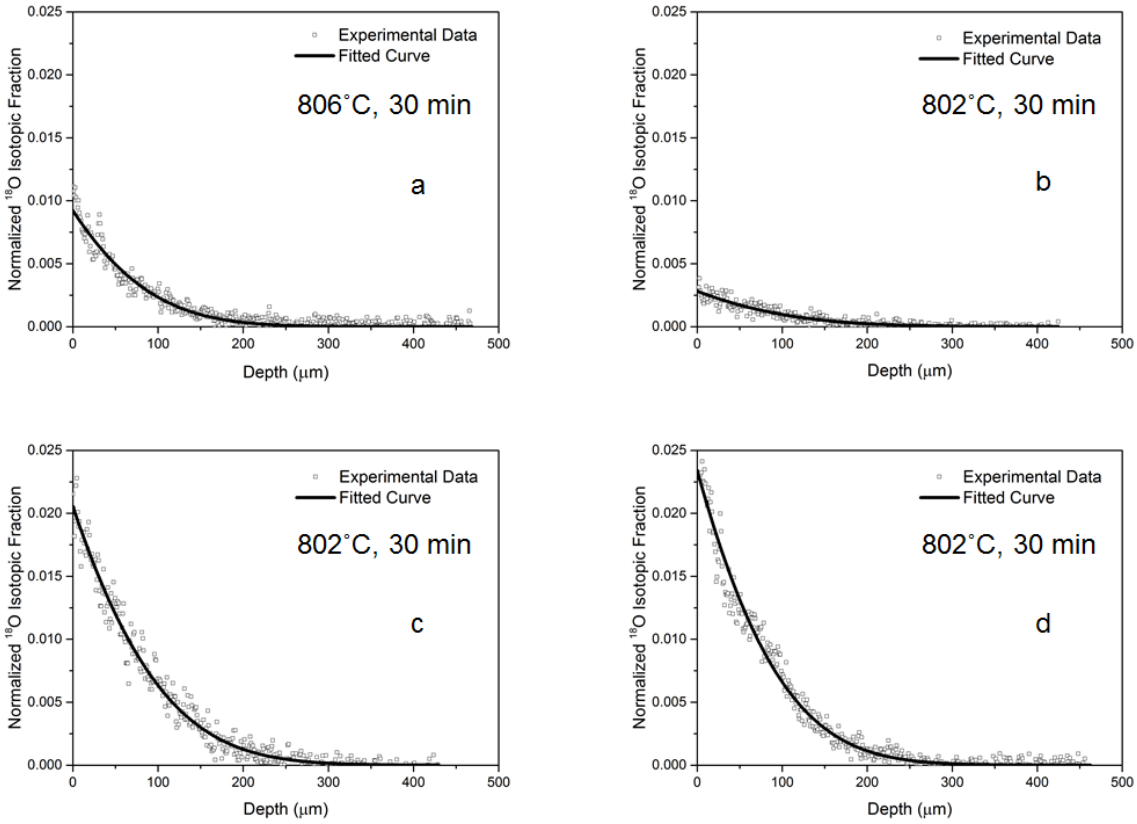

Figure 6.19: Normalized isotopic fraction depth profiles of 1Ce10ScSZ/LSCrF8255 dual-phase membrane before and after aging at 1000˚C for 1000 hours. Legend: a) unaged; b) aged in air; c) aged in 4%H_2-96%N_2; d) aged in 5%H_2-95%CO_2. Samples were annealed in ^{18}O environment (pO_2 = 200 mbar) at ~800˚C for 30 minutes after equilibrating in ^{16}O environment at the same temperature and pO_2 for 5 hours.

The self-diffusion coefficients, D^*, of 1Ce10ScSZ/LSCrF8255 were calculated from the fitted diffusion curves to be 5.3 (±0.5) x 10^{-8} cm^2 s^{-1} for the sample aged in air at 1000˚C for 1000 hours, 4.5 (±0.4) x 10^{-8} cm^2 s^{-1} for the sample aged in reducing 4%H_2-96%N_2 at 1000˚C for 1000 hours, and 3.9 (±0.4) x 10^{-8} cm^2 s^{-1} for the sample aged in reducing 5%H_2-95%CO_2 at 1000˚C for 1000 hours. The self-diffusion coefficient of the aged samples did not differ significantly from the self-diffusion coefficient of the unaged sample or with the samples aged for 300 hours, with all dual-phase samples possessing D^* on the order of 10^{-8} cm^2 s^{-1}. This provides further evidence that oxygen self-diffusion kinetics in the bulk of dual-phase 1Ce10ScSZ/LSCrF8255 are relatively unaffected by exposure to the selected aging environments at elevated temperatures up to 1000 hours.

Table 6-3**:** Oxygen transport kinetic parameters extracted from fitted diffusion profile for 1Ce10ScSZ/LSCrF8255 dual-phase membrane before and after aging (1000 hrs). Samples were annealed in ^{18}O environment (200 mbar, 800˚C) for 30 minutes after equilibrating in ^{16}O environment at the same temperature and pO_2 for 5 hours.

	Oxygen self-diffusion coefficient, D* (cm^2/s)	Oxygen surface exchange coefficient, k* (cm/s)
Unaged	3.5 (±0.3) x 10^{-8}	3.6 (±0.5) x 10^{-8}
Aged (1000˚C, 1000 h, air)	5.3 (±0.5) x 10^{-8}	1.4 (±0.2) x 10^{-8}
Aged (1000˚C, 1000 h, 4%H_2-96%N_2)	4.5 (±0.4) x 10^{-8}	9.2 (±0.9) x 10^{-8}
Aged (1000˚C, 1000 h, 5%H_2-95%CO_2)	3.9 (±0.4) x 10^{-8}	9.9 (±1.0) x 10^{-8}

However, changes exist in the surface exchange kinetics of the dual-phase 1Ce10ScSZ/LSCrF8255 samples. In particular, the surface exchange coefficient appears to be higher in the samples exposed to reducing environments (4% H_2-96% N_2, 5% H_2-95% CO_2) than in the sample aged in air, with k^* for the former approximately one order of magnitude higher than for the latter. The elevated ^{18}O isotopic fraction observed on the samples aged in reducing conditions (Figure 6.19 c and d) was observed to be ~2 % above the natural background fraction, but only ~0.2 % for the sample aged in air (Figure 6.19 b). One hypothesis for the elevated oxygen isotopic fraction observed for dual-phase 1Ce10ScSZ/LSCrF8255 exposed to reducing conditions could be the presence of an elevated surface fraction of the LSCrF8255 phase. Another hypothesis involves the effect on the oxidation state of the B-site cations to oxygen incorporation after exposure of the materials to reducing conditions. In either case, the increase in elevated oxygen isotope fraction for dual-phase 1Ce10ScSZ/LSCrF8255 observed in Figure 6.19 c and d is not statistically significant, and the effects of the two hypotheses mentioned above are likely to be negligible.

There appears to be a connection between the formation of a $SrCrO_4$ secondary phase observed for the material aged in air for 1000 h (Figure 6.17 b) and the elevated oxygen isotopic fraction observed during isotopic exchange experiments (Figure 6.19 b). The material exposed to air at elevated temperatures exhibited stronger formation of the secondary $SrCrO_4$ phase observed from XRD and lower elevated oxygen isotopic fraction

observed from IEDP-SIMS. This phenomenon was also observed for the material aged for 300 hours in 5% H_2-95% CO_2 (Figure 6.4 d). However, it was not observed in the material aged for 300 hours in air (Figure 6.4 b), with the formation of the secondary phase having a negligible effect on the elevated oxygen isotopic fraction and subsequently the oxygen surface exchange coefficient. The effect of secondary phase formation on the oxygen surface exchange kinetics is inconclusive based on the results obtained in this work.

No correlation was observed between the formation of the secondary phase in the samples aged in air and in 5% H_2-95% CO_2 atmosphere, and their oxygen bulk diffusion kinetics, which suggests that the presence of this phase has negligible effects on the oxygen bulk migration in dual-phase 1Ce10ScSZ/LSCrF8255. As with the samples aged for 300 hours, X-ray diffraction patterns of the samples aged for 1000 hours as shown in Figure 6.17 remain relatively unchanged with the presence of the secondary phase peaks, indicating that the crystal structure of the material remains mostly intact after aging.

6.2.2.2 Water Vapor ($H_2{}^{18}O$)

Oxygen incorporation into dual-phase membrane materials can occur from the presence of oxygen in water, H_2O, in addition to oxygen in gaseous form, O_2. The effect of oxygen incorporation in water vapor was performed via IEDP-SIMS on dual-phase 1Ce10ScSZ/LSCrF8255 before and after aging for 1000 hours. Preparation of the samples prior to isotope exchange was identical to that outlined in Section 6.2.2.1. Dual-phase 1Ce10ScSZ/LSCrF8255 samples were annealed in $H_2{}^{18}O$ atmosphere (pH_2O ~ 100 mbar) at 700°C for 30 minutes after equilibrating in $H_2{}^{16}O$ atmosphere at the same temperature and water vapor pressure for 5 hours. SIMS analysis of the exchanged samples adopted a "linescan" configuration outlined in Section 4.2.4, identical to the samples examined in Section 6.2.2.1. The oxygen diffusion profiles and corresponding fitted curves are shown in Figure 6.20. Oxygen self-diffusion and surface exchange coefficients were extracted in the same manner as outlined in Section 4.2.5.1, and are shown in Table 6-4.

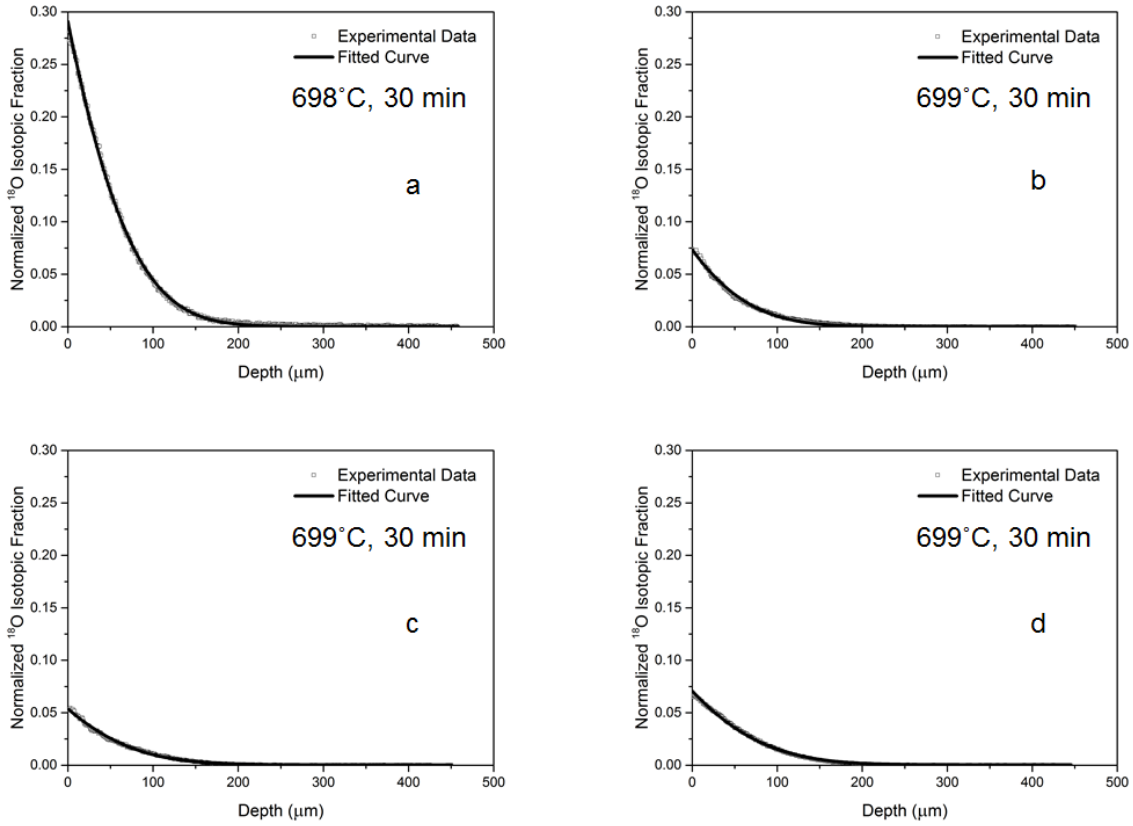

Figure 6.20: Normalized isotopic fraction depth profiles of 1Ce10ScSZ/LSCrF8255 dual-phase membrane before and after aging at 1000˚C for 1000 hours. Legend: a) unaged; b) aged in air; c) aged in 4% H_2-96% N_2; d) aged in 5% H_2-95% CO_2. Samples were annealed in $H_2{}^{18}O$ environment (pH_2O ~ 100 mbar) at ~700˚C for 30 minutes after equilibrating in $H_2{}^{16}O$ environment at the same temperature and pH_2O for 5 hours.

Comparisons of the diffusion profiles and oxygen transport kinetic parameters were made between dual-phase 1Ce10ScSZ/LSCrF8255 exchanged in ^{18}O atmosphere (shown in Figure 6.19 and Table 6-3) and in $H_2{}^{18}O$ atmosphere (shown in Figure 6.20 and Table 6-4).

The oxygen self-diffusion kinetics of the samples do not appear to differ significantly before and after aging. The self-diffusion coefficient D^* of 1Ce10ScSZ/LSCrF8255 before and after exposure to aging environments for 1000 hours approaches the low 10^{-8} cm^2 s^{-1} range under the $H_2{}^{18}O$ exchange environment. In addition, the oxygen self-diffusion coefficients of the samples annealed in $H_2{}^{18}O$ environments were similar to the D^* for the samples annealed in ^{18}O environments shown in Figure 6.19 and Table 6-3. The lower D^* values for the materials exchanged in the $H_2{}^{18}O$ environment are due to the lower exchange temperatures (~700˚C) compared to the exchange measurements performed in

the ^{18}O environment (~800˚C). The similarity in D^* suggests that oxygen tracer self-diffusion is relatively unaffected by the form the oxygen tracer assumes during isotope exchange.

Table 6-4: Oxygen transport kinetic parameters extracted from fitted curve of diffusion profile for 1Ce10ScSZ/LSCrF8255 dual-phase membrane before and after aging (1000 hrs). Samples were annealed in $H_2{}^{18}O$ environment (~100 mbar, 700˚C) for 30 minutes after equilibrating in $H_2{}^{16}O$ environment at the same temperature and p(H_2O) for 5 hours.

	Oxygen self-diffusion coefficient, D* (cm^2/s)	Oxygen surface exchange coefficient, k* (cm/s)
Unaged	1.9 (±0.2) x 10^{-8}	1.1 (±0.1) x 10^{-6}
Aged (1000˚C, 1000 h, air)	1.9 (±0.2) x 10^{-8}	3.0 (±0.3) x 10^{-7}
Aged (1000˚C, 1000 h, 4%H_2-96%N_2)	2.4 (±0.2) x 10^{-8}	2.4 (±0.2) x 10^{-7}
Aged (1000˚C, 1000 h, 5%H_2-95%CO_2)	2.8 (±0.2) x 10^{-8}	4.1 (±0.4) x 10^{-7}

In contrast, the surface exchange kinetics of the samples under $H_2{}^{18}O$ atmosphere differs significantly before and after aging. The oxygen isotopic surface fraction is significantly higher in the unaged sample than in the other three aged samples. The cause of this phenomenon is not clear. One hypothesis involves the microstructure of the unaged sample used in the $H_2{}^{18}O$ exchange. The unaged sample used for $H_2{}^{18}O$ isotope exchange was prepared by Z. Shen [14] of Imperial College London in her work on dual-phase 1Ce10ScSZ/LSCrF8255. The microstructure of this sample, shown in Figure 6.21, possesses significantly smaller aggregates than the samples prepared in this work. In addition, the homogeneity of the two component phases in the dual-phase material was higher. Prior to $H_2{}^{18}O$ exchange, it was thought that the degree of homogeneity of the unaged samples prepared by Z. Shen and the ones prepared for this work would be similar to a point where the diffusion profile would not be significantly different but this was proven, after the experiment, to be untrue.

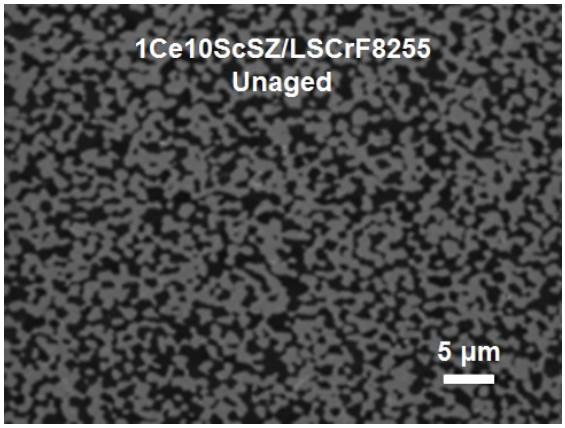

Figure 6.21: Backscattered electron micrograph of dual-phase 1Ce10ScSZ/LSCrF8255 prepared by Z. Shen [14]. Dark phases denote 1Ce10ScSZ component; bright phases denote LSCrF8255 component.

It was observed that the samples exchanged in $H_2{}^{18}O$ atmosphere exhibited significantly higher oxygen surface incorporation rate compared to the same material exchanged in ^{18}O atmosphere. The surface exchange coefficient k^* of unaged 1Ce10ScSZ/LSCrF8255 exchanged in $H_2{}^{18}O$ atmosphere reached 1.1 (±0.1) x 10^{-6} cm^2 s^{-1}, which is one order of magnitude higher than the k^* of 3.6 (±0.5) x 10^{-8} cm^2 s^{-1} achieved for the same material exchanged in ^{18}O atmosphere. Similar increases in k^* were also observed for the dual-phase material aged for 1000 hours in air. The increase in surface exchange coefficient was less pronounced in the materials aged in reducing conditions due to the relatively high k^* observed in the materials exchanged in ^{18}O environment.

The enhanced surface exchange kinetics observed in dual-phase 1Ce10ScSZ/LSCrF8255 undergoing isotope exchange in the presence of water vapor is consistent with work done by Sakai et. al. [26], who observed a significant enhancement of k^* on polycrystalline 8YSZ with minor additions of water vapor in the isotope exchange environment. Sakai et. al. [26] also observed that water vapor had no effect on the oxygen self-diffusivity D^*. Both observations were made by Ishihara et. al. [27] on $LaGaO_3$-based perovskite materials. Ishihara et. al. [27] also asserts that enhancement of oxygen surface exchange kinetics in the presence of H_2O are expected in other oxide materials undergoing oxygen reduction.

It is thought that the water adsorbed on the material surface plays an important role in oxygen incorporation. Sakai et. al. [26] proposes a series of reactions representing oxygen isotope exchange under a $H_2{}^{18}O$ environment, with the assumption that H^+ ions in H_2O exists as hydroxyl groups (OH^-) bonded to the cations in YSZ, which are shown in Equations 6.1 to 6.4:

$$H_2^{18}O\ (g) \rightarrow\ H_2^{18}O_{ad} \tag{6.1}$$

$$H_2^{18}O_{ad} + {}^{16}O_O^x\ \rightarrow\ V_O^{\bullet\bullet} + {}^{18}OH'_{ad} +\ {}^{16}OH'_{ad} \tag{6.2}$$

$${}^{18}OH'_{ad}\ +\ {}^{16}OH'_{ad} + V_O^{\bullet\bullet}\ \rightarrow\ H_2^{16}O_{ad} +\ {}^{18}O_O^x \tag{6.3}$$

$$H_2^{16}O_{ad}\ \rightarrow\ H_2^{16}O\ (g) \tag{6.4}$$

Equation 6.1 denotes the adsorption of the oxygen tracer water molecule, $H_2{}^{18}O$, onto the material surface. Equation 6.2 represents the reduction of oxygen in the tracer water molecule $H_2{}^{18}O$ into a hydroxyl OH^- group, with the remaining H^+ attaching to a ^{16}O present in the YSZ lattice, forming a Y-O-H structure. The formation of adsorbed $^{16}OH^-$ ($^{16}OH'_{ad}$) results in the formation of a single oxygen vacancy site. Equation 6.3 shows the recombination of the H^+ ion to the adsorbed $^{16}OH^-$ forming H_2O and the incorporation of the ^{18}O into the lattice. Equation 6.4 indicates the desorption of $H_2{}^{16}O$ from the material surface. The isotope exchange steps outlined by Sakai et. al. [26] are likely to apply congruently to 1Ce10ScSZ with Sc in place of Y as the site where the hydroxyl group forms, i.e. Sc-O-H.

The significant increase in oxygen surface exchange kinetics observed by Sakai et. al. [26] and in the work reported here indicates that the mechanism of formation of adsorbed hydroxyl groups is a likely method to incorporate oxygen tracer ions into the lattice as outlined in Equations 6.2 and 6.3 and is significantly faster than the oxygen incorporation process in dry O_2 outlined by Equations 2.10-2.14 in Chapter 2. This is likely due to the nature of oxygen reduction under dry and 'wet' (water vapor) conditions. For stabilized zirconia materials, the reduction and incorporation of oxygen ions from dry gaseous O_2 requires electrons on the surface of the material. If the electrons are not near the region of the adsorbed $O_{2(ad)}$ molecule, they must migrate towards the molecule if reduction is to take place. The steps for oxygen incorporation outlined in Equations 2.11 to 2.13 all require the presence of electrons to proceed. Since stabilized zirconia materials are widely accepted to be purely ionic conductors with low electron mobility, oxygen surface exchange of dual-phase 1Ce10ScSZ/LSCrF8255 under dry O_2 will be slow within the 1Ce10ScSZ surface regions exposed to gaseous oxygen. This results in slow surface exchange kinetics if 1Ce10ScSZ is present in high amounts on the surface. Indeed, the correlation between low oxygen incorporation and high 1Ce10ScSZ surface concentration of dual-phase 1Ce10ScSZ/LSCrF8255 was observed for every sample analyzed.

In contrast, under isotope exchange conditions in water vapor, electrons do not have to be supplied by the bulk material in order for oxygen reduction and incorporation to take place. Instead, isotope exchange takes place using the hydroxyl groups as a site of transfer for the oxygen tracer ion. The electrons in isotope exchange under 'wet' conditions come from the OH^- groups themselves, eliminating the rate-limiting step for electron mobility to oxygen surface exchange observed in zirconia-based materials. In addition, under 'wet' conditions, the incorporation of the oxygen tracer requires only one oxygen vacancy site on the surface, instead of two under dry conditions. Finally, excluding the initial oxygen tracer adsorption step, the steps required to incorporate the tracer oxygen into the bulk lattice is reduced from three (Equations 2.11-2.13) under dry O_2 conditions to two (Equations 6.2-6.3) under 'wet' H_2O conditions. All these factors likely contribute to the increased oxygen surface exchange kinetics observed in dual-phase 1Ce10ScSZ/LSCrF8255.

6.2.2.3 IEDP-SIMS Summary

The oxygen transport kinetics of dual-phase 1Ce10ScSZ/LSCrF8255 before and after aging for 1000 hours in three conditions (air, 4%H_2-96%N_2, and 5%H_2-95%CO_2) were determined using IEDP-SIMS. From dry O_2 isotope exchange measurements, the material exhibits similar characteristics of relatively low surface incorporation and relatively high oxygen penetration regardless of aging, similar to the materials aged for 300 hours examined in Section 6.1.2. The self-diffusion coefficients D^* were observed to have negligible change after aging for 1000 hours compared to both the unaged sample and the samples aged for 300 hours. Minor differences in D^* as a function of aging conditions after 1000 hours was also observed.

The surface exchange coefficients k^* of dual-phase 1Ce10ScSZ/LSCrF8255 before and after aging for 1000 hours showed elevated surface exchange kinetics for the materials aged in reducing conditions compared to the unaged sample. In contrast, lower surface exchange kinetics were observed for the material aged in air compared to the unaged sample.

The oxygen transport kinetics of dual-phase 1Ce10ScSZ/LSCrF8255 before and after aging for 1000 hours in three conditions (air, 4%H_2-96%N_2, and 5%H_2-95%CO_2) were also examined using IEDP-SIMS under water vapor. It was observed that the self-diffusion coefficient for all four samples was unchanged from the analogous experiment performed in dry O_2. However, the surface exchange coefficient was significantly improved for all four samples under humid $H_2{}^{18}O$ environment compared with the isotope exchange experiment performed in dry ^{18}O environment. An oxygen incorporation mechanism under 'wet' conditions was proposed that attempts to explain the increase in oxygen surface exchange kinetics in the presence of water for dual-phase 1Ce10ScSZ/LSCrF8255.

6.2.3 Surface Chemistry

As with dual-phase 1Ce10ScSZ/LSCrF8255 aged for 300 hours outlined in Section 6.1.3, the surface chemistry of 1Ce10ScSZ/LSCrF8255 aged for 1000 hours was examined using low energy ion scattering and X-ray photoelectron spectroscopy. The examination of the outer atomic surface of the dual-phase material via LEIS, coupled with the elemental quantification within the near-surface region (~10 nm) of the material via XPS was performed. The surface chemistry of dual-phase 1Ce10ScSZ/LSCrF8255 aged for 1000 hours will be compared with the materials aged for 300 hours to observe if any trends within the surface composition emerge as a function of exposure under static operating conditions.

6.2.3.1 Low Energy Ion Scattering – Outer Atomic Surface

The LEIS spectra ($^{20}Ne^{+}$, 5 keV) of dual-phase 1Ce10ScSZ/LSCrF8255 samples before and after aging for 1000 hours in three environments (air, 4%H_2-96%N_2, and 5%H_2-95%CO_2) are shown in Figure 6.22. As with the samples aged for 300 hours, the surfaces of the samples aged for 1000 hours were unmodified after exposure to aging conditions. The surfaces wrapped in Al foil used to protect them from contamination prior to surface analysis.

Two LEIS spectra are shown in Figure 6.22 from each of the four samples. One measurement was taken at the beginning of the analysis, represented by the dotted line. The other measurement was recorded when the primary ion dose density on the analysis area (a square 1 mm x 1 mm region) reached 1.0 x 10^{15} ions cm^{-2}, corresponding to the approximate dose density required to sputter one atomic layer of the material from the sample surface, represented by the solid line. This was repeated for the three aged samples. The LEIS spectra for the unaged material (Sample a in Figure 6.22) were measured during the analysis for the 300-hour aged samples (see Section 6.1.3.1) and are included for reference.

The outer atomic surface of the dual-phase 1Ce10ScSZ/LSCrF8255 samples aged for 1000 hours in the three environments does not differ significantly from the unaged sample. The absence of Cr on the outer surface was observed for all four LEIS spectra in Figure 6.22, which is consistent with the observations made on the samples aged for 300 hours shown in Figure 6.7. The same hypothesis of the presence of LSCrF8255 existing as lanthanum strontium ferrite on the outer atomic surface can be made for the materials aged for 1000 hours. However, the presence of Fe on the outer surface was observed for the two samples aged for 1000 hours in reducing conditions (Samples c and d in Figure 6.22), which was not observed in the analogous samples aged for 300 hours (Samples c

and d in Figure 6.7). It is unclear why Fe was observed to be absent in the samples aged for 300 hours but present in the unaged sample as well as the analogous samples aged for 1000 hours.

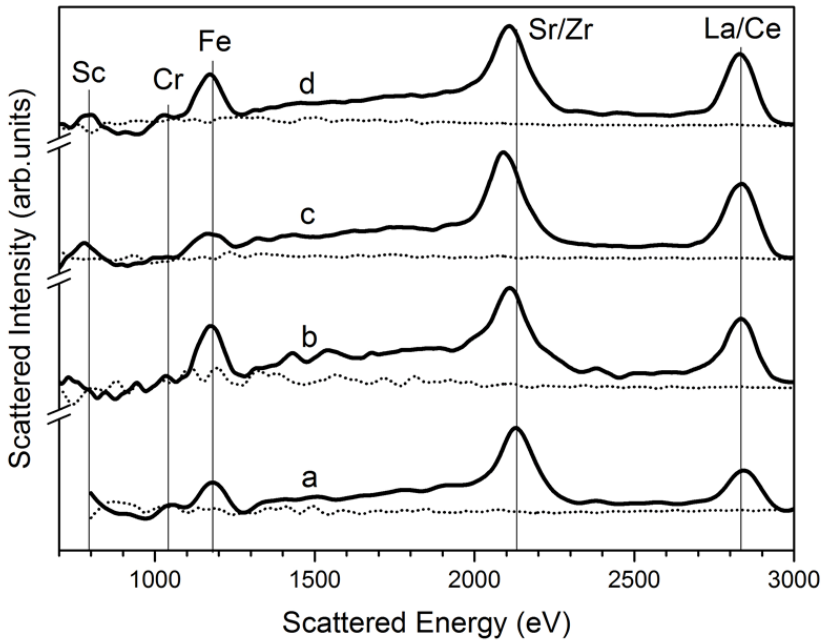

Figure 6.22: LEIS spectra ($^{20}Ne^{+}$, 5 keV) of 1Ce10ScSZ/LSCrF8255 before and after aging at 1000°C for 1000 hours. From bottom to top: a) unaged; b) aged in air; c) aged in 4% H_2-96% N_2; d) aged in 5% H_2-95% CO_2. Dotted line represents initial measurement; solid line represents measurement performed after primary ion dose density of $1x10^{15}$ ions cm^{-2} was reached. Vertical lines are added to guide the eye.

One hypothesis that may explain the presence of Fe on the outer surface of some dual-phase 1Ce10ScSZ/LSCrF8255 samples but not on others involves the inter-diffusion of Fe ions from the LSCrF8255 phase into the 1Ce10ScSZ phase and subsequent segregation of Fe onto the 1Ce10ScSZ surface above the solubility limit, estimated to be about 3 mol% [28], [29]. Fe inter-diffusion would have the detrimental effect of depleting Fe from the LSCrF8255 phase, resulting in lower density during sintering [5]. In addition, the formation of Fe on the 1Ce10ScSZ surface may further reduce oxygen surface incorporation on the 1Ce10ScSZ phase.

It was hypothesized in Section 6.1.3.1 that exposure to reducing conditions may be the cause of Fe deficiency on the outer surface of dual-phase 1Ce10ScSZ/LSCrF8255. However, examination of the materials aged for longer durations under the same conditions

confirmed the presence of Fe on the outer surface, disproving this hypothesis. A correlation between aging duration under reducing conditions and Fe presence on the outer surface of the dual-phase material could not be established from the results obtained.

Another anomaly was observed for the samples aged in 4%H_2-96%N_2 for 1000 hours (Sample c in Figure 6.22). The La/Ce peak signal was significantly stronger on this sample than on the corresponding sample aged for 300 hours (Sample c in Figure 6.7). It is unclear if the presence of La on the outer surface of dual-phase 1Ce10ScSZ/LSCrF8255 is significantly affected by exposure to reducing conditions. As with Fe, no direct correlation could be established between duration of exposure to reducing conditions and La presence on the outer surface from the results. As was mentioned in Section 6.1.3.1, peak deconvolutions for the La/Ce and Sr/Zr peak signals for 1Ce10ScSZ/LSCrF8255 aged for 1000 hours were attempted but were not successful, but it was expected that the convoluted La/Ce peak is comprised mostly of La due to the significantly higher concentration of La to Ce in the ideal bulk stoichiometry. However, it cannot be ruled out that the presence of Ce is not negligible due to observation of Ce on the outer surface of single-phase 1Ce10ScSZ observed in Chapter 5.

6.2.3.2 LEIS Summary

The chemical composition of the outer atomic layer of dual-phase 1Ce10ScSZ/LSCrF8255 was not observed to be significantly affected by the effects of exposure to the three environments (air, 4% H_2-96% N_2, and 5% H_2-95% CO_2) at 1000°C for 1000 hours. This suggests that dual-phase 1Ce10ScSZ/LSCrF8255 retains chemical stability on the outer surface after 1000 hours of aging. Comparisons of the LEIS spectra of the samples aged for 1000 hours to that of the unaged sample showed the presence of Fe, as well as the absence of Cr, on all four samples. The observation of Fe on the outer surface of 1Ce10ScSZ/LSCrF8255 aged in reducing conditions (4% H_2-96% N_2 and 5% H_2-95% CO_2) for 1000 hours but not in the analogous materials aged for 300 hours was attributed to possible inter-diffusion of Fe from the LSCrF8255 component to the 1Ce10ScSZ component and subsequent Fe_2O_3 surface segregation above the solubility limit of 1Ce10ScSZ. However, a correlation between the presence of Fe and aging duration could not be obtained from the results obtained. As with LEIS examinations performed on 1Ce10ScSZ/LSCrF8255 aged for 300 hours, it was not possible to deconvolute the Sr/Zr or La/Ce peaks due to insufficient energy resolution.

6.2.3.3 X-ray Photoelectron Spectroscopy – Near-Surface Quantification

The XPS survey spectra for dual-phase 1Ce10ScSZ/LSCrF8255 before and after aging at 1000˚C for 1000 hours in three environments (air, 4% H_2-96% N_2, and 5% H_2-95% CO_2) are shown in Figure 6.23. Surfaces of the samples aged for 1000 hours were unmodified after exposure to aging conditions.

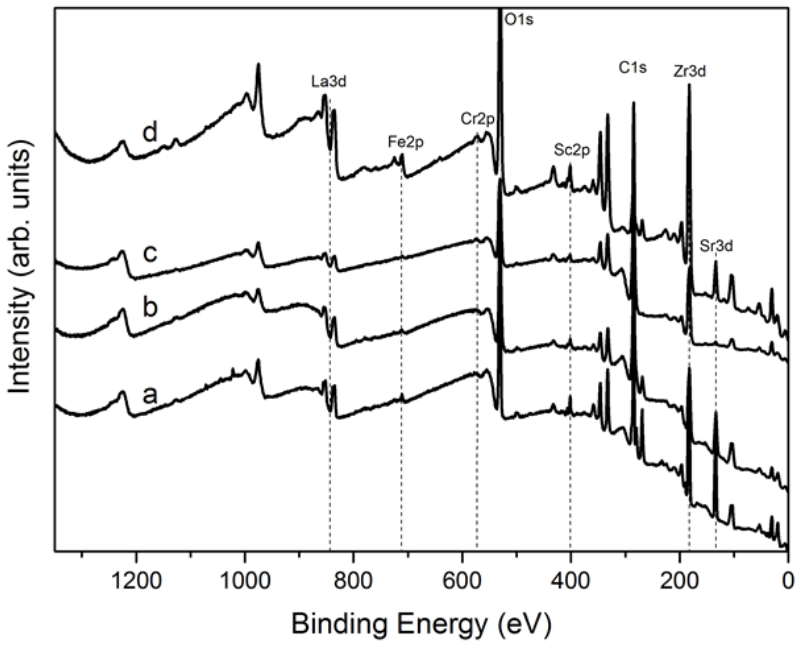

Figure 6.23: X-ray Photoelectron Survey Spectra of 1Ce10ScSZ/LSCrF8255 dual-phase membrane before and after aging at 1000˚C for 1000 hours. From bottom to top: a) unaged; b) aged in air; c) aged in 4% H_2-96% N_2; d) aged in 5% H_2-95% CO_2. Dotted lines are included to facilitate viewing.

The XPS survey spectra of dual-phase 1Ce10ScSZ/LSCrF8255 before and after aging for 1000 hours is similar in overall shape, suggesting that exposure to these environments does not significantly affect the chemical composition of the material within the near-surface (~10 nm) region. In addition, the spectra of the materials aged for 1000 hours is similar to the XPS spectra obtained for dual-phase 1Ce10ScSZ/LSCrF8255 aged for 300 hours shown in Figure 6.8. It was observed that the sample aged in 4% H_2-96% N_2 at 1000˚C for 1000 h (Figure 6.23c) exhibited a decrease in Sr content at the near-surface, which is the same phenomenon that was observed for the analogous sample aged for 300 hours (Figure 6.8c). The hypothesis made in Section 5.2.2.2 that exposure to reducing conditions causes Sr depletion on the surface of single-phase LSCrF8255 is further

corroborated with the results observed for dual-phase 1Ce10ScSZ/LSCrF8255 aged for 1000 hours.

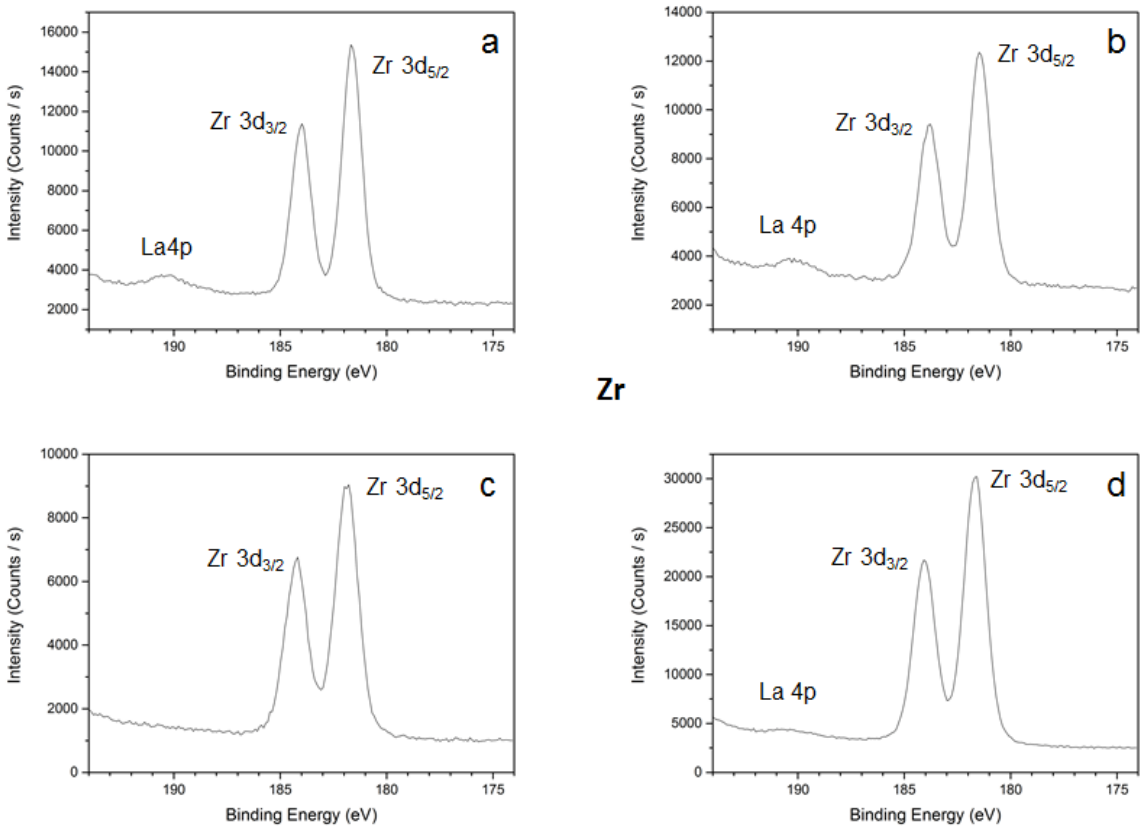

Figure 6.24: Zr 3d3/2 and Zr 3d5/2 peaks from high-resolution XPS measurement of 1Ce10ScSZ/LSCrF8255 dual-phase membrane. Legend: a) unaged; b) aged in air at 1000°C for 1000 h; c) aged in 4% H2-96% N2 at 1000°C for 1000 h; d) aged in 5% H2-95% CO2 at 1000°C for 1000 h. The La4p peak is observed for the samples aged in air (Sample b) and 5% H_2-95% CO_2 (Sample d). The Zr signal does not significantly change after exposure to aging environment for 1000 hours.

Figure 6.24 to Figure 6.30 present high-resolution X-ray photoelectron spectra of the component elements of dual-phase 1Ce10ScSZ/LSCrF8255 before and after aging for 1000 hours. As with the materials aged for 300 hours, XPS spectra were taken for the Zr 3d, Sc 2p, La 3d, Sr 3d, Cr 2p and Fe 2p peak signals, with the Ce 4d spectra omitted. The relative concentration of the elements comprising the dual-phase membrane before and after aging were determined and summarized in Figure 6.31.

The peak signals for Zr $3d_{3/2}$ and Zr $3d_{5/2}$ shown in Figure 6.24 show minimal change in shape or position of the Zr peaks after aging for 1000 hours. As with the analogous materials aged for 300 hours, the shape and position of the peaks indicates that Zr in the dual-phase material likely exists as ZrO_2 within ~10 nm of the surface.

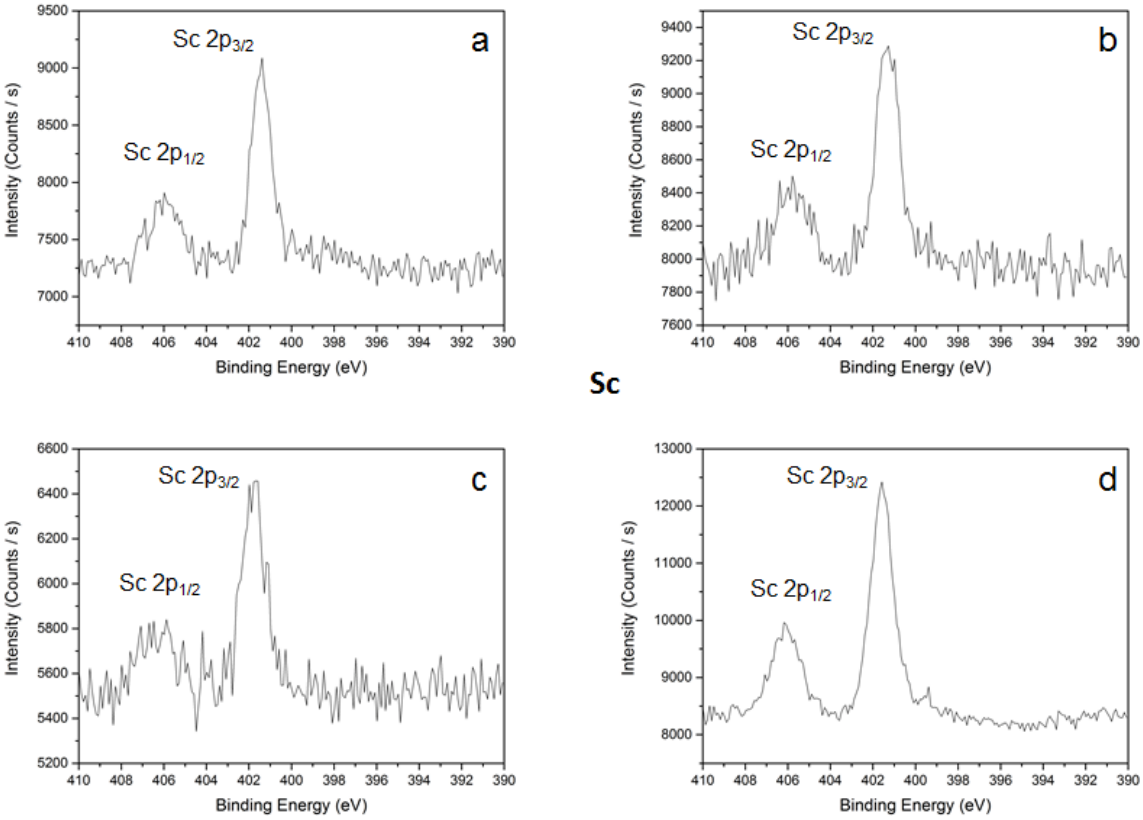

Figure 6.25: Sc $2p_{1/2}$ and Sc $2p_{3/2}$ peaks from high-resolution XPS measurement of 1Ce10ScSZ/LSCrF8255 dual-phase membrane. Legend: a) unaged; b) aged in air at 1000°C for 1000 h; c) aged in 4% H_2-96% N_2 at 1000°C for 1000 h; d) aged in 5% H_2-95% CO_2 at 1000°C for 1000 h.

The peak signals for Sc $2p_{1/2}$ and Sc $2p_{3/2}$ shown in Figure 6.25 also show minimal change in shape and position before and after aging for 1000 hours. The peak shapes and positions are also similar to the analogous materials aged for 300 hours shown in Figure 6.10. The Sc $2p_{3/2}$ peak position was observed to be at BE ~ 402 eV, corresponding to the peak signal for Sc(III) oxide [17], likely to be Sc_2O_3. The absence of Sc $2p_{3/2}$ peak signals at BE ~ 398 eV and BE ~ 403 eV on any of the high-resolution spectra suggests that metallic Sc or hydrated ScOOH is not present within the near-surface [17] of dual-1Ce10ScSZ/LSCrF8255 before and after aging for 1000 hours.

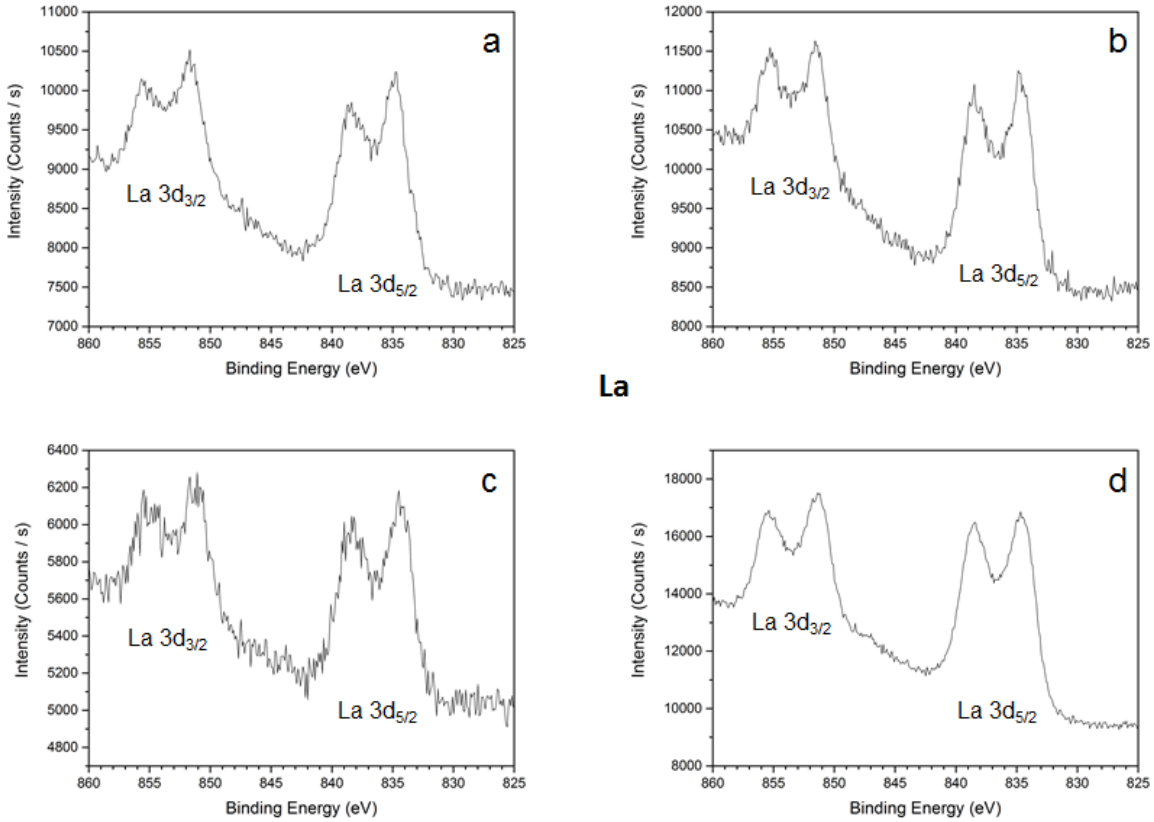

Figure 6.26: La $3d_{3/2}$ and La $3d_{5/2}$ peaks from high-resolution XPS measurement of 1Ce10ScSZ/LSCrF8255 dual-phase membrane. Legend: a) unaged; b) aged in air at 1000°C for 1000 h; c) aged in 4% H_2-96% N_2 at 1000°C for 1000 h; d) aged in 5% H_2-95% CO_2 at 1000°C for 1000 h.

The peak signals for La $3d_{3/2}$ and La $3d_{5/2}$ shown in Figure 6.26 were observed to be similar before and after aging for 1000 hours. As was observed for the materials aged for 300 hours, the difference in binding energy between the two peaks comprising the La $3d_{5/2}$ peak is ~3.9 eV for all four samples, suggesting that the La compound predominant in the near-surface of dual-phase 1Ce10ScSZ/LSCrF8255 aged for 1000 hours is lanthanum hydroxide, $La(OH)_3$ [19]. The XPS spectra shapes also remain relatively similar to the corresponding La high-resolution spectra for the materials aged for 300 hours shown in Figure 6.11, suggesting that the effects of aging do not significantly affect the chemical state of La within the near-surface region of the dual-phase material.

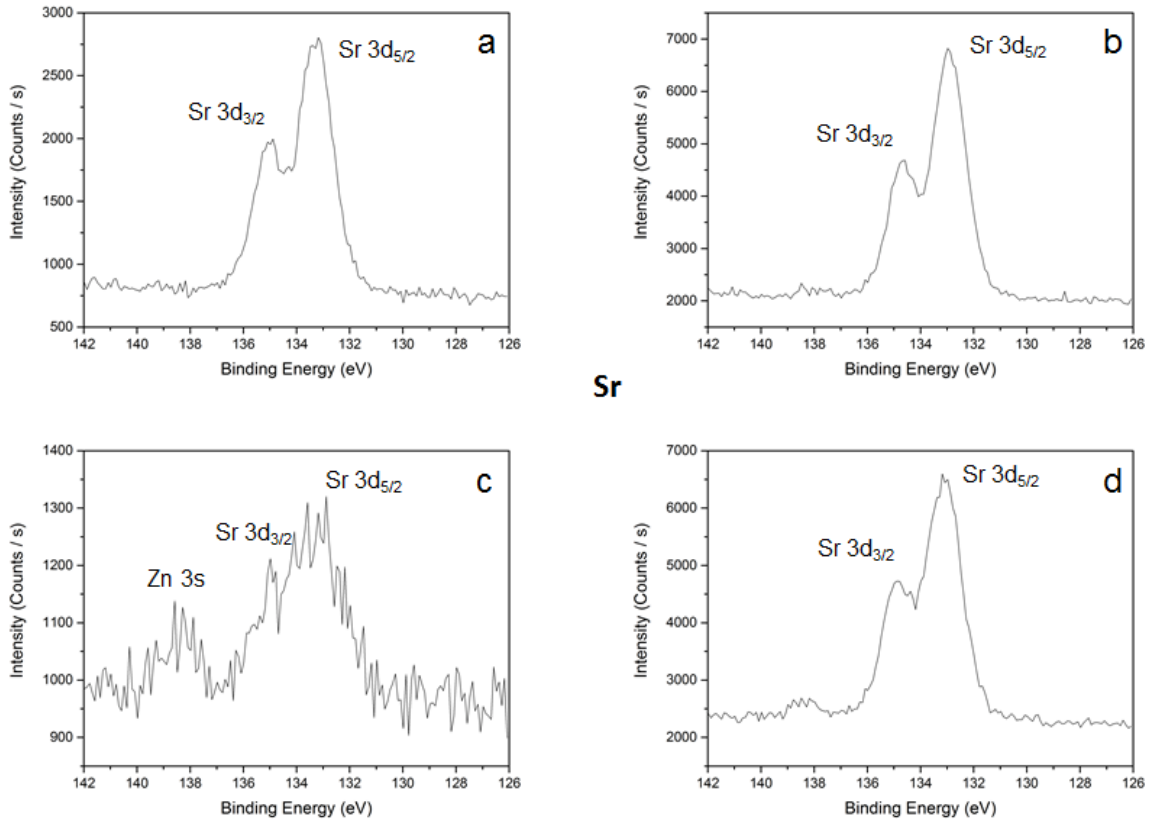

Figure 6.27: Sr $3d_{3/2}$ and Sr $3d_{5/2}$ peaks from high-resolution XPS measurement of 1Ce10ScSZ/LSCrF8255 dual-phase membrane. Legend: a) unaged; b) aged in air at 1000˚C for 1000 h; c) aged in 4% H_2-96% N_2 at 1000˚C for 1000 h; d) aged in 5% H_2-95% CO_2 at 1000˚C for 1000 h.

The peak signals for Sr $3d_{3/2}$ and Sr $3d_{5/2}$ shown in Figure 6.27 show a deficiency of Sr signal in the dual-phase sample aged in 4% H_2-96% N_2 (Sample c) for 1000 hours. The same phenomenon was observed for the analogous sample aged for 300 hours shown in Figure 6.12. The high-resolution Sr XPS spectra for 1Ce10ScSZ/LSCrF8255 aged for 1000 hours is similar to the analogous XPS spectra measured for 300 hours. The Zn impurity observed in the sample aged in 4% H_2-96% N_2 for 1000 hours was also observed for the sample aged for 300 hours.

Peak fitting was performed on the sample aged in air (Sample b) and in 5% H_2-95% CO_2 (Sample d) and are shown in Figure 6.28. As was observed in Section 6.1.3.3 for the analogous peak fitting of the samples aged for 300 hours, the fit of the Sr 3d peak shapes for Samples b and d suggests that the Sr within the near-surface of dual-phase 1Ce10ScSZ/LSCrF8255 likely exists as either as an oxide (SrO) or a carbonate ($SrCO_3$).

However, the binding energies of the Sr $3d_{5/2}$ peak for the samples aged in air and in 5% H_2-95% CO_2 shown in Figure 6.28 are 132.9 eV and 133.1 eV respectively, which is closer to the binding energy of 132.9 eV for strontium oxide, SrO, than to the binding energy of 133.4 eV for strontium carbonate, $SrCO_3$. It is not expected that Sr exists as SrO on the surface of the samples exposed to CO_2 due to the exothermic reaction of SrO to CO_2 to produce $SrCO_3$ in standard conditions.

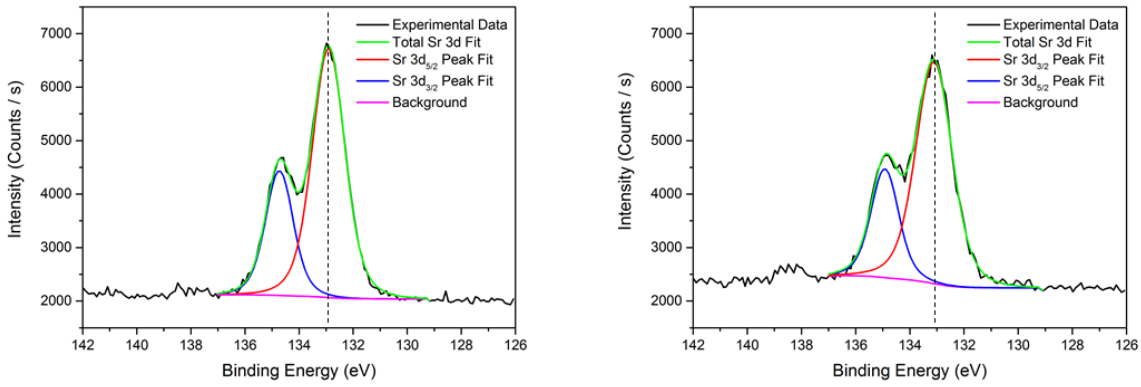

Figure 6.28: Sr 3d peak fits for 1Ce10ScSZ/LSCrF8255 aged at 1000°C for 1000 h in air (left) and 5% H_2-95% CO_2 (right)Figure 6.28. Dotted vertical line denotes binding energy of Sr $3d_{5/2}$ peak. Similar to the analogous materials aged for 300 h, accuracy of the peak fit suggests the presence of a single Sr compound on the near-surface of the dual-phase material is more likely than the presence of two Sr compounds.

The high-resolution XPS spectra for Cr $2p_{1/2}$ and Cr $2p_{3/2}$ of 1Ce10ScSZ/LSCrF8255 are shown in Figure 6.29. A Cr signal was observed on the near-surface of dual-phase 1Ce10ScSZ/LSCrF8255 aged for 1000 hours, although the Cr signal in the material aged in air (Sample b) suffers from low signal-to-noise ratio. The observation of Cr peak signals on the near-surface of 1Ce10ScSZ/LSCrF8255 is inconsistent with the absence of the signal for the analogous samples aged for 300 hours, in particular for the samples aged in 4% H_2-96% N_2 (Sample c) and in 5% H_2-95% CO_2 (Sample d). This suggests that depletion of Cr at the surface of dual-phase 1Ce10ScSZ/LSCrF8255 can be somewhat reversed under prolonged exposure to reducing conditions at elevated temperatures.

The vertical lines shown in Figure 6.29 denote the approximate positions for the Cr $2p_{1/2}$ and Cr $2p_{3/2}$ peaks of Cr (III) oxide, which match the peak positions of the XPS spectra. In addition, the high-resolution Cr 2p XPS spectra of the dual-phase material aged in 5% H_2-95% CO_2 shown in Figure 6.29 is similar to the high-resolution spectra reported by Biesinger et. al. [30] on Cr_2O_3 cleaved in a vacuum. Biesinger et. al. [30] determined that the Cr $2p_{3/2}$ peak positions for Cr metal and Cr (III) oxide were approximately 574.2 eV

and 576.8 eV respectively, suggesting that the oxidation state of Cr on the near-surface of dual-phase 1Ce10ScSZ/LSCrF8255 aged in 5% H_2-95% CO_2 (Figure 6.29d) is +3. The Cr 2p peak signals in the other XPS spectra are too noisy to accurately determine the oxidation state. The Cr $2p_{3/2}$ peak positions for the Cr (VI) compounds CrO_3, $(CrO_4)^{2-}$ and $(Cr_2O_7)^{2-}$ were found to be 579.2, 579.5 and 579.6 respectively, suggesting Cr does not adopt a +6 oxidation state in the near-surface for any of the materials.

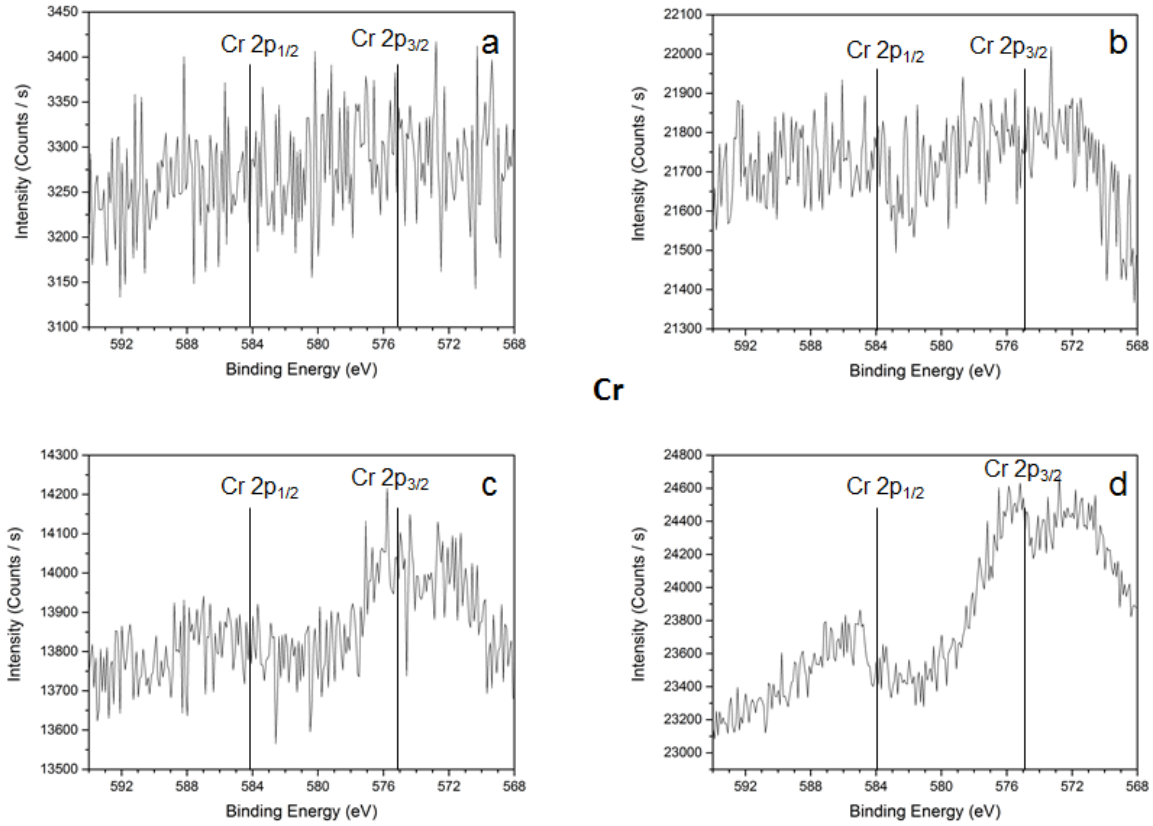

Figure 6.29: Cr $2p_{1/2}$ and Cr $2p_{3/2}$ peaks from high-resolution XPS measurement of 1Ce10ScSZ/LSCrF8255 dual-phase membrane. Legend: a) unaged; b) aged in air at 1000˚C for 1000 h; c) aged in 4% H_2-96% N_2 at 1000˚C for 1000 h; d) aged in 5% H_2-95% CO_2 at 1000˚C for 1000 h. Cr peak signals were observed within the near-surface of the materials aged in reducing conditions (Samples c and d).

The high-resolution XPS spectra for Fe $2p_{1/2}$ and Fe $2p_{3/2}$ of 1Ce10ScSZ/LSCrF8255 are shown in Figure 6.30. The peak signal was observed to be strongest in the material aged in 5% H_2-95% CO_2 (Sample d) but was present in all the samples aged for 1000 hours. The peak positions for Fe $2p_{1/2}$ and Fe $2p_{3/2}$ of Fe (III) oxide are estimated to be at BE ~ 722 eV and BE ~ 710 eV respectively, shown with vertical lines in Figure 6.30. The high-resolution XPS spectra for dual-phase 1Ce10ScSZ/LSCrF8255 also resemble the high-

resolution XPS spectra of Fe $2p_{3/2}$ observed by Grosvenor et. al. [24] for Fe_2O_3 or FeOOH, suggesting that Fe adopts a +3 oxidation state within the near-surface region of 1Ce10ScSZ/LSCrF8255 aged in 5% H_2-95% CO_2.

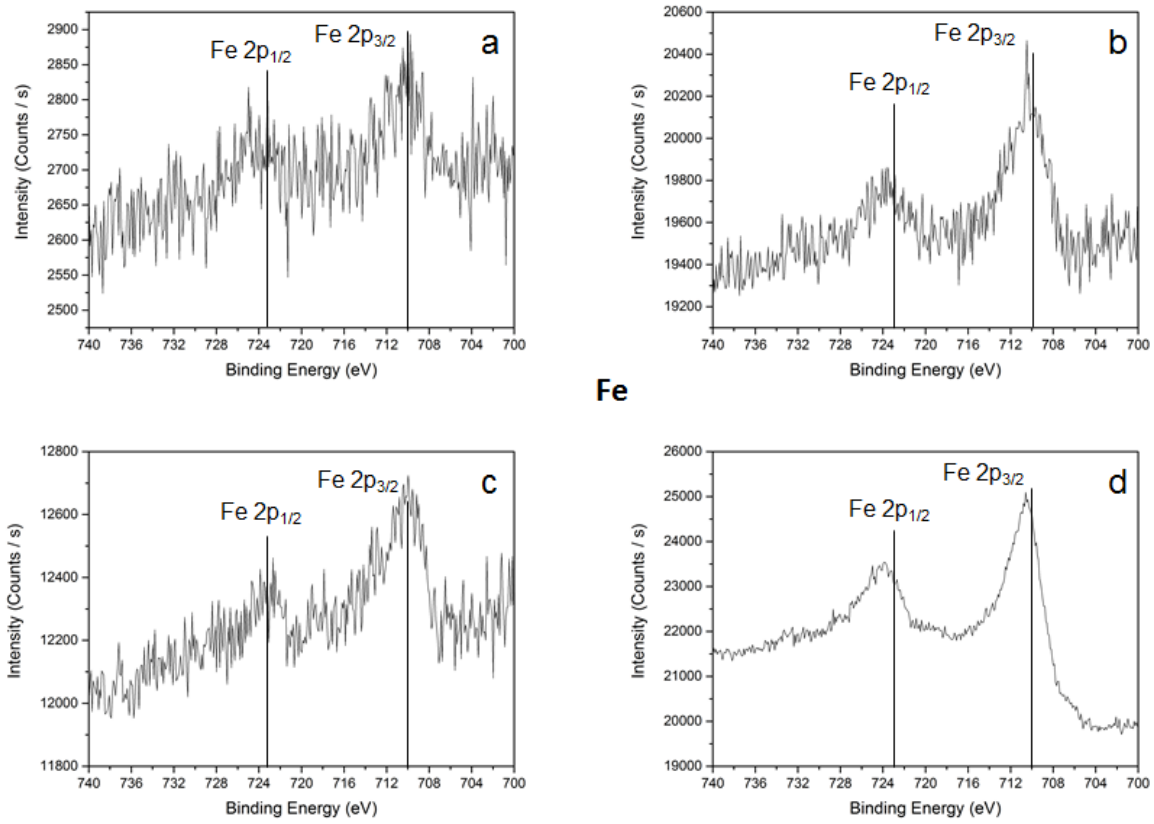

Figure 6.30: Fe $2p_{1/2}$ and Fe $2p_{3/2}$ peaks from high-resolution XPS measurement of 1Ce10ScSZ/LSCrF8255 dual-phase membrane. Legend: a) unaged; b) aged in air at 1000˚C for 1000 h; c) aged in 4% H_2-96% N_2 at 1000˚C for 1000 h; d) aged in 5% H_2-95% CO_2 at 1000˚C for 1000 h.

Figure 6.31 and Table 6-5 summarizes the relative concentrations at the near-surface of the elements comprising dual-phase 1Ce10ScSZ/LSCrF8255 aged for 1000 hours. The relative concentrations were calculated in the same manner as outlined in Section 6.2.3.3 for the dual-phase materials aged for 300 hours. Similar to the materials aged for 300 hours, dual-phase 1Ce10ScSZ/LSCrF8255 aged for 1000 hours shows that the near-surface (~10 nm) of the material is elevated in Zr content, particularly for the sample aged in 4% H_2-96% N_2. The presence of Zr on the near-surface for the sample aged in air (Sample b) for 1000 hours was calculated to be close to the ideal bulk stoichiometry, but observed a significant elevated presence of Sr. This observation was in contrast with the analogous material aged for 300 hours which showed a deficiency in Sr within ~10 nm of the sample

surface. As a result, it is unclear if the elevated Sr content observed in 1Ce10ScSZ/LSCrF8255 was due to prolonged exposure to air at elevated temperatures.

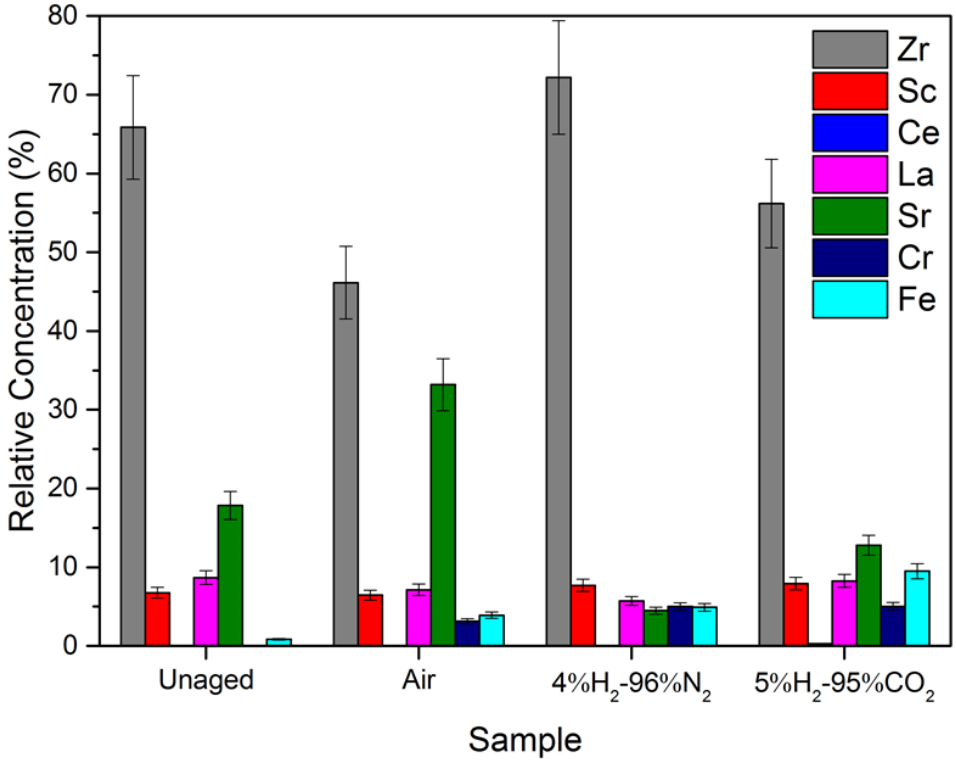

Figure 6.31: Relative concentration of component elements in near-surface (~10 nm) of 50/50 vol% 1Ce10ScSZ/LSCrF8255 dual-phase membrane after aging for 1000 h obtained from high-resolution XP spectra. The relative concentration of the unaged sample is added for reference. The relative concentration of Zr is significantly elevated on the near-surface (~10 nm) of the dual-phase material. The presence of both Cr and Fe were detected for all three aged samples. The Sr concentration was elevated for the sample aged in air for 1000 h.

The relative concentrations of the elements comprising the LSCrF8255 component are comparatively low. Unlike the materials aged for 300 hours, the presence of Cr was observed within ~10 nm of the sample surface for all three samples aged for 1000 hours. However, the presence of Cr and Fe on the near-surface was significantly below the expected bulk stoichiometric concentration, which was consistent with analyses of the near-surface for the dual-phase materials aged for 300 hours outlined in Section 6.1.3.3. This was consistent with the low concentrations of Cr observed on the outer atomic surface of 1Ce10ScSZ/LSCrF8255 as detailed in Section 6.1.3.1.

Table 6-5: Relative concentration of component elements in near-surface (~10 nm) of 50/50 vol% 1Ce10ScSZ/LSCrF8255 dual-phase membrane before and after aging for 1000 hours obtained from high-resolution XPS spectra. The phrase "und." denotes signal was undetected by the XPS instrument under the experimental parameters.

Element	Ideal Bulk Stoichiometry (%)	Unaged (%)	Aged Air (%)	Aged 4%H_2-96%N_2 (%)	Aged 5%H_2-95%CO_2 (%)
Zr	44.5	65.8	46.1	72.1	56.2
Sc	5.0	6.8	6.5	7.7	7.9
Ce	0.5	und.	und.	und.	0.3
La	20.0	8.7	7.1	5.7	8.3
Sr	5.0	17.8	33.2	4.5	12.8
Cr	12.5	und.	3.1	5.0	5.0
Fe	12.5	0.9	3.9	4.9	9.5

6.2.3.4 XPS Summary

X-ray photoelectron spectra were obtained for the dual-phase 1Ce10ScSZ/LSCrF8255 material aged for 1000 hours in three conditions (air, 4%H_2-96%N_2 and 5%H_2-95%CO_2) and compared to the unaged material. Observations made for the samples aged for 1000 hours are similar to those made in Section 6.1.3.3 for the analogous samples aged for 300 hours. Analysis of the high-resolution XPS spectra showed that Zr and Sc exists in oxide forms, ZrO_2 and Sc_2O_3, respectively. The shape and magnitude of energy separation for the La $3d_{5/2}$ peak suggests that La exists as hydroxide $La(OH)_3$ within ~10 nm of the sample surface regardless of aging condition. Peak fitting of the Sr signals shows that

strontium likely exists as carbonate $SrCO_3$, with the presence of other strontium compounds (such as SrO) unlikely. The presence of Cr was detected within the near-surface via XPS for the samples, and was determined to exist in Cr (III) oxide form [30]. The oxidation state of Fe is estimated to be +3 based on the position of the Fe $2p_{3/2}$ peak [24].

Relative quantification of the high-resolution XPS spectra shows that Zr is significantly elevated on the near-surface of the dual-phase 1Ce10ScSZ/LSCrF8255 samples after aging in reducing conditions (4% H_2-96% N_2 and 5% H_2-95% CO_2) compared to the ideal bulk stoichiometry. The sample aged for 1000 hours in air exhibited significantly elevated Sr concentration, which was not observed for the analogous sample aged for 300 hours. The relative concentrations of Cr and Fe were deficient within the near-surface of the dual-phase material regardless of aging conditions which was similarly observed for the materials aged for 300 hours.

6.2.4 Summary of the Effects of Aging (1000 hrs) on 1Ce10ScSZ/LSCrF8255

Characterization of dual-phase 1Ce10ScSZ/LSCrF8255 aged in three conditions (air, 4% H_2-96% N_2 and 5% H_2-95% CO_2) for 1000 hours was performed using X-ray Diffraction and Secondary Electron Microscopy. The oxygen transport kinetics of the material were determined via IEDP-SIMS under both ^{18}O and $H_2{}^{18}O$ conditions to observe the effects of water on oxygen transport kinetics. Surface chemistry of the material was examined using Low Energy Ion Scattering and X-ray Photoelectron Spectroscopy.

The presence of the $SrCrO_4$ phase observed in the materials aged for 300 hours in air and 5%H_2-95%CO_2 is present in all the samples aged for 1000 hours. Backscattered electron micrographs of the aged samples showed relatively high distribution of the two component phases after 1000 hours of aging.

Isotope exchange experiments of dual-phase 1Ce10ScSZ/LSCrF8255 before and after aging for 1000 hours were performed under dry ^{18}O environment at 800˚C. The self-diffusion coefficients D^* of the samples did not significantly change among the aged samples, with D^* reaching mid-10^{-8} cm^2 s^{-1} for the materials before and after aging. This suggests that oxygen self-diffusion in the bulk of dual-phase 1Ce10ScSZ/LSCrF8255 is relatively unaffected after 1000 hours of exposure to the aging conditions chosen in this work. The surface exchange coefficients k^* of dual-phase 1Ce10ScSZ/LSCrF8255 before and after aging for 1000 hours showed elevated surface exchange kinetics for the materials aged in reducing conditions, exhibiting a value one order of magnitude higher than the unaged sample. In contrast, k^* was observed to be lower in the sample aged in air.

Isotope exchange experiments of dual-phase 1Ce10ScSZ/LSCrF8255 before and after aging for 1000 hours were also performed under 'wet' $H_2{}^{18}O$ environment. It was observed that D^* for all four samples was relatively unchanged from the analogous experiment performed in dry ^{18}O environment, with a slight decrease in the self-diffusion coefficient attributed to the lower temperature chosen for $H_2{}^{18}O$ exchange experiments (700°C). However, the surface exchange coefficients k^* were observed to be significantly improved for all four samples under $H_2{}^{18}O$ environment compared with the isotope exchange experiment performed in dry ^{18}O environment, with k^* for the aged samples approximately one order of magnitude higher. The disparity in the k^* observed between the unaged and aged samples under humid $H_2{}^{18}O$ exchange conditions was attributed to the higher homogeneity achieved on the unaged sample. A possible oxygen incorporation mechanism in the presence of water was found [26] that attempts to explain the increase in oxygen surface exchange kinetics in the presence of water for dual-phase 1Ce10ScSZ/LSCrF8255.

6.3 Conclusions

This chapter discusses the effects of aging in three environments (air, 4% H_2-96% N_2 and 5% H_2-95% CO_2) on 50/50 vol% dual-phase 1Ce10ScSZ/LSCrF8255. The dual-phase material did not experience significant degradation in its microstructure when observed via SEM after aging for 300 and 1000 hours. In addition, the formation of the $SrCrO_4$ secondary phase observed in the samples aged for 300 and 1000 hours did not have a significant impact on the oxygen transport kinetics of the material, with both the oxygen self-diffusion coefficients and surface exchange coefficients remaining the 10^{-8} cm^2 s^{-1} and 10^{-8} cm s^{-1} range respectively after aging. Oxygen surface exchange kinetics was found to improve significantly in the presence of water in the environment, evidenced by the comparison between dry ^{18}O and 'wet' $H_2{}^{18}O$ isotope exchange experiments.

Analysis of the surface chemistry of dual-phase 1Ce10ScSZ/LSCrF8255 showed a significantly elevated Zr concentration within ~10 nm of the surface of the material before and after aging for 300 hours. It was unclear if the outer surface also exhibited elevated Zr due to the inability to separate the Zr signal from the Sr signal. Cr deficiency on the outer atomic surface was also observed for both the unaged and aged samples. In addition, Fe deficiency was observed on the outer surface for the samples aged in reducing conditions (4% H_2-96% N_2 and 5% H_2-95% CO_2). Cr and Fe were similarly depleted within ~10 nm of the sample surface for both the unaged and aged samples, which suggests that aging under the chosen conditions for 300 hours does not have a significant effect on the presence of Cr or Fe on the surface of 1Ce10ScSZ/LSCrF8255. The depletion of La on both

the outer atomic surface and within ~10 nm of the surface of the material aged in 4% H_2-96% N_2 for 300 hours was also observed.

The surface chemistry of dual-phase 1Ce10ScSZ/LSCrF8255 aged for 1000 hours in the three conditions showed similar behavior to the analogous samples aged for 300 hours. Cr deficiency was observed on the outer surface for the samples aged for 1000 hours. However, Fe and La were also present for all aging conditions for 1000 hours, in contrast to the outer surface of the analogous sampled aged for 300 hours. Cr and Fe were not as depleted in the samples aged for 1000 hours as the samples aged for 300 hours within ~10 nm of the sample surface, which may suggest elemental depletion is not solely caused by aging environment. Overall, the surface chemistry of the surface of 50/50 vol% 1Ce10ScSZ/LSCrF8255 was not significantly altered after aging in the chosen conditions (air, 4% H_2-96% N_2 and 5% H_2-95% CO_2) up to 1000 hours.

6.4 References

[1] J. Joo, K. Yun, Y. Lee, J. Jung, C. Yoo, and J. Yu, "Dramatically Enhanced Oxygen Fluxes in Fluorite-Rich Dual-Phase Membrane by Surface Modification," *Chem. Mater.*, vol. 26, pp. 4387–4394, 2014.

[2] A. Shaula, V. Kharton, F. Marques, A. Kovalevsky, A. Viskup, and E. Naumovich, "Oxygen permeability of mixed-conducting composite membranes: effects of phase interaction," *J. Solid State Electrochem.*, vol. 10, pp. 28–40, 2006.

[3] "Database of Ionic Radii," *Atomistic Simulation Group, Imperial College London*.

[4] R. Berg, "The crystal structure of $SrCrO_4$, a phase in $La_{0.8}Sr_{0.2}CrO_3$ samples, determined by Rietveld refinement of x-ray powder diffraction data," *High Temp. Electrochem. Ceram. Met.*, 1996.

[5] S. Gupta, M. Mahapatra, and P. Singh, "Lanthanum chromite based perovskites for oxygen transport membrane," *Mater. Sci. Eng. R Reports*, vol. 90, pp. 1–36, 2015.

[6] W. He, H. Huang, M. Chen, J. Gao, and C. Chen, "Stability and oxygen transport property of $La_{0.8}Sr_{0.2}Cr_{0.5}Fe_{0.5}O_{3-\delta}$," *Solid State Ionics*, vol. 260, pp. 86–89, 2014.

[7] M. Mori, T. Yamamoto, H. Itoh, and T. Watanabe, "Compatibility of alkaline earth metal (Mg, Ca, Sr)-doped lanthanum chromites as separators in planar-type high-temperature solid oxide fuel cells," *J. Mater. Sci.*, vol. 2, no. 31, pp. 2423–2431, 1997.

[8] C. Sun, R. Hui, and J. Roller, "Cathode materials for solid oxide fuel cells: A review," *J. Solid State Electrochem.*, vol. 14, no. 7, pp. 1125–1144, 2010.

[9] J. Fergus, "Effect of cathode and electrolyte transport properties on chromium

poisoning in solid oxide fuel cells," vol. 32, pp. 3664–3671, 2007.

[10] T. Wei, X. Liu, C. Yuan, Q. Gao, and X. Xin, "A modified liquid-phase-assisted sintering mechanism for $La_{0.8}Sr_{0.2}Cr_{1-x}Fe_xO_{3-d}$: A high density, redox-stable perovskite interconnect for solid oxide fuel cells," *J. Power Sources*, vol. 250, pp. 152–159, 2014.

[11] M. Oishi, K. Yashiro, K. Sato, J. Mizusaki, and T. Kawada, "Oxygen nonstoichiometry and defect structure analysis of B-site mixed perovskite-type oxide (La,Sr)(Cr,M)O_{3-d} (M = Ti, Mn and Fe)," *J. Solid State Chem.*, vol. 181, pp. 3177–3184, 2008.

[12] J. Crank, *The Mathematics of Diffusion*. Clarendon Press, 1979.

[13] S. Cooper, "Quantifying the Transport Properties of Solid Oxide Fuel Cell Electrodes," 2015.

[14] Z. Shen, "Mass Transport in Mixed-Conducting LSCrF-ScSZ Dual Phase Composites for Oxygen Transport Membrane Applications," Imperial College London, 2017.

[15] H. Brongersma, M. Draxler, M. Deridder, and P. Bauer, "Surface composition analysis by low-energy ion scattering," *Surf. Sci. Rep.*, vol. 62, no. 3, pp. 63–109, Mar. 2007.

[16] M. de Ridder, R. van Welzenis, and H. Brongersma, "Surface cleaning and characterization of yttria-stabilized zirconia," *Surf. Interface Anal.*, vol. 33, no. 4, pp. 309–317, 2002.

[17] M. Biesinger, L. Lau, A. Gerson, and R. Smart, "Resolving surface chemical states in XPS analysis of first row transition metals , oxides and hydroxides : Sc , Ti , V , Cu and Zn," *Appl. Surf. Sci.*, vol. 257, no. 3, pp. 887–898, 2010.

[18] R. Gupta and S. Sen, "Calculation of multiplet structure of core p-vacancy levels. II," *Phys. Rev. B*, vol. 12, no. 1, pp. 15–19, 1975.

[19] P. Mack, "Spectroscopic Analysis of Solid Oxide Fuel Cell Material with XPS," *Thermo Fisher Scientific*, 2011, pp. 2–4.

[20] P. Gallagher, M. Brown, and R. Kemp, *Handbook of Thermal Analysis and Calorimetry, Volume 1: Principles and Practice (1st Edition)*. 1998.

[21] N. Sakai, H. Yokokawa, and T. Horita, "Lanthanum Chromite-Based Interconnects as Key Materials for SOFC Stack Development," *Int. J. Appl. Ceram. Technol.*, vol. 30, pp. 23–30, 2004.

[22] Z. Yang, A. Harvey, and L. Gauckler, "Influence of CO_2 on $Ba_{0.2}Sr_{0.8}Co_{0.8}Fe_{0.2}O_{3-\delta}$ at

elevated temperatures," *Scr. Mater.*, vol. 61, pp. 1083–1086, 2009.

[23] M. Biesinger, B. Payne, A. Grosvenor, L. Lau, A. Gerson, and R. Smart, "Resolving surface chemical states in XPS analysis of first row transition metals, oxides and hydroxides: Cr, Mn, Fe, Co and Ni," *Appl. Surf. Sci.*, vol. 257, no. 7, pp. 2717–2730, 2011.

[24] A. Grosvenor, B. Kobe, M. Biesinger, and N. Mcintyre, "Investigation of multiplet splitting of Fe 2p XPS spectra and bonding in iron compounds," *Surf. Interface Anal.*, vol. 36, no. October, pp. 1564–1574, 2004.

[25] "CasaXPS: Processing Software for XPS, AES, SIMS and More." [Online]. Available: http://www.casaxps.com/. [Accessed: 18-Jul-2017].

[26] N. Sakai, K. Yamaji, T. Horita, and Y. Xiong, "Effect of Water on Oxygen Transport Properties on Electrolyte Surface in SOFCs I. Surface Reaction Mechanism of Oxygen Isotope Exchange on Solid," pp. 6–11, 2003.

[27] T. Ishihara, S. Fukui, and H. Matsumoto, "Effects of Water Coexisting on the Cathode Activity for the Solid Oxide Fuel Cells Using $LaGaO_3$-Based Perovskite Oxide Electrolyte," pp. 2035–2039, 2005.

[28] M. Verkerk, A. Winnubst, and A. Burggraaf, "Effect of impurities on sintering and conductivity of yttria-stabilized zirconia," *J. Mater. Sci.*, vol. 17, pp. 3113–3122, 1982.

[29] O. Bohnke, V. Gunes, K. Kravchyk, A. Belous, O. Yanchevskii, and O. Yunov, "Ionic and electronic conductivity of 3 mol% Fe_2O_3-substituted cubic yttria-stabilized ZrO_2 (YSZ) and scandia-stabilized ZrO_2 (ScSZ)," *Solid State Ionics*, vol. 262, pp. 517–521, 2014.

[30] M. Biesinger, C. Brown, J. Mycroft, R. Davidson, and N. Mcintyre, "X-ray photoelectron spectroscopy studies of chromium compounds," *Surf. Interface Anal.*, vol. 36, no. October, pp. 1550–1563, 2004.

7 Conclusions and Future Work

The degradation effects of aging in simulated operating environments on the oxygen transport kinetics and surface chemistry of 50/50 vol.% dual-phase $Sc_{0.10}Ce_{0.01}Zr_{0.89}O_{2-\delta}$/$(La_{0.8}Sr_{0.2})_{0.95}Cr_{0.5}Fe_{0.5}O_{3-\delta}$ (1Ce10ScSZ/LSCrF8255) was examined in this work.

The work began with the analysis of the 1Ce10ScSZ and LSCrF8255 single-phase components of the material. X-ray diffraction measurements showed single-phase 1Ce10ScSZ adopts a dual cubic-rhombohedral crystal structure in powder form that becomes cubic after sintering. Electrochemical Impedance Spectroscopy showed the material possesses high oxygen conductivity, with a decrease in activation energy at ~600˚C, corresponding to a likely change in crystal structure from stabilized cubic to natural cubic. Isotope exchange depth profiling/Secondary ion mass spectrometry (IEDP-SIMS) showed 1Ce10ScSZ exhibited high oxygen self-diffusion kinetics but very low surface exchange kinetics, requiring the use of a catalytic layer for oxygen incorporation. Surface chemical studies via low energy ion scattering (LEIS) showed the presence of stoichiometric elements, in addition to Na/Mg/Al/Si impurities, present on the outer atomic layer of 1Ce10ScSZ, with potential Ce surface segregation observed. Near-surface (~10 nm) quantification via X-ray photoelectron spectroscopy (XPS) of 1Ce10ScSZ showed possible Ce deficiency in this region. Quantification also showed minimal change in near-surface chemistry of the material after exposure to air or 5%H_2-95%CO_2 at 1000˚C for 300 hours.

X-ray diffraction measurements on single-phase LSCrF8255 adopts an orthorhombic crystal structure after sintering. The outer atomic surface of LSCrF8255 determined by LEIS exhibited Sr excess and Cr depletion. The stoichiometric elements were present within the near-surface of LSCrF8255 obtained via XPS, in addition to minor amounts of Ba impurities. Quantification of LSCrF8255 showed Sr excess and Fe deficiency within the near-surface (~10 nm) of the material. Quantification also showed that Sr excess and Cr deficiency was observed for LSCrF8255 exposed to air at 1000˚C for 300 hours, but Sr deficiency and Cr excess when exposed to 5%H_2-95%CO_2 for the same temperature and aging duration.

The effects of degradation on dual-phase 1Ce10ScSZ/LSCrF8255 was made by exposing the material to three separate conditions (air, 4%H_2-96%N_2, 5%H_2-95%CO_2) for two periods of time (300 hours, 1000 hours). The material did not experience significant degradation in its microstructure after any aging procedure. The formation of a $SrCrO_4$ secondary phase was observed for the material after 1000 hours of aging in all

environments, as well as in air and 5%H_2-95%CO_2 after 300 hours. The oxygen transport kinetics measured via IEDP-SIMS experiments for 1Ce10ScSZ/LSCrF8255 in dry ^{18}O environment showed minimal changes to the oxygen self-diffusion coefficient D^* and surface exchange coefficients k^* before and after aging for 300 hours and 1000 hours, with D^* and k^* on the order of 10^{-8} cm^2 s^{-1} and 10^{-8} cm s^{-1} respectively for all IEDP-SIMS measurements. Thus, it is concluded that aging under the three simulated operating environments for up to 1000 hours does not have a significant influence on the oxygen transport kinetics of dual-phase 1Ce10ScSZ/LSCrF8255.

Surface chemistry studies via LEIS of dual-phase 1Ce10ScSZ/LSCrF8255 showed Cr depletion on the outer surface regardless of environment or aging duration. In addition, Fe depletion was observed on the outer surface of 1Ce10ScSZ/LSCrF8255 exposed to reducing conditions (4%H_2-96%N_2, 5%H_2-95%CO_2) for 300 hours. However, Fe depletion was not observed for the analogous materials aged for 1000 hours, although Fe deficiency was observed for the material aged in 4%H_2-96%N_2 for 1000 hours. Quantification of the near-surface (~10 nm) via XPS showed that La deficiency was observed for all samples before and after aging. The presence of Zr is elevated for 1Ce10ScSZ/LSCrF8255 after aging for 300 hours from the ideal bulk stoichiometric composition. Ce and Cr was not present within the near-surface to instrumental detection limits, with Fe deficiency well below the ideal bulk stoichiometry observed for 1Ce10ScSZ/LSCrF8255 before and after 300 hours aging. Elevated Zr fraction, Fe deficiency, and Cr deficiency on the near-surface were not as prevalent for the analogous materials aged for 1000 hours. No linear correlation could be drawn between surface elemental composition examined via LEIS and XPS, and the aging duration.

Comparatively little analysis was done on the chemical composition of the intergranular region between the 1Ce10ScSZ and LSCrF8255 components. The chemical composition of the grain boundaries, in particular between the two components, may be important to examine to understand the behavior of cation migration from one phase to the other. Transmission Electron Microscopy with Energy Dispersive X-ray Spectroscopy (TEM-EDX) capability can be employed on a specially prepared sample of dual-phase 1Ce10ScSZ/LSCrF8255. Line scans beginning on a grain of one component across the grain boundary and ending on a grain of the other component can show the elemental concentration and how it changes with distance to the other component phase in 1Ce10ScSZ/LSCrF8255.

In addition, the effect of excessive concentrations of impurities on the oxygen transport kinetics would be of use to explore for dual-phase 1Ce10ScSZ/LSCrF8255. The impurity concentration of the powders used to make dual-phase samples for analysis in this work

were insufficiently low that any effects, beneficial or detrimental, were not observed. The intentional introduction of impurities typically present in the environment, such as Na, Si or Ca, on oxygen self-diffusion and surface exchange kinetics could be added to a point where D^* and k^* are significantly altered when examined using IEDP-SIMS experiments. Further studies could expose these samples to the aging conditions used in this work to determine the effects of environmental exposure to impurity behavior and overall oxygen transport kinetics.

Finally, longer aging durations could be employed on dual-phase 1Ce10ScSZ/LSCrF8255 to ascertain the approximate lifetime of these materials for use as oxygen transport membranes. To be commercially viable, it is estimated that the oxygen transport membrane must operate in excess of 20,000 hours before failure occurs [1]. Examinations via XRD, SEM/EDX, IEDP-SIMS, LEIS and XPS could be employed on these materials to ascertain the crystal structure, bulk chemical composition, oxygen transport kinetics or surface chemistry, and whether any of these factors contributed to failure of the material.

7.1 References

[1] S. Kelly, "Praxair's Oxygen Transport Membranes for Oxycombustion and Syngas Applications," 2014.

8 Appendix

8.1 Permissions

Figure 3.2

Order Summary

Order Date:	May 6, 2017
Order Number:	4103110716818
Publication:	Journal of the American Ceramic Society
Title:	The System Zirconia-Scandia
Type of Use:	Dissertation/Thesis
Order Total:	0.00 GBP

Figure 3.3

Order Summary

Order Date:	May 6, 2017
Order Number:	4103110954972
Publication:	Journal of Materials Science (full set)
Title:	Ionic conductivity ageing behaviour of 10 mol.% Sc2O3–1 mol.% CeO2–ZrO2 ceramics
Type of Use:	Thesis/Dissertation
Order Total:	0.00 USD

Table 3.1

Order Summary

Order Date:	May 6, 2017
Order Number:	4103190585191
Publication:	Materials Science and Engineering: R: Reports
Title:	Lanthanum chromite based perovskites for oxygen transport membrane
Type of Use:	reuse in a thesis/dissertation
Order Total:	0.00 USD